

**State-independent apparent aero-elastic properties of wind turbine rotors  
A method for the preliminary design of offshore wind support structures**

van der Male, P.

**DOI**

[10.4233/uuid:095689cb-03d4-458a-93a9-4a82c0f83cdc](https://doi.org/10.4233/uuid:095689cb-03d4-458a-93a9-4a82c0f83cdc)

**Publication date**

2021

**Document Version**

Final published version

**Citation (APA)**

van der Male, P. (2021). *State-independent apparent aero-elastic properties of wind turbine rotors: A method for the preliminary design of offshore wind support structures*. [Dissertation (TU Delft), Delft University of Technology]. <https://doi.org/10.4233/uuid:095689cb-03d4-458a-93a9-4a82c0f83cdc>

**Important note**

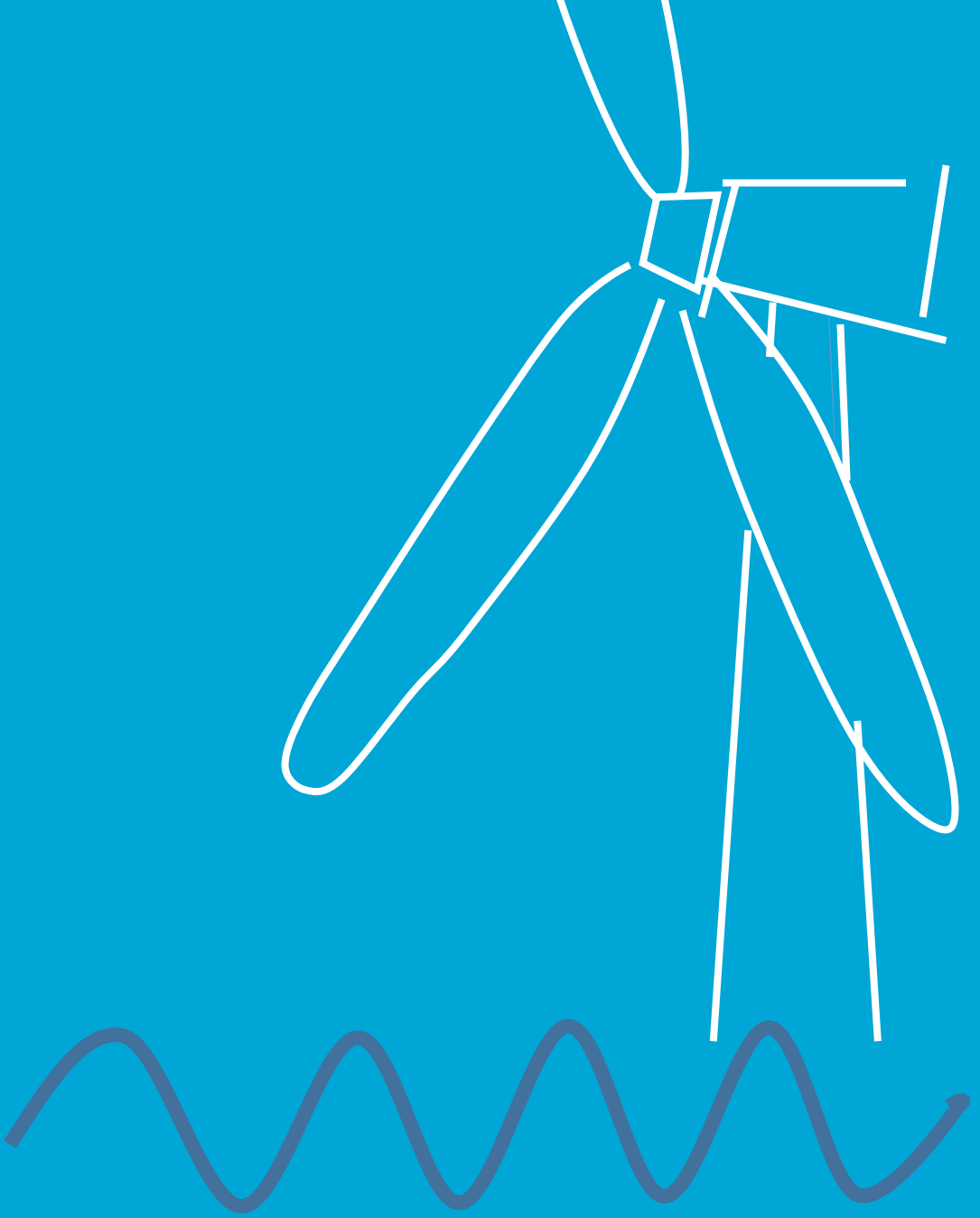
To cite this publication, please use the final published version (if applicable).  
Please check the document version above.

**Copyright**

Other than for strictly personal use, it is not permitted to download, forward or distribute the text or part of it, without the consent of the author(s) and/or copyright holder(s), unless the work is under an open content license such as Creative Commons.

**Takedown policy**

Please contact us and provide details if you believe this document breaches copyrights.  
We will remove access to the work immediately and investigate your claim.



**STATE-INDEPENDENT APPARENT AERO-ELASTIC  
PROPERTIES OF WIND TURBINE ROTORS  
A METHOD FOR THE PRELIMINARY DESIGN OF  
OFFSHORE WIND SUPPORT STRUCTURES**

Pim van der Male

# **STATE-INDEPENDENT APPARENT AERO-ELASTIC PROPERTIES OF WIND TURBINE ROTORS**

A METHOD FOR THE PRELIMINARY DESIGN OF OFFSHORE  
WIND SUPPORT STRUCTURES



# **STATE-INDEPENDENT APPARENT AERO-ELASTIC PROPERTIES OF WIND TURBINE ROTORS**

A METHOD FOR THE PRELIMINARY DESIGN OF OFFSHORE  
WIND SUPPORT STRUCTURES

## **Proefschrift**

ter verkrijging van de graad van doctor  
aan de Technische Universiteit Delft,  
op gezag van de Rector Magnificus Prof. dr. ir. T.H.J.J. van der Hagen,  
voorzitter van het College voor Promoties,  
in het openbaar te verdedigen op woensdag 10 maart 2021 om 12:30 uur

door

**Pim VAN DER MALE**

civiel ingenieur, Technische Universiteit Delft, Nederland  
geboren te Zwijndrecht, Nederland.

Dit proefschrift is goedgekeurd door de

promotor: Prof. dr. A.V. Metrikine

copromotor: Dr. ir. K.N. van Dalen

Samenstelling promotiecommissie:

Rector Magnificus,	voorzitter
Prof. dr. A.V. Metrikine,	Technische Universiteit Delft
Dr. ir. K.N. van Dalen,	Technische Universiteit Delft

*Onafhankelijke leden:*

Prof. dr. E. Bachynski,	Norwegian University of Science and Technology, Norway
Prof. dr. C. Su,	South China University of Technology, China
Prof. dr. J. Macdonald,	Bristol University, United Kingdom
Prof. dr. ir. A.S.J. Suiker,	Technische Universiteit Eindhoven
Prof. dr. D.A. von Terzi,	Technische Universiteit Delft
Prof. dr. M. Veljkovic,	Technische Universiteit Delft, reservelid



*Keywords:* wind turbines, support structures, aerodynamic force, aerodynamic damping, hydrodynamic force

*Printed by:* Gildeprint

*Cover design:* Pim van der Male

Copyright © 2020 by P. van der Male

ISBN 978-94-6419-155-4

An electronic version of this dissertation is available at  
<http://repository.tudelft.nl/>.

*Va, pensiero, sull'ali dorate;  
Va, ti posa sui clivi, sui colli*

Temistocle Solera





# CONTENTS

<b>Summary</b>	<b>xi</b>
<b>Samenvatting</b>	<b>xiii</b>
<b>1 Introduction</b>	<b>1</b>
1.1 The engineering practice . . . . .	2
1.1.1 Design procedure . . . . .	3
1.1.2 Design challenges . . . . .	4
1.2 Modelling strategies. . . . .	6
1.2.1 Aerodynamic interaction. . . . .	7
1.2.2 Hydrodynamic interaction. . . . .	12
1.2.3 Soil-structure interaction . . . . .	17
1.3 Code comparison and experimental validation . . . . .	21
1.4 Solution approaches . . . . .	24
1.4.1 Dynamic sub-structuring . . . . .	26
1.4.2 Load cases reduction. . . . .	27
1.4.3 Frequency-domain analysis . . . . .	29
1.5 Research focus . . . . .	31
1.6 Approach . . . . .	32
<b>2 Basic principles of rotor aerodynamics</b>	<b>35</b>
2.1 Fluid-structure interaction . . . . .	37
2.1.1 Idealized flow decompositions. . . . .	37
2.1.2 Wake vorticity . . . . .	38
2.1.3 Flow induction. . . . .	40
2.1.4 Viscous flows. . . . .	40
2.2 Modelling of the fluid-structure interaction. . . . .	41
2.2.1 Computational fluid dynamics techniques. . . . .	41
2.2.2 Momentum-balance methods . . . . .	42
2.2.3 Vortex methods . . . . .	49
2.3 Aerodynamic forcing . . . . .	50
2.3.1 Aerofoil definition . . . . .	50
2.3.2 Thin aerofoil theory . . . . .	51
2.3.3 Stationary inviscid flows . . . . .	53
2.3.4 Quasi-stationary aerofoil motions in inviscid flows . . . . .	55
2.3.5 Dynamic aerofoil oscillations in inviscid flows . . . . .	57
2.3.6 Incident airflow variations . . . . .	63
2.3.7 Viscous flow analysis. . . . .	70
2.3.8 Three-dimensional flows. . . . .	72

<b>3</b>	<b>Rotating blade analysis</b>	<b>73</b>
3.1	Rotating blade model . . . . .	75
3.1.1	Rotating beam modelling . . . . .	75
3.1.2	Model definition . . . . .	76
3.1.3	Equations of motion . . . . .	76
3.1.4	Eigenanalysis . . . . .	78
3.2	Aerodynamic interaction . . . . .	79
3.2.1	Force definitions . . . . .	79
3.2.2	Drag force model. . . . .	81
3.2.3	Instantaneous lift force model . . . . .	81
3.2.4	History-dependent lift force model . . . . .	82
3.2.5	Constituents of the air flow vector . . . . .	84
3.2.6	Reduced-frequency assessment . . . . .	85
3.3	Analysis procedure . . . . .	86
3.3.1	Aerodynamic force linearization . . . . .	86
3.3.2	Galerkin decomposition . . . . .	90
3.3.3	Fluctuating wind. . . . .	91
3.4	Results and discussion . . . . .	93
3.4.1	Linearized instantaneous aerodynamic forcing . . . . .	93
3.4.2	Linearized history-dependent aerodynamic forcing . . . . .	94
3.4.3	Non-linear aerodynamics . . . . .	96
3.5	Conclusions. . . . .	100
<b>4</b>	<b>State-independent apparent aero-elastic properties</b>	<b>103</b>
4.1	Rotor model. . . . .	107
4.1.1	System definition . . . . .	107
4.1.2	Equations of motion . . . . .	110
4.2	Aerodynamic excitation. . . . .	115
4.2.1	Force definitions . . . . .	115
4.2.2	Relative wind vectors . . . . .	117
4.2.3	Global aerodynamic forces. . . . .	118
4.3	Apparent aero-elastic properties . . . . .	119
4.3.1	Approximation procedure . . . . .	119
4.3.2	State-independent aerodynamic force approximations . . . . .	119
4.3.3	State-independent apparent stiffness approximations . . . . .	121
4.3.4	State-independent apparent damping approximations . . . . .	123
4.3.5	State-independent apparent mass approximations . . . . .	124
4.4	Apparent properties of an isotropic rotor . . . . .	125
4.4.1	Rotor definition and operational state . . . . .	125
4.4.2	Apparent stiffness for an isotropic rotor . . . . .	126
4.4.3	Apparent damping for an isotropic rotor . . . . .	128
4.4.4	Apparent mass for an isotropic rotor . . . . .	132

4.5	Turbine response analysis. . . . .	132
4.5.1	Turbine definition . . . . .	132
4.5.2	BLADED reference model. . . . .	134
4.5.3	Analysis approach . . . . .	136
4.5.4	Force analysis of a rotor on a rigid tower . . . . .	138
4.5.5	Response analysis to a step change in the upstream wind velocity . . . . .	138
4.5.6	Response analysis to a turbulent wind variation . . . . .	140
4.6	Conclusions. . . . .	149
<b>5</b>	<b>A wind and wave-excited pitch-regulated offshore wind turbine</b>	<b>151</b>
5.1	Model definition . . . . .	154
5.1.1	Turbine system definition . . . . .	154
5.1.2	System of equations of motion. . . . .	160
5.2	Extension of the state-independent apparent aero-elastic properties . . . . .	160
5.2.1	Influence of pitch actions on the aerodynamic excitation . . . . .	160
5.2.2	Approximation procedure . . . . .	163
5.2.3	Pitch angle-related state-independent expressions of the aerodynamic force . . . . .	164
5.2.4	Implementation of drive-train and pitch-control dynamics in terms of apparent aero-elastic properties. . . . .	166
5.3	Turbine response analysis. . . . .	168
5.3.1	Turbine definition . . . . .	168
5.3.2	Performance of the pitch control sub-system . . . . .	169
5.3.3	Analysis of simultaneous wind and wave excitations. . . . .	171
5.4	Conclusions. . . . .	181
<b>6</b>	<b>Conclusions</b>	<b>185</b>
	<b>References</b>	<b>191</b>
	<b>Epilogue</b>	<b>213</b>
	<b>Curriculum Vitae</b>	<b>215</b>
	<b>List of Publications</b>	<b>217</b>



# SUMMARY

**I**N the previous decade, offshore wind undeniably took off as an important player in the European energy market, which resulted in continuously enhancing turbine sizes and foundation structures pushing the boundaries of engineering, with the purpose of minimizing the levelized cost of energy to the range of optimal competitiveness. Regarding the foundation structure – or support structure – an important trade-off exists with respect to optimization and differentiation within an offshore wind farm on the one hand, and the required computational effort at an early stage of the design on the other. This effort comprises the extensive set of environmental conditions that require evaluation and the level of complexity of the modelling of the different environmental interactions, be it with wind, waves or soil.

Concerning the modelling of the environmental interactions with the structure, a decoupling of the turbine and the support structure is commonly applied, allowing the turbine manufacturer and the offshore contractor to develop their designs separately. The analysis of the support structure, however, has to account for the effect of the aerodynamic force, particularly for the aerodynamic damping, as this is known to affect the structural response to wave actions substantially. In this respect, the shared information usually concerns the damping ratio of the first fore-aft mode of vibration. This damping ratio does not explicitly express its dependency on the operational conditions of the turbine, e.g., the mean wind velocity and the rotor speed. Moreover, the provided ratio is only valid for the fore-aft motion in the first mode or vibration, and can therefore not be applied for higher fore-aft modes, or modes describing different motions, such as side-to-side or torsional.

This work investigates the possibility to describe the apparent aero-elastic properties, namely the added stiffness, damping and mass, for wind turbine rotors in closed form. To this end, first a single-blade analysis of a wind turbine blade is performed, to generate insight in the different modelling approaches of the aerodynamic excitation. The analysis distinguishes instantaneous and history-dependent force models and considers both non-linear and linearized expressions. It is shown that the response of the blade to turbulent inflow conditions can be estimated reasonably well with the linearized instantaneous force model, which provides the basis for the subsequent analysis of the apparent aero-elastic properties of the rotor as a whole.

Concerning the complete rotor, closed-form expressions for the apparent aero-elastic properties are presented, accounting for motions in three directions and cross-couplings between motions and forces. These system properties are presented state-independently, implying that they are independent of the structural motions. This independence allows for a linearized representation of the decoupled support structure system. At the same time, the explicit dependency on the operational conditions, as well as the control parameters – the blade pitch angle and the generator torque – allows for the response evaluation under different environmental circumstances. As the presented apparent aero-elastic

properties account for motions in three directions, the support structure response for yaw misalignments, and wind-wave misalignments can be assessed too.

The magnitudes of the apparent aero-elastic properties are illustrated for the rotor of the NREL 5 MW turbine, revealing the high contributions of the aerodynamic damping in yaw, and the aero-elastic coupling between the side-to-side and torsional motions. The performance of the presented method with the state-independent apparent aero-elastic properties is assessed by means of a comparison with a similar model defined with the software BLADED 4.6, which, contrarily to the current approach, accounts for the effect of flow separation on the aerodynamic force and includes higher-order contributions from the state-dependency of the aerodynamic force. Regarding the support structure, the dimensions of the UpWind monopile are adopted. To assess the response to combined wind-wave excitations, the presented method is extended with drive-train and control sub-systems – again based on the properties of the NREL 5 MW turbine – potentially allowing for the implementation of control strategies that aim for response reductions of the support structure.

The overall conclusions of this work is that the apparent aero-elastic properties, specifically the aerodynamic damping, of a rotor of a wind turbine can be defined in closed form and state-independently, accounting for motions in three directions and cross-couplings between motions and forces. The proposed method is shown to provide a good correspondence with the estimated response as obtained with the BLADED model, despite the mentioned restrictions of the application of the state-independent apparent aero-elastic properties. Additionally, an alternative method, which uses the response-independent aerodynamic force from the BLADED model, was considered, offering the benefit of a partial inclusion of the force contribution from flow separation. In obtaining the results, the focus is placed on the above-rated regime, in which the pitch-control system is activated.

With the application of the presented approach, the stress distribution in the support structure can be determined straightforwardly, depending explicitly on the operational conditions and the controller actions. With the inclusion of the controller response for transitions between the below and above-rated regime, the potential of the method can be increased further. This extension may involve the separate simulation of a drive-train model, which provides the response of the control variables as input for the decoupled simulations, offering the opportunity of frequency-domain analyses of the support structure of an offshore wind turbine.

# SAMENVATTING

**I**N in het afgelopen decennium is wind op zee ontegenzeggelijk een belangrijke speler op de Europese energiemarkt geworden, wat geresulteerd heeft in steeds grotere turbines en funderingsconstructies die de grenzen van de techniek bereikten, met het dusdanig minimaliseren van de *levelized cost of energy* als doel, dat de competitiviteit geoptimaliseerd wordt. Ten aanzien van de funderingsconstructie – of de ondersteuningsconstructie – is er aan de ene kant een belangrijke afweging aangaande de optimalisatie en differentiatie binnen een windpark op zee, en aan de andere kant de vereiste rekenkracht in een vroegtijdig ontwerpstadium. Deze rekenkracht is benodigd voor de analyse van de omvangrijke reeks aan weerkundige omstandigheden die beschouwd moet worden en de complexiteit die gepaard gaat met het modelleren van de verschillende hieruitvolgende omgevingsinteracties, met wind, golven en grond.

Wat betreft het modelleren van de omgevingsinteracties met de constructie, wordt doorgaans een ont koppeling van de turbine en de ondersteuningsconstructie toegepast, waardoor de turbinefabrikant en de offshore-aannemer hun ontwerpen afzonderlijk kunnen ontwikkelen. Bij de analyse van de ondersteuningsconstructie moet echter rekening worden gehouden met het effect van de aërodynamische kracht, in het bijzonder voor de aërodynamische demping, aangezien bekend is dat deze de structurele respons op golfbewegingen aanzienlijk beïnvloedt. In dit opzicht betreft de gedeelde informatie meestal de dempingsverhouding van de eerste voorwaartse trillingsmodus. Deze dempingsverhouding drukt niet expliciet zijn afhankelijkheid uit van de operationele omstandigheden van de turbine, bijvoorbeeld de gemiddelde windsnelheid en de rotorsnelheid. Bovendien is de verstrekte verhouding alleen geldig voor de voorwaartse beweging in de eerste trillingsmodus en kan daarom niet worden toegepast voor hogere modi van voor naar achter of modi die verschillende bewegingen beschrijven, zoals zijwaarts of torsie.

Dit werk onderzoekt de mogelijkheid om de schijnbare aëro-elastische eigenschappen, namelijk de toegevoegde stijfheid, demping en massa, te beschrijven voor windturbinerotoren in gesloten vorm. Hiertoe wordt eerst een enkelbladige analyse van een windturbineblad uitgevoerd om inzicht te verkrijgen in de verschillende modelleringsbenaderingen van de aërodynamische excitatie. De analyse maakt onderscheid tussen momentane en geschiedenis-afhankelijke krachtmodellen en houdt rekening met zowel niet-lineaire als gelineariseerde uitdrukkingen. Aangetoond wordt dat de reactie van het blad op turbulente instroomomstandigheden redelijk goed kan worden ingeschat met het gelineariseerde momentane krachtmodel, dat de basis vormt voor de daaropvolgende analyse van de schijnbare aëro-elastische eigenschappen van de rotor als geheel.

Wat betreft de volledige rotor worden uitdrukkingen in gesloten vorm voor de schijnbare aëro-elastische eigenschappen gepresenteerd, rekening houdend met bewegingen in drie richtingen en kruiskoppelingen tussen bewegingen en krachten. Deze systeemeigenschappen worden toestandsonafhankelijk gepresenteerd, wat impliceert dat ze onafhankelijk zijn van de structurele bewegingen. Deze onafhankelijkheid maakt

een gelineariseerde weergave van de ontkoppelde ondersteuningsconstructie mogelijk. Tegelijkertijd maakt de expliciete afhankelijkheid van de operationele omstandigheden, evenals de regelparameters – de bladhellingshoek en het generatorkoppel – een evaluatie van de respons mogelijk onder verschillende omgevingsomstandigheden. Aangezien de gepresenteerde schijnbare aëro-elastische eigenschappen corresponderen met bewegingen in drie richtingen, kan ook de respons van de ondersteuningsstructuur op wind en golven met een verschillende richting.

De omvang van de schijnbare aëro-elastische eigenschappen wordt geïllustreerd voor de rotor van de NREL 5 MW-turbine, waarbij de hoge bijdragen van de aërodynamische demping bij gieren en de aëro-elastische koppeling tussen de zijwaartse en torsiebewegingen worden onthuld. De prestatie van de gepresenteerde methode met de toestandsonafhankelijke schijnbaar aero-elastische eigenschappen wordt beoordeeld door middel van een vergelijking met een soortgelijk model gedefinieerd met de software BLADED 4.6, die, in tegenstelling tot de huidige benadering, het effect van stroomscheiding op de aërodynamische kracht beschrijft en bijdragen van hogere orden van de toestandafhankelijkheid van de aërodynamische kracht omvat. Wat betreft de ondersteuningsconstructie wordt rekening gehouden met de afmetingen van de UpWind-monopile. Om de respons op gecombineerde wind- en golfexcitatie te beoordelen, wordt de gepresenteerde methode uitgebreid met een aandrijflijn- en besturingssubstelsysteem - opnieuw gebaseerd op de eigenschappen van de NREL 5 MW-turbine - waardoor de implementatie van regelstrategieën die gericht zijn op voor responsvermindering van de ondersteuningsstructuur mogelijk wordt.

De algemene conclusies van dit werk zijn dat de schijnbare aero-elastische eigenschappen van een rotor van een windturbine, met in het bijzonder de aërodynamische demping, in gesloten vorm en toestandsonafhankelijk gedefinieerd kunnen worden, hierbij rekening houdend met bewegingen in drie richtingen en kruiskoppelingen tussen bewegingen en krachten. De voorgestelde methode blijkt een goede overeenkomst te bieden met de geschatte respons zoals verkregen met het BLADED-model, ondanks de genoemde beperkingen van de toepassing van de toestandsonafhankelijke schijnbare aëro-elastische eigenschappen. Bovendien wordt een alternatieve methode voorgesteld, die gebruik maakt van de responsonafhankelijke aerodynamische kracht van het BLADED-model, en die het voordeel biedt van een gedeeltelijke opname van de krachtbijdrage door stroomscheiding. Bij het verkrijgen van de resultaten wordt de focus gelegd op windsnelheden corresponderend met een bovennominale energie-opwekking, waarvoor de pitch-regeling geactiveerd wordt.

Met de toepassing van de gepresenteerde benadering kan de spanningsverdeling in de ondersteuningsconstructie expliciet afhankelijk van de operationele omstandigheden en de acties van het regelsysteem rechtstreeks worden bepaald. Met de opname van een beschrijvend van het regelsysteem voor transitie tussen windsnelheden in het beneden- en bovennominale regime, kan het toepassingsgebied van de methode verder worden vergroot. Deze uitbreiding kan de afzonderlijke simulatie van een aandrijflijnmodel omvatten, dat de respons van de regelvariabelen levert als input voor de ontkoppelde simulaties, wat de mogelijkheid biedt tot analyses in het frequentiedomein van de draagconstructie van een windturbine op zee.



# 1

## INTRODUCTION

*To meet the political goals regarding renewable energy production, offshore wind keeps expanding to waters with larger depths and harsher conditions, while the turbine size continues to grow and ever-larger foundation structures are required. This development can only be successful if not only the minimization of the direct levelized cost of energy is addressed, but also indirect costs concerning the industry's carbon footprint, the impact on biodiversity and end-of-life-time considerations. Regarding the design of the foundation structures, a particular challenge in this respect relates to the reduction of the total computational time required for the design. For both practical and commercial reasons, the decoupled modelling of offshore wind support structures finds a common application, especially during the preliminary design stage. This modelling approach aims at capturing the relevant characteristics of the different environmental interactions, while reducing the complexity as much as possible. This chapter presents a comprehensive review of the state-of-the-art approaches to modelling environmental interactions for offshore wind support structures. In this respect, the primary focus is on the monopile foundation, as this concept is expected to remain the prominent solution in the years to come. Current challenges in the field are identified, considering as well the engineering practice and the insights obtained from code comparison studies and experimental validations. It is concluded that the decoupled analysis provides valuable modelling perspectives, in particular for the preliminary design stage. In the further development of the different modelling strategies, however, the trade-off with computational costs should always be kept in mind.*

---

This chapter represents an adaptation of Van der Male *et al.* [1].

WHILE the current flourishing of offshore wind energy in Europe may very well become proverbial [2], the political debate still requires focus on the corresponding public costs – both financial and environmental. The extent to which this tendency of the discourse is biased, implying that no fair comparison with other methods of energy harvesting is conducted, should be the topic of decent investigation. Nevertheless, it cannot be disputed that a healthy industrial business should subject itself to restricting both costs mentioned.

Being still in its infancy<sup>1</sup>, the coming years will determine whether offshore wind<sup>2</sup> turns out to be either the prodigal child, or the outcast of its technological parents – onshore wind and offshore oil and gas [3]. Having the preferred horizontal axis rotor orientation already inherited from the former, the latter allowed for a thorough education from its decade-long experience in offshore developments, and moreover, scripted the genetic code for the preferred foundation solutions.

In order to raise healthily, the differences in reality should be recognized and faced. Contrarily to onshore wind turbines, its offshore siblings are exposed to both wind and wave excitations, affecting the dynamic behaviour and therefore the force distributions. Traditional offshore structures are commonly uniquely developed, while offshore wind farms generally consist of dozens of identical structures. On top of this, the risk profiles are incomparable, be it politically, technologically, economically, environmentally and with respect to public health and safety.

Lozano-Minguez *et al.* [4] presented a methodology for the systematic assessment of different conceptual designs for offshore wind support structures. The authors suggest to evaluate the different concepts not only on the basis of engineering and economic criteria, but emphasize the relevance of environmental aspects too, such as the carbon footprint and the potential beneficial impact on the biodiversity. Van Kuik *et al.* [5] indicate that the long-term impact on the marine ecosystem is not yet sufficiently analyzed. These impacts comprise, among others, the radiation of underwater noise and the hazards of the rotating blades for birds. On the other hand, the opportunity to employ offshore wind farms for sustainable food production and protein harvest is mentioned as well.

A responsible industry includes the end-of-life-time in its product development procedure. In order to really stand out with respect to the currently deplored fossil fuel industry, ‘offshore wind’ can no longer exclude a thorough life-cycle assessment and subsequent full-cycle optimization of its supply chain – contrarily to the traditional practice of sub-cycle optimization. Whether this optimization ends at cutting ‘the monopile and jacket foundations [...] into a depth more than 1 m below the mud line, so that the environmental impact is minimised and the process becomes more sustainable’ [6], may require some reassessment for the industry to become fully future-proof.

## 1.1. THE ENGINEERING PRACTICE

Whereas the minimization of the environmental impact during the complete life-time requires utmost attention, this work focusses on the design life-time of the support

<sup>1</sup>To the author’s believe, the growing up requires the first offshore wind farms to complete their full life-cycle.

<sup>2</sup>‘Offshore wind’ refers to the whole supply chain, including research, involved in the development of wind turbines at locations off-shore.

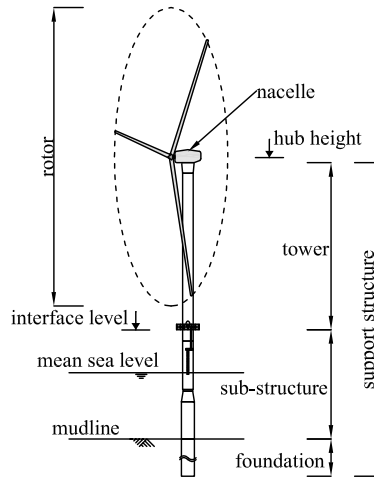


Figure 1.1: Schematic representation of a three-bladed monopile-based offshore wind turbines with the definitions according DNVGL-ST-0126 [7].

structure of single offshore wind turbines. In this respect, reference is made to the design standard DNVGL-ST-0126 [7], which defines the support structure as the structural component supporting the rotor-nacelle assembly. As an example, Figure 1.1 provides a schematic representation of a three-bladed monopile-based offshore wind turbine. The support structure itself is sub-divided into the tower, sub-structure and foundation, roughly corresponding to the elements exposed to air, water and soil, respectively.

### 1.1.1. DESIGN PROCEDURE

The stiffness of the foundation affects the aerodynamic excitation of a wind turbine. In addition, the hydrodynamic action on a support structure induces motions of the turbine rotor, which, as a result, experiences an aerodynamic resistance. For operating wind turbines, this resistance is of significant importance for the force distribution in the structure. As a result, an optimal analysis of the response of an offshore wind turbine requires an integrated design approach. Mainly for commercial reasons, however, the design of most offshore wind turbines takes place in a sequential – or iterative – manner, where one party designs the turbine and tower, and a second party designs the foundation, or sub-structure [8]. The sub-optimal assembly of an onshore wind turbine and a traditional offshore platform can easily be recognized here.

The design loop of a typical sequential design procedure of an offshore wind sub-structure is illustrated in Figure 1.2. As a first step, the foundation designer defines an initial geometry of the support structure. This initial geometry can be defined such, that the first natural frequency of the offshore wind turbine does not coincide with the aerodynamic and hydrodynamic frequency bands that contain most energy for structural excitation. In this respect, the rotational frequency of the rotor and the blade passing frequency are of particular relevance [9]. A procedure for the preliminary design of

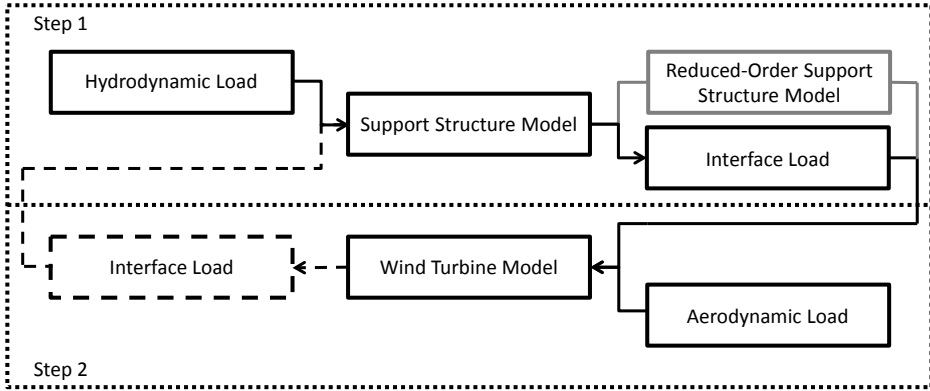


Figure 1.2: Schematic representation of the sequential design procedure for offshore wind turbines.

offshore wind monopile foundations was described by Arany *et al.* [10], resulting in rules of thumb to estimate the pile geometry for the initial design.

After defining the preliminary design of the support structure, the procedure starts with a model of the foundation structure, which is exposed to the hydrodynamic, and possibly seismic, loads (Step 1 in Figure 1.2). Subsequently, the model – or a reduced-order representation – and the response at the interface with the wind turbine are shared with the turbine designer, who evaluates the structural response of a wind turbine model to the aerodynamic excitations (Step 2). The response at the foundation interface can then be used to re-evaluate the structural model of the foundation structure, after which an updated foundation model initiates a subsequent design loop. Passon and Branner [11] provided a detailed description of this design sequence, and Van der Valk and Rixen [12] specifically addressed the derivation of equivalent interface forces, which are to be shared between the different design parties.

### 1.1.2. DESIGN CHALLENGES

The design of the support structures of offshore wind turbines involves multiple parties and models of varying complexity. At this point, the design of most offshore wind turbines involves a sequential procedure, requiring multiple iterations for optimized designs. On top of that, while the non-linear nature of the dynamic interactions between the structure and the environment results into digital brain-cracking simulations, the stochastic nature of these excitations imposes the necessity of a large number of such analyses to predict the governing stress distribution in the ultimate limit state and the accumulation of the fatigue damage. Because of these design iterations, the non-linearity of the structural interactions and the stochastic nature of the environmental excitations, the design procedure is incredibly time-consuming. Each design loop requires once again the simulation of the hydrodynamic load cases. Moreover, the aerodynamic analyses neither include the non-linear hydro-elastic coupling, nor the non-linear soil-structure interaction. As a consequence, the sequential design procedure is intrinsically sub-optimal.

Muskulus and Schafhirt [13] identified a number of challenges regarding the design of offshore wind support structures, the first of which concerns the non-linearity of wind excitations – wake development, dynamic flow, control – and wave excitations – wave slamming – as well as structural non-linearities, mainly from the soil-structure interaction. Vorpahl *et al.* [14] identified additional structural non-linearities, stemming from the active pitch and torque controls, and the large deflections of the commonly fibre-reinforced composite blades. With respect to the wind conditions, the characteristics of wake turbulence are of importance to evaluate a design within the context of the wind farm. The analysis of the hydrodynamic loads, from both waves and current, requires a valid assessment of both viscous and inertial aspects.

At the same time, the available tools to model for commercial applications do not account for the environmental interactions in full. For instance, the aerodynamic inflow is not described for non-uniform conditions and the effect of structural motions is not included. Concerning the hydrodynamic excitation, the load models are only valid for slender vertically submerged rigid cylinders and the action of irregular higher-order waves cannot be described. On the other hand, the available models do not allow for ‘quick-and-dirty’ preliminary design approaches either, leaving the designer with time-demanding tools, of which the actual accuracy is not fully known. Van Kuik *et al.* [5] recognized the different levels of fidelity of existing design tools for the different components relevant for the design of an offshore wind turbine. The need for holistic and comprehensive design methods is emphasized, which can be employed for different levels of design uncertainties.

Design analyses are required to assess both the ultimate and the fatigue limit states of the structure during its intended operational life-time. These analyses concern the load conditions during both operational and non-operational states of the turbine, as well as the transitional states of start-up or shut-down, under both normal and emergency conditions. Concerning the later, the occurrence of turbine faults negatively affecting the internal force distribution requires consideration [15].

The ultimate limit state assessment involves the definition of the extreme sea states and the corresponding extreme wave heights. Given the asymmetry of the support structure, due to the presence of appurtenances, Seidel *et al.* [9] suggested that twelve loading directions should be distinguished. In relating the water level and the extreme wave conditions, it should be noted that the lowest water level may induce breaking waves.

Seidel *et al.* [9] stated that the assessment of the fatigue limit state requires omnidirectional scatter tables, relating wind speeds at hub height to significant wave heights and significant wave heights to wave peak periods. Moreover, the wave directionality should be correlated to the directionality of the wind, ideally in bins of 30 degrees, distinguishing the mentioned twelve directions. If wind speed bins of 1 m/s are adopted, thousands of environmental states need to be evaluated for the full fatigue assessment.

After the installation of an offshore wind farm, metocean data is collected and structural accelerations are measured. These data allow for the validation of the designed structural properties, as well for the monitoring of the structural stress variations. Unfortunately, the amount of data available to the public is limited, but the published results of measurement campaigns reveal a discrepancy between the identified and the modelled

dynamic properties. Having the fatigue limit state as design driver, the most important consequence of this discrepancy is that the real accumulation of the fatigue damage deviates from the predicted accumulation, leaving the actual fatigue life-time of the structure unknown, unless a-posteriori estimation techniques are applied [16].

In summary, the following challenges in designing the foundation structures of offshore wind turbines are identified:

- The design of offshore wind turbines in a sequential manner, requiring multiple iterations for optimized designs.
- Given the non-linear dynamic interactions between the structure and the environment, and the stochastic nature of the environmental excitations, a large number of time-domain analyses are required to predict the governing stress distribution and the accumulation of the fatigue damage.
- The available modelling tools for commercial applications do not account for the environmental interactions in full, whereas these tools do not allow for quick preliminary designs either.
- Measurement campaigns, of which the results are publicly available, reveal a discrepancy between the identified and modelled dynamic properties, while the process of accumulation of the fatigue damage in the structure is not yet fully understood.

## 1.2. MODELLING STRATEGIES

The full analysis of an offshore wind turbine requires dynamic structural models of the support structure<sup>3</sup> and the rotor-nacelle assembly, including a model of the control system<sup>4</sup>, coupled to sufficiently large models of the surrounding media, involving the solving of the Navier-Stokes equations for the air and water flows and the applicable constitutive relations for the soil, see Figure 1.3. To the author's knowledge, such a comprehensive attempt has not taken place yet. Existing studies focus either on the modelling of one of the media, be it in the realm of academia or engineering [17–21], or on the dynamic description of the controlled offshore wind turbine [22–24]. The latter case is referred to as the integrated modelling approach, albeit that the full coupling with the surrounding media is not accounted for in full. The structural modelling is based on either finite elements or a multi-body approach, whereas the solution procedure generally involves a Galerkin decomposition. Existing software tools, such as BLADED and FAST [25] allow for the integrated analysis of offshore wind turbines, even though FAST requires coupling with separate modelling modules for the hydrodynamic and soil-structure interaction.

As a further simplification, the rotor-nacelle assembly and the support structure can be analysed in separate models. This so-called decoupled analysis finds practical application in the sequential design procedure, as described in Section 1.1.1, and in

<sup>3</sup>Support structures can be either bottom-founded or floating, i.e. bottom-moored, implying a large freedom of motion at the water level. Unless stated otherwise, the current study refers to the former type of structures.

<sup>4</sup>Many previous studies have been based on fixed-speed and/or stall-regulated turbines. For current analyses, variable-speed and pitch-regulated turbines are assumed, unless stated otherwise.

studies solely focussing on either the rotor sub-system or the support structure. The decoupled analysis of the support structure requires the definition of adequate boundary conditions at the tower top, as a substitute of a full rotor model. As an example, Figure 1.4 illustrates a decoupled support structure, modelled as a non-prismatic Euler-Bernoulli beam, in which the rotor-nacelle assembly is replaced by a concentrated mass at the tower top, an approach which is adopted in many studies [16, 26, 27], sometimes supplemented by the mass moments of inertia of the rigid rotor [28], so that the contribution of the rigid body motion of the rotor-nacelle assembly to the dynamic characteristics of the support structure is accounted for. In this example, the aerodynamic interaction is accounted for by an apparent mass and damping, whereas the soil-structure interaction is represented by distributed springs and dashpots. More realistic representations would account for frequency dependency of the interactions, as well as their non-linear character. Figure 1.4 does not present the apparent dynamic characteristics of the hydrodynamic interaction – mass and damping – which could affect the global dynamic characteristics of the system too.

The integrated analysis of an offshore wind turbine requires an explicit description of the different environmental interactions, with the surrounding fluids – air and water – and the soil. Moreover, the model needs to account for control actions, concerning the generator torque and the blade pitching, to realistically represent the force transfer to the support structure. For the decoupled analysis of a support structure, the aerodynamic rotor excitation including the turbine control is captured by a separate turbine model, and the aerodynamic interaction is accounted for by equivalent tower top forces and an additional damping. The following sections provide an overview of the various approaches and corresponding challenges to capture the environmental interactions in either integrated or decoupled models.

### 1.2.1. AERODYNAMIC INTERACTION

The aerodynamic inflow through the rotor plane of an operating wind turbine generates a circulatory flow around the aerofoil-shaped turbine blades, inducing a lift. The lift force distributed over the radii of the different blades produces an aerodynamic torque around the horizontal rotor axis, which drives the rotation of the rotor. The rotation of the horizontal axis generates a resisting torque at the generator – through either an indirect or a direct drive-train mechanism. Worth mentioning, in addition, is the fluid power transmission as a most recent development, for which no generator is required in the nacelle at the tower top [29].

Figure 1.5 depicts the aerodynamic torque and the thrust force on a turbine rotor as a function of the upstream wind speed. At relatively low wind speeds, when the generator does not produce its rated power, the rotational speed of the rotor is controlled by the generator torque. For above rated wind speeds, the torque is kept constant through a pitch control system [30, 31]. Whereas the aerodynamic torque extracts the energy from the airflow, the wind turbine is exposed to a thrust force, and tilt<sup>5</sup> and yaw moments too, as well as relatively small side and upward forces.

To a lesser extent, the viscous drag imposed by the flow on the blades contributes to

<sup>5</sup>Or pitch, the common term in aviation, which in the context of wind turbines may lead to confusion with the control system.

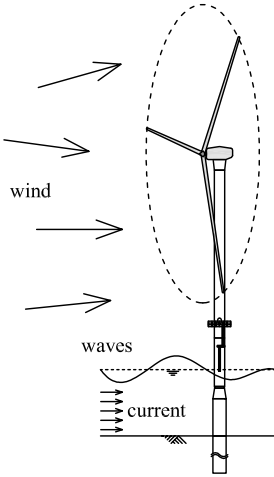


Figure 1.3: Schematic representation of a three-bladed monopile-based offshore wind turbine exposed to wind, waves and current.

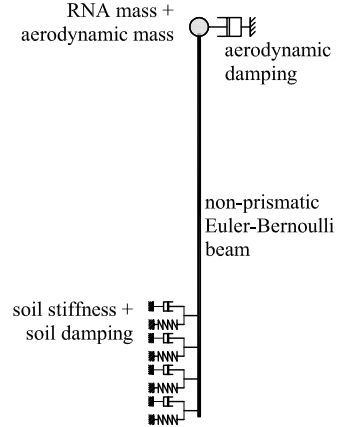


Figure 1.4: Example of a decoupled model of a monopile-based support structure, with the rotor-nacelle assembly (RNA) replaced by a concentrated mass.

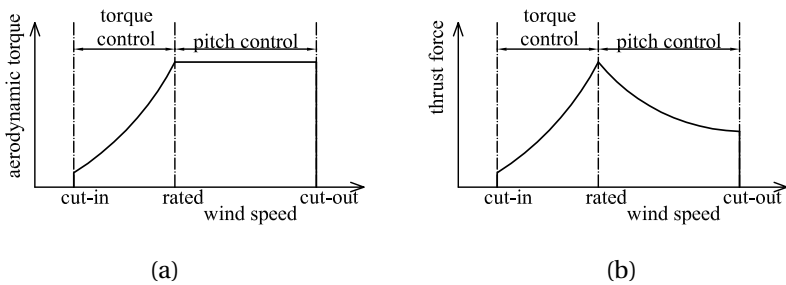


Figure 1.5: Schematic representation of (a) the aerodynamic torque, and (b) the thrust force on a turbine rotor as a function of the upstream wind speed.



the forcing. Both lift and drag are a function of the relative flow conditions, on the one hand, dependent on the inflow wind speed and the rotational velocity of the rotor, and, on the other hand, affected by the structural motions, see Figure 1.6. The dependency of the aerodynamic forcing on the relative motion is non-linear and history dependent<sup>6</sup>, implying that the load at a certain instance in time depends on the foregoing flow states. Besides, both forces depend on the inflow angle, or the angle of attack, which is defined as the inflow angle minus the geometrical twist and pitch of the blade. Structural motions induce variations in the angle of attack. For small angles of attack, the dependency of the drag force is negligible, as opposed to the lift force, which is strongly affected by the variations in the angle of attack. The aerodynamic aerofoil forcing has been addressed in both the frequency-domain and the time-domain in the historical works by Theodorsen [32] and Wagner [33].

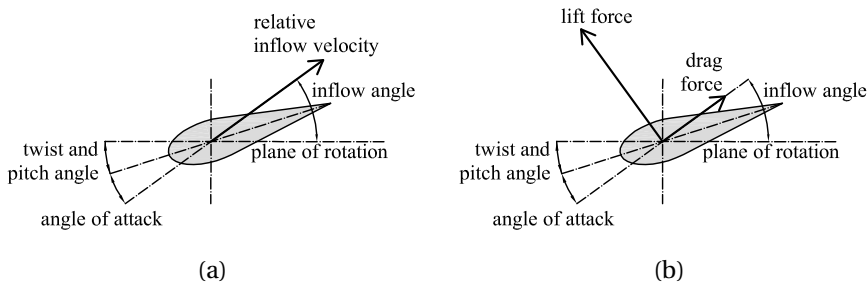


Figure 1.6: Schematic representation of (a) an aerofoil exposed to the relative inflow velocity resulting from the wind speed, the rotor speed and the structural motion, and (b) the resulting lift and drag forces acting on that aerofoil.

When considering the rotor as a whole, the flow conditions must obey the conservation laws (mass, momentum). The amount of extracted energy relates to the aerodynamic torque, which in turn results from the aerodynamic forcing on the rotor blades. As a consequence, the analysis of the aerodynamic excitation of a rotating rotor requires the combined analysis of both the global inflow conditions and the local blade forcing. This combined analysis is generally referred to as the blade element-momentum theory, which has been extensively described in several textbooks [34–36].

The one-dimensional blade element-momentum theory can account for both axial and tangential flow variations and the apparent inertia resulting from a time-varying inflow. To account for radially varying inflow conditions, the concepts of independent rotor annuli is adopted. For the estimation of the flow field at the rotor plane, the actuator disc concept is applied. The blade element-theory was extended to yawed flows [37], however, the upstream inflow conditions should still be uniform. The free wake vortex ring model, which is based on the discretization of the tubular vortex wake concept, offers an alternative approach to estimate the flow conditions at the rotor plane, for both

<sup>6</sup>An aerodynamicist would speak of 'unsteady', which is ambiguous in the field of structural dynamics.

time-varying and radially varying inflow conditions [38, 39]. Approaches to estimate the azimuthal variation of the inflow for finite-bladed rotors require the evaluation of the Biot-Savart law for each time step [40, 41], or involve solving the Navier-Stokes equations – representing the rotor blades by actuator lines [42, 43] or actuator surfaces [44, 45] – and quickly lose the applicability for design purposes because of the increasing computational demands. A schematic representation of some different approaches to estimate the flow field is provided by Figure 1.7. The estimation of the inflow conditions, while accounting for structural motions, requires the coupling of a computational fluid dynamics analysis with a dynamic structural model, a combination requiring tremendous skill and effort [46].

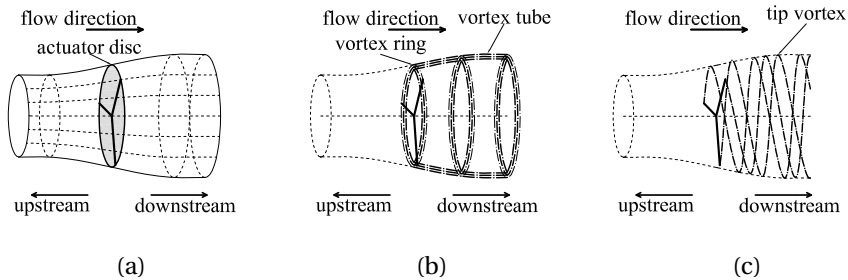


Figure 1.7: Schematic representation of different inflow and near-wake modelling approaches, distinguishing (a) the stream tube model for the momentum-balance method, (b) the free wake vortex ring model, and (c) the free vortex wake model.

Structural motions of the rotor also affect the relative inflow conditions, which subsequently affect the aerodynamic forcing on the blades. These motions result from vibrations of the blades, the drive-train or the support structure. Concerning the decoupled analysis of a support structure, the aerodynamic interaction can only depend on the tower top motion, which affects the relative velocity between the inflow and the structure. Despite the non-linear dependency of the aerodynamic excitation on the structural velocity, in decoupled analyses the aerodynamic interaction is commonly accounted for in terms of a modal damping, which is defined for the first mode of vibration only [47, 48].

The relevance of the aerodynamic damping for the force distribution of an offshore wind support structure was illustrated by Kühn [49]. The estimation of the life-time fatigue damage involves the response analysis to sea states which may induce resonance in the structure. The dynamic amplification at these frequencies is heavily affected by the amount of mobilized damping, to which the aerodynamic damping may give a substantial contribution. Garrad [50] derived a closed-form expression for this aerodynamic damping for a constant-speed turbine and attached-flow conditions, based on the analysis of the blade-element forcing on a rigid rotor. The derivation expresses the strong dependence of the damping coefficient on the rotational velocity of the rotor, implying an increase in damping for increasing below-rated wind speeds and a constant maximum damping for above-rated wind speeds. The closed-form expression was extended by Valamanesh and Myers [51], who included the drag contribution to the aerodynamic damping and explicitly related the damping to the rotor-induced flow velocities. Moreover, the authors provided an expression for the side-to-side damping of a turbine rotor.

Having an integrated model of an offshore wind turbine available, the aerodynamic damping can be identified as the real part of the complex eigenvalues of the dynamic stiffness matrix [49]. This approach does allow for variations in rotor speed and separation of the flow, even though the eigenvalues can only be obtained after establishing a state-independent dynamic stiffness matrix. As an alternative, Kühn [49] suggested to analyse the tower top vibrations of a wind turbine in either steady or turbulent wind conditions after the release of an additional pre-thrust loading, from which the aerodynamic damping can be estimated from the logarithmic decrement of the transient decay. This approach accounts for the state-dependent aerodynamic interaction and can include the contribution of the control system. Regarding the latter, however, the pre-thrust loading will violate the validity of its initial conditions. Moreover, for systems with closely spaced modes, such as the first fore-aft and side-to-side modes of an offshore wind turbine, the identified damping cannot be interpreted purely as modal damping. Whereas Kühn [49] implemented an artificial additional thrust force, Cerda Salzmann and Van der Tempel [52] identified the aerodynamic damping from the ratio between variations in the thrust force and the wind speed, therefore requiring uniform inflow conditions. Liu *et al.* [53] presented a comparison between the latter method and the closed-form expression of Garrad [50] with a correction for variable-speed turbines. The different approaches to estimate the aerodynamic damping are summarized in Table 1.1.

Table 1.1: Overview of studies presenting approaches to estimate the aerodynamic damping of an operating wind turbine.

study	approach
Garrad [50]	closed-form expression fore-aft damping
Kühn [49]	real part of complex eigenvalue of dynamic stiffness matrix
	response analysis to additional pre-thrust loading
Cerda Salzmann and Van der Tempel [52]	ratio of thrust force and wind speed variations
Valamanesh and Myers [51]	extension of [50] including rotor-induced velocities and side-to-side damping
Liu <i>et al.</i> [53]	extension of [50] for variational speed turbines

The validity of the model decoupling by means of the application of a single dashpot at the tower top was studied by Ong *et al.* [54]. In their study, wind turbines with a full-height lattice tower and a lattice-tower hybrid support (or ‘jacket’) structure were considered. The aerodynamic damping for the decoupled modelling was estimated from the thrust-force derivative with respect to the wind speed. It was concluded that decoupled support structure model with a linear aerodynamic damping gives reasonable mean and standard deviation results when compared to a fully coupled simulation for environmental conditions for wind-force dominated load cases. A lower accuracy was obtained for load cases with a more pronounced wave contribution.

Instead of assuming a single discretized dashpot acting in the fore-aft direction, or estimating the total aerodynamic damping in the modal domain from an integrated analysis, Schafhirt and Muskulus [55] distinguished the damping for the six translational and

rotational motion of the tower top. The corresponding damping values are obtained from an optimization procedure, relating the decoupled support structure model to an integrated wind turbine model. It was shown that the decoupled model with the six dashpots gives a much better fit with the integrated model than a decoupled model with a single fore-aft dashpot. Additionally, it was observed that the aerodynamic damping increases for higher wind speeds, also for above-rated velocities. It was suggested, however, that a linear damping model does not suffice to describe the aerodynamic interaction.

In addition, the control system of the turbine allows for variations of the rotational speed and the pitch angle of the blades, affecting the relative inflow and the angle of attack. Apart from optimizing the power output of the wind turbine, the control system can also be employed to control the motion of the support structure [56]. Individual pitch control systems, which affect the pitch angle of each blade separately offer the possibility to reduce asymmetric loads on the rotor plane, for instance resulting from altitudinal wind speed variations [57–59]. Alternatively, Fischer *et al.* [60] studied the influence of both the generator torque and pitch control systems on the mitigation of side-to-side motions. Zhang *et al.* [61] presented a generator torque control system with the same purpose.

In conclusion, the available literature reveals a need for closed-form expressions for the aerodynamic damping corresponding to the six translational and rotational tower top motions. The resulting aerodynamic damping matrix, which establishes the relation between the structural motions and the resulting aerodynamic forces, should account for off-diagonal contributions as well. Such a matrix should cover the varying conditions within the operational range of the wind turbine. Furthermore, the underlying assumptions regarding the aero-elastic modelling, including attached flow conditions and the effect of the control system should be regarded, and the validity of a linearization should be assessed. It could be considered to account for higher-order contributions of the aerodynamic interaction as well, even though this immediately impairs the computational efficiency.

### 1.2.2. HYDRODYNAMIC INTERACTION

The implementation of the hydrodynamic excitation requires the selection of valid incoming wave and wave-induced force models. Figure 1.8 illustrates the validity of different wave theories for varying water depths and wave heights. Provided that the wave steepness is small, the waves can be modelled linearly. The linear wave theory can be applied straightforwardly to define stochastic sea states too. For shallow waters and/or high waves, the linear wave theory is no longer valid and the definition of the wave profile requires higher-order harmonic corrections [62, 63], or breaking wave theory should be adopted. The profiles of these different waves is depicted in Figure 1.9 and an overview of the different wave theories can be found in [64].

In practical situations, non-linear waves are defined deterministically. To analyze the response to non-linear waves in a random sea, Henderson and Zaaier [65] suggested that a linear stochastic wave model could be applied to determine the initial conditions for the assessment of the excitation of a regular non-linear wave. The propagation of non-linear gravity waves in irregular seas can be evaluated with the potential theory, using non-linear free surface boundary conditions. Agarwal and Manuel [66] generated irregular nonlinear

wave profiles by employing the second-order correction proposed by Sharma and Dean [67]. To increase the computational efficiency, Marino *et al.* [68] proposed a domain-decomposition strategy, in which the occurrence of non-linear waves is assessed in a linear irregular wave profile, after which a non-linear wave profile is determined to replace the linear profile in a sufficiently large domain, using a higher-order boundary-element method. This approach is schematized in Figure 1.10.

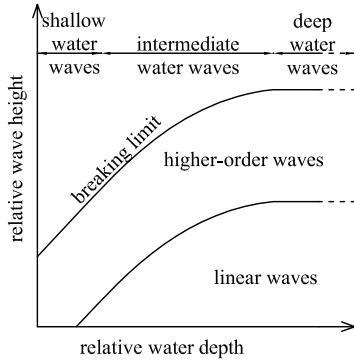


Figure 1.8: Schematic representation of the different wave-theory regimes for varying water depths and wave heights.

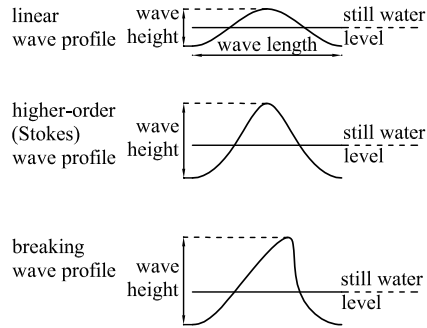


Figure 1.9: Schematic representation of wave profiles corresponding with different wave theories.

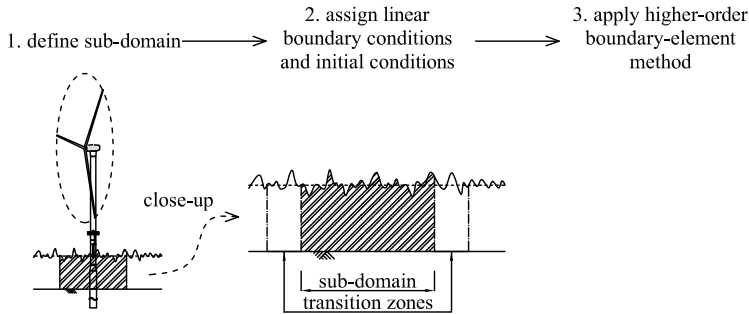


Figure 1.10: Schematization of the sub-domain analysis approach of non-linear irregular waves [68].

Once the wave kinematics have been adequately defined, the Morison equation can be employed to predict the resulting forces on submerged vertical slender cylinders [69]. The equation distinguishes the inertia force, composed of the Froude-Krylov and the added mass components – as predicted by the potential flow theory – and the drag force resulting from the viscosity of the flow, and requires the definition of time-averaged

added mass and drag coefficients, which depend on the shape of the structure, the Reynolds regime and the history of the relative motion between fluid and structure. The empirical Morison equation can be applied to structures that do not significantly affect the incident wave field, provided that the predicted force is either drag or inertia dominated [70]. This is illustrated by Figure 1.11, with Figure 1.11(a) depicting the disturbance of the incoming wave field by a cylindrical structure, and with Figure 1.11(b) indicating the governing hydrodynamic force on a cylinder based on the ratios between the wave length and height and the diameter of the cylinder. For shallow waters and/or non-slender cylinders, the effects of wave diffraction and reflection can no longer be neglected. On the basis of linear potential theory, and therefore linear waves, MacCamy and Fuchs [71] derived the hydrodynamic inertia force for a cylinder, accounting for both effects. For an elaborate overview of the wave force models on cylindrical structures, reference is made to [70, 72].

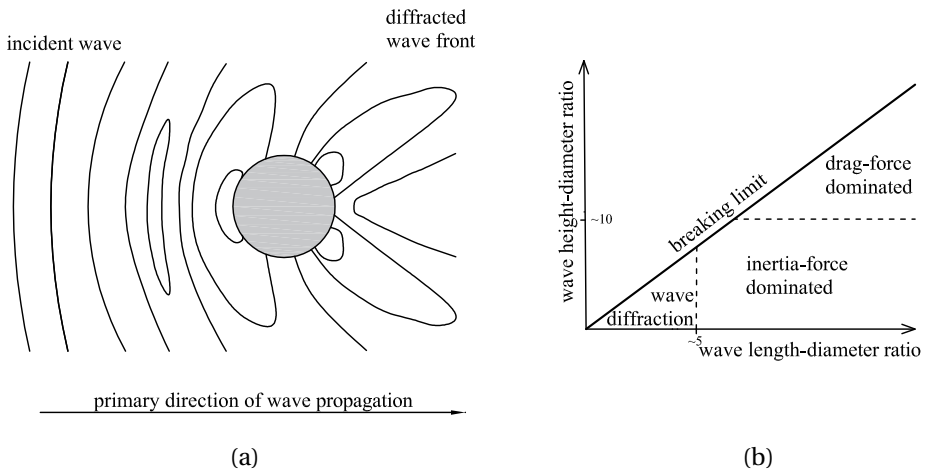


Figure 1.11: (a) Schematic representation of the diffracted wave field around a cylindrical structure [73], and (b) the governing hydrodynamic force on a cylindrical structure as a function of the wave length-diameter and wave height-diameter ratios.

To account for the hydrodynamic interaction with a flexible structure, the hydrodynamic force is expressed in terms of the relative kinematics between the fluid particles and the structure, implying that the structural velocity affects the drag force and the structural acceleration the added mass component of the inertia force [74]. It should be noted that the coefficients for drag and inertia of the Morison equation, which are for rigid structures, may lose their validity for this adaptation [70]. Regarding the dynamic response of a monopile-based wind turbine to irregular waves, Bachynski *et al.* [75] conducted model scale experiments for a 7 m diameter support structure. The results demonstrated the contribution of the second mode of vibration for a parked turbine under extreme sea state conditions.

For increasing wave heights, induced by the wind in developing seas or resulting from wave-wave interactions in random seas, the water particle velocity in the crest of the

wave may reach the wave celerity, as a result of which the wave breaks [76]. Birkinshaw *et al.* [77] compared the measured kinematics of resulting so-called ‘spilling breakers’ with predictions through Dean’s stream theory and found the measured velocities and accelerations in the crest region to be slightly higher. Computational fluid dynamics approaches to model the kinematics of spilling breakers were presented by Jacobsen *et al.* [78] and Alagan Chella *et al.* [79]. Marino *et al.* [80] studied the wind-wave energy transfer for the development of steep waves in the vicinity of offshore wind turbines.

Plunging breakers occur when moderate waves run up a seabed slope, enforcing the wave to break. Computational fluid dynamics techniques are commonly employed to study the wave impact on cylindrical structures, such as monopile-based offshore wind turbines [81–83]. Marino *et al.* [84] modelled the wave kinematics of a plunging breaker by means of their domain-decomposition strategy and estimated the impulsive force on an offshore wind turbine with an analytical impact model. Chan *et al.* [85] performed a detailed laboratory study on the mechanics of plunging wave impacts on vertical cylindrical structures. Experimental results of breaking wave excitations of a flexible vertical cylinder with a top mass, resembling an offshore wind turbine, were presented by Bredmose *et al.* [86]. The experiments showed how breaking wave events induce an impulsive excitation of the first mode of vibration, while the second and the third modes were excited too.

The difficulty of predicting hydrodynamic forces for regimes within which fluid-structure interaction is of relevance was mentioned by Van Kuik *et al.* [5] as an important long-term research for offshore wind. Especially the impact load from breaking waves still requires a description in terms of time-history and statistical characteristics. Additionally, it is recognized that the existing concepts for stochastic non-linear waves ‘are based on spectral synthesis and the superposition principle of linear wave theory’. The need for a useful concept for non-linear irregular waves is expressed. Moreover, as computational fluid dynamics do not provide an applicable approach for design purposes, the Morison equation and the potential flow theory may lose their validity for larger and novel foundation concepts, generating the need for mid-fidelity modelling approaches.

Apart from the hydrodynamic action from waves and currents, certain regions require the analysis of the action of floating level ice, ice floes and ice ridges on the support structures of offshore wind turbines. The prediction of loads from ice requires sufficient data regarding the ice thickness, drifting speed and strength, where the latter relates non-linearly to the rate of loading. Thus, in interaction with vertical-sided structures, the pattern of the structural motion varies with the relative incident velocity of the ice, for which the following regimes for increasing ice speeds are distinguished: intermittent crushing, frequency lock-in and continuous brittle crushing, see Figure 1.12.

Several models have been developed to predict the loads from the interaction between floating level ice and vertical-sided compliant structures [88–90], recognizing the relevance of the relative incident velocity and assuming a specific crushing length, or applying an effective negative damping to account for the non-linear dependency of the ice strength on the relative motion. These approaches, however, have failed to predict the measured ice loads over a sufficiently wide range of drifting speeds. A phenomenological model developed by Hendrikse and Metrikine [91], and subsequently validated [87, 92], recognized the dependency of the contact area between ice and structure on the speed of

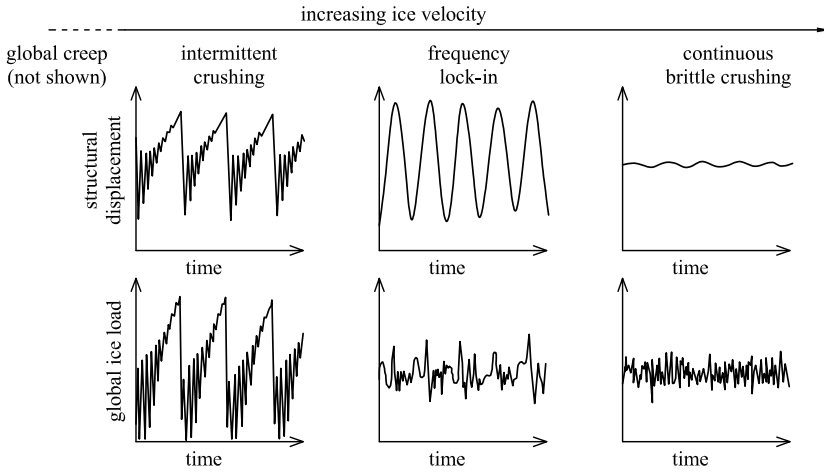


Figure 1.12: Illustrations of ice-load and structural-response patterns of vertical-sided structures in interaction with ice with varying speed [87].

loading. With the application of this approach, which was already applied in an integrated analysis of an offshore wind turbine [93], the modelling of the non-linear ice-structure interaction requires the distinction of a sufficient number of elements in the contact area between the ice and the structure, significantly enhancing the duration of the required load simulations. Still, the existing model only accounts for one-directional ice-structure interaction, whereas the aerodynamic forcing excites the offshore wind turbine in both the fore-aft and the side-to-side directions. An extended analysis of the interaction in two directions is therefore required. On a different note, large uncertainty exists regarding the occurring ice conditions throughout the life-time of offshore wind turbines. Similar to the concept of sea states which are used for the long-term statistics of the ocean conditions, so-called 'ice states' would serve the ultimate and fatigue limit state analyses of wind turbines in ice-exposed regions, requiring an extended database of occurring ice conditions.

In analyzing the dynamic response of an operating offshore wind turbine to either hydrodynamic or ice loads, the corresponding aerodynamic interaction cannot be neglected, given the substantial contribution to the damping of the system. As the aerodynamic damping is commonly accounted for in terms of the ratio of the critical damping per mode of vibration, an understanding of the modal contributions to the total response is important. Given the non-linear nature of the interactions between the structure and hydrodynamic actions – particularly breaking waves – and ice loads, response contributions from higher global bending modes cannot be neglected, especially from modes with relatively large modal amplitudes around the sea level [94]. For such modes, the contribution to the critical damping from the aerodynamic interaction may result to a lesser extent from the lateral motion of the tower top, the motion which is considered dominant for the modal damping of the first mode, whereas the nodding motion may provide a considerable contribution. In principle, integrated models intrinsically account



for the aerodynamic damping contribution for the varying motions from the different modes of vibration, provided that the mode shapes are estimated accurately. Decoupled modelling approaches, however, require more advanced representations of the aerodynamic damping, to avoid erroneous contributions to the damping ratios of higher bending modes.

### 1.2.3. SOIL-STRUCTURE INTERACTION

For monopile-based support structures, which represent the vast majority of the installed offshore wind turbines, the main soil-structure interaction takes place laterally. This interaction varies with the soil characteristics, e.g., the density, the cohesion, the overconsolidation ratio. Close to the surface, the soil fails in wedges, whereas at deeper layers circumferential sliding of the soil will take place, see Figure 1.13. For offshore wind applications, not just the ultimate resistance of the soil is of importance. The structural response to the time-varying excitations of wind and waves relies on the dynamic stiffness of the soil and the damping through radiation and hysteresis.

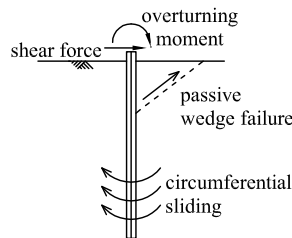


Figure 1.13: Schematic representation of the soil-failure mechanisms for laterally loaded piles.

The industry-standard approach to model the soil-structure interaction of laterally loaded piles is the  $p-y$  curve method [7], an overview of which is provided by Reese and Van Impe [95], which defines the interaction in terms of non-linear force-deflection relations, see Figure 1.14. For soft normally consolidated marine clay, this method finds its basis in the empirical testing of piles with a diameter of 0.32 m and an embedded length of 12.80 m [96], implying a length-diameter ratio of approximately 40. Tests were performed for short-term static loading, cyclic loading (corresponding to emerging storm conditions) and subsequent reloading with forces smaller than the previous maximums. Cox *et al.* [97] and Reese *et al.* [98] presented  $p-y$  curves for soils consisting of clean fine sand to silty fine sand. The tests on which these curves were based had been done with piles with a length-diameter ratio of approximately 34 (diameter 0.61 m and an embedded length of 21.03 m). These tests were performed for both static and cyclic loadings at a frequency of approximately 0.06 Hz, which corresponds to the quasi-static range of a typical bottom-founded offshore wind turbine.

In conclusion, the  $p-y$  curve method was developed for the modelling of large displacements of flexible piles, whereas monopile foundations for offshore wind turbines must be characterized as rigid (for diameters in the range of 4 to 6 m, the length-diameter ratios are in the order of five to six [99]), for which the soil-structure interaction must

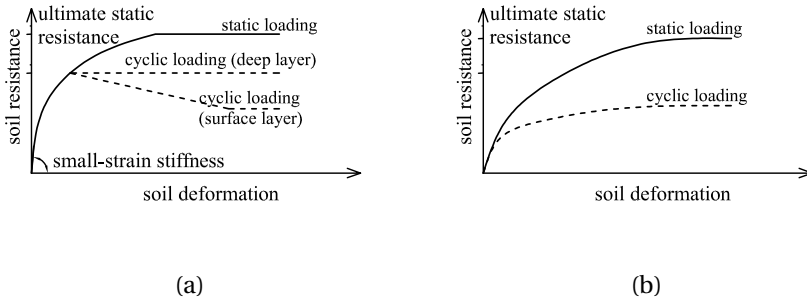


Figure 1.14: Representations of  $p$ - $y$  curves for (a) clay and (b) sand, distinguishing the soil-structure interaction for static or cyclic loading.

be characterized differently (see Figure 1.15). Shadlou and Bhattacharya [100] stated that with the application of the  $p$ - $y$  curve method, the stiffness of the foundation of an offshore wind turbine is underpredicted. Moreover, the studies resulting in the standardized force-displacement curves primarily focussed on the soil reaction for large deformations. For the estimation of the fatigue damage accumulation in offshore wind support structures, the small-strain stiffness of the soil is of particular relevance see Figure 1.14(a).

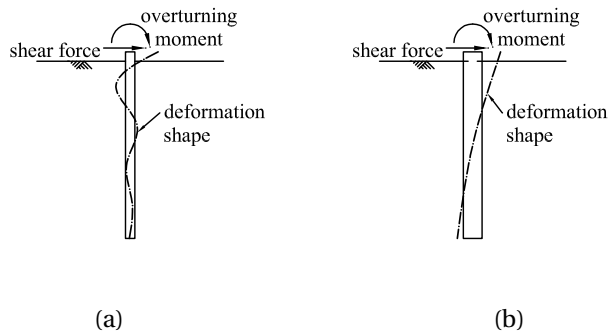


Figure 1.15: Schematic representation of the lateral pile deformation resulting from a shear force and overturning moment at the soil surface, distinguishing (a) a flexible pile and (a) a rigid pile.

For piles with a diameter larger than 1.0 m, the design standard DNVGL-ST-0126 [7] requires the validation of the  $p$ - $y$  curve method with a finite-element analysis. In research, the small-strain stiffness of sand and clay for rigid piles has been investigated on the basis of the finite-element method, as well as small and full-scale experiments. Versteijlen *et al.* [20] used in situ measured small-strain shear moduli to develop a three-dimensional finite-element model of an embedded monopile to validate the soil stiffness predicted by the  $p$ - $y$  method. The predicted pile deflections with the three-dimensional

model were smaller than the deflections predicted with the  $p - y$  curve method. Sørensen *et al.* [101] and Kallehave *et al.* [102] have proposed a modified initial stiffness for piles in sand, depending on the diameter, internal friction angle and the depth below the mudline.

Cyclic loading conditions allow for kinematic hardening and ratcheting – or cyclic creep – of non-cohesive soils, affecting the soil-structure interaction [103, 104]. Schafhirt *et al.* [105] demonstrated the influence of soil conditions changing over time on the fatigue life-time of monopile foundations. For saturated and cohesive soils, cyclic loading may induce gapping and subsequent expulsion of water carrying soil particles. As a consequence, both the resistance and the stiffness of the soil reduce, even for relatively small deformations [95]. The behaviour of monopile foundations under lateral cyclic loading was investigated by Achmus *et al.* [106], focussing specifically on cohesionless soil. The soil response is represented by a degradation stiffness model, which combines finite-element simulations of the pile–soil interaction and an evaluation of drained cyclic triaxial tests. The work established a relation between the pile performance under cyclic loading and its embedded length, and defines design criteria for large-diameter monopiles. Damgaard *et al.* [107] suggested an increased soil stiffness for cyclic motions to account for the pore pressure generation in saturated soils. Jardine *et al.* [108] provided a historical review of empirical studies to the response of cyclically loaded piles. As yet, the principles behind the cyclic soil-structure interaction and the subsequent pile deformations are not fully understood [109], and the reliability of existing methods to estimate the long-term pile deflections and rotations at the mudline should be considered from that perspective [10].

Given the inconvenience of the standardized force-deflection curves for piles with a small diameter-length ratio, alternative modelling approaches are required for offshore wind applications. For design purposes, these alternative models need to be computationally efficient, rendering the three-dimensional finite-element approach undesirable. As a consequence, a need exists for simplified equivalent representations of the three-dimensional soil-structure interaction for rigid piles. Dutta and Roy [110] published a survey, in which a selection of alternative methods for the modelling of soil-structure interaction is gathered and reviewed. The work focussed on both 1D idealizations and continuum models. Zaaijer [111] suggested to replace the embedded monopile by a stiffness matrix at the mudline, to simplify the modelling of the foundation of offshore wind turbines, where the components of the stiffness matrix can be estimated with the Randolph's method. Bhattacharya and Adhikari [112] adopted a similar stiffness modelling, but neglected the coupling between translations and rotations. A similar approach was taken by Andersen *et al.* [113], who investigated the dynamic characteristics of an offshore wind turbine model with stochastic  $p - y$  curves. Other studies proposed a discretized foundation model for a monopile support structure, recognizing the relevance of the coupling between the translational and rotational motions. As an alternative, the application of an equivalent fixity depth was suggested [114, 115]

Varun *et al.* [116] and Versteijlen *et al.* [117] presented a procedure to define an effective one-dimensional Winkler foundation from a three-dimensional response obtained with a finite-element model. The effective foundation models capture the three-dimensional effects of the soil-structure interaction of piles with a large diameter compared to the embedded length – in other words, piles with a small length-diameter ratio.

This method was extended further in the work of Versteijlen *et al.* [118], where global stiffness kernels were extracted from simulations with a three-dimensional inhomogeneous continuum. On the basis of these kernels – which can include soil stiffness, inertia and damping – a one-dimensional non-local Winkler foundation can be defined, with which the three-dimensional dynamic response of a ‘vast range of soil-pile systems can be mimicked’. Corciulo *et al.* [119] used a three-dimensional finite-element model to analyze the dynamic response of a wind turbine on a monopile foundation. This study particularly focussed on the effect of hydro-mechanical coupling on the cyclic soil response. In a second study, Corciulo *et al.* [120], uncoupled lateral and rotational springs were suggested to replace the three-dimensional soil-structure interaction.

The damping due to the interaction between the structure and the soil exists through radiation and hysteresis. The former type of damping is considered irrelevant for the frequency range of interest for offshore wind applications, i.e., below 1 Hz [121–123]. Carswell *et al.* [123] defined a viscous damping representation for the lumped-parameter modelling of an offshore wind turbine, based on a two-dimensional finite-element representation including hysteretic damping. Corciulo *et al.* [120] defined a viscous damper to replace the hysteretic dissipation of energy at the dominant frequency of oscillation.

While many studies on the modelling of the soil-structure interaction for offshore wind turbines have been done, no final substitution for the  $p - y$  method has been defined yet. As to date, all alternatives require the modelling of a foundation in a three-dimensional continuum, from which the soil-structure interaction characteristics to be adopted for the modelling of the wind turbine foundation can be extracted. As suggested by Van Kuik *et al.* [5], a re-evaluation of the  $p - y$  curve method for pile sizes applicable in the offshore wind industry is required. The establishment of new curves requires full-scale and long-term measurements, to correctly account for the rigidity of the foundation structures, as well as the history-dependency of the soil properties under cyclic loading. For offshore wind foundations, the small-strain stiffness and the damping potential of the soil are of particular relevance.

For alternative foundation solutions, the application of the  $p - y$  curve method is less disputed, or not considered at all. Multi-member support structures, such as so-called jackets and tripods are often founded on multiple flexible piles, for which the validity of the  $p - y$  method is still assumed. In this respect, Abhinav and Saha [27] illustrated the relevance of soil-structure interaction for a multi-member support structure, founded on multiple flexible piles. Concerning the soil-structure interaction, both lateral and axial springs were implemented, based on the  $p - y$  method. Other foundation concepts involve gravity-based solutions and suction buckets. Regarding the modelling of gravity-based foundations, Andersen [121] investigated the lumped-parameter representation of the dynamic characteristics of homogeneous and layered soils. A three-dimensional finite-element model for a suction bucket foundation was presented by Achmus *et al.* [124], whereas Zhang *et al.* [125] presented a three-dimensional limit method for the stability analysis of suction buckets. The modelling of gravity-based and suction bucket foundations still require the definition of an applicable dynamic stiffness, accounting for cyclic degradation and liquefaction [126, 127]. An increasing popularity of these alternative foundation concepts may instigate the need for industry-standard force-response relations as well.

### 1.3. CODE COMPARISON AND EXPERIMENTAL VALIDATION

Models for offshore wind turbines, either integrated or decoupled, and including formulations for the different environment-structure interactions, predict responses to wind and wave excitations for which the structures are designed. The overview of the different approaches to model the interactions between the structure and the environment reveals that many uncertainties still exist. In this respect, a number of design tool comparison programmes have been executed over time [128–132].

Vorpahl *et al.* [14] presented a comparison of the capabilities of available design tools. Concerning the aerodynamic models, all considered tools employ the blade-element/momentum theory, whereas most allow for the implementation of dynamic stall. The linear wave theory in combination with Morison's equation is the standard model for the evaluation of wave loads. Some packages allow for the application of the stream function wave theory, and the linear potential flow theory for the implementation of diffraction and radiation is offered by few. The industry-standard structural modelling approach is the finite-element method or a multi-body dynamics formulation. For the future development of design tools, Vorpahl *et al.* [14] suggested, among others, the validation of the hydrodynamic models for multi-member support structures, the implementation of non-linear blade deflection models, the coupling of the aerodynamic analyses with computational fluid dynamic approaches and the corresponding integration of the turbine within the context of the complete wind farm, and the development of a validated model for the prediction of ice loads.

A benchmark study regarding the comparison of software tools available for the integrated analysis of a 5 MW offshore wind turbine was performed by Vorpahl *et al.* [133]. A main finding was that the agreement between the estimated structural responses was quite good, differences resulting particularly from varying model fidelities and aerodynamic and hydrodynamic load implementations. Robertson *et al.* [134] and Robertson *et al.* [135] have performed a comparative study with the focus on the hydrodynamic load on a cylindrical structure, including the effect of a sloped seabed. The added value of fully non-linear potential flow analyses and computational fluid dynamics techniques for highly non-linear wave conditions was recognized. Furthermore, it was concluded that none of the tested codes was capable to capture the total force resulting from a breaking wave event. Concerning the existing design tools, Muskulus and Schafhirt [13] pointed out that only a few specialized software packages are available to evaluate the combined aerodynamic and hydrodynamic excitations of offshore wind turbines. Moreover, the functionality of these packages is often limited and customizations to perform non-standard simulations may not always be possible.

Validation by means of full-scale measurements of installed offshore wind turbines are required to further develop the modelling strategies for future turbines. Measurement campaigns on offshore wind turbines have aimed in particular at the identification of the fundamental natural frequencies, both in fore-aft and side-to-side directions and the estimation of the corresponding damping. Operational modal analysis based on assumed broadband ambient excitations, response measurements to rotor stop tests and the seismic testing of the soil are examples of applied identification strategies [20, 136, 137].

Regarding the natural frequencies of offshore wind turbines, many studies have addressed the identification of the natural frequencies and used the results to calibrate a

structural model [122, 136, 138] – of either onshore or offshore wind turbines – while addressing the reliability of different identification techniques. In the following, an overview is presented of studies that compare the natural frequencies predicted with a structural model with identified frequencies from measurements, as these validations can be used to address the validity of the modelling approach, and studies identifying the damping corresponding to the first modes of vibration. This overview is based on a chronological ordering of results related to specific measurement campaigns. Tables 1.2 and 1.3 present an overview of the natural frequency comparisons and the identified damping ratios.

Zaaijer [111] performed a natural frequency validation, using the measured nacelle acceleration of operating wind turbines from two wind farms in the Netherlands for a comparison between predicted and identified first natural frequencies, and compared those with the predicted frequencies from a structural model. Whereas the predicted first natural frequencies at the wind farm Irene Vorrink slightly underestimated the identified natural frequencies, up to 5%, the predicted natural frequencies at the wind farm Lely showed an underestimation of 9% and 37%, respectively. An explanation for the difference at the Irene Vorrink farm was primarily found in the selection of the soil parameters and the modelling of the soil-structure interaction. A specific explanation for the large differences at the Lely wind farm was not found, but it was expected to be due to erroneous inputs for the structural model.

Even though not offshore, Hansen *et al.* [136] focussed on the identified damping ratios of an onshore pitch-regulated, variable speed 2.75 MW turbine by means of pitch angle and generator torque variations and operational modal analysis based on stochastic sub-space identification. The most reliable results were obtained with the operational modal analysis, as with the pitch angle and generator torque variations, it turned out to be difficult to isolate the damping corresponding with the first fore-aft and side-to-side modes. Concerning the first fore-aft mode, damping ratios with an average of 12% were identified, with a standard deviation of 1.2%, for a variation of wind speeds. The lateral damping varied from 7.9% at low wind speeds to 3.2% at higher wind speeds, a decrease which is explained by the increasing pitch angle of the blades. As the damping ratios were obtained from an operating turbine, the values include the high apparent damping from the aerodynamic interaction, on top of the structural and soil damping contributions.

Evaluating the measurement data of a series of consecutive rotor stop tests at the Burbo Banks wind farm, Versteijlen *et al.* [137] identified a damping ratio of 3% of the critical damping of the first fore-aft mode, 1.5% of which was believed to be generated by soil-structure interaction. The identified damping ratio is significantly lower than the value presented by Hansen *et al.* [136], since the contribution of the aerodynamic damping is negligibly small in case of rotor stop tests.

Damgaard *et al.* [139] identified the damping ratio for a monopile-based offshore wind turbine in the North Sea from a series of rotor stop tests. The obtained damping ratios were in the range from 2.2% to 2.4%. An extended study was presented by Damgaard *et al.* [122], who considered both rotor stop tests and acceleration measurements of monopile-based wind turbines in five offshore wind parks, and focussed on the time dependency of the modal parameters and the identification of the side-to-side – or cross-wind – damping. The amount of soil damping was identified as 0.06, in terms of the logarithmic decrement, which corresponds to a modal damping of approximately 1.0%. The rotor stop tests

resulted in an identified first fore-aft mode damping ratio from 2.4% to 2.5%, whereas from measurements on operating turbines, an average side-to-side damping in the range of 2.5 to 2.9% was identified. It was suggested that the backfilling of the scour hole around the monopile foundation is the main source of the time dependency of the identified dynamic characteristics.

Concerning the fundamental natural frequencies, Damgaard *et al.* [107] reported values identified from rotor stops tests on 3 MW turbines in the North Sea. The identified frequencies were significantly higher, in the range of 2 to 13%, than the first natural frequencies obtained with a computational model, for which  $p - y$  curves were applied. The observed deviations were attributed to the pore pressure build-up in dynamic soil-structure interaction of saturated soils. In this respect, Versteijlen *et al.* [20] adopted the small-strain shear modulus from in-situ measurements to construct a three-dimensional soil-structure interaction of an offshore wind turbine. The model was used to estimate the static deflection of the wind turbine, which was compared with the deflection determined with the industry-standard  $p - y$  curve method. The later was shown to predict up to 50% larger deflections at the mudline.

The experimental data from a measurement campaign in the Belgian North Sea was used by Shirzadeh *et al.* [140] to identify the dynamic properties of a 3 MW offshore wind turbine on a monopile foundation. The measurement data were obtained during rotor stops, as well as from idling turbines. The identified first natural frequencies were compared with the frequencies obtained from a numerical model. The identified first natural frequency from the rotor stop test was 4.5% lower than the predicted natural frequency, whereas for the idling turbine the identified frequency was 2.9% lower. The soil-structure interaction was accounted for by  $p - y$  curves. Regarding the damping ratio of the first fore-aft mode, from both tests a ratios of 1.05% of the critical damping was identified. Devriendt *et al.* [141] presented a comparative study on the different techniques for system identification with the same measurement data, identifying also a damping ratio of 1.27%, corresponding to the first side-to-side mode. The higher side-to-side damping, compared to the fore-aft damping, was explained by the large blade pitch angle, resulting in a larger exposed blade area in the side-to-side direction. In a subsequent work, Devriendt *et al.* [142], presented the identification of the modal damping ratios from continuous measurements on an idling or parked wind turbine. Average damping ratios of 1.86% and 2.49%, corresponding to the first fore-aft and side-to-side modes of vibrations, respectively, were identified. These values are higher than the identified damping in the previous studies [140, 141], as during these measurements a tuned-mass damper was active. The most extensive comparison was presented by Shirzadeh *et al.* [143], who compared the identified natural frequencies with frequencies predicted by a numerical model and presented the variation in damping ratios with the wind speed, both for parked conditions. In comparison with the natural frequencies estimated from time-simulations, the first fore-aft frequency provided a virtually perfect fit, whereas in the first side-to-side frequency was overestimated by 1.37%. Again,  $p - y$  curves were adopted to represent the soil-structure interaction. The mean identified damping ratio corresponding with the first fore-aft mode increased from 1.73% to 2.77% with increasing wind speed, whereas the mean first side-to-side damping ratio varied from 2.18% to 3.19% with the increasing wind speed, with the tuned-mass damper active,

again showing a higher damping in the side-to-side direction due to the larger exposed blade area.

To validate the modelling of the soil-structure interaction specifically, Versteijlen *et al.* [144] presented the results of vibration measurements of an in-situ monopile foundation in a near-shore wind farm, with a stiff sandy soil composition. From the pile-only measurements, the identified low-frequency soil stiffness was 140% higher than the stiffness prescribed by the  $p - y$  curve method. With the application of the identified soil stiffness in the numerical model, using a one-dimensional effective stiffness [117], a good prediction of the identified fundamental natural frequency was obtained.

A comparison of the measured response of a North Sea wind turbine to models with different representations of the soil-structure interaction was presented by Page *et al.* [145], including  $p - y$  curves and a macro-element representation. In comparing the identified first fore-aft and side-to-side natural frequencies with the predicted frequencies from a model with  $p - y$  curves, the predictions underestimated the actual natural frequencies by 12.3% and 12.8%, respectively. These differences confirm the findings of Damgaard *et al.* [107] and Versteijlen *et al.* [144], who illustrated the weak performance of the industry-standard  $p - y$  curves for monopile-based support structures of offshore wind turbines too.

When considering the different natural frequency comparisons, listed in Table 1.2, the importance of adequate modelling of the soil-structure interaction must be recognized. This relates to a correct representation of the small-strain stiffness, the cyclic degradation and the selection of the applicable sea bed level, as for non-cohesive soils and in absence of adequate scour protection a variation in soil level and compaction at the mudline is to be expected [146, 147]. Other sources of modelling inaccuracy may exist in the shape of the representation of the rotor-nacelle assembly and the mass distribution of the transition piece and the electrical equipment. These components, however, were not present in the full-scale experiments of Versteijlen *et al.* [144], leaving the hydrodynamic added mass as the only other source of modelling inaccuracy, next to the representation of the soil-structure interaction.

Regarding the identified damping ratios, Table 1.3, it becomes clear that fore-aft damping values for operating conditions are lacking. The only exception are the results presented by Hansen *et al.* [136], which were obtained from an onshore turbine. These results give an insight in the high potential of the aerodynamic damping. The reported damping values from rotor stop tests and for parked-idling turbines are all within the same range of magnitude. These values can be expected to represent the structural damping, as well as the damping from the soil-structure interaction. In this respect, the identified side-to-side damping is slightly higher than fore-aft damping, as for non-operating conditions the wind turbine blades provide a larger lateral resistance.

## 1.4. SOLUTION APPROACHES

In Section 1.2 of this work, the existing approaches to model the environmental interactions with offshore wind support structures were considered. An overview of different code comparison studies, as well as experimental validations, was presented in Section 1.3 to give an impression of the validity of the modelling strategies. Apart from different approaches to modelling the structure, different approaches to predict the response to



Table 1.2: Overview of studies presenting validations of the first fore-aft and side-to-side natural frequencies of wind turbines, indicating the underestimation of the modelled frequencies compared to the identified frequencies.

study	turbine	fore-aft	side-to-side	operational state
Zaaijer [111]	Irene Vorrink wind farm	up to 5%	–	power production
	Lely wind farm	9 to 37%	–	power production
Damgaard <i>et al.</i> [107]	North Sea 3MW turbines	2 to 13%	–	rotor stop
Shirzadeh <i>et al.</i> [140]	North Sea 3MW turbine	–4.5% –2.9%	–	rotor stop idling
Shirzadeh <i>et al.</i> [143]	North Sea 3MW turbine	0.00%	–1.37%	parked
Page <i>et al.</i> [145]	North Sea turbine	12.3%	12.8%	idling

Table 1.3: Overview of studies presenting validations of the first fore-aft and side-to-side damping ratios of wind turbines.

study	turbine	fore-aft	side-to-side	operational state
Hansen <i>et al.</i> [136]	2.75MW turbine (onshore)	12%	3.2 to 7.9%	power production
Versteijlen <i>et al.</i> [137]	Burbo Banks	3%	–	rotor stop
Damgaard <i>et al.</i> [139]	North Sea wind turbine	2.2 to 2.4%	–	rotor stop
Damgaard <i>et al.</i> [122]	North Sea wind farms	–	2.5 to 2.9%	power production
		2.4 to 2.5%	–	rotor stop
Shirzadeh <i>et al.</i> [140]	North Sea 3MW turbine	1.05%	–	rotor stop idling
Devriendt <i>et al.</i> [141]	North Sea 3MW turbine	1.05%	1.27%	idling
Devriendt <i>et al.</i> [142]	North Sea 3MW turbine	1.86%	2.49%	parked/ idling
Shirzadeh <i>et al.</i> [143]	North Sea 3MW turbine	1.73 to 2.77%	2.18 to 3.19%	parked

environmental excitations exist, with the aim of generating sufficiently accurate results, against as low as possible computational costs. In this respect, three approaches are distinguished here:

- Reduction of the total number of coupled differential equations that need to be solved.
- Reduction of the required number of load cases that need to be analysed.
- Reduction of the complexity of the numerical operations, i.e., transforming the system of equations to the frequency domain.

A finite-element formulation of an offshore wind support structure including the environment-structure interactions generally consists of a large number of coupled second-order differential equations. As a consequence of the non-linear nature of the system, the structural response to wind and wave excitations is commonly estimated by means of time-domain simulations. With the application of a Galerkin reduction [148], the number of equations that require simultaneous solving can be kept within ‘reasonable’ limits. Within the iterative solution procedure, resulting from the decoupled modelling approach, dynamic sub-structuring techniques allow for the separate analysis of structural components, and the subsequent assembly of reduced component models. These techniques aim at capturing the most relevant dynamic characteristics of a structural component, and, subsequently, analyzing the structure as a whole [149].

Instead of reducing the number of degrees of freedom, it has been attempted to reduce the number of required simulations, mainly resulting from the analysis of the fatigue limit state [150]. Other researchers aimed at defining the dynamic system in terms of a system of algebraic equations, by transforming a reduced-order model to the frequency domain [151]. To circumvent the non-linear aero-elastic interaction of the rotor, Kühn [49] and Van der Tempel [152] suggested a hybrid time-frequency domain approach.

#### 1.4.1. DYNAMIC SUB-STRUCTURING

Instead of employing the full structural matrices of the foundation structure for the aerodynamic analysis, with the application of a model reduction technique a set of reduced structural matrices – or ‘super elements’ – can be extracted, which can subsequently be applied as boundary conditions for the turbine model. Figure 1.16 presents a schematization of this technique for offshore wind turbines. Concerning these reduction techniques, which are generally referred to as dynamic sub-structuring, the Guyan reduction represents the foundation structure only quasi-statically, whereas the Craig-Bampton technique accounts for both the static condensation and the fixed- or free-interface dynamic response, allowing for a reduced-order model, which includes the dynamic characteristics relevant for the required simulations [153]. Impulse-based techniques employ a set of Green’s functions to represent a structural component in a reduced manner for the analysis of the complete system [154, 155].

The equations of motion of the reduced system based on the Craig-Bampton technique are coupled, since the adopted modes of vibration are not orthogonal. The selection of the modal basis requires a convergence analysis, to ensure a sufficiently accurate dynamic representation of the system. In case too few dynamic modes are selected, the

reduced model does not capture the ‘real’ resonance frequencies of the system. Although the Craig-Bampton technique primarily aims at the spectral convergence of the modal basis, without spatial convergence – required for the forced-response analysis of a dynamic system – a sufficient accuracy of the reduced-order model is not guaranteed. With the inclusion of a set of modal truncation vectors – or load-dependent residual vectors – the modal basis can be augmented and the estimation of the forced dynamic response can be improved, a method referred to as the Augmented Craig-Bampton technique [149]. Alternatively, the forces acting on a sub-structured component can be represented by equivalent forces acting on the interfaces between the structural components. The concept of blocked forces and equivalent free-interface displacements was originally developed for the frequency domain, and extended by Van der Valk and Rixen [12] to applications in the time domain.

The benefits of the reduced-order modelling are enlarged for foundation structures consisting of multiple members, such as space-frame structures, which require a large number of structural degrees of freedom for accurate modelling. The sub-structuring technique finds its basis in the principle of linear superposition, implying that a super element represents a linearized projection of the foundation structure. Given the non-linear nature of both the hydrodynamic interaction and the soil-structure interaction, different load cases may require the derivation of different super elements. Moreover, the non-linear aero-elastic coupling possibly requires an enhanced modal basis for the derivation of the super element, since higher-order modes may contribute to the dynamic response of the system too.

The commercially available simulation tool **BLADED**<sup>7</sup> employs a sub-structuring technique to simulate the response of an offshore wind turbine to environmental excitations. The reduced-order modelling is based on the static deformation shapes and the fixed-interface modes of vibration. In this respect, an important point of attention relates to the natural frequency convergence of the applied component-mode synthesis with the number of estimated modes. The preliminary design of a support structure is commonly based on a frequency analysis, which aims at the estimation of the natural frequencies to avoid interference of the natural frequencies with the rotor and blade-passing frequencies. The accuracy of the estimated frequencies may be low if only few estimated modes are included.

### 1.4.2. LOAD CASES REDUCTION

Apart from the efforts to reduce the complexity of the required simulations for the design of an offshore wind support structure – concerning both the non-linear environment-structure interactions and the number of degrees of freedom – a reduction of the vast amount of simulations that need assessment would allow for a speed-up of the entire analysis of an offshore wind support structure. Concerning the analysis of the ultimate limit state, Morató *et al.* [24] considered the relevance of the load cases for power production and parked conditions. The design load case combining power production with severe wave conditions was found to be design driving, with respect to the maximum overturning moment at the mudline.

The analysis of the fatigue limit state demands a joint-probability distribution of the

<sup>7</sup>Within the context of this work, reference is made to **BLADED** 4.6.

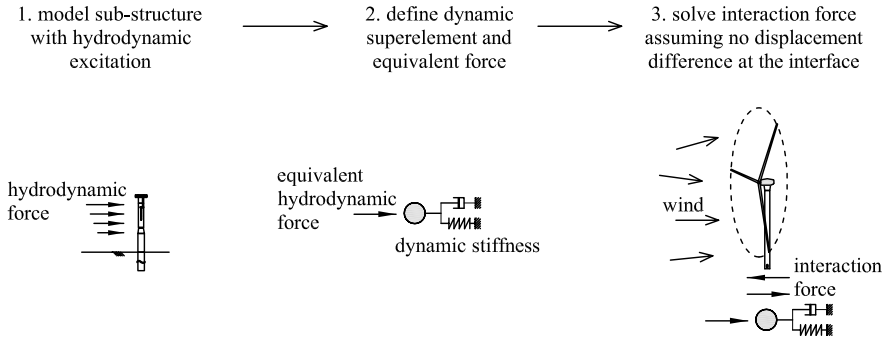


Figure 1.16: Schematization of the dynamic sub-structuring technique for offshore wind turbines [149].

wind and wave states at the location under consideration, providing stationary Gaussian descriptions of the occurring environmental conditions. In a practical situation, long-term measurement of combined wind speeds, significant wave heights and wave periods – zero-upcrossing, zero-downcrossing or peak – as well as directionality data should be available. The assessment of the expected fatigue damage entails the evaluation of this joint-probability distribution with sufficiently small bin sizes, having the number of simulations grow to several tens of thousands easily.

Kühn [49] introduced the concept of load case lumping to the field of offshore wind turbines. Establishment of the sets of wind and wave conditions, which together define the lumped load case, is initially based on some rules of proportionality, which relate the separate environmental conditions to an expected fatigue damage. From a comparison with the damage resulting from the elementary load cases, the lumped load cases can be refined. As the operational state of the wind turbine depends on the governing wind conditions, the distribution of sea states is often considered for a given wind state, assuming that the system properties are independent of the stochastic wave conditions. On this basis, the objective is to find a single equivalent sea state that predicts a damage similar to the full set of states from the probability distribution.

Seidel [156] considered the lumping of wave conditions, based on a frequency-domain analysis of the wave-induced fatigue damage of monopile support structures. Provided a low damping ratio, which de facto limits the method to non-operating turbines, an equivalent spectral density of the wave elevation is obtained from the spectral densities of a set of sea states at the first natural frequency of the offshore wind turbine. The suggested method accounts for the first mode of vibration only and is invalid for drag-dominated wave conditions.

The lumped load cases obtained in accordance with Kühn [49] and Seidel [156] may not imply damage equivalency at different locations critical for the fatigue assessment. In this regard, Passon [157] suggested to determine the damage contour lines for two well-separated locations and to select the damage equivalent wave conditions for associated wind conditions from the intersection point of both lines. Passon and Branner [150] presented a more extensive comparison of the different lumping methods.

Another line of research focussed on the identification of the load cases with the largest contribution to the damage accumulation. Neglecting the contribution of the structural response, Velarde and Bachynski [158] defined a fatigue damage parameter to quantify the contribution of different sea states to the fatigue development. Focussing on a jacked-based wind turbine, Häfele *et al.* [159] addressed the reduction of the set of load cases based on statistical evaluations. The work shows that reduced set can produce results which are comparable to those of the complete set. Moreover, it was discovered that the introduced uncertainty grows at a lower rate than the dimension reduction of the set. Stieng and Muskulus [160] showed that a small set of the most severe fatigue design load cases for a particular turbine suffice for an accurate prediction of the fatigue damage of a slightly different design, for instance for a related or optimized design.

An accurate prediction of the fatigue damage requires a sufficiently long simulation of the environmental conditions, exceeding the commonly adopted  $6 \times 10$  minutes [161], as well as a stochastic distribution of the sea state parameters within a considered wind speed bin [162]. This recommendations are more relevant for the more severe load cases than for the milder conditions. Based on this idea, Hübler *et al.* [163] introduced different load case reduction concepts, using Monte Carlo simulations, basing the number of simulations on either the probability of occurrence, the expected damage or the equivalence of load conditions. The sampling approaches proposed by Hübler *et al.* [163] were validated by Hübler *et al.* [164] on the basis of an extensive data set from the Northwind wind farm. The study demonstrated an improved performance compared to standard sampling methods. Nevertheless, it is concluded that the uncertainty in life-time prediction remains high, depending significantly on the design of the offshore wind turbine and controller actions. A summary of the different approaches to reduce the number of load cases is given by Table 1.4.

In conclusion, it has been demonstrated that the accumulated fatigue damage can be approximated with a limited set of load cases only. Regarding the selection of these load cases, the required simulation time and the definition of the environmental conditions – either deterministically or stochastically – remains a topic of ongoing research. Approaches that select the load cases based on the relation between the expected damage and the operational state seem to be most promising for practical applications.

### 1.4.3. FREQUENCY-DOMAIN ANALYSIS

Instead of aiming to reduce the sheer amount of required simulations for the design of an offshore wind support structure, the simulation time of each single realization could virtually be nullified if the system allowed for analysis in the frequency domain. This approach has found its application in the analysis of offshore structures for oil and gas applications [76], for which the main environmental excitations are of hydrodynamic nature. In this respect, the drag force dependency on the relative velocity is non-linear, introducing both linear and non-linear interaction terms to the model of the offshore wind support structure (provided that the drag contribution is governing, which only applies to high/long waves, relative to the structural diameter). With the purpose of analyses in the frequency domain, several works presented spectral densities of the drag force on rigid structures [165–167]. Attempts to assess the response to the non-linear drag force on compliant structures in the frequency domain have been done by Kareem [168],

Table 1.4: Overview of studies presenting approaches to reduce the number of environmental load cases.

study	approach	comment
Kühn [49]	sea-state lumping based on damage-equivalence	no dynamic interaction
Seidel [156]	sea-state lumping based on wave spectral density at the first natural frequency	only non-operating turbines
Passon [157]	sea-state parameters from damage-contour lines ensuring simultaneous compliance with damage equivalency criteria at different locations	damage-contour lines require many simulations
Velarde and Bachynski [158]	fatigue damage parameter for different sea states	no dynamic interaction
Häfele <i>et al.</i> [159]*	exclusion of load cases with non-critical directionality and/or low probability of occurrence	pre-knowledge required on structural response
Hübler <i>et al.</i> [163]	variable wind speed bin sizes	expert knowledge to define bin sizes required

\* this study focusses on jacket-based support structures.

Kareem *et al.* [169], Kareem *et al.* [170] and Carassale and Kareem [171], who employed the Volterra series expansion technique.

Concerning the aerodynamic excitation of the turbine rotor, Halfpenny [151] attempted to derive the frequency-response function between a homogeneous turbulent inflow field and the forcing acting on the tower top. Kühn [49], however, concluded that the frequency-domain approach to wind turbines is inapplicable, first of all because of the non-linear aero-elasticity. Besides, the considerable geometrical non-linearity, mainly resulting from the flexibility of the rotor blades, renders the frequency-domain approach unsuitable too. Moreover, a transfer function between the inflow and the tower top excitation does not capture the transience resulting from varying operational conditions.

As an alternative, Kühn [49] introduced a hybrid time-frequency domain approach, in which the aerodynamic interaction is assessed in the time domain and the hydrodynamic excitation in the frequency domain, while accounting for the present aerodynamic damping. This approach is illustrated by Figure 1.17. For the analysis of the fatigue limit state, the fatigue damages from the separate analyses were combined by means of a quadratic superposition procedure. Van der Tempel [152] used time-domain simulations for the aerodynamic analysis as well, employing a model of a flexible rotor mounted on a rigid tower. The power spectral density of the resulting tower top forces was subsequently used for a frequency-domain analysis of the support structure, combined with a spectral definition of a corresponding sea state. The aerodynamic interaction was accounted for by an additional modal damping. This hybrid time-frequency domain approach circumvents the difficulties arising from the non-linear aerodynamic interaction and the control system. Besides the auto-spectra of the wind and wave excitations, however, this approach requires a cross-spectral input as well.

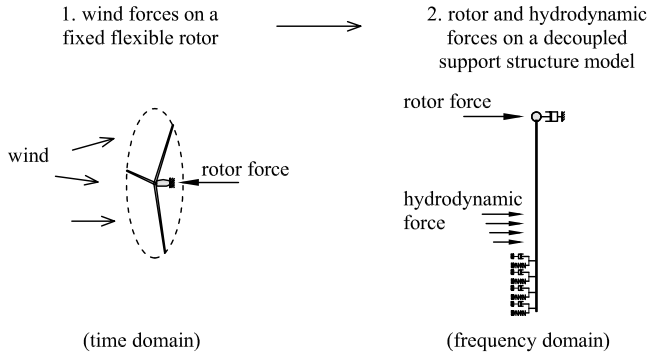


Figure 1.17: Schematization of the hybrid analysis by Kühn [49]. Regarding the properties of the decoupled model, reference is made to Figure 1.4.

## 1.5. RESEARCH FOCUS

In the previous sections, an overview is provided of the challenges related to the design of offshore wind support structures. The overview also shows the tremendous efforts that have been undertaken to either enhance the fidelity of the modelling techniques or to reduce the computational load required for the design analysis of these structures. Regarding the latter, it is recognized that the environmental interactions for the response analysis of support structures at a preliminary stage in the design process still leaves room for improvement, be it the aerodynamic, hydrodynamic or soil structure interaction. In this respect, the focus is specifically put on the representation of the aerodynamic interaction of the turbine rotor in a decoupled support structure model.

In a decoupled model of an offshore wind support structures, the aerodynamic interaction is accounted for by means of an additional modal damping, or a discretized dashpot dissipating the energy of the fore-aft tower top motions. A drawback of the former is that the damping value can only be estimated from an integrated model with specific dynamic characteristics. Moreover, the dependency on the operational conditions is not easily expressed in terms of modal damping ratios. The second approach does not account for the damping of tilt and yaw motions, the damping contribution of which – especially for higher-order modes – may be considerable, and the damping of side-to-side motion, and moreover, the couplings of the different damping mechanisms, through the eccentricity of the rotor, as well as the shapes of the orthogonal modes.

Based on the above, the question arises to what extent the coupling between an operating turbine and its support structure can be captured with the help of an added damping matrix, with which the aerodynamic force that is induced due to the non-zero structural velocity can be mimicked. Such a matrix should define the coupled aerodynamic damping mechanism corresponding to the three translations and the three rotations of the tower top. Moreover, the matrix should explicitly express the dependency on the operational conditions, so that the varying damping characteristics are easily accounted for.

Defining the aerodynamic interaction in terms of an added damping matrix involves

a linearization procedure, while the aerodynamic loading on the wind turbine blades depends non-linearly on the structural motions. Before state-independent expressions for the added damping are to be obtained, first the state-dependent aerodynamic loading of a single turbine blade is to be addressed. This analysis not only considers the validity of a linearized representation of the aerodynamic interaction, but also the applicability of a simple instantaneous load model to begin with, in comparison with a more accurate history-dependent definition of the loads.

Any definition of the added damping depends on the operational conditions of the turbine, and consequently on the control system. When concerning a load simulation of a pitch-regulated turbine, it must be possible to define a good prediction of the pitch angle variations, based on the inflow conditions. In this respect, the question is to what extent the decoupled design procedure can be improved by separating the aerodynamic forcing related to the pitching actions of the turbine from the aerodynamic interaction.

Given that a definition of the aerodynamic damping in terms of a state-independent added damping matrix already involves a linearization of the dependency of the forcing on the structural response, it may be worthwhile to re-consider the applicability of the frequency-domain analysis for the design of offshore wind support structures, at least during the preliminary design stage. Provided that offshore wind turbines are excited simultaneously by wind and waves, this aspect should address the correlation between these stochastic processes.

## 1.6. APPROACH

The analysis of the dynamics of offshore wind turbines is by default case-based. At the moment of writing, new turbines are being designed, new support structure concepts developed and new control strategies defined, while the search for wind energy resources enters deeper waters and harsher offshore conditions. The details of these developments seep only to a very limited extent through to the public domain. Within the context of this research, it was chosen to base the analysis on the 5 MW reference turbine, presented by the NREL institute [172], with the monopile-based support structure defined in the UpWind study [173], simply because the majority of the existing studies are still based on this offshore wind turbine concept.

The studies presented in this work find their basis in numerical simulations. This involves simulations with the proposed new models and comparisons with the certified aero-elastic software BLADED, allowing for a quantitative assessment of the presented result. In this respect it is worth mentioning that BLADED is a closed-source commercial software, as a result of which the differences between simulation results are sometimes subjected to interpretation.

Before it is attempted to express the aerodynamic interaction in terms of an added damping matrix, Chapter 2 contains the theoretical framework of this study, and addresses the basic theories regarding the aero-elasticity of a rotating rotor. These theories provide the basis for the further derivations in the following chapters, as well as give an insight in the many assumptions that render any simplification of the aerodynamic interaction. Subsequently, the linearization of the state-dependency of the aerodynamic loading of a single rotating turbine blade is assessed in Chapter 3. Apart from the linearization, the chapter also addresses the history-dependency of the aerodynamic load. Chapter 4



defines a structural model of a rotating rotor, exposed to time-varying inflow conditions. On this basis, state-independent expressions for the aerodynamic damping are obtained, accounting for tower top motions in three dimensions, and response simulations with different inflow conditions are compared with results obtained with BLADED. The further separation of the pitch-induced forcing from the rotor loading is addressed in Chapter 5, where the performance of the proposed method is demonstrated for simultaneous wind and wave excitations. Ultimately, Chapter 6, summarizes the main conclusions and presents subsequent recommendations for future research.



# 2

## BASIC PRINCIPLES OF ROTOR AERODYNAMICS

*The dynamic analysis of offshore wind support structures requires understanding of the basic principles of rotor aerodynamics. The interaction of the rotating blades with the ambient wind field determines the aerodynamic force that needs to be transferred to the foundation. Moreover, this interaction causes a resistance against wave-induced motions, reducing the amplitude of the resulting stress variations in the support structure. In providing the basic understanding, the focus is on established analytical approaches to capture the flow conditions around and the loads on a rotor. In this regard, this chapter provides a description of the fluid-structure interaction at blade level and of varying methods to estimate the flow conditions around a rotor. The largest part of this chapter concerns the aerodynamic loads on an aerofoil, distinguishing stationary, quasi-stationary and dynamic flow conditions. The presented theory serves as a basis for the analysis of the rotating blade and the state-independent apparent aero-elastic properties of a wind turbine rotor in the subsequent chapters.*

THE aerodynamic excitation defines the reason of existence of offshore wind turbines. Regarding the support structure, design optimizations seek a balance between structural efficiency and power output maximization. Given the complexity of the excitation in interaction with the rotating blades, the aerodynamic excitation is an ongoing subject of research.

This research is predominantly focused on the aero-elastic performance of the turbine rotor, addressing aspects as the wake development and aerofoil performance, and numerical validations by means of computational fluid dynamics of ever larger turbines [39, 174–176]. Even though it is recognized that these topics can undeniably be related to the forcing of the support structure of the turbine, this link is generally not pursued.

In line with the modern view on design, the integration of the support structure into an overall design approach for wind turbines is often acclaimed. The flexible support structure allows for wind and wave induced lateral and rotational rotor motions, which affect the aerodynamic action on the rotor blades. Hence, the modelling of the rotor aerodynamics requires theories that capture the influence of these motions on the development of the flow and the loads on the blades. One could wonder, however, to what extent the detailed modelling of the rotor aerodynamics is relevant for the design of the support structure, especially if the computational efforts are included in this equation. In this respect, the blade-element momentum theory is the most common approach to predict the loads on the rotor, and subsequently on the support structure.

The one-dimensional axial momentum balance theory regards the rotor as an actuator disc, implying an infinite number of blades and assumes that the axial flow velocity over the plane is uniform, i.e., independent of the radial distance from the axis of rotation. Moreover, the flow is constant in time. By describing the rotor wake in terms of helical vortices, a more physically realistic representation of the downstream airflow is created. Further modifications accounted for tip and yaw corrections and dynamic flows [177]. To account for radial variations, the method assumes independent annuli for which the momentum balance is considered. Yu *et al.* [38] proposed a free wake vortex ring model to account for radial and time-varying load conditions. More accurate results are obtained with vortex wake methods, assuming an inviscid incompressible flow and applying the Biot-Savart law [40], and computational fluid dynamics techniques. In terms of computational efficiency, however, these concepts disqualify for the application in simplified tools for the integrated modelling of offshore wind turbines. Nevertheless, in absence of available full-scale measurements, these methods are most relevant for the interpretation of the results of simpler tools (and the other way around!)<sup>1</sup>.

The claim that all contemporary models applied for assessing the performance of and forcing on wind turbine rotors find their origin in the field of aviation theory, and more particularly in the field of helicopter research, can easily be verified. A simple comparison between textbooks from both fields reveals the similarity straight away. In this respect, reference is made to Katz and Plotkin [178] and Anderson Jr. [179] concerning the potential flow theory for aerofoils, Saffman [180] for the theory of vorticity, Anderson Jr. [179] for the thin aerofoil theory, Johnson [181], Leishman [182] and Wright and Cooper

<sup>1</sup>Here, it should be highlighted that the objective of the analyses with so-called 'hi-fi' and 'low-fi' models usually differs tremendously, rendering the comparison of results invalid.

[183] for the analysis of non-stationary aerodynamic loads and Bisplinghoff *et al.* [184] and Fung [185] for aero-elasticity theory.

Still, the differences are easily observed too, first of all regarding size and rotational regime. In addition, wind turbines commonly operate around a horizontal axis, resulting in blade rotation through varying aerodynamic regimes. Another significant difference is the fact that the rotor of a wind turbine is mounted on the top of a flexible tower. When considering the rotor aerodynamics of wind turbines, the textbooks by Manwell *et al.* [34], Burton *et al.* [35] and Hansen [36] considered basic theories of the momentum balance. An elaborated overview of the momentum balance theory for horizontal axis wind turbines was published by Sørensen [177], whereas Branlard [41] addressed vorticity-based methods for wind turbine applications.

The decoupled analysis of a support structure of an offshore wind turbine requires a representation of the relation between the motion of the support structure and the aerodynamic excitation of the rotor. To obtain such a relation, a theoretical framework of the aerodynamic interaction of the rotor is a necessity, and the underlying concepts need to be considered. These concepts cover the inflow and wake developments of a rotating rotor and the aerodynamic loads on an aerofoil-shaped body.

This chapter addresses the relevant aspects for the assessment of the aerodynamic excitation of the support structures of offshore wind turbines. This assessment is restricted to a three-bladed rotor on a monopile foundation, since these represent the vast majority of wind turbine structures applied offshore. As rotor aerodynamics is still a thriving field of research, this chapter aims to summarize the established theories, with the focus on analytical methods. Detailed insight can be generated with the application of sophisticated numerical tools, but these approaches cannot be adopted yet for the decoupled analyses of offshore wind support structures.

In this respect, Section 2.1 first addresses the development of the flow around a rotating wind turbine blade. Subsequently, Section 2.2 considers the modelling of the near-wake, from which the flow conditions and the aerodynamic blade forces can be obtained. Different approaches to describe these aerodynamic forces are then regarded in Section 2.3.

## 2.1. FLUID-STRUCTURE INTERACTION

### 2.1.1. IDEALIZED FLOW DECOMPOSITIONS

The generation of electrical energy by a rotating rotor affects the airflow in the vicinity of the rotor. The other way around, the affected airflow imposes pressures on the rotor blades, resulting in the aerodynamic forcing that induce the rotation of the rotor. Apart from the rotor rotation affecting the airflow, the structural motions induce changes in the wind velocity pattern too. On top of that, the ambient airflow is far from being stationary and uniform, which complicates the interaction even further.

This interaction between the air field and the turbine is generally explained in terms of wake vorticities and induced velocities. Before addressing these terms in more detail, first the flow around an aerofoil is analyzed. Figure 2.1(a) shows the pattern of a stationary inviscid flow around an aerofoil-shaped cross-section of a rotating turbine blade. The incident flow is composed of the stationary wind velocity and the rotational velocity of

the blade. The angle of attack of the flow is sufficiently small to ensure attached flow conditions, i.e. no vorticity is generated at the downstream side of the blade.

The disturbed flow pattern can be decomposed into a symmetric flow pattern and a circulatory flow, Figure 2.1 (b) and (c), respectively. Along the length of the blade, the circulatory flow can be perceived as a line vortex. This line vortex is referred to as the bound circulation  $\Gamma_{B;b}(r_B, t)$ , where 'B' indicates blade. Since the vortex strength varies over the length of the blade, due to changes in both the cross-sectional geometry and airflow, the bound circulation is a function of the radial distance along the blade,  $r_B$ . Moreover, as the actual flow conditions are never stationary, the bound circulation is a function of time  $t$  too.

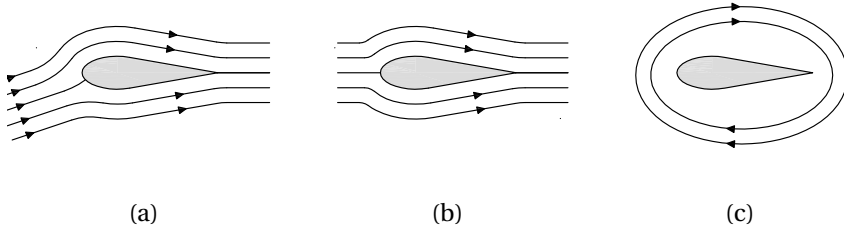


Figure 2.1: Schematic representation of the streamlines of an inviscid flow around an aerofoil, with (a) the attached flow for a small angle of attack, (b) a symmetric flow pattern, and (c) the induced circulatory flow.

### 2.1.2. WAKE VORTICITY

The bound circulation along the length of a single rotating blade is illustrated by Figure 2.2. Due to the spatial variation of its vortex strength, vorticity is emitted from the blade. The resulting panel vortex is referred to as the trailed vorticity  $\gamma_{B;t}(r_B, t)$  and can be calculated as

$$\gamma_{B;t}(r_B, t) = \frac{\partial \Gamma_{B;b}(r_B, t)}{\partial r_B}. \quad (2.1)$$

Variations in time of the wind velocity or the rotational velocity disturb the flow pattern equilibrium of Figure 2.1(a). This disturbed flow pattern is depicted in Figure 2.3(a), and results in a time-variation of the bound circulation. To compensate for this variation, vortices are emitted at the trailing edge of the blade (see Figure 2.3(b)). This panel vortex is referred to as shed vorticity  $\gamma_{B;s}(r_B, t)$  and can be derived as

$$\gamma_{B;s}(r_B, t) = \frac{\partial \Gamma_{B;b}(r_B, t)}{\partial t}. \quad (2.2)$$

The shed vortex panel is illustrated in Figure 2.2. Control actions, such as blade pitching, and structural motions result into trailed and shed vorticity too.

At the tip of each blade of a rotor with radius  $R$ , a helical vortex of strength  $\Gamma_{B;tip}(t) = \Gamma_{B;b}(R, t)$  is convected into the rotor wake. The helix angle of this tip vortex will initially coincide the inflow angle  $\phi_{B;tip}(t)$  at the blade tip. In a similar way, a helical vortex  $\Gamma_{B;root}(t) = \Gamma_{B;b}(r_H, t)$  is emitted at the root at each blade. Since the hub radius  $r_H$  is relatively small compared to the rotor radius, the total root vortex of a rotor is generally

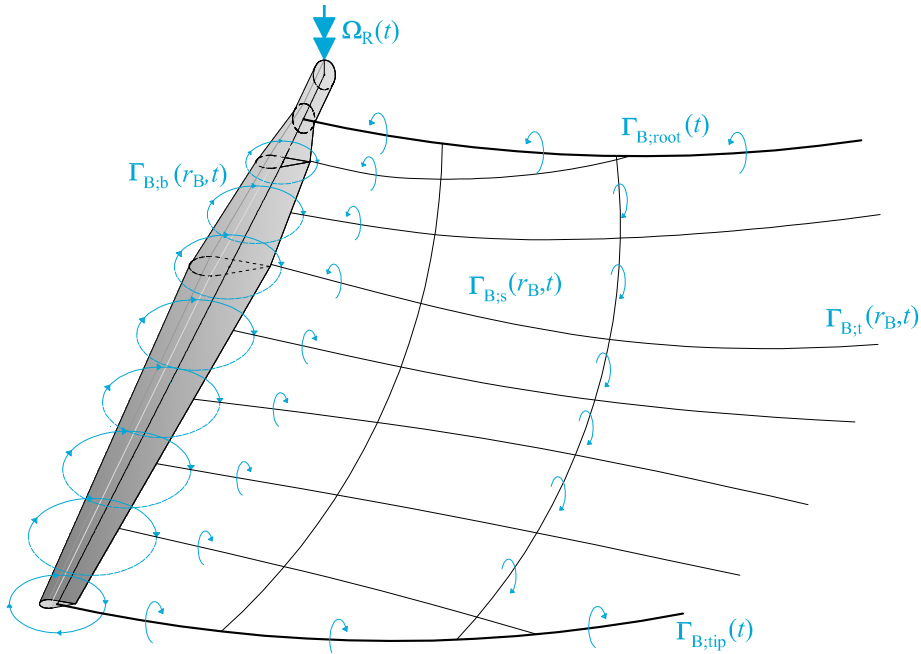


Figure 2.2: Schematic representation of the bound circulation around a rotating blade, the vortex sheet composed of trailed and shed vorticities and the tip and root vortices.

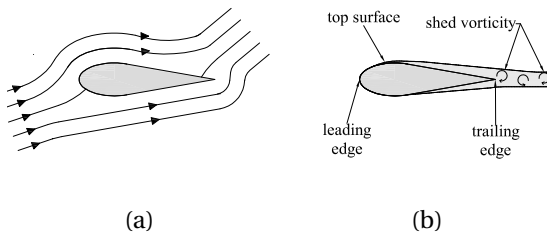


Figure 2.3: Schematic representation of an aerofoil in a disturbed flow, with (a) the streamline pattern and (b) the shed vorticity at the trailing edge.

defined as a line vortex with the strength of the combined blade root vortices. Figure 2.2 illustrates the vorticity convected from the blade tip and root of a rotor blade, rotating with rotor speed  $\Omega_R$ .

The total wake vorticity consists of the combined tip and root line vortices, and the trailed and shed panel vortices. From the equilibrium of the convected wake vorticity and the operational state of the turbine, the aerodynamic forces on the turbine rotor can be estimated. Once the bound circulation is known, the pressure variation on the blade surface can be derived, the circumferential integration of which gives the lift force, which drives the rotation of the rotor.

### 2.1.3. FLOW INDUCTION

With the generation of the wake vorticity, energy is extracted from the incoming airflow. As a result, the flow velocity in the wake must be smaller than the upstream velocity. The difference between the axial upstream and downstream wind velocity is referred to as the axially induced wind velocity.

The axially induced wind velocity, or the axial induction factor, which is calculated as the ratio of the difference velocity and the upstream velocity, is an important concept in the analysis of the aerodynamic forcing on wind turbine rotors. The momentum balance theory employs the axial induction velocity to obtain an equilibrium between the aerodynamic forces on the rotor blades and the upstream and downstream flow conditions. This theory is addressed in more detail in Section 2.2.2.

Considering the concept of axial flow induction from the description of the wake vorticity in Section 2.1.2, it can straight away be concluded that the axial induction varies both radially and azimuthally. The axial induction will be higher in the vicinity of the blades, leaving a smaller wind velocity reduction in the area between the blades. Due to the variation in aerofoil geometry along the length of the blades, and the increase of the rotational velocity towards the blade tips, the vorticity along the blade lengths is non-uniform, with the tip vortex as most significant discontinuity, resulting in the radial variation of the induced wind velocity.

Adhering to the conservation of momentum, the axial induction of the wind velocity comes with an expansion of the airflow, implying that an airflow passing the a rotating rotor inhibits a larger cross-sectional area at the downstream side of the rotor than at the upstream side. This increase in cross-sectional area comes with an induced radial velocity. Furthermore, the rotation of the rotor induces a rotational or tangential component to the downstream airflow. In the description of the wake vorticity, this tangentially induced flow can be recognized from the helical vortex travelling in downstream direction.

### 2.1.4. VISCOUS FLOWS

The description of the wake vorticity is based on inviscid incompressible flow conditions. For viscous flows, the airflow adjacent to the blade surface acquires the velocity of this surface. As a result, a boundary layer develops around the aerofoil, i.e., an air layer surrounding the aerofoil, in which "the velocity gradient is steep and the viscous stresses are significant" [70]. The resulting shear stress on the aerofoil is referred to as friction drag.

The thickness of the boundary layer is different for laminar and turbulent flows, and



depends on the Reynolds number. Considering an aerofoil, the boundary layer always starts as a laminar layer and changes after a certain distance from the leading edge into a turbulent boundary layer [179]. As a consequence, the total skin friction is composed of a combination of the laminar and turbulent skin frictions.

A flow of air at the top surface of an aerofoil first experiences a strong drop in pressure at the leading edge, after which the pressure slowly recovers to the ambient air pressure over the length of the chord. As a result of this increase of pressure over the aerofoil surface, the flow velocity reduces. In addition, for viscous flows, the skin friction reduces the airflow in the boundary layer. These combined effects may result in a zero velocity gradient normal to the aerofoil surface. At this point, the flow velocity is reversed and the airflow separates from the aerofoil. As a consequence, the pressure at the top surface does not recover to the ambient pressure within the length of the chord and a so-called stalled flow condition is obtained.

## 2.2. MODELLING OF THE FLUID-STRUCTURE INTERACTION

### 2.2.1. COMPUTATIONAL FLUID DYNAMICS TECHNIQUES

Understanding the wake development behind a rotating rotor is a key concept in estimating the aerodynamic forces on the structure. Defining the wake vorticity allows for the estimation of the pressure distribution behind the rotor and subsequently the pressure drop in the airflow across the rotor. However, the fundamental law that computational efficiency and accuracy never come hand in hand finds its application here too, and it is generally understood that good approximations are not obtained cheaply.

The Navier-Stokes equations allow for the formulation of rotational viscous flows, and can be applied to model the vortex shedding behind a rotor in an airflow numerically [70]. The numerical integration of the Navier-Stokes equations is referred to as computational fluid dynamics, and the analysis technique allows for the computation of arbitrary flows. Given its numerical nature, the application of computational fluid dynamics requires the generation of a mesh, two-dimensional or three-dimensional. Generating such a mesh is a very dedicated task, particularly in the region surrounding the rotating blades – given the high shear – and in the vicinity of the shed vortices.

The explicit closing<sup>2</sup> of the Navier-Stokes equations requires a powerful numerical solver. This issue can be overcome by solving a time-averaged system of equations, for example on the basis of Reynolds-averaged Navier-Stokes, accounting for the integral length scale of the turbulence only, and adding a model to account for the smaller length scales. The Large Eddy Simulation approach is used to model turbulent flows, including the energy content at the micro-scale. Solving the Navier-Stokes equations in full, including the turbulence at the Kolmogorov dissipation scale is done by the explicit Direct Numerical Simulation technique, which represents the most computationally demanding approach. A full analysis of a flow field around this rotor, accounting for the rotor rotation and blade, drive-train and tower flexibilities, imposes the need for a dynamic mesh. Given the tremendous skill and effort demanded, the computational fluid dynamics only finds application for research or validation purposes [186–188], using

<sup>2</sup>In other words, solving the Navier-Stokes equations while accounting for the mixing of the different turbulence length scales.

deforming-spatial-domain/stabilized space-time formulation.

### 2.2.2. MOMENTUM-BALANCE METHODS

Computational fluid dynamics techniques aim at solving the viscous flows in terms of velocities and pressures. With the assumption that the air is inviscid, incompressible and irrotational, the flow field can be described by the Laplace equation

$$\nabla^2 \Phi(\mathbf{X}_R, t) = 0, \quad (2.3)$$

where the velocity potential  $\Phi(\mathbf{X}_R, t)$  is defined as

$$\nabla \Phi(\mathbf{X}_R, t) = \mathbf{W}(\mathbf{X}_R, t), \quad (2.4)$$

with the differential operators  $\nabla = \frac{\partial}{\partial \mathbf{X}_R}$  and  $\nabla^2 = \frac{\partial^2}{\partial \mathbf{X}_R^2}$ .  $\mathbf{W}(\mathbf{X}_R, t)$  expresses the velocity vector at location  $\mathbf{X}_R$  within the inertial  $X_R Y_R Z_R$  reference frame (the subscript 'R' indicates rotor). The Laplace equation results from the substitution of the velocity potential into the conservation of mass expression for inviscid, incompressible and irrotational flows.

A second principle that governs the velocity conditions of the flow field is the conservation of momentum. The full expression of the momentum balance is given by the Navier-Stokes equations, but for inviscid and incompressible flows, the Navier-Stokes equations can be approximated by the Euler equations. From Eqs. (2.3), and the formulation of the appropriate boundary and initial conditions, a non-stationary flow field can be solved for, and the actual flow conditions at a rotor plane be obtained. Subsequently, the pressure distribution and the resulting forces on the rotor structure can be obtained from the Euler equations. It goes without saying that solving the Laplace and Euler equations for arbitrary boundary and initial conditions, still requires a powerful numerical solver.

#### STATIONARY UNIFORM AXIAL FLOWS

For stationary flow conditions, the time-dependency of the Laplace and the Euler equations disappears. The description of the fluid-structure interaction can be simplified even further, by assuming the flow to be uniform and axial and defining impermeability boundary conditions at the blade surfaces, stating that the relative flow velocity normal to the surface of the blades is zero. Within the potential flow framework, these boundary conditions can be defined by means of time and space-dependent sink/source and doublet velocity fields.

After some mathematical manipulations, the Euler equations can be reformulated into the celebrated Bernoulli's equation. With the application of Bernoulli's equation, the uniform axial airflow through the rotor plane can be represented by a stream tube, as illustrated by Figure 2.4. As a further simplification, the rotor is modelled as an actuator disc, effectively implying a rotor with an infinite number of blades and small solidity, i.e. the ratio between the total blade area and the rotor disc area. Adopting the rotor disc concept and the stream tube representation, a uniform flow distribution at the rotor plane in the axial  $Y_R$  direction is obtained.

The momentum-balance analysis allows to formulate the axial flow velocity at the rotor plane  $W_{R,Y}$  within the stream tube to be expressed in terms of the axial upstream

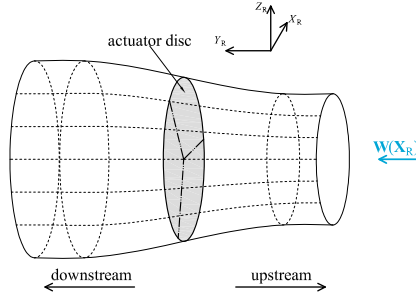


Figure 2.4: Schematic illustration the stream tube model, representing a uniform constant flow through an actuator disc.

velocity,  $W_{U;Y}$  ('U' indicates upstream):

$$W_{R;Y} = (1 - a_{R;Y}) W_{U;Y}. \quad (2.5)$$

Here, the coefficient  $a_{R;Y}$  represents the induction ratio, i.e., the ratio between the induced flow velocity at the rotor plane and the upstream wind velocity:

$$a_{R;Y} = 1 - \frac{W_{R;Y}}{W_{U;Y}}. \quad (2.6)$$

With the application of Bernoulli's equation, the axial downstream flow velocity  $W_{D;Y}$  can be expressed as

$$W_{D;Y} = (1 - 2a_{R;Y}) W_{U;Y}, \quad (2.7)$$

and the magnitude of the resulting thrust force on the rotor plane  $F_{R;Y}$  as

$$F_{R;Y} = \frac{1}{2} \pi \rho_{\text{air}} C_{R;T;Y} R^2 W_{U;Y}^2, \quad (2.8)$$

with the air density  $\rho_{\text{air}}$  and the axial thrust coefficient  $C_{R;T;Y}$ :

$$C_{R;T;Y} = 4a_{R;Y}(1 - a_{R;Y}). \quad (2.9)$$

To find a solution for the flow field at the rotor plane, an additional equation for the induction coefficient is required. This additional equation can be derived from the analysis of the aerodynamic forcing on the blades. In Section 2.3, the aerodynamic forcing on the rotor blades is considered. This aerodynamic forcing is a function of the flow velocity at the rotor plane, for which again Eq. (2.5) can be adopted. The aerodynamic forcing, with the unknown coefficient  $a_{R;Y}$  can subsequently be solved with the application of Eq. (2.8). Instead of the stream tube of Figure 2.4, the momentum balance can also be considered for independent annuli with thickness  $\delta r_B$ . Likewise, the aerodynamic forcing can be considered for small blade elements too. If the momentum balance and the aerodynamic forcing are equalled per annulus, a radius-dependent thrust force  $F_{R;Y}(r_B)$

and induction coefficient  $a_{R,Y}(r_B)$  are obtained. This approach is generally known as the blade element/momentum theory.

The analysis of the flow velocity on the basis of the Bernoulli's equation does correctly predict a larger wake diameter, compared to the diameter of the rotor. On the other hand, as a result of the assumption of the actuator disc, the induction coefficient is azimuth-independent, whereas the actual induced velocity is higher in the vicinity of the blades. Moreover, the momentum balance does not account for the rotation of the wake, which is induced by the rotational velocity of the rotor. In addition, the stream tube model assumes a transition of the flow velocity within the tube from the upstream velocity  $W_{U,Y}$  to the downstream velocity  $W_{D,Y}$ . Outside the tube, the flow velocity remains unaffected and equals  $W_{U,Y}$ . The resulting jump in flow velocity at the interface, however, is non-physical.

Solving Bernoulli's equation under the assumption of a uniform and constant axial inflow results in the computationally cheapest description of the flow field at the rotor plane. The resulting flow field is referred to as a static wake formulation. When analyzing time-varying flows, a dynamic formulation of the flow conditions would allow for a better description of the forces on the blades. The one-dimensional momentum theory, however, only accounts for variation of the axial flow, implying that the induced radial and rotational flows are not considered. Moreover, the concept of the tubular axial flow disregards a smooth transition between the flows inside and outside the stream tube. The adopted actuator disc assumes an infinite number of blades, a concept which contains little resemblance with actual wind turbine rotors. Finally, the one-dimensional momentum theory requires axial and uniform inflow conditions over the rotor plane, rendering the theory invalid for skewed inflows and analysis within the atmospheric boundary layer.

Sørensen [177] derived a general momentum theory for uniform axial inflows, including the induced azimuthal flow directly behind the rotor plane. This derivation does not allow to solve the flow conditions for a turbine rotor, without the supplementary computational fluid dynamics simulations or the implementation of unvalidated assumptions. Regarding the latter, Glauert [189] derived a closed model under the assumptions of negligibly small radial pressure forces and an invariable azimuthal flow velocity in the rotor wake. Defining the azimuthal flow velocity at the rotor plane in a rotating reference frame as  $W_{R,\Psi}$ , the radially varying rotationally induced velocity coefficient  $a_{R,\Psi}(r_B)$  can be defined as

$$a_{R,\Psi}(r_B) = -\frac{W_{R,\Psi}}{\Omega_Y r_B}. \quad (2.10)$$

Here,  $\Omega_Y$  represents the rotor speed around the  $Y$  axis. The minus sign appears because the wake and rotor rotations have opposite directions. From Glauert's derivation, the induction coefficient  $a_{R,\Psi}(r_B)$  can subsequently be solved as follows:

$$a_{R,Y}(1 - a_{R,Y}) = \lambda_{\text{tip}}^2 \mu^2 a_{R,\Psi}(r_B)(1 + a_{R,\Psi}(r_B)), \quad (2.11)$$

where  $\lambda_{\text{tip}} = \frac{\Omega_Y R}{W_{U,Y}}$ , or the tip speed ratio, and  $\mu = \frac{r_B}{R}$ , or the relative radius.

Burton *et al.* [35] assumed a balance between the axial upstream and downstream pressures and the kinetic energy from the induced rotational flow. The assumption that the ratio between the induced velocities in wake and at the rotor plane equals two

was released by Joukowsky [190], requiring a complementary equation expressing the difference in the upstream and downstream pressures.

The actuator disc concept supposes an infinite number of blades. As a consequence, the application allows for the prediction azimuthally invariant axial induction coefficients. For finite-bladed rotors, however, the induced flow varies with the azimuth angle. Glauert [189] proposed the a correction for the axial induction coefficient, with the application of the tip correction  $F_{B;\text{tip}}(r_B)$ :

$$F_{B;\text{tip}}(r_B) = \frac{\pi}{2} \arccos \left( e^{-\frac{N_B(1-\mu)}{2\mu \sin \phi_B(r_B)}} \right). \quad (2.12)$$

Here,  $N_B$  represents the number of blades, whereas  $\phi_B(r_B)$  is the local inflow angle.

### NON-UNIFORM ROTOR PRESSURE

The momentum balance on the basis of the Bernoulli's equation requires a uniform pressure jump across the rotor plane. As a result, the flow velocity at the interface of the stream tube is non-continuous. Kinner [191] found that, if the Laplace equation is adopted for the pressure field instead of the velocity potential, the pressure distribution can be expressed in ellipsoidal coordinates and a solution can be obtained in terms of Legendre polynomials, which describe a continuous transition of the flow velocity at the interface of the stream tube. Joglekar and Loewy [192] extended this method to include induced velocities in all directions. These approaches, however, were specifically developed for helicopter applications. Van Bussel [193] adjusted the method for wind turbine rotors.

Adopting again the stream tube model and the actuator disc concept, the stationary flow field can be described as a summation of the upstream velocity field and the induced velocity field in the vicinity of the rotor. It is assumed that the components of latter are small compared to the former. After substitution of this formulation of the velocity field into the stationary Euler equations, and linearization with respect to the induced velocity field, the Laplace equation can now be applied to describe the pressure field:

$$\nabla^2 p(\mathbf{X}_R) = 0. \quad (2.13)$$

After a coordinate transformation to ellipsoidal coordinates, the pressure field can be found in terms of Legendre polynomials of the first and second kinds, which is referred to as the Kinner's solution of the pressure distribution on a rotor disc, expressing the pressure field as a summation of harmonics. The required mathematical operations to obtain this expression can be found in Whittaker and Watson [194].

Figure 2.5(a) presents the solution of the first term of the Kinner's pressure distribution, in terms of the thrust coefficient  $C_{R;T;Y}$ , for a uniform axial flow. The maximum pressure is obtained at the hub, whereas the pressure drops to zero towards the edge of the rotor disc. The actual pressure on a rotating wind turbine rotor should also be zero at the hub. This can be achieved by adding a second term to the description of the pressure distribution, illustrated in Figure 2.5(b). The resulting relative pressure distribution is shown in Figure 2.5(c), for which the pressure is zero at both  $r_B \rightarrow R$  and  $r_B = 0$ . In general, turbine rotors are designed such, that a uniform pressure distribution over the blade

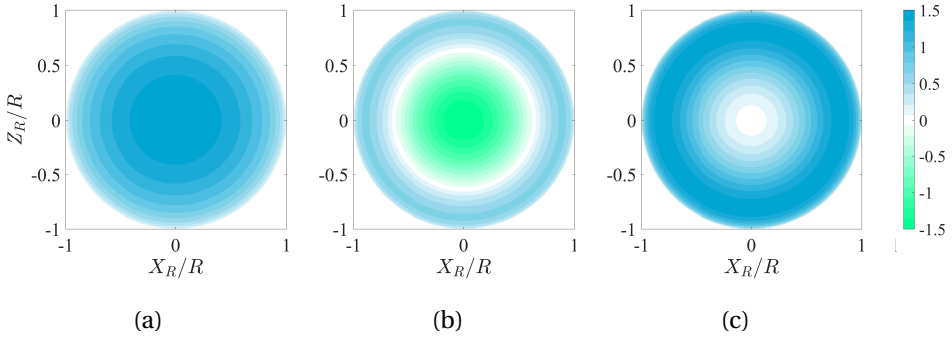


Figure 2.5: Kinner's solutions for uniform axial flows, with(a) the first-term solution, (b) the second-term solution, and (c) the combined first and second-term solution.

spans is obtained. Using Kinner's solution to describe such a pressure distribution would require more terms.

After defining the pressure distribution at the rotor plane, the induced velocity field can be estimated by spatial integration of the linearized Euler equations for the induced velocity field. For uniform and axial flows, Mangler and Squire [195] calculated the induction coefficient  $a_{R;Y}$  at the rotor plane:

$$a_{R;Y}(\mu) = \frac{15}{16} C_{R;T;Y} \mu^2 \sqrt{1 - \mu^2}. \quad (2.14)$$

In deriving the Euler equations for the induced velocity field, the Euler equations for the total velocity field were linearized with respect to the induced velocity, implying that Eq. (2.14) is only valid if  $a_{R;Y}(\mu)$  is small compared to one. From, Eq. (2.14), the thrust coefficient can be expressed in terms of the average induced velocity over the rotor area,  $\bar{a}_{R;Y}$ :

$$C_{R;T;Y} = \frac{1}{4} \bar{a}_{R;Y}. \quad (2.15)$$

Solving the Euler equations by means of Kinner's solution results in non-uniform pressure distribution, and zero pressures at the hub and blade tips specifically. The presented approach, however, does not account for wake rotations and corresponding in-plane induced velocities. Moreover, a comparison between Eqs. (2.9) and (2.15) shows that the flow field obtained from the acceleration potential is only valid for small values of  $\bar{a}_{R;Y}$ .

### NON-AXIAL UNIFORM FLOWS

Figure 2.6 illustrates an actuator disc exposed to a non-axial flow. The rotor plane is directed with the yaw angle  $\gamma_{R;Z}$  with respect to the uniform upstream inflow  $\mathbf{W}(\mathbf{X}_R)$ . As a result, the centre line of the wake is skewed at an angle  $\chi_{R;Z}$  with respect to the global  $Y_R$  axis, for which it applies that  $\chi_{R;Z} > \gamma_{R;Z}$ . Under these inflow conditions, the pressure distribution on the actuator disc is no longer axi-symmetric.

The Kinner's solution can be adopted to describe an anti-symmetric pressure distribution on a rotor disc exposed to a non-axial flow. These pressure distributions result in

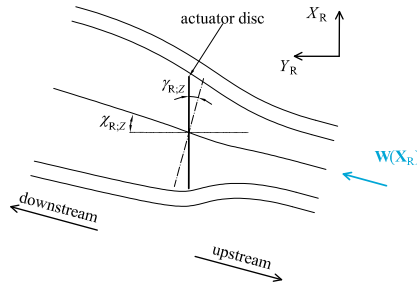


Figure 2.6: Schematic representation of an actuator disc exposed to a skewed airflow.

to moments around the  $X_R$  and  $Z_R$  axis,  $T_{R;X}$  and  $T_{R;Z}$ , respectively – also referred to as tilting and yawing moments – which can be expressed in terms of the moment coefficients  $C_{R;M;Z}$  and  $C_{R;M;X}$ , respectively:

$$T_{R;Z} = \frac{1}{2} \rho_{\text{air}} \pi R^3 C_{R;M;Z} |\mathbf{W}(\mathbf{X}_R)|^2, \quad (2.16)$$

and

$$T_{R;X} = \frac{1}{2} \rho_{\text{air}} \pi R^3 C_{R;M;X} |\mathbf{W}(\mathbf{X}_R)|^2. \quad (2.17)$$

The resulting anti-symmetric pressure distributions are depicted in Figures 2.7(a) and (b), respectively. The pressure distributions are shown relative to  $C_{R;M;Z}$  and  $C_{R;M;X}$ .

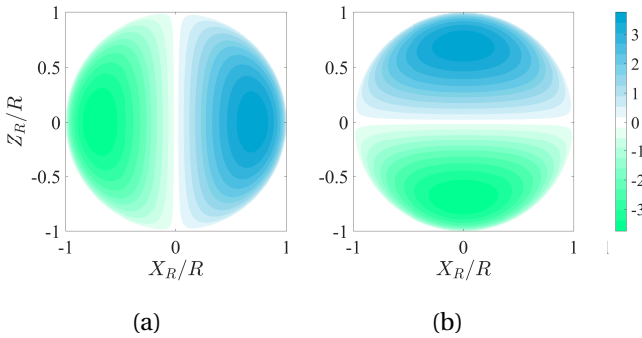


Figure 2.7: Kinner's solutions for anti-symmetric pressure distributions, with (a) the first-term solution for a yawed rotor and (b) the first-term solution for a tilted rotor.

As shown in Figure 2.6, the expansion of the flow through a yawed rotor is asymmetric. As a result, the blades of the yawed rotor experience a larger lift force during the upwind sweep than during the downwind sweep, and the rotor experiences a yawing moment around the global  $Z_R$  axis. At the same time, the yawing affects the incident velocity of a vertically oriented blade, resulting into a tilting moment around the global  $X_R$  axis.

Pitt and Peters [196] determined the induced flow velocity at a helicopter rotor for varying inflow angles, by means of numerical integration of the linearized Euler equations for the induced velocity field, basing the numerical integration on the linearized Euler equations. For the numerical integration, the pressure distributions at the rotor plane of the Kinner's term for anti-symmetric pressure distributions was adopted. Based on the numerical results, an analytical fit for the induction coefficient perpendicular to the rotor plane was defined:

$$a_{R;Y} = \bar{a}_{R;Y} + a_{R;YZ}\mu \sin \psi + a_{R;YX}\mu \cos \psi, \quad (2.18)$$

which describes the induction coefficient as a function of the azimuth angle  $\psi$ .  $\bar{a}_{R;Y}$  defines the mean value of the induction coefficient and the  $a_{R;YX}$  and  $a_{R;YZ}$  the variations about the  $X_R$  and  $Z_R$  axes, respectively. Pitt and Peters [196] defined the  $3 \times 3$  matrix  $\mathbf{L}_R$ , which relates the thrust and moment coefficients to the induction coefficients of Eq. 2.18:

$$\mathbf{C}_R(t) = \mathbf{L}_R^{-1} \mathbf{a}_{R;Y}(t). \quad (2.19)$$

Here,  $\mathbf{C}_R(t)$  is a vector containing the thrust and moment coefficients of Eqs. (2.8), (2.16) and (2.17).  $\mathbf{a}_{R;Y}(t)$  is a vector with the corresponding induction coefficients from Eq. (2.18.)

Moreover, with the inclusion of the second-order pressure term for the anti-symmetric pressure distribution, the derivative of the pressure at the hub of the rotor can be enforced to be zero. The inclusion of higher-order pressure terms allows for a better description of the pressure distribution over the radius of the rotor. Furthermore, an azimuthal variation of the pressure over the rotor plane could be accounted for. In-plane induced velocities were not accounted for yet either, but may be included with higher-order Legendre polynomials too.

The matrix  $\mathbf{L}_R$  as defined by Pitt and Peters [196] does not account for the skewed wake. At an earlier stage, Coleman *et al.* [197] suggested a dependency of the axial induction on both the yaw angle  $\gamma_{R;Z}$  and the wake angle  $\chi_{R;Z}$ . For this derivation, a vortex cylinder model for the rotor wake was applied.

### NON-STATIONARY FLOWS

For non-stationary flows, the time-dependent induced flow velocity can be determined from the stationary Euler equations – with the velocity field decomposed into the up-stream and induces velocity components – for either an axial or a non-axial flow fields. Such a quasi-static approach results in the definition of a so-called equilibrium wake, for which the induced velocity instantaneously adapts to variations in the inflow conditions. Solving the Euler equations, however, with the inclusion of the acceleration terms allows for the derivation of a dynamic wake and the corresponding time-dependent induced velocity field.

Assuming an induced velocity field which is small compared to the ambient velocity field, the flow can be again described in terms of the pressure potential instead of the velocity potential. Gaonkar and Peters [198] defined the  $3 \times 3$  added inertia matrix  $\mathbf{M}_R$  to account for the time-dependency of the force-induction relation:

$$\mathbf{C}_R(t) = \mathbf{M}_R \dot{\mathbf{a}}_{R;Y}(t) + \mathbf{L}_R^{-1} \mathbf{a}_{R;Y}(t). \quad (2.20)$$



The entries of the  $\mathbf{M}_R$  matrix are not affected by the yawing of the rotor. Furthermore, no cross-couplings between the induced accelerations and the aerodynamic coefficients are introduced. Peters *et al.* [37] generalized the dynamic wake model, so that it accounts for an arbitrary number of inflow harmonics and radial shapes. An overview of the further developments of the dynamic wake modelling is provided by Peters *et al.* [199].

### 2.2.3. VORTEX METHODS

In deriving a general momentum theory, Sørensen [177] accounted for the azimuthal flow in the rotor wake. The derivation allowed for the description of the wake as a rotating body – which was argued to be unphysical – or a free vortex flow. The subsequent attempts to describe the flow in terms of vorticity, instead of velocities and pressures – as is the case with computational fluid dynamics techniques and the momentum-balance methods – is associated with vortex methods [41].

The free vortex flow provides a basis for the Joukowski's cylindrical vortex model [200] and the tubular vortex model, the latter of which allowing for the expansion of the wake. These methods still employ the actuator disc concept, a correction for which was presented by Prandtl [201]. The modelling approach can be improved with the inclusion of a root vortex and bound vorticity disk at the rotor plane, a full derivation of which was presented by Branlard and Gaunaa [202] for axial flows and Branlard and Gaunaa [203] for skewed flows. The discretization of the tubular vortex wake model introduces the vortex ring model. Yu *et al.* [38] illustrated the applicability of this approach to non-stationary and radially varying axisymmetric inflows, a work which was experimentally substantiated for transient loads [39].

The actuator disc concept consists of a homogeneous rotor plane, as a result of the assumed infinite-bladed turbine. Modelling the individual blades by their aerodynamic performance, in terms of their distributed bound circulation, allows for a finite-bladed rotor representation and the prediction of an inhomogeneous induced velocity field. Instead of these so-called lifting lines, the blades can be represented by lifting surfaces too, by which the chord lengths of the blade sections are explicitly accounted for. If rigid prismatic blades are assumed, the wake can be modelled in terms of the emitted tip and root vortices, through the application of the Biot-Savart law. Neglecting the wake expansion, this approach provides the basic helical vortex model representation, from which analytical predictions for the induced velocity field can be obtained [41].

More advanced wake representations, for instance for radially varying bound circulations and wake involves the explicit modelling of shed vorticity by means of line or panel elements. To meet the requirement of irrotationality of the potential flow theory, the modelling of the shed vorticity requires the explicit modelling of the vortex wake, for instance by means of vortex panels. This requirement restricts the analysis of the rotating rotor, including the wake development, to the numerical domain, providing an alternative for computational fluid dynamics analysis approaches [40, 204]. Leishman [40] distinguished prescribed and free vortex techniques, the former used for the validation of experimental results, while the later can be employed for predictive purposes. In the application to transient analyses, the modelling of vortex wake models can be characterized as tedious and prone to numerical instabilities. The repetitive evaluation of the Biot-Savart law, required for the estimation of the wake vortices, still renders the methods computationally

expensive, while providing the advantage of a physically more realistic representation of the rotor wake, compared to the momentum-balance approaches. Wang and Coton [205] applied a vortex filament approach to analyze the tower shadow load effect on the blades of a downwind wind turbine. Gebhardt *et al.* [206] developed a vortex-lattice approach, with which the velocity field around a flexible rotor-tower structure in non-stationary aerodynamic conditions has been predicted [207, 208].

## 2.3. AERODYNAMIC FORCING

### 2.3.1. AEROFOIL DEFINITION

This section addresses the aerodynamic forcing on an aerofoil in a two-dimensional flow. As the main theory to describe this forcing, the thin aerofoil theory – which reduces the aerofoil to a vortex panel – is introduced. On this basis, first the forcing on an aerofoil in a stationary inviscid flow is considered. Subsequently, this analysis is expanded towards aerofoils in non-stationary inviscid flows. This second scenario induces added inertia force components too, which are addressed separately. As a final generalization of the two-dimensional analysis, the aerodynamic forcing in a viscous flow is addressed. Due to the viscosity, the airflow may separate from the aerofoil surface, resulting a stalled flow condition. The analyses in this work, however, are restricted to attached flow conditions. As a final generalization, the aerodynamic forcing in a three-dimensional flow is briefly addressed. It should be noted, that only incompressible flows are considered in this section.

As a starting point, Figure 2.8(a) presents the important geometric definitions of a typical aerofoil. The side cutting into the airflow is referred to as the leading edge, whereas at the trailing edge the separated airflow comes back together. The length of an aerofoil is expressed in terms of its chord, the straight line between the leading and the trailing edges. The camber line is defined by the points halfway the top and bottom surfaces. For symmetric aerofoils, the chord line and the camber line coincide. The aerodynamic theories presented in this section, often refer to the semi-chord, which is half the length of the chord.

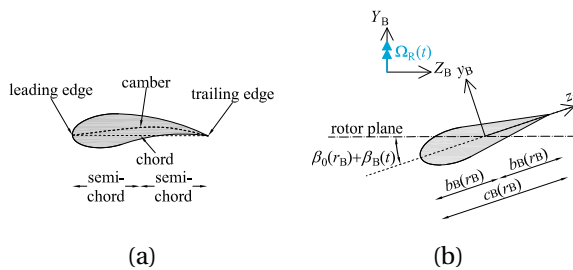


Figure 2.8: Aerofoil representation, with (a) the important geometric definitions and (b) the parametric representation of the relevant aerofoil properties, depicted within the global moving reference frame.

Figure 2.8(b) presents the positioning of a symmetric aerofoil with respect to the global moving reference frame  $r_B Y_B Z_B$ , of which the  $Y_B$  defines the axis of the rotor rotation  $\Omega_{R,Y}$ . The principal axes of the aerofoil section are defined by the local  $r_B y_B z_B$  reference

frame, the origin of which is located at the semi-chord, or mid-chord. The  $r_B$  axis of the local frame coincides with the  $r_B$  axis of the global moving  $r_B Y_B Z_B$  frame. The  $y_B$  and  $z_B$  axes are rotated over an angle  $\beta_0(r_B) + \beta_B(t)$  with respect to the global moving frame. Here, the angle  $\beta_0(r_B)$  represents the geometric rotation, or twist, which generally varies over the length of the blade, rendering the twist angle a function of  $r_B$ .  $\beta_B(t)$  is the pitch angle, which is actively controlled at above-rated wind velocities for pitch-regulated turbines. For this reason, the pitch angle is presented as a function of time. The chord length  $c_B(r_B)$ , and consequently the semi-chord length  $b_B(r_B)$  vary over the length of the blade and are therefore presented as functions of  $r_B$ . As far as two-dimensional flows are considered, the dependencies of the aerofoil properties, the flow conditions and the aerodynamic forcing on the blade radius are omitted.

### 2.3.2. THIN AEROFOIL THEORY

Figure 2.9(a) shows a symmetric aerofoil exposed to the effective airflow velocity  $\mathbf{W}_{B,\text{eff}}$ . This effective airflow is composed of the rotational velocity, the inflow velocity and the induced wind velocity components within the rotor plane. For the time-being, this velocity is assumed to be stationary, but it does vary along the length of the blade. Assuming inviscid flow conditions, an effective airflow acting along the symmetry axis of the aerofoil does not induce aerodynamic forces on this aerofoil. If the airflow acts under a small angle of attack  $\alpha_B$  with respect to the symmetry axis, see Figure 2.9(a), a circulatory flow develops around the aerofoil. This circulatory flow was introduced in Section 2.1 as the bound circulation  $\Gamma_{B;b}$ , which for stationary flows is independent of time.

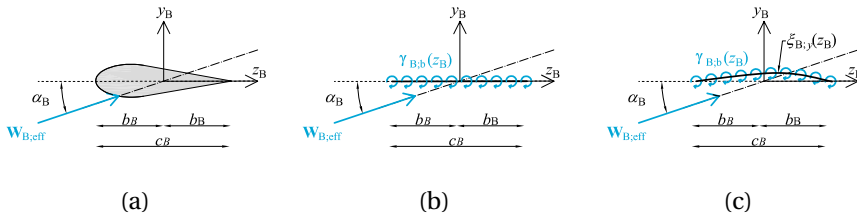


Figure 2.9: Schematic illustration of the thin aerofoil theory, with (a) an aerofoil exposed to an effective airflow velocity, (b) the representation of a symmetric aerofoil by means of a vortex sheet and (c) the representation of a cambered aerofoil by means of a vortex sheet.

The bound circulation around an aerofoil can be estimated with the thin aerofoil theory. Among others, Anderson Jr. [179], Leishman [182] have addressed this theory extensively. As a main principle, the bound circulation is replaced by a streamline of a the vortex sheet  $\gamma_{B;b}(z_B)$  along the camber line of the aerofoil:

$$\Gamma_{B;b} = \int_{-b_B}^{b_B} \gamma_{B;b}(z_B) dz_B. \quad (2.21)$$

For symmetric aerofoils, the camber line coincides with the chord line, and as illustrated by Figure 2.9(b), a straight vortex sheet is obtained. For a cambered aerofoil, however, the camber line is curved and described by the function  $\xi_{B;y}(z_B)$ , as shown in Figure 2.9(c).

The vortex sheet  $\gamma_{B;b}(z_B)$  obeys two additional conditions. First, the pattern of a stationary flow around an aerofoil, as illustrated by Figure 2.1(a), is dictated by the Kutta condition, that is, the flow leaves the aerofoil smoothly. For aerofoils with a finite angle at the trailing edge, the Kutta condition even implies that the flow velocity at the trailing edge is zero. Second, for the camber line to be a stream line, the resulting velocity normal to the camber line along the length of the aerofoil must be zero.

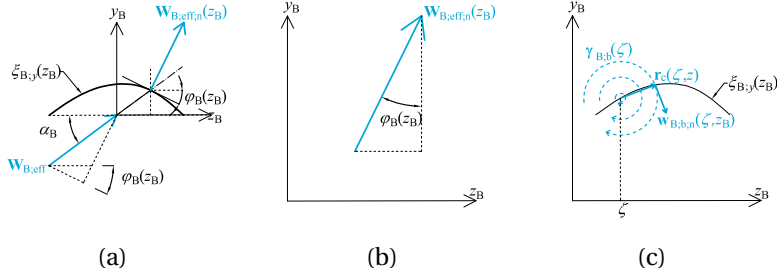


Figure 2.10: Schematic representation of the velocity vectors defining the blade vortex sheet, with (a) the effective inflow velocity vector and the velocity vector normal to the blade camber, (b) the angle defining the slope of the camber line, and (c) the induced velocity normal to the camber line resulting from the bound vorticity.

Figure 2.10(a) illustrates the effective velocity normal to the camber line,  $\mathbf{W}_{B;eff;n}(z_B)$ , which due to the camber is a function of  $z_B$ . The angle  $\varphi_B(z_B)$  defines the slope of the camber line along:

$$\tan\{\varphi_B(z_B)\} = -\frac{\partial \xi_{B;y}(z_B)}{\partial z_B}. \quad (2.22)$$

With this angle, the magnitude of the vector  $\mathbf{W}_{B;eff;n}(z_B)$  can be defined as follows:

$$|\mathbf{W}_{B;eff;n}(z_B)| = |\mathbf{W}_{B;eff}| \sin\{\alpha_B + \varphi_B(z_B)\}, \quad (2.23)$$

with the vector components in the  $y_B z_B$  plane as shown in Figure 2.10(b).

$$\mathbf{W}_{B;eff;n}(z_B) = |\mathbf{W}_{B;eff;n}(z_B)| \begin{bmatrix} \cos\{\varphi_B(z_B)\} \\ \sin\{\varphi_B(z_B)\} \end{bmatrix}. \quad (2.24)$$

Figure 2.10(c) illustrates the induced circulation at the point  $z_B = \zeta$  on the camber line. The resulting velocity component normal to the camber line at an arbitrary point  $z_B$  is given by  $\mathbf{w}_{B;b;n}(\zeta, z_B)$ :

$$\mathbf{w}_{B;b;n}(\zeta, z_B) = \frac{1}{2\pi} \frac{\left( \gamma_{B;b}(\zeta) \times \frac{\mathbf{r}_c(\zeta, z_B)}{|\mathbf{r}_c(\zeta, z_B)|} \right)}{|\mathbf{r}_c(\zeta, z_B)|}, \quad (2.25)$$

where  $\mathbf{r}_c(\zeta, z)$  is the vector between  $\zeta$  and  $z_B$ , as indicated in Figure 2.10(c). On this basis, the resulting velocity along the length of the camber is obtained as follows

$$\mathbf{W}_{B;b;n}(z_B) = \frac{1}{2\pi} \int_{-b_B}^{b_B} \frac{\left( \gamma_{B;b}(\zeta) \times \frac{\mathbf{r}_c(\zeta, z_B)}{|\mathbf{r}_c(\zeta, z_B)|} \right)}{|\mathbf{r}_c(\zeta, z_B)|} d\zeta. \quad (2.26)$$

For symmetric aerofoils, the velocity normal to the camber line is directed in the local  $y_B$  direction and the expression for  $\mathbf{W}_{B;b;n}(z_B)$  can be simplified:

$$\mathbf{W}_{B;b;n}(z_B) = \frac{1}{2\pi} \int_{-b_B}^{b_B} \frac{(\boldsymbol{\gamma}_{B;b}(\zeta) \times \mathbf{e}_{B;z})}{z_B - \zeta} d\zeta, \quad (2.27)$$

where  $\mathbf{e}_{B;z}$  is the unit vector in the local  $z_B$  direction. The second condition which the vortex sheet  $\boldsymbol{\gamma}_{B;b}(z_B)$  needs to fulfil now results from the superposition of the normal effective velocity  $\mathbf{W}_{B;eff;n}(z_B)$  and the normal vorticity  $\mathbf{W}_{B;b;n}(z_B)$ , given by Eq. (2.24) and (2.27), respectively:

$$\mathbf{W}_{B;eff;n}(z_B) + \mathbf{W}_{B;b;n}(z_B) = \mathbf{0}. \quad (2.28)$$

With the application of the Kutta condition and the assumption of an asymmetry, Eq. (2.28) can be solved and the bound circulation is obtained from Eq. (2.21):

$$\Gamma_{B;b} = \frac{1}{2} c_B |\mathbf{W}_{B;eff}| \left( C_{B;L}^\alpha \sin \alpha_B + C_{B;L}^c \right) \mathbf{e}_{B;r}, \quad (2.29)$$

with the lift coefficients  $C_{B;L}^\alpha$ , relating to the angle of attack  $\alpha_B$ , and  $C_{B;L}^c$  depending on the shape of the camber only.  $\mathbf{e}_{B;r}$  is the unit vector defining the direction of the longitudinal  $r_B$  axis. For symmetric aerofoils,  $C_{B;L}^\alpha = 2\pi$  and  $C_{B;L}^c = 0$ :

$$\Gamma_{B;b} = \pi c_B |\mathbf{W}_{B;eff}| \sin \alpha_B \mathbf{e}_{B;r}. \quad (2.30)$$

From the bound circulation, obtained by either Eq. (2.29) or Eq. (2.30), the two-dimensional aerodynamic forcing on an aerofoil in a stationary inviscid flow can be defined.

### 2.3.3. STATIONARY INVISCID FLOWS

Figure 2.1 depicted the division of a stationary airflow around an aerofoil into a symmetric flow and a circulatory flow, the bound circulation  $\Gamma_{B;b}$ . Under inviscid conditions, the symmetric flow does not induce any skin friction and the resulting force on the aerofoil, in accordance with d'Alembert's paradox is zero. It goes therefore without saying that the stationary inviscid flow remains attached to the aerofoil.

Magnus [209] described how a rotating body in a stationary flow experiences a lift force  $\mathbf{F}_{B;L}$  perpendicular to the direction of the flow, on which basis the Kutta-Joukowski theorem was developed:

$$\mathbf{F}_{B;L} = \rho_{\text{air}} (\mathbf{W}_{B;eff} \times \Gamma_{B;b}). \quad (2.31)$$

For an effective airflow in accordance to Figure 2.9(a), Figure 2.11 illustrates the resulting lift force on the aerofoil.

The solution of Eq. (2.31) for an aerofoil can, after the implementation of Eq. (2.29), be expressed in terms of the lift coefficient  $C_{B;L}$ :

$$\mathbf{F}_{B;L} = \frac{1}{2} \rho_{\text{air}} c_B C_{B;L} |\mathbf{W}_{B;eff}| (\mathbf{W}_{B;eff} \times \mathbf{e}_{B;r}), \quad (2.32)$$

where, with reference to Eq. (2.29),  $C_{B;L}$  is given by

$$C_{B;L} = C_{B;L}^\alpha \sin \alpha_B + C_{B;L}^c. \quad (2.33)$$

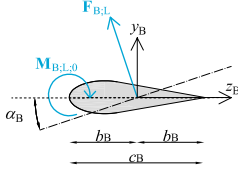


Figure 2.11: Schematic representation of the aerofoil lift force and moment, with the lift force at mid-chord and the corresponding moment around the leading edge.

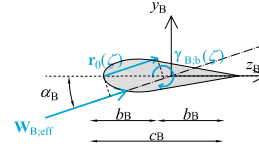


Figure 2.12: Schematic representation of the contribution of the vortex strength at  $z_B = \zeta$  to the lift moment around the leading edge.

The range of applicability of Eq. (2.33) is restricted to relatively small angles of attack. The reason being that real flows are viscous, and for large angles of attack the flow separates from the aerofoil. Eq. (2.33) is not valid for separated flows.

In addition to the lift force, the bound circulation induces a lift moment on the aerofoil too. This moment can be obtained from integrating the vortex strength times the distance to a reference point over the chord length. If the leading edge is chosen as the reference point, see Figure 2.12, the lift moment  $\mathbf{M}_{B,L;0}$  is obtained as follows:

$$\mathbf{M}_{B,L;0} = \rho_{\text{air}} \int_{-b_B}^{b_B} \{(\mathbf{W}_{B;\text{eff}} \times \boldsymbol{\gamma}_{B;b}(\zeta)) \times \mathbf{r}_0(\zeta)\} d\zeta. \quad (2.34)$$

As indicated in Figure 2.12, the vector  $\mathbf{r}_0(\zeta)$  defines the distance between the leading edge and the work line of the local lift force at  $z_B = \zeta$ . Here, the subscript "0" refers to the zero-chord point, i.e., the leading edge of the aerofoil. Eq. (2.34) can be elaborated on into

$$\mathbf{M}_{B,L;0} = \frac{1}{2} \rho_{\text{air}} (c_B)^2 C_{M;0} |\mathbf{W}_{B;\text{eff}}| (\mathbf{W}_{B;\text{eff}} \times \mathbf{e}_L). \quad (2.35)$$

The unit vector  $\mathbf{e}_L$  defines the direction of the lift force  $\mathbf{F}_{B,L}$  as indicated in Figure 2.11(a). The lift moment is expressed in terms of the lift moment coefficient  $C_{B;M;0}$ , which, in turn, can be related to the lift coefficient  $C_{B,L}$ :

$$C_{B;M;0} = -\left(\frac{1}{4} C_{B;L} + C_{B;M}^c\right). \quad (2.36)$$

The coefficient  $C_{B;M}^c$  depends on the shape of the camber and is zero for symmetric aerofoils. As a result, the coefficient for the lift moment around the leading edge is negative for symmetric aerofoils, implying that the moment indicated in Figure 2.11 acts in the counter-clockwise direction.

The moment coefficient for the lift moment around an arbitrary point  $\zeta$  on the chord line is obtained as follows:

$$C_{B;M;\zeta} = C_{B;M;0}(r) + \left(1 + \frac{\zeta}{b_B}\right) C_{B,L}. \quad (2.37)$$

From this, it can be shown that for thin aerofoils, the coefficient for the lift moment

around the one-quarter chord point  $C_{B;M;c/4}$  can be expressed as

$$\begin{aligned} C_{B;M;c/4} &= C_{B;M;0} + \frac{1}{4} C_{B;L} \\ &= C_{B;M}^c. \end{aligned} \quad (2.38)$$

This leads to the conclusion that for symmetric thin aerofoils, the coefficient of the lift moment around the one-quarter chord point is zero. For cambered thin aerofoils, this lift moment coefficient is not equal to zero, but it is independent of the angle of attack. The one-quarter chord point is generally referred to as the aerodynamic centre.

### 2.3.4. QUASI-STATIONARY AEROFOIL MOTIONS IN INVISCID FLOWS

For an oscillating aerofoil, the stationary flow pattern is disturbed. This disturbance comes with accelerations of the airflow, inducing a so-called non-circulatory excitation of the aerofoil. Furthermore, with a change in the flow pattern, a new circulation equilibrium must be found, such that the Kutta condition is met. This equilibrium is not obtained instantaneously, implying a delay in the development of the bound circulation and the corresponding lift force on the aerofoil.

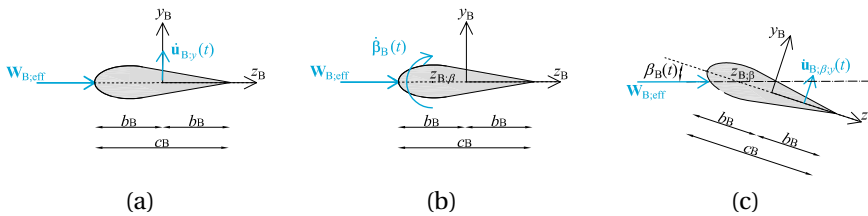


Figure 2.13: Quasi-stationary aerofoil motion, with (a) heave motion, and (b) pitch motion, and (c) the vertical motion at the three-quarter chord length affecting the equivalent angle of attack for pitch motions.

Assuming first a low-frequency motion of the aerofoil, the flow conditions can be defined as quasi-stationary. This implies that the accelerations of the flow are very small and can be neglected, and the new circulation equilibrium is found with a negligible delay. Figure 2.13(a) shows an aerofoil exposed to the effective inflow velocity  $\mathbf{W}_{B;eff}$ , directed in the positive  $z_B$  direction, undergoing the heave motion  $\dot{\mathbf{u}}_{B;y}(t) = \dot{u}_{B;y}(t)\mathbf{e}_y$  in the positive  $y_B$  direction. The overdot indicates that the motions represents the time-derivative of the displacement  $\mathbf{u}_{B;y}(t)$ . The quasi-stationary – or instantaneous – angle of attack can straightforwardly be determined from the uniform normal velocity along the chord of the aerofoil:

$$\sin \alpha_B^{qs}(t) = -\frac{\dot{u}_{B;y}(t)}{|\mathbf{W}_{B;rel}(t)|}, \quad (2.39)$$

with the superscript ‘qs’ indicating quasi-stationary. The angle is negative, because the heave motion induces a flow in the negative  $y_B$  direction  $\mathbf{W}_{B;rel}(t)$  is the relative airflow velocity experienced by the aerofoil, including the induced wind velocity, the rotational velocity of the rotor and the structural motion:

$$\mathbf{W}_{B;rel}(t) = \mathbf{W}_{B;eff} - \dot{\mathbf{u}}_{B;y}(t). \quad (2.40)$$

If the heave motion is small compared to the effective inflow velocity, the instantaneous angle of attack can be approximated as:

$$\alpha_B^{\text{qs}}(t) \approx -\frac{\dot{u}_{B;y}(t)}{|\mathbf{W}_{B;\text{eff}}|}. \quad (2.41)$$

A pitch motion  $\dot{\beta}_B(t) = \dot{\beta}_B(t)\mathbf{e}_r$ , depicted in Figure 2.13(b), first imposes an angle of attack equal to the pitch rotation  $\beta_B(t)$ . Moreover, the pitch motion introduces a linearly varying normal velocity along the chord of the aerofoil. If the pitch axis is assumed at  $z_B = z_{B;\beta}$ , the velocity profile  $W_{B;y}(z_B, t)$  can be expressed as

$$W_{B;y}(z_B, t) = -\dot{\beta}_B(t)(z_B - z_{B;\beta}). \quad (2.42)$$

A symmetric aerofoil with a linearly varying velocity profile along its chord length is equivalent to a cambered aerofoil with a uniform velocity profile, with a parabolic camber  $\xi_{B;y}(z_B, t)$ :

$$\xi_{B;y}(z_B, t) = \int \frac{W_{B;y}(z_B, t)}{|\mathbf{W}_{B;\text{rel}}(t)} dz_B. \quad (2.43)$$

With the application of the thin aerofoil theory for cambered aerofoils, the quasi-stationary equivalent angle of attack of an aerofoil in pitch motion can be defined as

$$\sin \alpha_B^{\text{qs}}(t) = \sin \beta_B(t) + \frac{\dot{u}_{B;\beta;y}(t)}{|\mathbf{W}_{B;\text{rel}}(t)|}, \quad (2.44)$$

with  $\dot{u}_{B;\beta;y}(t)$ , the magnitude of the motion vector  $\dot{\mathbf{u}}_{B;\beta;y}(t)$  depicted in Figure 2.13(c), defined as

$$\dot{u}_{B;\beta;y}(t) = -\left(\frac{1}{2}b_B - z_{B;\beta}\right)\dot{\beta}_B(t). \quad (2.45)$$

If the pitch axis is located at the three-quarter chord point, i.e.,  $z_{B;\beta} = \frac{1}{2}b_B$ , the effective angle of attack resulting from the pitch motion is the actual pitch angle, while for a pitch axis at the one-quarter chord point, i.e.,  $z_{B;\beta} = -\frac{1}{2}b_B$ , the effective angle of attack corresponds with the angle of attack at the three-quarter chord point.

The quasi-stationary angle of attack from a combined heave and pitch angle can now be expressed as

$$\sin \alpha_B^{\text{qs}}(t) = \sin \beta_B(t) - \frac{\dot{u}_{B;y}(t)}{|\mathbf{W}_{B;\text{rel}}(t)|} + \left(\frac{1}{2}b_B - z_{B;\beta}\right) \frac{\dot{\beta}_B(t)}{|\mathbf{W}_{B;\text{rel}}(t)|}. \quad (2.46)$$

For small pitch motions, the equivalent angle of attack can be approximated:

$$\alpha_B^{\text{qs}}(t) \approx \beta_B(t) - \frac{\dot{u}_{B;y}(t)}{|\mathbf{W}_{B;\text{eff}}|} + \left(\frac{1}{2}b_B - z_{B;\beta}\right) \frac{\dot{\beta}_B(t)}{|\mathbf{W}_{B;\text{eff}}|}. \quad (2.47)$$

Combining Eqs. (2.33) and (2.47), the quasi-stationary lift coefficient of a symmetric aerofoil in heave and pitch can be approximated as

$$C_{B;L}^{\text{qs}}(r_B, t) \approx 2\pi \left\{ \beta_B(t) - \frac{\dot{u}_{B;y}(t)}{|\mathbf{W}_{B;\text{eff}}|} + \left(\frac{1}{2}b_B - z_{B;\beta}\right) \frac{\dot{\beta}_B(t)}{|\mathbf{W}_{B;\text{eff}}|} \right\}. \quad (2.48)$$



The lift moment coefficient for the moment around the leading edge can be obtained from Eq. (2.36). As a result of the induced camber, the coefficient  $C_{B;M}^C$ , see Eq. (2.36), is non-zero:

$$C_{B;M;0}^{qs}(t) = \frac{1}{4} C_{B;L}^{qs}(t) - \frac{\pi}{4} b_B \frac{\dot{\beta}_B(t)}{|\mathbf{w}_{B;rel}(t)|}. \quad (2.49)$$

On this basis and with the application of Eq. (2.37), the lift moment coefficient around an arbitrary point  $\zeta$  can be defined:

$$C_{B;M;\zeta}^{qs}(t) = C_{B;M;0}^{qs}(t) + \frac{1}{2} \left(1 + \frac{\zeta}{b_B}\right) C_{B;L}(t), \quad (2.50)$$

from which the moment coefficient with respect to the one-quarter chord point can be obtained:

$$C_{B;M;c/4}^{qs}(t) = -\frac{\pi}{4} b_B \frac{\dot{\beta}_B(t)}{|\mathbf{w}_{B;rel}(t)|}. \quad (2.51)$$

The pitch motion results in a moment around the one-quarter chord point, which is independent of the location of the pitch axis.

### 2.3.5. DYNAMIC AEROFOIL OSCILLATIONS IN INVISCID FLOWS

For aerofoils oscillating at higher frequencies, the acceleration of the flow cannot any longer be neglected, as a result of which a so-called non-circulatory flow force on the aerofoil is induced. Furthermore, the violation of the Kutta condition is compensated by a shed vorticity and the new bound circulation is established with a delay. The lift force on an aerofoil in a non-stationary inviscid flow was analysed by Theodorsen [32] by means of the potential flow theory. This analysis specifically addressed the non-stationary lift force on an aerofoil oscillating in heave and pitch. The Laplace equation can be solved by both sink/source and vortex velocity fields, the former inducing the so-called non-circulatory lift force – or apparent inertia force – and the latter resulting in a circulatory lift.

Concerning the aerodynamic forces on an aerofoil in a non-stationary inviscid flow, this section specifically considers the forcing on oscillating aerofoils. The following section, Section 2.3.6 considered the aerodynamic forces on an aerofoil for varying inflow conditions. In the case of varying inflow conditions, the instantaneous angle of attack changes gradually along the length of the chord. Moreover, under these conditions the potential flow theory is, strictly speaking, not valid.

#### NON-CIRCULATORY LIFT

Bisplinghoff *et al.* [184] presented a detailed elaboration of the Theodorsen's solution for the non-circulatory lift force. The force is predicted with the potential flow theorem and the definition of source/sink velocity fields. After applying Joukowski's conformal transformation, the non-circulatory lift force  $\mathbf{F}_{B;l}(t)$  of an aerofoil moving in heave and pitch was derived as

$$\mathbf{F}_{B;l}(t) = \pi \rho_{\text{air}} b_B^2 \left\{ -\ddot{\mathbf{u}}_{B;y}(t) + \mathbf{w}_{B;eff} \times \dot{\beta}_B(t) - z_{B;\beta} (\mathbf{e}_B; z \times \ddot{\beta}_B(t)) \right\}. \quad (2.52)$$

The first and second term of this force relate to the uniform acceleration, experienced by the aerofoil for a plunging type of motion. The third term expresses the acceleration at mid-chord due to the accelerated pitching actions.

The corresponding moment around the pitch axis  $\mathbf{M}_{B;I}(t)$  is

$$\begin{aligned} \mathbf{M}_{B;I}(t) = & \pi \rho_{\text{air}} b_B^2 \{ \dot{\mathbf{u}}_{B;y}(t) \times \mathbf{W}_{B;\text{eff}}(r) + z_{B;\beta}(r) (\mathbf{e}_{B;z} \times \dot{\mathbf{u}}_{B;y}(t)) \\ & + \mathbf{W}_{B;\text{eff}}(r) \times \dot{\boldsymbol{\beta}}_B(t) \times (\mathbf{W}_{B;\text{eff}}(r)) - \left( \frac{1}{8} (b_B(r))^2 + (z_{B;\beta}(r))^2 \right) \ddot{\boldsymbol{\beta}}_B(t) \}. \end{aligned} \quad (2.53)$$

Here, the first and third terms result from an antisymmetric pressure distribution, with zero pressure at mid-chord and pressures increasing to plus and minus infinity towards the trailing and leading edges respectively. This pressure distribution does not generate a net force on the aerofoil and therefore, these terms cannot be related to any of the terms of the non-circulatory lift force. The second term expresses the moment around the pitch axis, resulting from the heave motion of the aerofoil. This term vanishes if the pitch axis is located at the mid-chord point. The last term expresses the moment resulting from the pitching acceleration.

The flow pattern corresponding to the non-circulatory flow does not satisfy the Kutta condition. As a consequence, an additional velocity field is required, which first of all represents a solution of the Laplace equation and secondly satisfies the Kutta condition, in superposition with the non-circulatory flow.

### CIRCULATORY LIFT

For a flow pattern satisfying the Kutta condition, the lift force can be determined from Eqs (2.29) and (2.31). If the stationary flow pattern is disrupted, as depicted in Figure 2.3, the Kutta condition is violated. As a result of this loss of equilibrium, the flow converges to a new bound circulation, such that the Kutta condition is again satisfied. Until the new equilibrium is found, shed vorticity  $\boldsymbol{\gamma}_{B;s}(t)$  is emitted from the trailing edge, as defined by Eq. (2.2). With reference to Eq. (2.27), the velocity component normal to the camber line, now results from the following integral equation:

$$\mathbf{W}_{B;b;n}(z_B, t) = \frac{1}{2\pi} \int_{-b_B}^{b_B} \frac{(\boldsymbol{\gamma}_{B;b}(\zeta, t) \times \mathbf{e}_{B;z})}{z_B - \zeta} d\zeta + \frac{1}{2\pi} \int_{b_B}^{\infty} \frac{(\boldsymbol{\gamma}_{B;s}(\zeta, t) \times \mathbf{e}_{B;z})}{z_B - \zeta} d\zeta. \quad (2.54)$$

The bound circulation can be solved from Eq. (2.54) with the application of the Kutta condition and the Kelvin's circulation theorem. The disturbance of the stationary flow pattern, and therefore the establishment of the new equilibrium depends on the nature and the time scale of the disruption [40]. Causes of non-stationarity are time-varying inflow conditions, variations in rotational velocity, blade pitch and turbine yaw actions and blade flexibility.

Different theories exist to describe the transition to a new equilibrium, depending on the cause of the non-stationarity. This section first explains the non-stationary aerodynamic forcing on an aerofoil moving in oscillatory heave and pitch. To this end, the Theodorsen's function is introduced, which allows for the analysis of the oscillatory lift force in the frequency domain. The time-domain equivalent, employing Küssner's indicial function, is introduced subsequently.

### FREQUENCY-DOMAIN AEROFOIL OSCILLATIONS

The quasi-stationary analysis of the lift force and moment implies an instantaneous variation of the effective angle of attack and does not account for the shed vorticity  $\boldsymbol{\gamma}_{B;s}(t)$

according to Eq. (2.54). On the basis of the potential theory and the thin aerofoil theory, Theodorsen [32] developed the exact frequency-dependent complex function  $C(k)$ , with the reduced frequency  $k$ , to describe the non-stationary lift coefficient for harmonic oscillation in heave and pitch.

The Theodorsen's function can be expressed in terms of the Hankel's functions of the second kind,  $H_n^{(2)}(k)$ :

$$C(k) = F(k) + iG(k) = \frac{H_1^{(2)}(k)}{H_1^{(2)}(k) + iH_0^{(2)}(k)}, \quad (2.55)$$

and the reduced frequency is determined as

$$k = \frac{\omega b_B}{|\mathbf{W}_{B;\text{eff}}|}, \quad (2.56)$$

where  $\omega$  is the angular frequency of the oscillation and  $i = \sqrt{-1}$ , i.e., the imaginary unit. For a rotating wind turbine blade, the reduced frequency varies along the length of the blade, and attains its lowest value at the tip of a rotating blade.

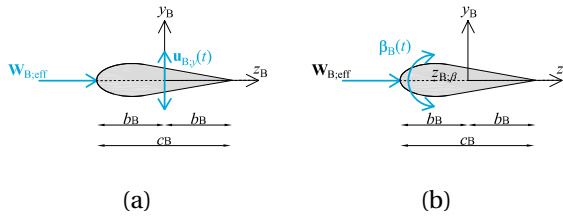


Figure 2.14: Schematic representation of an oscillating aerofoil, with (a) an aerofoil oscillating in heave, and (b) an aerofoil oscillating in pitch.

Figure 2.14(a) shows a symmetric aerofoil exposed to the horizontal inflow  $\mathbf{W}_{B;\text{eff}}$ , which is assumed to be constant in time. The aerofoil experiences a heave oscillation  $\mathbf{u}_{B;y}(t) = \bar{u}_{B;y} \mathbf{e}_{B;y} e^{i\omega t}$ , as a result of which the quasi-stationary angle of attack  $\alpha_B^{\text{qs}}(t)$  can be expressed as

$$\sin \alpha_B^{\text{qs}}(t) = -\frac{i\omega \bar{u}_{B;y}}{|\mathbf{W}_{B;\text{eff}}(t)|} e^{i\omega t}. \quad (2.57)$$

Here, it is assumed that the heave motion does not significantly affect the relative inflow velocity, implying that the latter can be approximated with the effective inflow velocity.

With the application of the Theodorsen's function, the lift coefficient of a symmetric thin aerofoil in oscillating heave can be expressed as

$$C_{B;L}^{\text{ns}}(k) = -2\pi C(k) \frac{i\omega \bar{u}_{B;y}}{|\mathbf{W}_{B;\text{eff}}(t)|} e^{i\omega t}, \quad (2.58)$$

with the superscript 'ns' indicating non-stationary.

Theodorsen's function can also be used to describe the frequency-dependent lift coefficient for a oscillating pitch motion  $\beta_B(t) = \bar{\beta}_B \mathbf{e}_r e^{i\omega t}$  of a symmetric aerofoil, see

Figure 2.14(b). The pitch oscillation takes place around the pitch axis, which is assumed at  $z_{B;\beta}$  on the local  $z_B$  axis. Theodorsen's evaluation resulted in the following lift coefficient for this oscillating pitch motion:

$$C_{B;L}^{\text{ns}}(k) = 2\pi C(k) \left\{ 1 + i\omega \left( \frac{1}{2} b_B - z_{B;\beta} \right) \right\} \bar{\beta}_B e^{i\omega t}. \quad (2.59)$$

The Theodorsen's function affects both the amplitude and the phase of the lift coefficient with respect to the quasi-stationary lift. Figure 2.15 illustrates the Theodorsen's function for four typical reduced frequencies,  $k = 0.05, 0.2, 0.5$  and  $1.0$ . The figure presents the oscillations  $C(k)e^{k\tau}$ , with the non-dimensional – or reduced – time  $\tau$ , the time counterpart of the reduced frequency:

$$\tau = \int_0^t \frac{|\mathbf{w}_{B;\text{rel}}(t)|}{b_B} dt, \quad (2.60)$$

and compares these against the quasi-stationary Theodorsen's function, i.e.,  $C(k)$ , as  $k$  converges to 0. At  $k = 0.05$ , see Figure 2.15(a), a slight reduction in amplitude and a small phase shift can be observed. Both the reduction in amplitude and the shift in phase increase for  $k = 0.2$ , as shown in Figure 2.15(b). For higher reduced frequencies, Figures 2.15(c) and (d), the amplitude reduction stabilizes at a factor 0.5, while no increase in the phase lag can be observed.

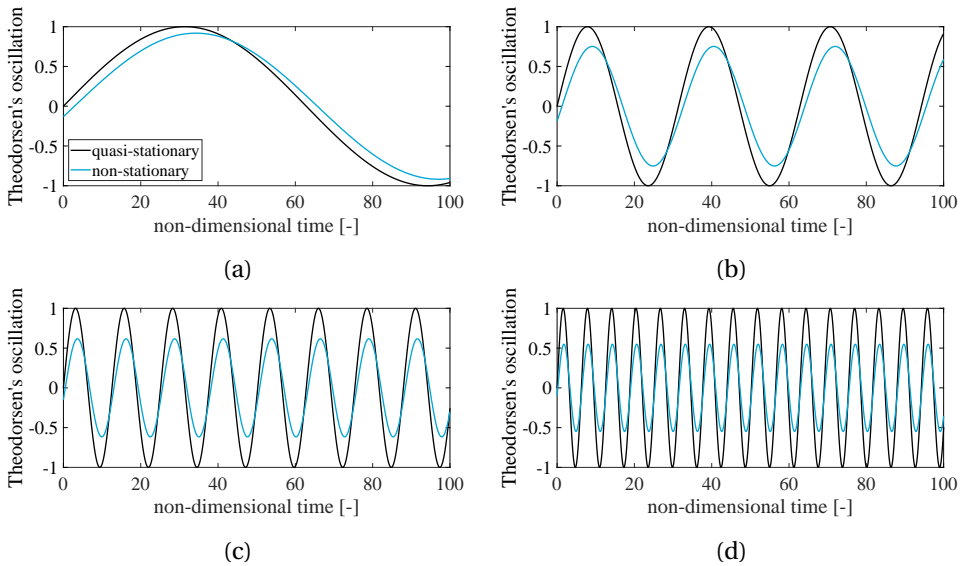


Figure 2.15: Illustrations of the Theodorsen's function against the quasi-stationary Theodorsen's function, with (a) the reduced frequency  $k = 0.05$ , (b) the reduced frequency  $k = 0.2$ , (c) the reduced frequency  $k = 0.5$ , and (d) the reduced frequency  $k = 1.0$ .

Figure 2.16 presents the amplitude and phase angle of the Theodorsen's function over a range of reduced frequencies. It is shown that the amplitude reduces quickly for low reduced frequencies,  $k < 1$ , after which it converges to a factor 0.5. The phase lag reaches

a maximum of approximately 15 degrees at  $k \approx 0.3$ . For higher values of  $k$ , the phase lag converges to zero.

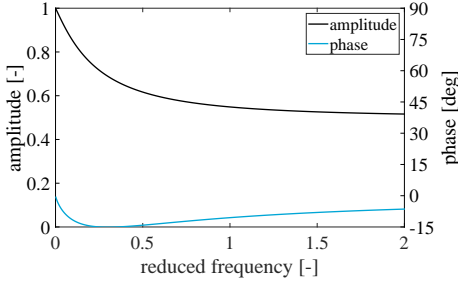


Figure 2.16: Amplitude and phase angle of the Theodorsen's function as a function of the reduced frequency.

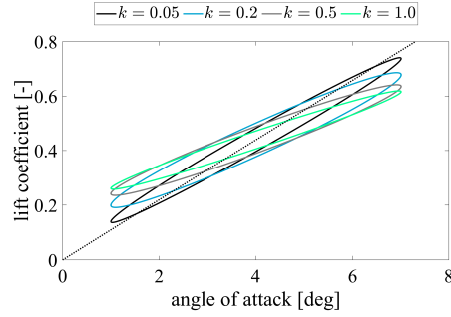


Figure 2.17: Variation of the lift coefficient for angle of attack oscillations for a variation of reduced frequencies, obtained with the Theodorsen's function.

A last illustration of the Theodorsen's function is given by Figure 2.17, which presents the variation of the lift coefficient  $C_{B;L}(k)$ , for different oscillations of the angle of attack:

$$\boldsymbol{\alpha}(r, t) = \left( \bar{\alpha}(r) + \Delta\alpha(r)e^{ikt} \right) \mathbf{e}_r^f. \quad (2.61)$$

The lift coefficient oscillations are determined for a mean angle of attack  $\bar{\alpha}(r) = 4$  degrees and an amplitude of oscillation  $\Delta\alpha(r) = 3$  degrees. The figure distinguishes the oscillation of the lift coefficient for the reduced frequencies  $k = 0.05, 0.2$  and  $1.0$ . As a reference, the quasi-stationary lift coefficient is shown. The amplitude effect of the Theodorsen's function can be deduced from the decreasing slope of the oscillation as  $k$  increases. As a result of the phase lag, the evolution of the lift coefficient is elliptical. In correspondence with Figure 2.16, the width of the ellipse is largest for  $k = 0.2$ .

From the lift coefficient of an aerofoil in oscillatory motion, as given by Eqs. (2.58) and (2.59), the lift moment around the leading edge can be obtained from the lift moment coefficient given by Eq. (2.49). For pitch motions, this lift moment coefficient contains a second term, which is independent of the Theodorsen's function. This term concerns, therefore, a quasi-stationary moment contribution of the circulatory flow.

#### TIME-DOMAIN AEROFOIL OSCILLATIONS

Wagner [33] derived the time-domain equivalent of the Theodorsen's function. The indicial Wagner's function describes the evolution of the lift coefficient after a step change in the angle of attack. A sudden change in the angle of attack can result from a step change in the inflow velocity, for instance by an increase in the rotational velocity of the rotor, or a pitch action of the blade. The heave and pitch blade motions that induce angle of attack variations were presented in Figure 2.13. A sudden heave motion  $\dot{\mathbf{u}}_{B;y}(t)$  after time  $t = 0$ ,

in the negative local  $y_B$  direction, can be expressed as follows:

$$\dot{\mathbf{u}}_{B;y}(t) = \begin{cases} \mathbf{0}, & \text{for } t \leq 0, \\ -\dot{u}_{B;y} \mathbf{e}_{B;y}, & \text{for } t > 0. \end{cases} \quad (2.62)$$

The corresponding instantaneous angle of attack can be expressed in terms of the relative airflow velocity  $\mathbf{W}_{B;rel}(t)$ , which is given by Eq. (2.40):

$$\sin \alpha_B^{qs}(t) = \begin{cases} 0, & \text{for } t \leq 0, \\ \frac{\dot{u}_{B;y}}{|\mathbf{W}_{B;rel}(t)|}, & \text{for } t > 0. \end{cases} \quad (2.63)$$

The change in the angle of attack resulting from the pitch motion depicted in Figure 2.13(b) is twofold. First, the changing pitch angle immediately changes the angle of attack of the effective airflow velocity. In addition, the imposed velocity in the local  $y_B$  direction at the three-quarter chord point results in an additional heave contribution. Defining the pitch rotation  $\dot{\beta}_B(t)$  around the point  $z_{B;\beta}$  as

$$\dot{\beta}_B(t) = \begin{cases} \mathbf{0}, & \text{for } t \leq 0, \\ \dot{\beta}_B \mathbf{e}_{B;r}, & \text{for } t > 0, \end{cases} \quad (2.64)$$

the instantaneous angle of attack can be obtained from Eq. (2.44):

$$\sin \alpha_B^{qs}(t) \approx \begin{cases} 0, & \text{for } t \leq 0, \\ \sin \beta_B(t) + \left(\frac{1}{2} b_B - z_{B;\beta}\right) \frac{\dot{\beta}_B(t)}{|\mathbf{W}_{B;rel} t|}, & \text{for } t > 0. \end{cases} \quad (2.65)$$

Here, it should be noted that the pitch motion affects the relative inflow velocity too. If the amplitude of the motion remains small, the relative inflow velocity could be approximated with the effective inflow velocity, which does not account for the structural motion.

For instantaneous angles of attack, resulting from a step change in the pitch velocity, the non-stationary bound circulation can be expressed in terms of the Wagner's function  $\Phi_W(\tau)$ :

$$\Gamma_{B;b}^{ns}(\tau) = \pi c_B |\mathbf{W}_{B;rel}(\tau)| \sin \alpha_B^{qs}(\tau) \Phi_W(\tau) \mathbf{e}_{B;r}. \quad (2.66)$$

For small variations of the angle of attack, the non-stationary bound circulation can be approximated as

$$\Gamma_{B;b}^{ns}(\tau) \approx \pi c_B |\mathbf{W}_{B;eff}| \alpha_B^{qs}(\tau) \Phi_W(\tau) \mathbf{e}_{B;r}. \quad (2.67)$$

The Wagner's function is obtained from the inverse Laplace transform of the Theodorsen's function  $C(k)$  [185]. Given the inconvenience of the Wagner's function in practical applications, the function has been approximated in algebraical terms [210], and employing exponential expressions [211, 212]:

$$\Phi_W(\tau) \approx 1 - \frac{2}{\tau+4}, \quad \text{for } \tau > 0, \quad (2.68)$$

or

$$\Phi_W(\tau) \approx 1 - \Psi_1 e^{-\eta_1 \tau} - \Psi_2 e^{-\eta_2 \tau}, \quad \text{for } \tau > 0. \quad (2.69)$$

Table 2.1: Coefficients of the approximated indicial Wagner's function.

coefficient	Wagner's function $\Phi_W(\tau)$ [212]
$\Psi_1$	0.165
$\Psi_2$	0.335
$\eta_1$	0.0455
$\eta_2$	0.3

The coefficients of the double time-lag approximation, Eq. (2.69) have been defined for aerofoils with various aspect ratios. Table 2.1 presents the coefficients that are applicable under the thin aerofoil assumption.

Figure 2.18 presents both the algebraic and the exponential approximations of the Wagner's function. The initial value of the Wagner's function is  $\Phi_W(0) = 0.5$ , implying that half of the bound circulation develops instantaneously after the step change in the angle of attack. The Wagner's function converges to 1.0 as  $\tau \rightarrow \infty$ . The exponential expression, Eq. (2.69), approximates the Wagner's function best, whereas the Eq. (2.68) agrees within two percent with the Wagner's function over the entire range of  $\tau$ .

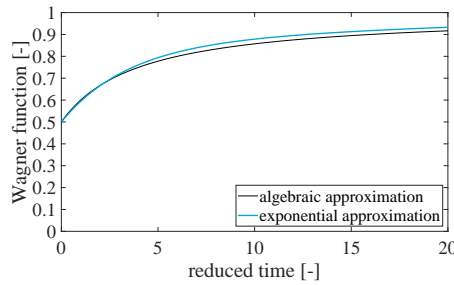


Figure 2.18: Approximations of Wagner's indicial function.

The bound circulation of an arbitrarily oscillating aerofoil can be obtained from the Wagner's function by means of the Duhamel integral:

$$\Gamma_{B;b}^{ns}(\tau) = \pi c_B |\mathbf{W}_{B;eff}| \left\{ \Phi_W(\tau) \alpha_B^{qs}(0) + \int_0^\tau \Phi_W(\tau - \tilde{\tau}) \frac{\partial \alpha_B^{qs}(\tilde{\tau})}{\partial \tilde{\tau}} d\tilde{\tau} \right\} \mathbf{e}_{B;r}, \quad (2.70)$$

for  $\tau \geq 0$ .  $\tilde{\tau}$  is a dummy variable, required for the convolution integral. It should be noted that this expression is derived with the assumption that the variations in the structural motion are small compared to the effective inflow velocity.

### 2.3.6. INCIDENT AIRFLOW VARIATIONS

Theodorsen addressed the lift force on an oscillating aerofoil with a time-invariant incident airflow. The Theodorsen's function is not necessarily applicable for a stationary moving aerofoil with time-varying inflow conditions. Particularly for high-frequency inflow variations, the instantaneous angle of attack along the length of the aerofoil chord is

non-uniform and the Theodorsen's and Wagner's function are not applicable for the analysis of the non-stationary aerodynamic forcing. For analyses in the frequency-domain, the Sears's function was derived on the basis of the potential flow theory [213]. As for the oscillating aerofoil, a time-domain equivalent was derived in the form of an indicial function. This time-domain equivalent is known as the Küssner's function [184]. Both the Sears's and the Küssner's functions address the non-stationary aerodynamic forcing for a lateral, or gust-like, airflow variation, i.e., a variation of the inflow conditions in the local  $y - B$  direction of the aerofoil depicted in Figure 2.8. As an extension of the theory, Leishman [182] considered a variation of the effective inflow in the local  $z_B$  axis too.

#### FREQUENCY-DOMAIN INCIDENT AIRFLOW VARIATIONS

Figure 2.19 shows an aerofoil exposed to the constant effective wind velocity  $\mathbf{W}_{B;\text{eff}}$  in the local  $z_B$  direction and a harmonically varying airflow velocity in the local  $y_B$  direction:

$$\mathbf{w}_{B;y}(z_B, t) = \bar{w}_{B;y} e^{i(\omega_w t - 2\pi \frac{z_B}{\lambda_w})} \mathbf{e}_{B;y}, \quad (2.71)$$

with the amplitude of the oscillation  $\bar{w}_{B;y}$ , the frequency of oscillation  $\omega_w$  and the corresponding wavelength  $\lambda_w$ . Regarding the harmonically varying airflow, two scenarios can be distinguished. First, the wavelength of the oscillation can be large, i.e.  $\lambda_w \gg b_B$ . In this situation, which is depicted in Figure 2.19(a), the airflow variation over the length of chord is almost linear, or even constant. Hence, the Theodorsen's function can be expected to describe the non-stationary lift force relatively well. For  $\lambda_w \sim b_B$ , the airflow varies strongly over the length of the chord and Theodorsen's derivations cannot any longer be expected to be valid. This scenario is depicted in Figure 2.19(b).

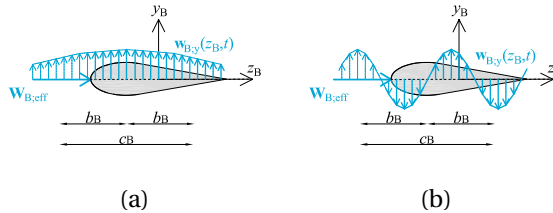


Figure 2.19: Schematic representation of an aerofoil exposed to a harmonically varying lateral inflow, with (a) the wave length of the lateral inflow much larger than the semi-chord length, and (b) the wave length of the lateral inflow in the same order of magnitude as the semi-chord length.

Von Karman [213] analyzed the aerodynamic forcing on an aerofoil in non-uniform motion. In this study, the mid-chord point was chosen as a reference. The local  $y_B$  axis, however, was located at the leading edge of the aerofoil, see Figure 2.20, introducing the phase shift  $k_w$  in the harmonically varying airflow:

$$k_w = 2\pi \frac{b_B}{\lambda_w}. \quad (2.72)$$

This wavelength-dependent phase shift is referred to as the reduced frequency for a



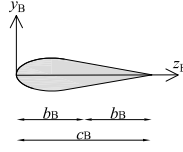


Figure 2.20: Schematic representation of an aerofoil with the origin of the local frame of reference positioned at the leading edge.

harmonically varying airflow. Estimating the quasi-stationary angle of attack as

$$\alpha_B^{\text{qs}}(t) \approx \frac{\bar{w}_{B,y}}{|\mathbf{w}_{B,\text{eff}}|} e^{i\omega_w t}, \quad (2.73)$$

the non-stationary lift coefficient can be approximated with the application of the Sears's function  $S(k_w)$ :

$$C_{B,L}^{\text{ns}}(k_w) \approx 2\pi S(k_w) \frac{\bar{w}_{B,y}}{|\mathbf{w}_{B,\text{eff}}|} e^{i\omega_w t}. \quad (2.74)$$

An exact expression of the Sears's function can be given in terms of the Theodorsen's function  $C(k_w)$ , with the phase shift  $k_w$  replacing the reduced frequency  $k$ :

$$S(k_w) = \{J_0(k_w) - iJ_1(k_w)\} C(k_w) + iJ_1(k_w), \quad (2.75)$$

where  $J_0(k_w)$  and  $J_1(k_w)$  are Bessel's functions of the first kind.

Similarly to the Theodorsen's function, the Sears's function affects both the amplitude and the phase of the lift coefficient with respect to the quasi-stationary lift. This is illustrated by Figure 2.21, which shows the Sears's function for four typical reduced frequencies,  $k_w = 0.05, 0.2, 0.5$  and  $1.0$ . The figure presents the oscillations  $S(k)e^{k_w \tau}$  against the quasi-stationary Sears' function. Contrarily to the Theodorsen's function, the amplitude reduction does not converge to a constant value for an increasing  $k_w$ . For the lower values of  $k_w$ , a phase lag between the Sears's and the quasi-stationary oscillations can be observed, as shown in Figures 2.21(a), (b) and (c). The oscillation depicted in Figure 2.21(d), however, shows a positive shift in phase for  $k_w = 1.0$ , with respect to the quasi-stationary oscillation.

The amplitude and phase shift of the Sears's function are depicted as a function of the reduced frequency  $k_w$  in Figure 2.22. The amplitude of the Sears's function decreases for an increasing reduced frequency, and converges to zero. The phase angle initially shows phase lag slightly smaller than 15 degrees for  $k_w \approx 0.2$ , after which the phase shift increases and converges asymptotically to  $k_w - \frac{\pi}{4}$ . This reduced frequency dependency counteracts the wavelength dependency of the airflow oscillation at the mid-chord point, so that the actual phase shift converges to  $-\frac{\pi}{4}$ . For small reduced frequencies,  $k = k_w < 0.1$ , the Theodorsen's and Sears's function behave similarly.

Likewise for the Theodorsen's function, the variation of the lift coefficient resulting from an oscillating angle of attack is determined for the Sears' function, as presented in

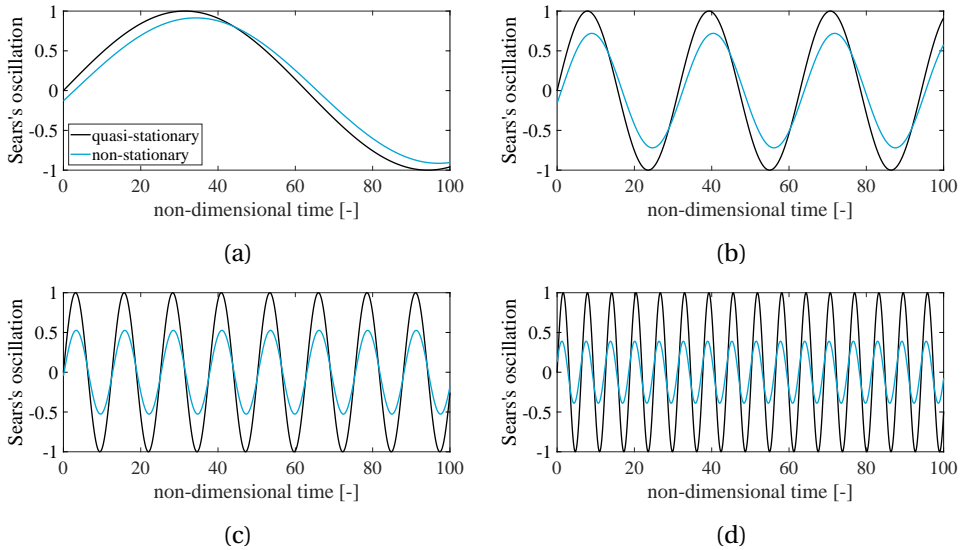


Figure 2.21: Illustrations of the Sears's function against the quasi-stationary Sears's function, with (a) the reduced frequency  $k = 0.05$ , (b) the reduced frequency  $k = 0.2$ , (c) the reduced frequency  $k = 0.5$ , and (d) the reduced frequency  $k = 1.0$ .

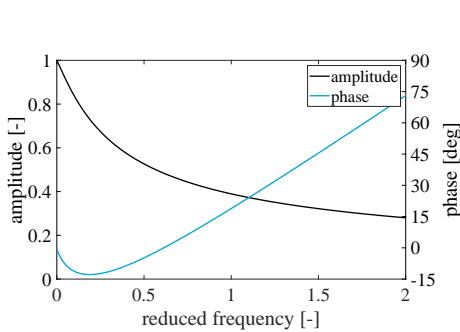


Figure 2.22: Amplitude and phase angle of the Sears's function as a function of the reduced frequency.

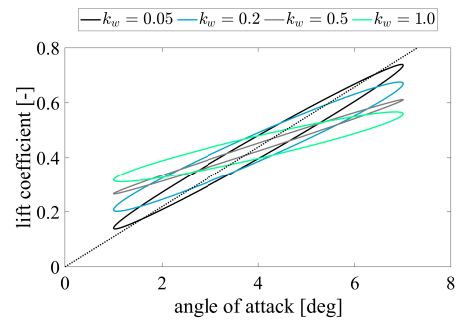


Figure 2.23: Variation of the lift coefficient for an angle of attack oscillations for a variation of reduced frequencies, obtained with the Sears's function.

Figure 2.23. The figure is created on the basis of an angle of attack oscillation given by Eq. (2.61), with  $\bar{\alpha}_B = 4$  degrees and  $\Delta\alpha_B = 3$  degrees. The amplitude and phase shift effects of the non-stationary lift coefficient can again clearly be distinguished. The variation for  $k_w = 0.05$  is very similar to the variation of the lift coefficient of an oscillation aerofoil with  $k = 0.05$ , see Figure 2.17. The comparison of the Figures 2.16 and Figures 2.22 already hinted towards this finding. For higher reduced frequencies,  $k_w = 0.2$  and  $k_w = 0.5$ , a substantial amplitude reduction and phase shift can be observed.

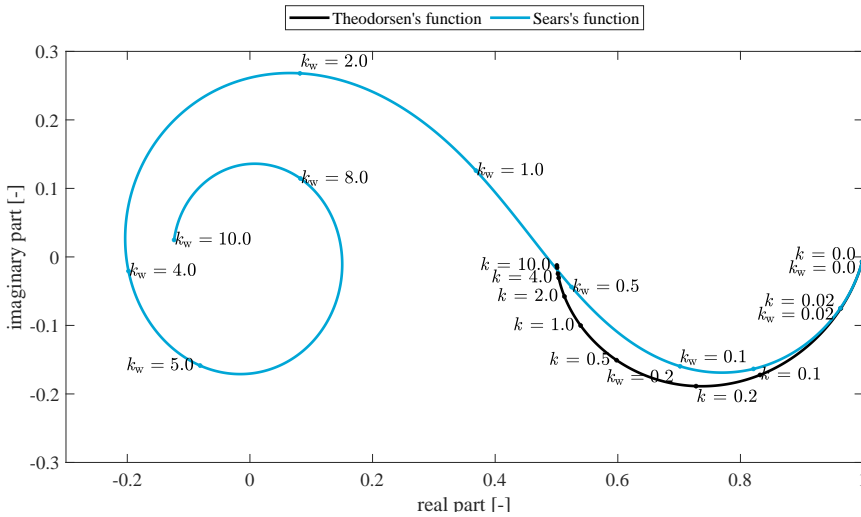


Figure 2.24: Comparison of the Theodorsen's and Sears's functions.

A comparison between the real and imaginary parts of the Theodorsen's and Sears's functions is presented in Figure 2.24. Both functions are presented for reduced frequencies in the range  $(0.0, 10.0]$ . Again, it is shown that for reduced frequencies  $k = k_w < 0.1$ , both functions behave similarly. Considering the Theodorsen's function, the real part decreases for an increasing  $k$  and converges to a value of 0.5. The imaginary part first reduces until  $k \approx 0.2$  and then increases and converges to zero. These observations correspond to the amplitudes and phase shifts presented in Figure 2.16. The Sears's function shows the sign change of the imaginary part for an increasing reduced frequency, which corresponds to the positive phase shift that was visible Figure 2.22. For large values of  $k_w$ , the Sears's function converges spirally to zero. This shape only occurs when the harmonically varying airflow velocity is referenced to the mid-chord point, and as a result contains a reduced frequency-dependent phase shift. If the airflow is referenced to the leading edge, with  $z_B = 0$  according to Figure 2.19(c), the shape of the Sears's function is similar to the Theodorsen's function, and both the real and imaginary parts converge to zero.

### TIME-DOMAIN INCIDENT AIRFLOW VARIATIONS

The Wagner's function is not valid for the analysis of the development of the bound circulation after a step change in the airflow conditions. Figure 2.25 shows how an aerofoil cuts with a velocity  $\mathbf{W}_{B;rel}(t)$  through a gust, so that the aerofoil experiences the flow velocity  $\mathbf{w}_{B;y}(z_B, t)$  in the local  $y_B$  direction, along the length of the chord. Locating the local  $y_B$  axis at the leading edge of the aerofoil, this vertical velocity profile can be described as follows:

$$\mathbf{w}_{B;y}(z_B, t) = \begin{cases} 0, & \text{for } \tau < \frac{z}{b_B}, \\ w_{B;y} \mathbf{e}_{B;y}, & \text{for } \tau \geq \frac{z}{b_B}. \end{cases} \quad (2.76)$$

For  $\tau \geq 2$ , the aerofoil is exposed to a uniform flow velocity  $w_{B;y}$  in the local  $y_B$  direction along the chord length, and the angle of attack can be expressed as:

$$\sin \alpha_B^{qs}(t) = \frac{w_{B;y}(t)}{|\mathbf{W}_{B;rel}(t)|}. \quad (2.77)$$

Here, the relative inflow velocity  $\mathbf{W}_{B;rel}(t)$  is composed of  $\mathbf{W}_{B;eff}$  and  $\mathbf{w}_{B;y}(t)$  and no aerofoil motion is assumed.

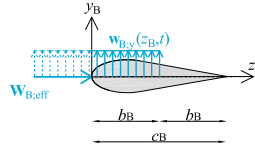


Figure 2.25: Schematic representation of an aerofoil exposed to a step change in the lateral inflow velocity.

If the gust velocity is small compared to the effective inflow velocity, the angle of attack can be approximated as

$$\alpha_B^{qs}(t) \approx \frac{w_{B;y}(t)}{|\mathbf{W}_{B;eff}|}. \quad (2.78)$$

Assuming that the effective inflow velocity is much larger than the vertical gust velocity, the non-stationary bound circulation can be expressed in terms of the Küssner function  $\Phi_K(\tau)$ :

$$\Gamma_{B;b}^{ns}(\tau) = \pi c_B |\mathbf{W}_{B;rel}(\tau)| \sin \alpha_B^{qs}(\tau) \Phi_K(\tau) \mathbf{e}_{B;r}. \quad (2.79)$$

For small variations of the angle of attack, the non-stationary bound circulation can be approximated as

$$\Gamma_{B;b}^{ns}(\tau) \approx \pi c_B |\mathbf{W}_{B;eff}| \alpha_B^{qs}(\tau) \Phi_K(\tau) \mathbf{e}_{B;r}. \quad (2.80)$$

Sears and Sparks [214] suggested to define the Küssner's function, which relates to the inverse Laplace transform of the Sears' function, in similar terms as the exponential approximation of the Wagner's function:

$$\Phi_K(\tau) \approx 1 - \Psi_1 e^{-\eta_1 \tau} - \Psi_2 e^{-\eta_2 \tau}, \quad \text{for } \tau > 0, \quad (2.81)$$

with the coefficients for a thin aerofoil given in Table 2.2. An algebraic approximation was presented by Bisplinghoff *et al.* [184]:

$$\Phi_K(\tau) \approx \frac{\tau^2 + \tau}{\tau^2 + 2.82\tau + 0.80}, \quad \text{for } \tau > 0. \quad (2.82)$$

Figure 2.26 illustrates both Küssner's function approximations. Contrarily to the Wagner's function, the initial value of the Küssner's function is  $\Phi_K(0) = 0$ . The Küssner's function converges to 1.0 as  $\tau \rightarrow \infty$ .

Table 2.2: Coefficients of the approximated indicial Küssner's function.

coefficient	Küssner's function $\Phi_K(\tau)$ [214]
$\Psi_1$	0.5
$\Psi_2$	0.5
$\eta_1$	0.13
$\eta_2$	1.0

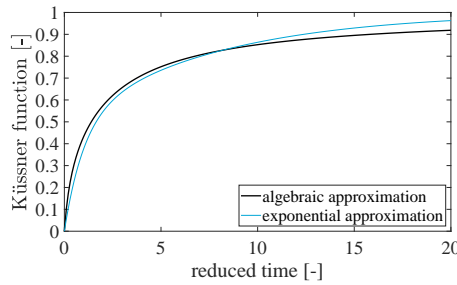


Figure 2.26: Approximations of Küssner's indicial function.

With the application of the angle of attack in accordance with Eq. (2.78) and the Küssner's function, the non-stationary bound circulation for arbitrary variations of the wind velocity in the local  $y_B$  direction is obtained from

$$\Gamma_{B;b}^{\text{ns}}(\tau) = \pi c_B \left\{ \Phi_K(\tau) w_{B;y}(0) + \int_0^\tau \Phi_K(\tau - \bar{\tau}) \frac{\partial w_{B;y}(\bar{\tau})}{\partial \bar{\tau}} d\bar{\tau} \right\} \mathbf{e}_{B;r}, \quad (2.83)$$

for  $\tau \geq 0$ .

Due to the assumptions that both the structural motion and the gust velocity are small compared to the effective flow velocity, Eqs. (2.70) and (2.83) are linear functions of these time-variations and the combined non-stationary bound circulation can be obtained by means of superposition. Dropping this assumption implies, that both the angle of attack and the bound circulation should be determined on the basis of the time-dependent relative flow velocity  $\mathbf{W}_{B;\text{rel}}(t)$ :

$$\mathbf{W}_{B;\text{rel}}(t) = \mathbf{W}_{B;\text{eff}}(t) + \mathbf{w}_{B;y}(t) - \dot{\mathbf{u}}_{B;y}(t) - \left(\frac{1}{2} b_B\right) - z_{B\beta} \beta \left( \mathbf{e}_{B;z} \times \dot{\hat{\mathbf{p}}}_B(t) \right). \quad (2.84)$$

The effective flow velocity  $\mathbf{W}_{B;\text{eff}}(t)$  is here expressed as a function of time, because its orientation in the  $y_B z_B$  plane is affected by the pitch angle  $\beta_B(t)$ .

With the application of  $\mathbf{W}_{B;\text{rel}}(t)$  in accordance with Eq. (2.84), the angle of attack depends non-linearly on both the structural motion and the gust velocity. As a consequence, the non-stationary flow cannot be separated into linear components and the combined non-stationary bound circulation cannot be determined on the basis of the indicial Wagner and Küssner functions.

#### TIME-DOMAIN EFFECTIVE INFLOW VARIATIONS

So far, only variations in the local  $y_B$  direction were considered, while the effective inflow in the local  $z_B$  direction was assumed constant in time. With the application of helicopter aero-elasticity, Leishman [182] considered the non-stationary aerodynamic forcing for a time-variant effective inflow too. Such time-variations can result from a non-stationary rotational velocity of the rotor and oscillations in the wind velocity. As a result of the time-varying effective inflow velocity, the convection speed of the shed wake is no longer constant.

If the direction of this time-dependent effective airflow velocity is assumed to be time-invariant, the non-stationary bound circulation can be expressed in terms of the instantaneous downwash<sup>3</sup>  $W_{B;y}(t)$ :

$$W_{B;y}(t) = |\mathbf{W}_{B;\text{eff}}(t)| \sin \alpha_B^{\text{qs}}(t). \quad (2.85)$$

Here, the contributions of plunging and pitching motions could be included in the definition of the instantaneous downwash as well. On this basis, the bound circulation can be expressed as

$$\Gamma_{B;b}^{\text{ns}}(\tau) = \pi c_B \left\{ \Phi_W(\tau) W_{B;y}(0) + \int_0^\tau \Phi_W(\tau - \tilde{\tau}) \frac{\partial W_{B;y}(\tilde{\tau})}{\partial \tilde{\tau}} d\tilde{\tau} \right\} \times \mathbf{e}_{B;z}. \quad (2.86)$$

The non-stationary bound circulation is here expressed in terms of the Wagner's function, while the non-stationarity may result from both instantaneous aerofoil motions and gradual variations in the wind velocity. This implies that the varying inflow velocity is effectively replaced by a structural oscillation in the local  $z_B$  direction. Strictly speaking, this approach is only valid for inflow variations with long wave lengths, compared to the blade geometry.

Van der Wall and Leishman [215] illustrated the applicability of Eq. (2.86) in a comparison with a number of alternative models [32, 181, 216, 217]. It was also observed that for the analysis of inflow variations with long wave lengths in the frequency domain, the Theodorsen's function can be applied to predict the resulting lift forces.

#### 2.3.7. VISCOUS FLOW ANALYSIS

Contrarily to inviscid flows, shear stresses develop within viscous flows, resulting in friction forces on the aerofoil. As a result, a boundary layer develops around an aerofoil in

<sup>3</sup>The term 'downwash' is borrowed from the field of aeronautics, where it refers to the change in direction of the airflow, which is deflected by an aerodynamic action of an airfoil, wing or blade in motion, as part of the process of producing lift.

an airflow, within which the flow velocity decreases to zero towards the aerofoil surface. The resulting friction force on the aerofoil, which is referred to as skin-friction drag, depends on the Reynolds number of the flow and the roughness of the aerofoil surface, which dictate the thickness of the boundary layer and the characteristics of the flow within this layer.

Assuming a thin aerofoil and a very small angle of attack, it can be shown that the flow in the boundary layer starts out from the leading edge as laminar [179]. Towards the trailing edge, a transition to a turbulent flow occurs and the thickness of the boundary layer increases. The resulting skin-friction drag depends on the location of the transition along the length of the chord, determining the contribution of the skin friction from the laminar flow and the skin friction from the turbulent flow.

The boundary layer flow around an aerofoil first experiences an increase in velocity, resulting in a reduction of the pressure. Because of the friction, the pressure in the flow increases and the flow velocity decreases, until the point a negative flow velocity should occur. At this point, the flow separates from the aerofoil surface, forming a vortex travelling towards the trailing edge, and inducing a zone with a lower pressure than the pressure that would exist in an attached flow. For non-zero angles of attack, the separation occurs at the side of the aerofoil with the longest travelling distance of the flow, inducing in a pressure difference between both sides of the aerofoil. The force resulting from the integrated pressure along the aerofoil surface is referred to as pressure drag, or form drag.

For small angles of attack, the total drag is governed by friction, the resulting force of which is relatively small for aerofoil-shaped cross-section and independent of the angle of attack, whereas for large angles of attack the pressure drag becomes dominant, and the force increases steeply with an increase in the angle of attack. The total drag force  $\bar{\mathbf{F}}_{B;D}(t)$  is generally expressed as follows:

$$\mathbf{F}_{B;D}(t) = \frac{1}{2} \rho c_B C_{B;D} \mathbf{W}_{B;rel}(t) |\mathbf{W}_{B;rel}(t)|. \quad (2.87)$$

The drag coefficient  $C_{B;D}$  expresses the combined contribution of friction drag and pressure drag, which is determined empirically, and depends on the Reynolds regime and the temperature. In a non-stationary airflow, the boundary layer needs to adapt continuously, implying that the drag coefficient cannot be considered constant in time. Provided that the flow remains attached to most of the aerofoil surface, however, the contribution of the drag force to the total aerodynamic forcing is small, and the drag coefficient can be assumed to be independent of time and the drag force to react instantaneously to changes in the flow conditions.

The separation of the flow, having vortices shed from the trailing edge, results in a drop in the bound circulation and the lift force. This development of stall is a transient process, as the vorticity generated at the separation point is not immediately shed from the trailing edge, implying that the bound circulation does not drop immediately after an increase in the angle of attack forces the flow to separate. As a consequence, the lift force initially keeps increasing after the angle of attack exceeds the limit of static stall, showing a steep drop once the stall is completely established [35]. Multiple semi-empirical models have been developed to describe the non-linear relation between the lift coefficient and the angle of attack [218–221].

### 2.3.8. THREE-DIMENSIONAL FLOWS

The models presented in this section, describe the two-dimensional aerodynamic forcing on an aerofoil cross-section, based on the inflow velocity perpendicular to the longitudinal blade axis. For actual rotor blades the two-dimensional flow is disturbed because of the finite blade length, with a vortex being shed from the tip. Moreover, radial flows are induced because of the expansion of the wake and the trailed vorticity from the varying bound circulation along the blade span. Non-axial components of the ambient wind field contribute to the three-dimensional airflow as well.

The assumption of two-dimensional flows agrees with the assumed independent annuli of the blade element-momentum theory. Leishman [40] argued, based on experimental work [222, 223] that for below-stall angles of attack, the principle of independent annuli is justified, whereas the onset of dynamic stall was observed at a higher angle of attack for flows acting under a sweep angle, inducing a radial flow. On this basis, Leishman and Beddoes [218] developed a model to predict the dynamic stall under three-dimensional sweep.

Lorber *et al.* [224] investigated the dynamic stall of an oscillating finite blade, both swept and unswept. It was observed the assumption of independent annuli is justified on the inboard portion, allowing for the analysis of the two-dimensional flow. At the blade tip, however, the tip vortex was shown to reduce the effective angle of attack, inducing a delay in the onset of dynamic stall. This effect was stronger for the unswept blade than for the swept blade.



# 3

## ROTATING BLADE ANALYSIS

*Existing models for the analysis of offshore wind turbines account for the aerodynamic action on the turbine rotor in detail, requiring a high computational price. When considering the foundation of an offshore wind turbine, however, a reduced rotor model may be sufficient. To define such a model, the significance of the non-linear velocity and history dependency of the aerodynamic force on a rotating blade should be known. Aerodynamic interaction renders the dynamics of a rotating blade in an ambient wind field non-linear in terms of the dependency on the wind velocity relative to the structural motion. Moreover, the development in time of the aerodynamic force does not follow the flow velocity instantaneously, implying a history dependency. In addition, both the non-uniform blade geometry and the aerodynamic interaction couple the blade motions in and out of the rotational plane. Therefore, this chapter presents the Euler-Bernoulli formulation of a twisted rotating blade connected to a rigid hub, excited by either instantaneous or history-dependent aerodynamic forces. On this basis, the importance of the history dependency is determined. Moreover, to assess the non-linear contributions, both models are linearized. The structural response is computed for a stand-still and a rotating blade, based on the NREL 5-MW turbine. To this end, the model is reduced on the basis of its first three free-vibration mode shapes. Blade tip response predictions, computed from turbulent excitation, correctly account for both modal and directional couplings, and the added damping resulting from the dependency of the aerodynamic force on the structural motion. Considering the deflection of the blade tip, the history-dependent and the instantaneous force models perform equally well, providing a basis for the potential use of the instantaneous model for the decoupled modelling of the rotor and the support structure. The linearized instantaneous model provides similar results for the rotating blade, indicating its potential application for this scenario, and allowing for the definition of an added damping matrix, applicable for the dynamic analysis of rotating turbine blades.*

---

This chapter represents an adaptation of Van der Male *et al.* [225]

WITH the enhanced interest in renewable energy, the development of offshore wind power has soared. The forces on offshore wind turbines mainly result from environmental interactions – aerodynamic and hydrodynamic – which are coupled through the response of the structure. The coupled analysis requires an integrated model, accounting for the rotor, nacelle assembly, tower and foundation. Available commercial and academic software codes allow for a detailed analysis of the aerodynamic interaction [133].

A detailed integrated analysis of offshore wind turbines comes with a high computational price. In order to reduce the complexity of the integrated models, recent research has focussed on the reduction of the foundation structure [12, 149, 155]. As an alternative, models can be developed with a reduced rotor representation, in particular when the engineering focus is on the foundation of the structure. This would require a simplified rotor model, accounting for the aerodynamic forcing that results from the operational state. Such a rotor simplification cannot account in full detail for the non-linear velocity and history dependency of the aerodynamic interaction. The question rises to what extent these interaction characteristics are of importance for the preliminary integrated analysis of offshore wind turbines.

The aerodynamic interaction models for turbine blades stem from preceding developments in the aircraft industry [32, 212, 215, 218, 226]. Larsen *et al.* [221] presented an overview of aerodynamic models for wind turbine application, valid for the lower flow velocities. In case of unsteady aerodynamics, either through a non-stationary flow or structural motion, a change in the angle of attack results in a brief separation of the flow until again a wake equilibrium – that is, an aerodynamic equilibrium of the near wake behind the trailing edge of the aerofoil – is found, thus delaying the transition to a new aerodynamic state. Hansen *et al.* [219] presented a modified Beddoes-Leishman model [182], with which experimental data derived for attached-flow conditions was predicted. This model expresses the history dependency in terms of aerodynamic states, through which a delay in the development of the aerodynamic coefficients – lift and drag – is established. Different history-dependent aerodynamic force models have been applied in the study on aero-elastic instabilities of wind turbine blades [227–231].

In many cases, the aerodynamic interaction is described by means of an instantaneous force model [34, 35, 232]. Such a model neglects the disturbance of the near wake and the consequent delayed development of the new aerodynamic equilibrium. The validity of this approach can in principle be assessed on the basis of the reduced frequency, a non-dimensional parameter relating the period of the blade oscillations to the time required for the air flow to travel across the blade chord [183]. The air flow velocity of wind turbine blades varies along the length of the blade, and so does the reduced frequency. Moreover, the contribution of the structural motion to the relative air flow velocity is not known beforehand. Consequently, the history dependency of the aerodynamic interaction of wind turbine blades cannot straightforwardly be determined.

This chapter addresses the aerodynamics of a single rotating blade, with the purpose of assessing the significance of the non-linear velocity and history-dependent aerodynamic interaction. The blades of a wind turbine are large, flexible and non-uniform elements, twisted along their length. This implies that the flexural modes of vibration are not easily defined, and, moreover, cannot be described within one plane. Given the environmental

conditions, the rotational speed can be adjusted, which affects the centrifugal stiffening. To control the aerodynamic interaction, the blades can be pitched towards or away from the direction of the wind. As a result, the coupling between the motions in and out of the plane of rotation depends on the operational state, implicitly affecting the natural frequencies and the modal shapes of the blade. Moreover, added damping and mass are introduced as a result of the aerodynamic interaction, through which the in-plane and out-of-plane blade motions are coupled. Given the nature of the aerodynamic interaction, this coupling is non-linear.

A geometrically linear model of a twisted non-uniform aerofoil is derived and the true undamped modes corresponding to different operational states are obtained by means of the finite element method. The structural and aero-elastic properties of the blade are based on the conceptual NREL 5MW turbine [172]. Subsequently, an instantaneous and a history-dependent aerodynamic force model are defined, accounting for the dependency on the structural motion of the turbine blade. These non-linear aerodynamic models, which are restricted to attached flows, couple the blade motions in and out of the rotational plane. After expanding and truncating the response, by means of the Galerkin decomposition, added damping and the modal and directional coupling are assessed for both a stand-still and a rotating aerofoil on the basis of linearized aerodynamic models. To this end, frequency-response functions of the blade tip motions are computed, which either include or exclude the contribution of aerodynamic interaction terms. Subsequently, the relevance of the non-linear velocity and history dependency of the aerodynamic interaction is assessed. In a previous preliminary study, the coupled non-linear system was analyzed with the help of a Volterra series expansion [233]. In this chapter, the full non-linear response is determined for a turbulent wind signal on the basis of a Kaimal turbulence spectrum, using time integration on the basis of an explicit Runge Kutta scheme. By comparing the blade tip motions derived with the non-linear and the linearized models, the influence of the non-linear velocity and history dependency of the forcing on the structural response is addressed.

## 3.1. ROTATING BLADE MODEL

### 3.1.1. ROTATING BEAM MODELLING

Numerous examples of the free-vibration analysis of rotating beams can be found in literature. Many of those have focussed on the linear motion of a uniform Euler-Bernoulli beam [234–241], or a Timoshenko beam [242–245]. Most works are limited to motion either in or out of the rotational plane, while some have specifically addressed the flexural-flexural coupling [234, 242, 245], the flexural-axial coupling [237, 239, 240, 244, 246] – introducing the Coriolis effect – or the flexural-torsional coupling [247]. Apart from uniform beams, many studies have focussed on tapered beams [235, 238, 245, 248, 249] or non-uniform beams with an axial twist or asymmetrical cross-section [245–247]. The finite element method has frequently been adopted to derive the natural frequencies and the modal shapes [234, 235, 239, 240, 242, 245, 248], while the Galerkin expansion is a commonly applied method too, to assess the dynamic response of the system [236, 237, 245–247, 250]. Some works particularly focussed on the application of alternative approaches such as the direct stiffness method and the extended power series method

[238, 243, 249]. The effect of geometrical non-linearities has been included in a number of studies [247, 250–252], where perturbation methods and non-linear normal modes were used to analyze the dynamic behaviour of such beams. Some authors have specifically focussed on the modelling of a helicopter blade [253, 254], providing a basis for the derivation of the equation of motion of rotating wind turbine blades [232, 255].

### 3.1.2. MODEL DEFINITION

The adopted model is illustrated in Figure 3.1. The blade of radius  $R$  is defined in the rotating global frame of reference  $r_B Y_B Z_B$ , defined by the unit vectors  $\mathbf{e}_{B;r}$ ,  $\mathbf{e}_{B;Y}$  and  $\mathbf{e}_{B;Z}$ , within the fixed global frame of reference  $X_R Y_R Z_R$ , with  $Y_R = Y_B$  (Figure 3.1(a)). The  $r_B$  axis coincides with the longitudinal axis of the blade. The rotation is expressed by the vector  $\Omega_R(t) = \Omega_{R;Y}(t)\mathbf{e}_{B;Y}$ , implying a clockwise rotation round the  $Y_B$  axis. The blade is fixed to a rigid hub with radius  $r_H$ . Figure 3.1(b) depicts a blade cross-section at  $r_B$ , with chord width  $c_B$ . For each cross-section, the principal axes are defined by the local  $r_B y_B z_B$  coordinate system, where the principal axes vary with twist  $\beta_{B;0}(r_B)$  about the  $r_B$  axis. Furthermore, the blade can be pitched, introducing a pitch  $\beta_B(t)$ , which is constant along  $r_B$ , but can vary in time, in addition to  $\beta_{B;0}(r_B)$ . It should be noted that the definition of the positive angles  $\beta_{B;0}(r_B)$  and  $\beta_B(t)$ , as indicated in Figure 3.1(b), does not correspond to the right-hand rule sign convention.

Regarding the control of the blade, both the rotational speed and the pitch angle are assumed to be constant in time, i.e.,  $\Omega_{R;Y}(t) = \bar{\Omega}_{R;Y}$  and  $\beta_B(t) = \bar{\beta}_B$ , with the bar indicating that the mean value is adopted. The amplitudes of vibration are assumed to be sufficiently small, justifying a geometrically linear analysis. This also implies that the centrifugal stiffening, resulting from the rotation of the beam, does not vary during the vibration. Furthermore, cross-sections under deformation are assumed to remain plane and normal to the neutral axis, i.e., the beam is assumed to satisfy the Euler-Bernoulli theory. Similar models have been presented by Rao and Gupta [245] and Lin *et al.* [246], the former addressing a free-vibration analysis of a non-uniformly twisted non-prismatic rotating Timoshenko beam, and the latter studying the Green's functions of a rotating Euler-Bernoulli beam with an elastic root and a tip mass.

### 3.1.3. EQUATIONS OF MOTION

The equations of motion are defined in the global rotating  $r_B Y_B Z_B$  reference frame; the deformation vector  $\mathbf{u}_B(r_B, t)$  defines the local deflection  $u_{B;Y}(r_B, t)$  in  $Y_B$  direction and the local deflection  $u_{B;Z}(r_B, t)$  in  $Z_B$  direction:

$$\mathbf{u}_B(r_B, t) = \begin{bmatrix} u_{B;r}(r_B, t) \\ u_{B;Y}(r_B, t) \\ u_{B;Z}(r_B, t) \end{bmatrix}. \quad (3.1)$$

In the remainder of this chapter, the  $Y_B$  and  $Z_B$  direction will be indicated as out-of-plane and in-plane, respectively, referring to the plane of rotation. Since the model is restricted to flexural motion,  $u_{B;r}(r_B, t)$  equals zero for all  $r_B$ . The strain energy  $U_B(t)$  of the rotating

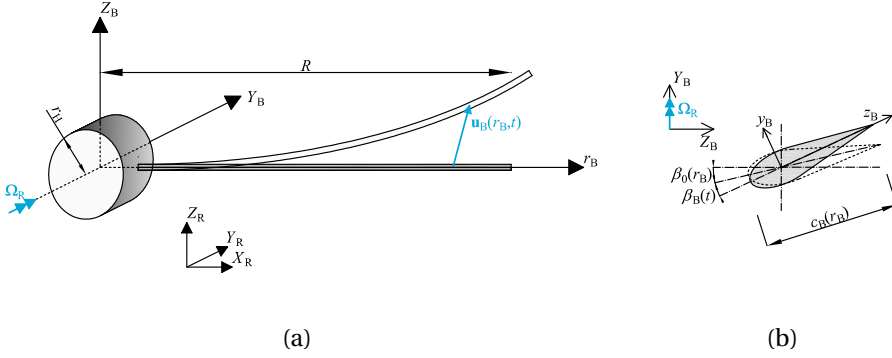


Figure 3.1: The rotating blade model, with (a) the global configuration of the rotating beam and (b) the local configuration of an arbitrary cross-section.

beam can be expressed as

$$U_B(t) = \int_{r_H}^R \frac{1}{2} \{ \mathbf{u}_B''(r_B, t) \}^T \mathbf{EI}_B(r_B) \mathbf{u}_B''(r_B, t) dr_B + \int_{r_0}^R \frac{1}{2} \{ \mathbf{u}_B'(r_B, t) \}^T \mathbf{P}_B(r_B) \mathbf{u}_B'(r_B, t) dr_B, \quad (3.2)$$

where  $\mathbf{EI}_B(r_B)$  represents the bending stiffness tensor, consisting of the  $r_B$ -dependent diagonal terms  $EI_{B;YY}(r_B)$  and  $EI_{B;ZZ}(r_B)$ , and the cross-term  $EI_{B;YZ}(r_B)$ . The primes indicate spatial derivatives with respect to  $r_B$ . The diagonal tensor  $\mathbf{P}_B(r_B)$  represents the deflection-restoring force, i.e., centrifugal force, resulting from the rotation of the blade:

$$\mathbf{P}_B(r_B) = \bar{\Omega}_{R;Y}^2 \int_{r_H+r_B}^R \mathbf{M}_B(\xi) \xi d\xi. \quad (3.3)$$

$\mathbf{M}_B(r_B)$  is the diagonal mass matrix, with the distributed mass  $m_B(r_B)$  as its diagonal entries, and  $\xi$  is a dummy variable replacing  $r_B$ .

The definition of the kinetic energy  $T_B(t)$  is as follows:

$$T_B(t) = \int_{r_H}^R \frac{1}{2} \{ \mathbf{v}_B(r_B, t) \}^T \mathbf{M}_B(r_B) \mathbf{v}_B(r_B, t) dr_B. \quad (3.4)$$

The velocity vector  $\mathbf{v}_B(r_B, t)$  defines the local velocity of the rotating and vibrating blade:

$$\begin{aligned} \mathbf{v}_B(r_B, t) &= \bar{\Omega}_R \times (r_B \mathbf{e}_{B;r} + \mathbf{u}_B(r_B, t)) + \dot{\mathbf{u}}_B(r_B, t) \\ &= \begin{bmatrix} \bar{\Omega}_{R;Y} u_{B;Z}(r_B, t) \\ 0 \\ -\bar{\Omega}_{R;Y} r_B \end{bmatrix} + \begin{bmatrix} 0 \\ \dot{u}_{B;Y}(r_B, t) \\ \dot{u}_{B;Z}(r_B, t) \end{bmatrix}. \end{aligned} \quad (3.5)$$

This formulation of the velocity accounts for both the blade deflection and the local vibration velocity  $\dot{\mathbf{u}}_B(r_B, t)$  affecting the arm of rotation, where the overdot indicates a

derivative with respect to time. As the analysis does not include longitudinal motions, the entries of Eq. (3.5) in the  $r_B$  direction are disregarded.

By applying Hamilton's principle [148], the equations of motion for the beam can be obtained:

$$\mathbf{M}_B(r_B)\ddot{\mathbf{u}}_B(r_B, t) + \mathbf{K}_B(r_B)\mathbf{u}_B(r_B, t) = \mathbf{0}, \quad (3.6)$$

where  $\mathbf{K}_B$  represents a  $2 \times 2$  operator matrix, which results from the superposition of three matrices:

$$\mathbf{K}_B(r_B) = \frac{\partial^2}{\partial r^2} \mathbf{EI}_B(r_B) \frac{\partial^2}{\partial r^2} - \frac{\partial}{\partial r_B} \mathbf{P}_B(r_B) \frac{\partial}{\partial r_B} - \mathbf{G}_B(r_B). \quad (3.7)$$

The matrix  $\mathbf{G}_B(r_B)$  expresses the increase in kinetic energy due to an in-plane deflection within the geometrically linear model definition [251]:

$$\mathbf{G}_B(r_B) = \begin{bmatrix} m_B(r_B)\bar{\Omega}_{R,Y}^2 & 0 \\ 0 & 0 \end{bmatrix}. \quad (3.8)$$

In a similar manner, Hamilton's principle allows for the derivation of the boundary conditions, which for the fixed-free blade take the form of

$$\mathbf{u}_B(r_H, t) = \mathbf{u}'_B(r_B, t) \Big|_{r_B=r_H} = 0, \quad (3.9)$$

and

$$\frac{\partial}{\partial r_B} \mathbf{EI}_B(r_B) \mathbf{u}''_B(r_B, t) \Big|_{r_B=R} = \mathbf{EI}_B(r_B) \mathbf{u}''_B(r_B, t) \Big|_{r_B=R} = 0. \quad (3.10)$$

### 3.1.4. EIGENANALYSIS

Given the boundary conditions of Eqs. (3.9) and (3.10), the operator matrix  $\mathbf{K}_B$  is self-adjoint. On this basis, the displacement vector  $\mathbf{u}_B(r_B, t)$  satisfying Eq. (3.6) and the boundary conditions can be expanded in an absolutely and uniformly convergent series of eigenfunctions [148]. If  $\omega_{B,n}^2$  is the  $n$ -th eigenvalue corresponding to the  $n$ -th eigenfunction of the system  $\mathbf{u}_{B,n}(r_B)$ , the eigenvalue problem can be expressed in accordance with Lin *et al.* [246]:

$$\left\{ \mathbf{K}_B(r_B) - \omega_{B,n}^2 \mathbf{M}_B(r_B) \right\} \mathbf{u}_{B,n}(r_B) = \mathbf{0}. \quad (3.11)$$

In physical terms,  $\omega_{B,n}$  and  $\mathbf{u}_{B,n}(r)$  represent the  $n$ -th natural frequency and mode, respectively.

The developed model is applied to describe the dynamic characteristics of a wind turbine blade. Hereto, the structural properties of the NREL 5MW blade [172] are adopted. This blade has a length of 61.5 m and is attached to a hub with a radius of 1.5 m. The cross-sectional shape varies along the length of the blade to optimize the aero-elastic performance. For the same reason, the blade twist varies from  $13.3^\circ$  near the hub to  $0^\circ$  at the blade tip. The first three natural frequencies have been estimated with the software program FAST as 0.70 Hz, 1.08 Hz and 2.02 Hz. The effect of rotation was not explicitly taken into account and the coupling of the in-plane and out-of-plane motions was not addressed.

Since no closed-form solution for Eq. (3.11) can be found, a finite element code is developed to find the eigenvectors and eigenvalues of the model. To this end, use is made of the model presented by Yokoyama [242]. The first three mass-normalized mode shapes are derived for two different operational scenarios: (i) stand-still, pitched  $\bar{\beta}_B = 90^\circ$ , and (ii) at an operational rotation of  $\bar{\Omega}_{R;Y} = 12.1$  rpm and zero additional pitch  $\bar{\beta}_B$  (see Table 3.1).

Table 3.1: Operational scenarios.

scenario	rotation $\bar{\Omega}_{R;Y}$ [rpm]	pitch angle $\bar{\beta}_B$ [°]
i	0	90
ii	12.1	0

Figure 3.2 presents the in-plane and out-of-plane components of the first three mode shapes, where Figure 3.2(a) and (b) represent the in-plane and out-of-plane components of the first mode shape, respectively. In the stand-still scenario, the component in the in-plane direction almost exclusively represents the modal shape, with only little contribution in the out-of-plane direction due to the twist  $\beta_{B;0}(r_B)$  of the blade, i.e., the coupling through the bending stiffness tensor. The opposite is observed for the rotating blade, with a larger out-of-plane component resulting from the zero-pitch  $\bar{\beta}_B$ . The corresponding natural frequency increases from 0.70 Hz (scenario i) to 0.73 Hz (scenario ii). The increase results from the centrifugal stiffening, induced by the rotation of the blade.

The second and third natural frequencies change from 1.11 Hz to 1.13 Hz, and from 2.01 Hz to 2.06 Hz, respectively. The corresponding mode shapes are depicted in Figures 3.2(c) and (d), and Figures 3.2(e) and (f). The figures again show the interchange of the dominant modal components due to the pitching of the blade.

## 3.2. AERODYNAMIC INTERACTION

### 3.2.1. FORCE DEFINITIONS

Figure 3.3(a) depicts a cross section of the blade model subjected to a relative incident air flow  $\mathbf{W}_{B;rel}(r_B, t)$  under the angle of attack  $\alpha_B(r_B, t)$ . The relative incident flow velocity is composed of the wind speed at the blade section, the rotational speed of the blade and the structural motion. It should be noted that the definition of the positive angle of attack  $\alpha_B(r_B, t)$ , as indicated in Figure 3.3(a), contradicts the right-hand rule sign convention.

Figure 3.3(b) illustrates the drag force  $\mathbf{F}_{B;D}(r_B, t)$  and the circulatory lift force  $\mathbf{F}_{B;L}(r_B, t)$ , acting on the aerofoil. The forces act on the aerodynamic centre of the blade, which approximately coincides with the quarter-chord point on the blade. This implies that a change in the angle of attack does not affect the torsional moment about this point [179]. The angle of attack can be defined in terms of the so-called downwash, the relative flow velocity  $W_{B;rel;y}(r_B, t)$  in the local  $y_B$  direction. The downwash is defined at the three-quarter chord point and serves the determination of the angle of attack [183].

The time-varying aerodynamic forces introduce a time-dependent torque about the shear centre, inducing a torsion of the blade. Since the natural frequency of the first torsional mode is relatively high, 5.56 Hz in case of a rigid connection at the hub, the corresponding motion can be assumed to be quasi-static. Moreover, given the large torsional stiffness, the amplitude of the torsional motion will be small and its effect on

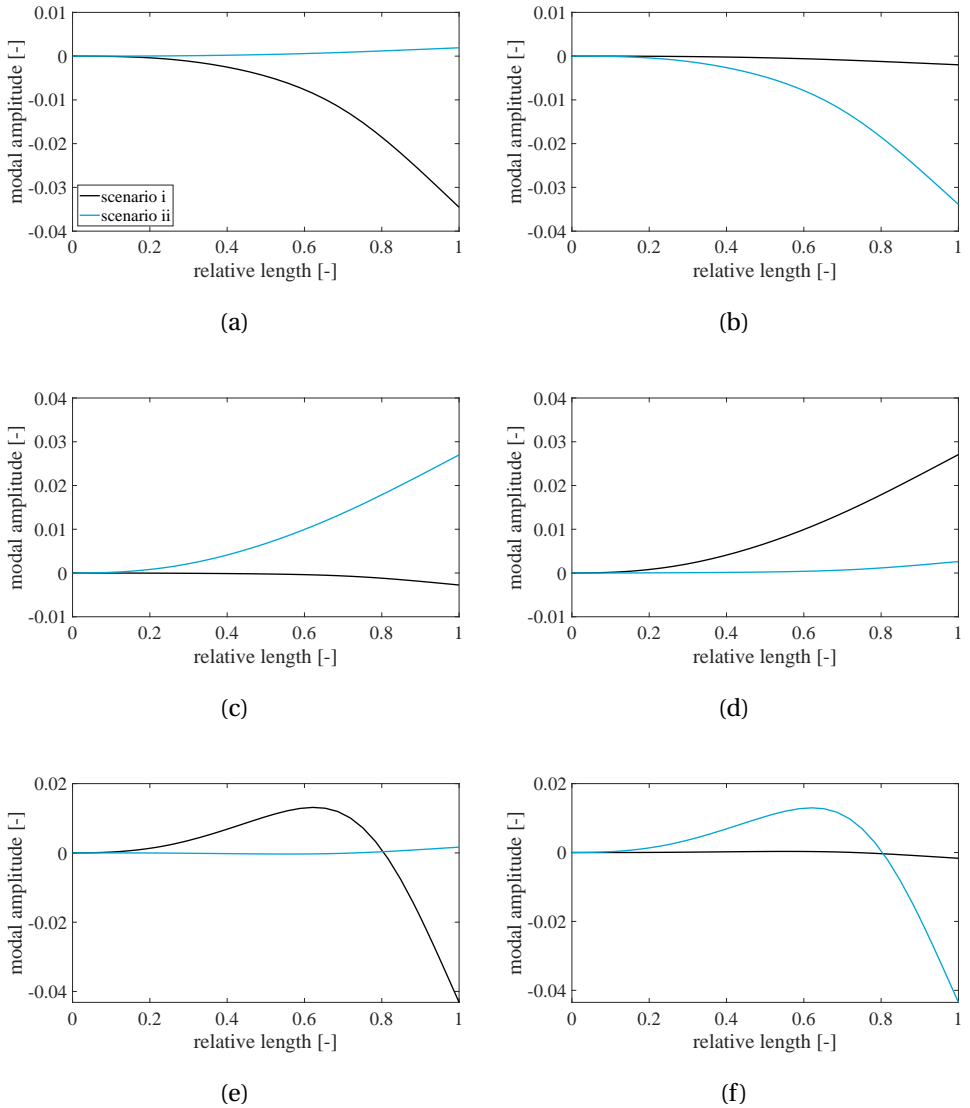


Figure 3.2: First three mode shapes, with (a) the in-plane direction component of the first mode shape, (b) the out-of-plane component of the first mode shape, (c) the in-plane direction component of the second mode shape, (d) the out-of-plane component of the second mode shape, (e) the in-plane direction component of the third mode shape, and (f) the out-of-plane component of the third mode shape



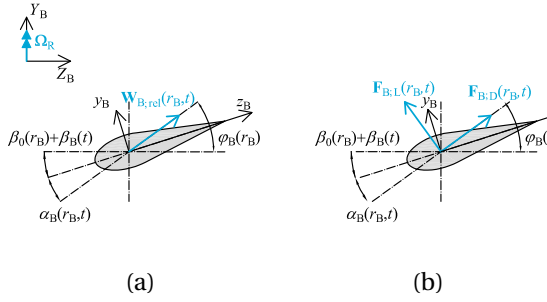


Figure 3.3: Aerodynamic configuration, with (a) the definition of the angle of attack and (b) the definition of the drag and the lift forces.

the aerodynamic interaction is therefore assumed to be small. Since the current model does not account for the torsional motion of the blade, the downwash does not vary along the chord length. Therefore, the downwash can be determined from the relative air flow at the aerodynamic centre and the angle of attack can conveniently be defined at the quarter-chord point as depicted in Figure 3.3.

### 3.2.2. DRAG FORCE MODEL

As described in Section 2.3.7, the drag force can be distinguished into viscous – or, skin friction – drag and pressure drag. The current analysis is restricted to attached flows, implying that the angle of attack is relatively small, and for which the contribution of the pressure drag is negligible. Based on this assumption, the static drag  $\mathbf{F}_{B;D}(r_B, t)$  can be estimated by determining the viscous drag only:

$$\mathbf{F}_D(r_B, t) = \frac{1}{2} \rho_{\text{air}} c_B(r_B) C_{B;D}(r_B) \mathbf{W}_{B;\text{rel}}(r_B, t) \left| \mathbf{W}_{B;\text{rel}}(r_B, t) \right|. \quad (3.12)$$

Drag coefficients of aerofoils are obtained empirically from stationary flows. Given the dependency on the Reynolds number, Eq. (3.12) is in principle not necessarily valid for non-stationary flow analyses. Since no alternative formulation for non-stationary flows is available, Eq. (3.12) is used in the current analysis to model the drag force for non-stationary flows.

### 3.2.3. INSTANTANEOUS LIFT FORCE MODEL

For quasi-stationary flows, it can be assumed that the Kutta condition is met instantaneously, when a change in the flow conditions occurs. As a consequence, the quasi-stationary bound circulation – as described in Section 2.3.4 – can be adopted to model the lift force acting on the aerofoil:

$$\begin{aligned} \mathbf{\Gamma}_{B;b}^{\text{qs}}(r_B, t) &= \frac{1}{2} \pi c_B(r_B) C_{B;L}^c(r_B, t) \left| \mathbf{W}_{B;\text{rel}}(r_B, t) \right| \mathbf{e}_{B;r} + \frac{1}{2} \pi c_B(r_B) C_{B;L}^\alpha(r_B, t) W_{B;\text{rel};y}(r_B, t) \mathbf{e}_{B;r} \\ &\quad \mathbf{\Gamma}_{B;b}^{c;\text{qs}}(r_B, t) + \mathbf{\Gamma}_{B;b}^{\alpha;\text{qs}}(r_B, t), \end{aligned} \quad (3.13)$$

where the lift coefficient  $C_{B;L}(r_B, t)$  for cambered aerofoils and attached flows is expressed in accordance with Eq. (2.33). As a consequence, the quasi-stationary bound circulation

can be separated into a camber-dependent and an  $\alpha$ -dependent contribution,  $\Gamma_{B;b}^{c;qs}(r_B, t)$  and  $\Gamma_{B;b}^{\alpha;qs}(r_B, t)$ , respectively:

$$\Gamma_{B;b}^{qs}(r_B, t) = \Gamma_{B;b}^{c;qs}(r_B, t) + \Gamma_{B;b}^{\alpha;qs}(r_B, t). \quad (3.14)$$

The instantaneous lift force  $\mathbf{F}_{B;L}^{qs}(r_B, t)$  on a blade in a quasi-stationary inviscid incompressible flow can be derived from the Kutta-Joukowski theorem:

$$\mathbf{F}_{B;L}^{qs}(r_B, t) = \rho_{\text{air}} \left( \mathbf{W}_{B;\text{rel}}(r_B, t) \times \Gamma_{B;b}^{qs}(r_B, t) \right). \quad (3.15)$$

In addition, a non-circulatory lift force – or apparent inertia force – should be accounted for. For this apparent inertia force  $\mathbf{F}_{B;I}(r_B, t)$ , the formulation presented in Section 2.3.5 is adopted:

$$\mathbf{F}_{B;I}(r_B, t) = \frac{1}{4} \rho \pi c_B(r_B)^2 \dot{\mathbf{W}}_{B;\text{rel}}(r_B, t). \quad (3.16)$$

The complete definition of the instantaneous aerodynamic force  $\mathbf{F}_{B;i}(r_B, t)$  is given by

$$\mathbf{F}_{B;i}(r_B, t) = \mathbf{F}_{B;D}(r_B, t) + \mathbf{F}_{B;L}^{c;qs}(r_B, t) + \mathbf{F}_{B;L}^{\alpha;qs}(r_B, t) + \mathbf{F}_{B;I}(r_B, t). \quad (3.17)$$

### 3.2.4. HISTORY-DEPENDENT LIFT FORCE MODEL

To assess the history dependency of the aerodynamic interaction, a non-stationary flow analysis is required, as addressed in Section 2.3. In the time-domain, the non-stationary bound circulation  $\Gamma_{B;b}^{ns}(r_B, t)$  can be calculated with the application of the indicial Wagner's and Küssner's functions, the former of which being applicable for aerofoils oscillating in heave and pitch and the latter for variations in the lateral inflow velocity. For a description of these functions, reference is made to Sections 2.3.5 and 2.3.6

The bound circulation can again be separated into a camber-dependent and an  $\alpha$ -dependent contribution:

$$\Gamma_{B;b}^{ns}(r_B, t) = \Gamma_{B;b}^{c;ns}(r_B, t) + \Gamma_{B;b}^{\alpha;ns}(r_B, t), \quad (3.18)$$

where the camber-dependent contribution is equal to the camber-dependent bound circulation of the quasi-stationary lift force:

$$\Gamma_{B;b}^{c;ns}(r_B, t) = \Gamma_{B;b}^{c;qs}(r_B, t) = \Gamma_{B;b}^c(r_B, t). \quad (3.19)$$

With the application of the Wagner's function, in correspondence with [215], the  $\alpha$ -dependent non-stationary bound circulatory flow for arbitrary variations in the lateral inflow can then be derived from

$$\Gamma_{B;b}^{\alpha;ns}(r, \tau) = \frac{1}{2} c_B(r_B) C_{B;L}^\alpha(r_B) \left\{ \Phi_W(r_B, \tau) W_{B;\text{rel};y}(r_B, 0) + \int_0^\tau \Phi_W(r_B, \tau - \tilde{\tau}) \frac{\partial W_{B;\text{rel};y}(r, \tilde{\tau})}{\partial \tilde{\tau}} d\tilde{\tau} \right\} \mathbf{e}_{B;r}, \quad (3.20)$$

expressed in terms of the non-dimensional time  $\tau = \frac{2}{c_B(r_B)} \int_0^t |\mathbf{W}_{B;\text{rel}}(r_B, t)| dt$ , and with  $\Phi_W(r_B, \tau)$  representing the Wagner's function.  $W_{B;y}(r_B, t)$  is the relative downwash, or the relative flow velocity in the local  $y_B$  direction:

$$W_{B;\text{rel};y}(r_B, t) = \{\bar{\boldsymbol{\beta}}_B(r_B)\}^T \mathbf{W}_{B;\text{rel}}(r_B, t), \quad (3.21)$$

where

$$\bar{\boldsymbol{\beta}}_B(r_B) = [0 \quad \cos(\beta_B^0(r_B) + \bar{\beta}_B) \quad -\sin(\beta_B^0(r_B) + \bar{\beta}_B)]^T. \quad (3.22)$$

Were blade pitching and torsion accounted for, the relative downwash would have to be determined at the three-quarter chord point. Alternatively, the relative downwash can be expressed in terms of the instantaneous angle of attack and the magnitude of the relative inflow velocity:

$$\sin(\alpha_B^{\text{qs}}(r_B, t)) = \frac{W_{B;\text{rel};y}(r_B, t)}{|\mathbf{W}_{B;\text{rel}}(r_B, t)|}. \quad (3.23)$$

For thin plates, the Wagner's function can be approximated with a double time-lag function [212]:

$$\Phi_W(r_B, \tau) \approx 1 - \sum_{i=1}^2 \Psi_{W;i}(r_B) e^{-\eta_{W;i}(r_B)\tau}, \quad (3.24)$$

for  $\tau \geq 0$ .  $\Psi_{W;i}(r_B)$  and  $\eta_{W;i}(r_B)$  are aspect-ratio dependent coefficients, accounting for both low- and high-frequency flow separation effects [221].

The term within curly brackets of Eq. (3.20) is referred to as effective downwash. After some mathematical manipulations and inclusion of Eq. (3.24), the non-stationary bound circulation can be rewritten as

$$\boldsymbol{\Gamma}_{B;b}^{\alpha;\text{ns}}(r_B, t) = \frac{1}{2} c_B(r_B) C_{B;L}^\alpha(r_B) \sin(\alpha_B^{\text{ns}}(r_B, t)) |\mathbf{W}_{B;\text{rel}}(r_B, t)| \mathbf{e}_{B;r}, \quad (3.25)$$

where the non-stationary angle of attack is obtained from

$$\sin(\alpha_B^{\text{ns}}(r_B, t)) = \left(1 - \Psi_{W;1}(r_B) - \Psi_{W;2}(r_B)\right) \sin(\alpha_B^{\text{qs}}(r_B, t)) + \zeta_{W;1}(r_B, t) + \zeta_{W;2}(r_B, t), \quad (3.26)$$

with the aerodynamic states  $\zeta_{W;i}(r_B, t)$ . The aerodynamic states  $\zeta_i(r_B, t)$  can be obtained from two first-order differential equations [219]:

$$\begin{aligned} \dot{\zeta}_{W;i}(r_B, t) + \frac{2}{c_B(r_B)} |\mathbf{W}_{B;\text{rel}}(r_B, t)| \left( \frac{c_B(r_B)}{2} \frac{\partial}{\partial t} \left( \frac{|\mathbf{W}_{B;\text{rel}}(r_B, t)|}{|\mathbf{W}_{B;\text{rel}}(r_B, t)|^2} + \eta_{W;i}(r_B) \right) \zeta_{W;i}(r_B, t) = \right. \\ \left. \frac{2}{c_B(r_B)} \eta_{W;i}(r_B) \Psi_{W;i}(r_B) |\mathbf{W}_{B;\text{rel}}(r_B, t)| \sin(\alpha_B^{\text{qs}}(r_B, t)), \right. \end{aligned} \quad (3.27)$$

for  $i = 1, 2$ . On this basis, the history-dependent lift force  $\mathbf{F}_{B;L}^{\text{ns}}(r, t)$  is obtained from

$$\mathbf{F}_{B;L}^{\text{ns}}(r_B, t) = \rho_{\text{air}} \left( \mathbf{W}_{B;\text{rel}}(r_B, t) \times \boldsymbol{\Gamma}_{B;b}^{\text{ns}}(r_B, t) \right). \quad (3.28)$$

The total history-dependent aerodynamic force  $\mathbf{F}_{B;u}(r_B, t)$  can now be composed as the superposition of  $\mathbf{F}_{B;D}(r_B, t)$ ,  $\mathbf{F}_{B;L}^c(r_B, t)$ ,  $\mathbf{F}_{B;L}^{\alpha;\text{ns}}(r_B, t)$  and  $\mathbf{F}_{B;i}(r_B, t)$ :

$$\mathbf{F}_{B;u}(r_B, t) = \mathbf{F}_{B;D}(r_B, t) + \mathbf{F}_{B;L}^c(r_B, t) + \mathbf{F}_{B;L}^{\alpha;\text{ns}}(r_B, t) + \mathbf{F}_{B;i}(r_B, t). \quad (3.29)$$

### 3.2.5. CONSTITUENTS OF THE AIR FLOW VECTOR

The vector  $\mathbf{W}_{B;\text{rel}}(r_B, t)$  can be thought of as a summation of vectors:

$$\begin{aligned} \mathbf{W}_{B;\text{rel}}(r_B, t) &= \mathbf{w}_B(r_B, t) - \mathbf{v}_B(r_B, t) \\ &= \begin{bmatrix} w_{B;r}(t) \\ w_{B;Y}(t) \\ w_{B;Z}(t) \end{bmatrix} + \begin{bmatrix} \bar{\Omega}_{R;Y} u_{B;Z}(r_B, t) \\ 0 \\ \bar{\Omega}_{R;Y} r_B \end{bmatrix} - \begin{bmatrix} 0 \\ \dot{u}_{B;Y}(r_B, t) \\ \dot{u}_{B;Z}(r_B, t) \end{bmatrix}, \end{aligned} \quad (3.30)$$

where the entries in the  $r_B$  direction are disregarded, as the aerodynamic forcing is described in the cross-sectional plane only.

The vector  $\mathbf{v}_B(r_B, t)$  is given by Eq. (3.5), and includes the rotational velocity and the time derivative of  $\mathbf{u}_B(r_B, t)$ . By inclusion of this response term, the dependency of the aerodynamic forces on the structural response, and thus the aerodynamic interaction, is explicitly accounted for.

The drag and lift force vectors contain the absolute value of the relative inflow vector  $|\mathbf{W}_{B;\text{rel}}(r_B, t)|$ , which can be expressed as:

$$|\mathbf{W}_{B;\text{rel}}(r_B, t)| = \sqrt{(W_{B;\text{rel};Y}(r_B, t))^2 + (W_{B;\text{rel};Z}(r_B, t))^2}, \quad (3.31)$$

with

$$W_{B;\text{rel};Y}(r_B, t) = w_{B;Y}(r_B, t) - \dot{u}_{B;Y}(r_B, t), \quad (3.32)$$

and

$$W_{B;\text{rel};Z}(r_B, t) = \bar{\Omega}_{R;Y} r_B + w_{B;Z}(r_B, t) - \dot{u}_{B;Z}(r_B, t). \quad (3.33)$$

The lift force vector contains the cross product  $\mathbf{e}_{B;r} \times \mathbf{W}(r_B, t)$ :

$$\mathbf{W}_{B;\text{rel}}(r_B, t) \times \mathbf{e}_{B;r} = \begin{bmatrix} 0 \\ W_{B;\text{rel};Y}(r_B, t) \\ W_{B;\text{rel};Z}(r_B, t) \end{bmatrix} \times \begin{bmatrix} 1 \\ 0 \\ 0 \end{bmatrix} = \begin{bmatrix} 0 \\ W_{B;\text{rel};Z}(r_B, t) \\ -W_{B;\text{rel};Y}(r_B, t) \end{bmatrix}. \quad (3.34)$$

Since axial motion is not accounted for and the aerodynamic analysis is limited to two-dimensional flows, this  $r_B$  component is omitted in the remainder of this chapter.

With reference to Eq. (3.16), the apparent inertia force depends on the relative acceleration of the air flow  $\dot{\mathbf{W}}_{B;\text{rel}}(r_B, t)$ , which can be decomposed into

$$\dot{\mathbf{W}}_{B;\text{rel}}(r_B, t) = \dot{\mathbf{w}}_B(r_B, t) - \dot{\mathbf{v}}_B(r_B, t). \quad (3.35)$$

Eqs. (3.31), (3.34), and (3.35) clearly show the dependency of the aerodynamic excitation on the structural response velocity and acceleration. Furthermore, it can be concluded that the in-plane and out-of-plane motions are coupled aerodynamically. This response dependency of the aerodynamic forcing and the associated motion coupling, representing the aerodynamic interaction, are non-linear.

In Section 3.3.1, the aerodynamic forces are linearized under the assumption of small structural motion. These linearized forces will be expressed in terms of the effective

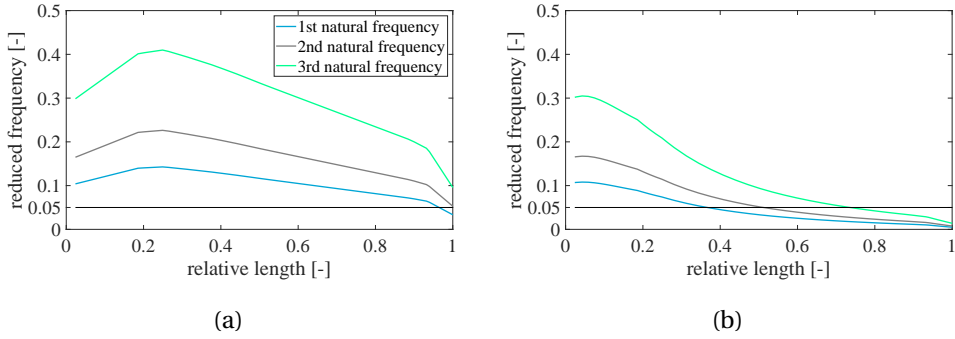


Figure 3.4: Reduced frequencies as functions of the relative blade length (a) for a stand-still blade (scenario i), and (b) for a rotating blade (scenario ii). The black lines represent the transition from a quasi-instantaneous aerodynamic force to a history-dependent aerodynamic force.

incident air flow  $W_{B;\text{eff}}(t)$ , which accounts for the wind speed and the rotational speed only:

$$\mathbf{W}_{B;\text{eff}}(r_B, t) = \begin{bmatrix} w_{B;Y}(r_B, t) \\ w_{B;Z}(r_B, t) \end{bmatrix} + \begin{bmatrix} 0 \\ \bar{\Omega}_{R;Y} r_B \end{bmatrix}, \quad (3.36)$$

consisting of components in the  $Y_B$  and the  $Z_B$  directions only.

### 3.2.6. REDUCED-FREQUENCY ASSESSMENT

The instantaneous lift force model can be assumed to be valid for reduced frequencies in the range  $0 \leq k(r_B) \leq 0.05$  [182]. If  $k(r_B) \geq 0.05$ , the interaction should be considered history-dependent and for  $k(r_B) \geq 0.2$ , a high degree of history dependency can be assumed, implying that a non-stationary lift force model should be adopted. Figure 3.4 presents the reduced frequencies as a function of the relative position along the blade for a stand-still blade (scenario i, see Figure 3.4(a)) and a rotating blade (scenario ii, see Figure 3.4(b)). The effective incident velocity is determined on the basis of Eq. (3.36), with a constant wind velocity of 11.4 m/s and the rotational velocity  $\bar{\Omega}_{R;Y}$  in correspondence with Table 3.1. As oscillation frequencies, the first three natural frequencies as derived in Section 3.1.4 are adopted.

The reduced frequency is larger for higher oscillation frequencies and smaller effective velocities. This can clearly be seen in Figure 3.4, which shows the stand-still blade (scenario i) to give higher reduced frequency values than the rotating blade (scenario ii). Apart from that, the third natural frequency oscillations show the highest values.

According to the definition of history dependency, the aerodynamic interaction of the standstill blade (scenario i) can be expected to be history-dependent or highly history-dependent, depending on the actual frequency of oscillation. The rotating blade (scenario ii), on the other hand, shows a more mixed picture. Towards the centre of rotation, where the velocity due to rotation is relatively low, the interaction is bound to be history-dependent, whereas towards the blade tip, the airflow velocity increases and the

interaction is more quasi-instantaneous. Whether the interaction of the blade is dominated by instantaneous or history-dependent aerodynamics cannot be concluded on the basis of Figure 3.4 only. Besides, the reduced frequency as defined by Eq. (2.56) cannot be expected to define the history dependency of the interaction accurately. The influence of the structural motion, for instance, is not accounted for in the airflow velocity.

### 3.3. ANALYSIS PROCEDURE

#### 3.3.1. AERODYNAMIC FORCE LINEARIZATION

In Section 3.1, the equations of motion of a rotating blade with a varying twist were derived. Subsequently, in Section 3.2, two non-linear aerodynamic models were defined, both accounting for the influence of the structural response. The resulting system consists of two coupled non-linear fourth-order partial differential equations describing the structural motion:

$$\mathbf{M}_B(r_B)\ddot{\mathbf{u}}_B(r_B, t) + \mathbf{K}_B(r_B)\mathbf{u}_B(r_B, t) = \mathbf{F}_B(r_B, t), \quad (3.37)$$

where the forcing vector  $\mathbf{F}_B(r_B, t)$  represents either the instantaneous model  $\mathbf{F}_{B;i}(r_B, t)$  or the history-dependent model  $\mathbf{F}_{B;u}(r_B, t)$ . The latter forcing depends on two aerodynamic states, which are defined by two first-order differential equations, non-linearly coupled with the structural response.

One objective of this study is to identify the significance of the non-linearity of the coupled dynamic system. For this reason, a linearized representation of the forcing equations is derived in this section. A comparison of the structural response to the linearized and the non-linear aerodynamic interaction, presented in Section 3.4, provides insight in the non-linear forcing contributions. The non-linear forcing is linearized with the help of the Taylor series expansion. The forcing expressions are expanded into first-order polynomials. In this regard, the state vectors  $\mathbf{S}_B^{\text{qs}}(t)$  and  $\mathbf{S}_B^{\text{ns}}(t)$  are defined:

$$\mathbf{S}_B^{\text{qs}}(t) = [\{\mathbf{u}_B(t)\}^T \quad \{\dot{\mathbf{u}}_B(t)\}^T \quad \{\ddot{\mathbf{u}}_B(t)\}^T \quad \{\dot{\mathbf{w}}_B(t)\}^T \quad \{\ddot{\mathbf{w}}_B(t)\}^T], \quad (3.38)$$

and

$$\mathbf{S}_B^{\text{ns}}(t) = [\mathbf{S}_B^{\text{qs}}(r_B, t) \quad \zeta_{W;1}(r_B, t) \quad \zeta_{W;2}(t)]. \quad (3.39)$$

The linearization is done with respect to the mean states  $\bar{\mathbf{S}}_B$ , for either the quasi-stationary or the non-stationary forcing, which are defined as:

$$\bar{\mathbf{S}}_B = \{\mathbf{S}_B^{\text{qs}}(t) = \bar{\mathbf{S}}_B^{\text{qs}}\}, \quad (3.40)$$

or

$$\bar{\mathbf{S}}_B = \{\mathbf{S}_B^{\text{ns}}(r_B, t) = \bar{\mathbf{S}}_B^{\text{ns}}(r_B)\}. \quad (3.41)$$

The aerodynamic forcing can now be expressed in terms of the deviations of the structural motion and the wind speed,  $\Delta\mathbf{u}_B(t)$  and  $\Delta\mathbf{w}_B(t)$ , with respect to the means,  $\bar{u}_B(t)$  and  $\bar{w}_B(t)$ . By adopting the time-varying wind speed and its time derivative as Taylor variables as well, the Taylor expansion is developed with respect to the mean operational conditions,

for which the mean rotational speed and pitch angle can be defined. As a consequence, the force coefficients are time-independent. Furthermore, the force expressions can easily be used to investigate the response to specific deviations of the mean conditions, for instance a step excitation or a turbulence that relates to a mean wind speed. These benefits come with a loss of accuracy of the force approximations.

The linearized approximation of the drag force model can be expressed in terms of the perturbations  $\Delta \mathbf{u}_B(t)$  and  $\Delta \mathbf{w}_B(t)$ :

$$\mathbf{F}_{B;D}(r_B, t) \approx \left[ \mathbf{F}_{B;D}(r_B, t) \right]_{\bar{s}_B} + \left[ \frac{\partial \mathbf{F}_{B;D}(r_B, t)}{\partial \{\dot{\mathbf{u}}_B(t)\}} \right]_{\bar{s}_B} \Delta \dot{\mathbf{u}}_B(t) + \left[ \frac{\partial \mathbf{F}_{B;D}(r_B, t)}{\partial \{\mathbf{w}_B(t)\}} \right]_{\bar{s}_B} \Delta \mathbf{w}_B(t). \quad (3.42)$$

The first term on the right hand side of this drag force approximation represents the mean force component, which is obtained as

$$\mathbf{F}_{B;D}(r_B, t) \Big|_{\bar{s}_B} = \frac{1}{2} \rho_{\text{air}} c_B(r_B) C_{B;D}(r_B) |\bar{\mathbf{W}}_{B;\text{eff}}(r_B)| \begin{bmatrix} \bar{w}_{B;Y}(r_B) \\ \bar{w}_{B;Z}(r_B) + \bar{\Omega}_{R;Y} r_B \end{bmatrix}. \quad (3.43)$$

The mean flow velocity in the local  $Z_B$  direction, which rotates around the  $Y_R$  axis, could represent the tangentially induced velocity field.

The linear dependencies on the structural motion and the wind speed variation are expressed as

$$\begin{aligned} \left[ \frac{\partial \mathbf{F}_{D;B}(r_B, t)}{\partial \{\dot{\mathbf{u}}_B(t)\}} \right]_{\bar{s}_B} &= - \left[ \frac{\partial \mathbf{F}_{D;B}(r_B, t)}{\partial \{\mathbf{w}_B(t)\}} \right]_{\bar{s}_B} = \\ &= - \frac{1}{2} \rho_{\text{air}} c_B(r_B) C_{B;D}(r_B) |\bar{\mathbf{W}}_{B;\text{eff}}(r_B, t)| \begin{bmatrix} \left( \frac{(\bar{w}_{B;Z}(r_B) + \bar{\Omega}_{R;Y} r_B)^2}{|\bar{\mathbf{W}}_{B;\text{eff}}(r_B)|^2} + 1 \right) \frac{(\bar{w}_{B;Z}(r_B) + \bar{\Omega}_{R;Y} r_B) \bar{w}_{B;Y}(r_B)}{|\bar{\mathbf{W}}_{B;\text{eff}}(r_B)|^2} \\ \frac{(\bar{w}_{B;Z}(r_B) + \bar{\Omega}_{R;Y} r_B) \bar{w}_{B;Y}(r_B)}{|\bar{\mathbf{W}}_{B;\text{eff}}(r_B)|^2} \left( \frac{(\bar{w}_{B;Z}(r_B) + \bar{\Omega}_{R;Y} r_B)^2}{|\bar{\mathbf{W}}_{B;\text{eff}}(r_B)|^2} + 1 \right) \end{bmatrix}. \end{aligned} \quad (3.44)$$

The matrices expressing the linear dependency on the structural velocity and the wind speed fluctuation are equal, but of different sign.

The lift force was separated into a camber-dependent and an  $\alpha$ -dependent component. Considering first the former, the linearized expression can be written as

$$\mathbf{F}_{B;L}^c(r_B, t) \approx \left[ \mathbf{F}_{B;L}^c(r_B, t) \right]_{\bar{s}_B} + \left[ \frac{\partial \mathbf{F}_{B;L}^c(r_B, t)}{\partial \{\dot{\mathbf{u}}_B(t)\}} \right]_{\bar{s}_B} \Delta \dot{\mathbf{u}}_B(t) + \left[ \frac{\partial \mathbf{F}_{B;L}^c(r_B, t)}{\partial \{\mathbf{w}_B(t)\}} \right]_{\bar{s}_B} \Delta \mathbf{w}_B(t), \quad (3.45)$$

the mean force component of which is obtained as

$$\mathbf{F}_{B;L}^c(r_B, t) \Big|_{\bar{s}_B} = \frac{1}{2} \rho_{\text{air}} c_B(r_B) C_{B;L}^c(r_B) |\bar{\mathbf{W}}_{B;\text{eff}}(r_B)| \begin{bmatrix} (\bar{w}_{B;Z}(r_B) + \bar{\Omega}_{R;Y} r_B) \\ -\bar{w}_{B;Y}(r_B) \end{bmatrix}. \quad (3.46)$$

The following matrices express the linear dependency of the camber-dependent lift force

on the structural motion and the wind speed variation:

$$\left[ \frac{\partial \mathbf{F}_{B;L}^c(r_B, t)}{\partial \{\dot{\mathbf{u}}_B(t)\}} \Big|_{\bar{s}_B} \right] = - \left[ \frac{\partial \mathbf{F}_{B;L}^c(r_B, t)}{\partial \{\dot{\mathbf{w}}_B(t)\}} \Big|_{\bar{s}_B} \right] = - \frac{1}{2} \rho_{\text{air}} c_B(r_B) C_{B;L}^c(r_B) |\bar{\mathbf{W}}_{B;\text{eff}}(r_B)| \begin{bmatrix} \frac{(\bar{w}_{B;Z}(r_B) + \bar{\Omega}_{R;Y} r_B) \bar{w}_{B;Y}(r_B)}{|\bar{\mathbf{W}}_{B;\text{eff}}(r_B)|^2} & \left( \frac{(\bar{w}_{B;Z}(r_B) + \bar{\Omega}_{R;Y} r_B)^2}{|\bar{\mathbf{W}}_{B;\text{eff}}(r_B)|^2} + 1 \right) \\ - \left( \frac{(\bar{w}_{B;Z}(r_B) + \bar{\Omega}_{R;Y} r_B)^2}{|\bar{\mathbf{W}}_{B;\text{eff}}(r_B)|^2} + 1 \right) & - \frac{(\bar{w}_{B;Z}(r_B) + \bar{\Omega}_{R;Y} r_B) \bar{w}_{B;Y}(r_B)}{|\bar{\mathbf{W}}_{B;\text{eff}}(r_B)|^2} \end{bmatrix}. \quad (3.47)$$

With the application of the mean state of Eq. (3.40), the  $\alpha$ -dependent lift force is approximated as

$$\mathbf{F}_{B;L}^{\alpha;\text{qs}}(r_B, t) \approx \left[ \mathbf{F}_{B;L}^{\alpha;\text{qs}}(r_B, t) \Big|_{\bar{s}_B} \right] + \left[ \frac{\partial \mathbf{F}_{B;L}^{\alpha;\text{qs}}(r_B, t)}{\partial \{\dot{\mathbf{u}}_B(t)\}} \Big|_{\bar{s}_B} \right] \Delta \dot{\mathbf{u}}_B(t) + \left[ \frac{\partial \mathbf{F}_{B;L}^{\alpha;\text{qs}}(r_B, t)}{\partial \{\dot{\mathbf{w}}_B(t)\}} \Big|_{\bar{s}_B} \right] \Delta \dot{\mathbf{w}}_B(t) \quad (3.48)$$

the mean force component of which is obtained as

$$\mathbf{F}_{B;L}^{\alpha;\text{qs}}(r_B, t) \Big|_{\bar{s}_B} = \frac{1}{2} \rho_{\text{air}} c_B(r_B) C_{B;L}^\alpha(r_B) \bar{W}_{B;\text{eff};y}(r_B) \begin{bmatrix} \bar{w}_{B;Z}(r_B) + \bar{\Omega}_{R;Y} r_B \\ -\bar{w}_{B;Y}(r_B) \end{bmatrix}, \quad (3.49)$$

and the dependency on the structural motion and the wind speed variation is expressed as

$$\left[ \frac{\partial \mathbf{F}_{B;L}^{\alpha;\text{qs}}(r_B, t)}{\partial \{\dot{\mathbf{u}}_B(t)\}} \Big|_{\bar{s}_B} \right] = - \left[ \frac{\partial \mathbf{F}_{B;L}^{\alpha;\text{qs}}(r_B, t)}{\partial \{\dot{\mathbf{w}}_B(t)\}} \Big|_{\bar{s}_B} \right] = - \frac{1}{2} \rho_{\text{air}} c_B(r_B) C_{B;L}^\alpha(r_B) \bar{W}_{B;\text{eff};y}(r_B) \cdot \begin{bmatrix} \frac{(\bar{w}_{B;Z}(r_B) + \bar{\Omega}_{R;Y} r_B)}{\bar{W}_{B;\text{eff};y}(r_B)} \cos(\beta_{B;0}(r_B) + \bar{\beta}_B) & 1 - \frac{(\bar{w}_{B;Z}(r_B) + \bar{\Omega}_{R;Y} r_B)}{\bar{W}_{B;\text{eff};y}(r_B)} \sin(\beta(r) + \beta_{B;0}) \\ -1 - \frac{\bar{w}_{B;Y}(r_B)}{\bar{W}_{B;\text{eff};y}(r_B)} \cos(\beta_{B;0}(r_B) + \bar{\beta}_B) & \frac{\bar{w}_{B;Y}(r_B)}{\bar{W}_{B;\text{eff};y}(r_B)} \sin(\beta_{B;0}(r_B) + \bar{\beta}_B) \end{bmatrix}. \quad (3.50)$$

The matrices that relate to the structural velocity constitute an added damping  $\mathbf{C}_{B;A}(r_B)$ . The combined added damping matrix from the drag and lift force approximations is obtained as:

$$\mathbf{C}_{B;A}(r_B) = - \left( \left[ \frac{\partial \mathbf{F}_{B;D}(r_B, t)}{\partial \{\dot{\mathbf{u}}_B(t)\}} \Big|_{\bar{s}_B} \right] + \left[ \frac{\partial \mathbf{F}_{B;L}^{\alpha;\text{qs}}(r_B, t)}{\partial \{\dot{\mathbf{u}}_B(t)\}} \Big|_{\bar{s}_B} \right] + \left[ \frac{\partial \mathbf{F}_{B;L}^{\alpha;\text{qs}}(r_B, t)}{\partial \{\dot{\mathbf{w}}_B(t)\}} \Big|_{\bar{s}_B} \right] \right). \quad (3.51)$$

Given that the drag coefficient  $C_{B;D}(r_B)$  is very small, the lift component gives the dominant contribution to the added damping. The matrix clearly illustrates the directional coupling of the structural motions through the aerodynamic forces. Moreover, it should be noted that the added damping resulting from the camber-dependent lift force consists of a negative entry on its diagonal, potentially inducing instability. The apparent inertia force of Eq. (3.16) was already expressed as a linear function of the wind and structural accelerations, implying that no further linearization steps are required to approximate this force.

The linear approximation of the non-stationary  $\alpha$ -dependent lift force can be expressed in terms of the quasi-stationary  $\alpha$ -dependent lift force and the aerodynamic



states  $\zeta_{W;1}(r_B, t)$  and  $\zeta_{W;2}(r_B, t)$ :

$$\begin{aligned} \mathbf{F}_{B;L}^{\alpha;ns}(r_B, t) &\approx \left(1 - \Psi_{W;1}(r_B) - \Psi_{W;2}(r_B)\right) \mathbf{F}_{B;L}^{\alpha;qs}(r_B, t) \\ &+ \left[ \frac{\partial \mathbf{F}_{B;L}^{\alpha;ns}(r_B, t)}{\partial \{\zeta_{W;1}(t)\}} \bigg|_{\bar{s}_B} \right] \zeta_{W;1}(r_B, t) + \left[ \frac{\partial \mathbf{F}_{B;L}^{\alpha;ns}(r_B, t)}{\partial \{\zeta_{W;2}(t)\}} \bigg|_{\bar{s}_B} \right] \zeta_{W;2}(r_B, t), \end{aligned} \quad (3.52)$$

where  $\mathbf{F}_{B;L}^{\alpha;qs}(r_B, t)$  is approximated in accordance Eq. (3.48) and the coefficients for the aerodynamic states can be expressed as

$$\left[ \frac{\partial \mathbf{F}_{B;L}^{\alpha;ns}(r_B, t)}{\partial \{\zeta_{W;1}(t)\}} \bigg|_{\bar{s}_B} \right] = \left[ \frac{\partial \mathbf{F}_{B;L}^{\alpha;ns}(r_B, t)}{\partial \{\zeta_{W;2}(t)\}} \bigg|_{\bar{s}_B} \right] = \frac{1}{2} \rho_{\text{air}} c_B(r_B) C_{B;L}^{\alpha}(r_B) |\bar{\mathbf{W}}_{B;\text{eff}}(r_B)| \begin{bmatrix} \bar{w}_{B;Z}(r_B) + \bar{\Omega}_{R;Y} r_B \\ -\bar{w}_{B;Y}(r_B) \end{bmatrix}. \quad (3.53)$$

The history-dependent lift force requires the time-dependent aerodynamic states as input. These states can be obtained from Eq. (3.27), which after linearization reduces to

$$\dot{\zeta}_{W;i}(r_B, t) + \frac{2}{c_B(r_B)} \eta_{W;i}(r_B) |\bar{\mathbf{W}}_{B;\text{eff}}(r_B)| \zeta_{W;i}(r_B, t) = \frac{2}{c_B(r_B)} \eta_{W;i}(r_B) \Psi_{W;i}(r_B) W_{B;y}(r_B, t). \quad (3.54)$$

With reference to Eqs. (3.24) and (3.54), it can be stated that for  $\eta_{W;i}(r_B) \rightarrow \infty$ , or  $\Psi_{W;i}(r_B) \rightarrow 0$  and  $\eta_{W;i}(r_B) \rightarrow 0$ , the equations of the history-dependent lift force model reduce to the equations of the instantaneous lift force model. For step excitations  $\Delta \mathbf{w}_B(r_B, t) = \Delta \mathbf{w}_B(r_B)$  for  $t > 0$  s, the linearized aerodynamic states reduce to the following steady states:

$$\lim_{t \rightarrow \infty} \zeta_{W;i}(r_B, t) = \Psi_{W;i}(r_B) \frac{W_{B;y}(r_B, t)}{|\bar{\mathbf{W}}_{B;\text{eff}}(r_B)|}. \quad (3.55)$$

Substitution of these aerodynamic states into Eq. (3.52), and using Eq. (3.21), gives

$$\begin{aligned} \lim_{t \rightarrow \infty} \mathbf{F}_{B;L}^{\alpha;ns}(r_B, t) \bigg|_{\bar{s}_B} &= \lim_{t \rightarrow \infty} \mathbf{F}_{B;L}^{\alpha;qs}(r_B, t) \bigg|_{\bar{s}_B} \\ &- \frac{1}{2} \rho_{\text{air}} c_B(r_B) C_{B;L}^{\alpha}(r_B) (\Psi_{W;1}(r_B) + \Psi_{W;2}(r_B)) \bar{W}_{B;Y}(r_B) \begin{bmatrix} \Delta w_{B;Z}(r_B) \\ -\Delta w_{B;Y}(r_B) \end{bmatrix}. \end{aligned} \quad (3.56)$$

The second term on the right hand side of Eq. (3.56) results from the linearization of the force models around the mean wind speed  $\bar{\mathbf{w}}_B(r_B)$ . As a result, the linearized quasi-stationary and non-stationary force models predict a difference between the steady-state forces resulting from a step excitation between the two linearized models. It can easily be demonstrated that for a step excitation the non-linear unsteady circulation (Eq. (3.25)) eventually reduces to the non-linear instantaneous circulation, Eq. (3.13), which should be the case, because a new stationary flow has developed. A similar analysis shows that the non-linear instantaneous lift force, Eq. (3.15), approaches its linearized expression, Eq. (3.48). Hence, it can already be concluded that in case of step excitations the linearized history-dependent lift force model will perform poorer than the other aerodynamic models.

### 3.3.2. GALERKIN DECOMPOSITION

The forcing vector  $\mathbf{F}_B(r_B, t)$  depends non-linearly on the time-dependent wind fluctuation vector  $\mathbf{w}_B(r_B, t)$ , the structural response velocity vector  $\dot{\mathbf{u}}_B(r_B, t)$  and the time derivatives of both. Moreover, the history-dependent model includes two aerodynamic state variables, which are governed by first-order time-variant differential equations that include the vectors  $\mathbf{w}_B(r_B, t)$  and  $\dot{\mathbf{u}}_B(r_B, t)$ . In order to analyze the aerodynamic interaction, the system of partial differential equations describing the continuous-space system is now reduced to a system of coupled ordinary differential equations by means of the Galerkin decomposition [148], which assumes that the response of the blade  $\mathbf{u}_B(r_B, t)$  can be expressed in terms of an infinite series of generalized coordinates  $q_{B;n}(t)$  associated with the admissible functions  $\mathbf{s}_{B;n}(r_B)$ :

$$\mathbf{u}_B(r_B, t) = \sum_{n=1}^{\infty} \mathbf{s}_{B;n}(r_B) q_{B;n}(t), \quad (3.57)$$

where  $\mathbf{s}_{B;n}(r_B)$  is a vector consisting of the  $n$ -th admissible function components  $s_{B;Y;n}(r_B)$  and  $s_{B;Z;n}(r_B)$  [246]. The Galerkin decomposition requires the admissible functions to be differentiable to the order of the differential equations, and to satisfy the boundary conditions of the system. These requirements are fulfilled by the modes  $\mathbf{u}_{B;n}(r_B)$  of the homogeneous system of equations, see Eq. (3.6) and Section 3.1.4, which moreover are orthogonal with respect to the mass matrix  $\mathbf{M}_B(r_B)$  and the operator matrix  $\mathbf{K}_B(r_B)$ . Therefore, adopting these modes as admissible functions allows for the diagonalizing of the  $\mathbf{M}_B(r_B)$  and  $\mathbf{K}_B(r_B)$  matrices. These modes, however, do not allow for the full decoupling of system of equations of motions, because of the response dependency of the aerodynamic excitation vector  $\mathbf{F}_B(r_B, t)$ .

Practical application of Eq. (3.57) requires truncation after a finite number of generalized coordinates  $N$ . The  $n$ -th equation of the system of ordinary differential equations can be obtained by substituting Eq. (3.57) into Eq. (3.37):

$$\sum_{n=1}^N \mathbf{M}_B(r_B) \mathbf{u}_{B;n}(r_B) \ddot{q}_{B;n}(t) + \sum_{n=1}^N \mathbf{K}_B(r_B) \mathbf{u}_{B;n}(r_B) q_{B;n}(t) \approx \mathbf{F}_B(r_B, t). \quad (3.58)$$

After premultiplication with  $\{\mathbf{u}_{B;m}(r_B)\}^T$  and integration over the length of the blade, the  $m$ -th equation reads:

$$\begin{aligned} \sum_{n=1}^N \int_{r_H}^R \left[ \{\mathbf{u}_{B;m}(r_B)\}^T \mathbf{M}_B(r_B) \mathbf{u}_{B;n}(r_B) \ddot{q}_{B;n}(t) + \{\mathbf{u}_{B;m}(r_B)\}^T \mathbf{K}_B(r_B) \mathbf{u}_{B;n}(r_B) q_{B;n}(t) \right] dr_B \approx \\ \sum_{n=1}^N \int_{r_H}^R \{\mathbf{u}_{B;m}(r_B)\}^T \mathbf{F}_B(r_B, t) dr_B. \end{aligned} \quad (3.59)$$

Given that the modes are mass-normalized, the modal components of Eq. (3.59) can as follows be decoupled on the basis of the orthogonality relations:

$$\int_{r_H}^R \{\mathbf{u}_{B;m}(r_B)\}^T \mathbf{M}_B(r_B) \mathbf{u}_{B;n}(r_B) dr_B = \delta_{mn}. \quad (3.60)$$

$$\int_{r_H}^R \{\mathbf{u}_{B;m}(r_B)\}^T \mathbf{K}_B(r_B) \mathbf{u}_{B;n}(r_B) dr_B = \omega_{B;n}^2 \delta_{mn}, \quad (3.61)$$

with the Kronecker delta  $\delta_{mn}$ . The right-hand sides, however, remain coupled:

$$\int_{r_H}^R \{\mathbf{u}_{B;m}(r_B)\}^T \mathbf{F}_B(r_B, t) dr_B = \int_{r_H}^R \{u_{B;Y;m}(r_B) F_{B;Y}(r, t) + u_{B;Z;m}(r) F_{B;Z}(r_B, t)\} dr_B, \quad (3.62)$$

where it should be noted that the total structural response  $\mathbf{u}_B(r_B, t)$  is embedded in both the forcing vector  $\mathbf{F}_B(r_B, t)$  and the aerodynamic states  $\zeta_{W;1}(r_B, t)$  and  $\zeta_{W;2}(r_B, t)$  as well.

### 3.3.3. FLUCTUATING WIND

In Section 3.4, the aerodynamic interaction of the blade will first be assessed by means of frequency-response functions. Subsequently, the structural response to fluctuating wind signals will be analyzed, which allows for a comparison of the non-linear and the linearized aerodynamic models. This analysis requires fluctuating wind signals, which are derived in this section.

Determining the energy distribution of a turbulent wind field disturbed by a rotating blade is a field of research on its own. The ambient wind field can be expressed in terms of auto- and cross-spectra, which define the energy distribution over the turbulence frequencies and which can be obtained from literature. These spectra allow for the definition of a time-dependent wind field within the fixed global frame of reference. For the analysis of the rotating blade, however, wind data as experienced by the blade is required. On the basis of rotational sampling, turbulence spectra applicable for the rotating frame of reference can be derived [256, 257]. Apart from the turbulence being homogeneous and isotropic, this technique assumes the wind field to obey Taylor's frozen turbulence hypothesis. Moreover, it does not account for the so-called induced velocity and the distortion of the wind field due to the presence of the blade.

For this study, some important simplifications are adopted. First of all, to define the fluctuating wind signals, the input vector  $\Delta \mathbf{w}_B(r_B, t)$  is separated in time and space:

$$\Delta \mathbf{w}_B(r_B, t) = \mathbf{S}_{B;w}(r_B) \mathbf{v}_B(t), \quad (3.63)$$

where  $\mathbf{S}_{B;w}(r_B)$  is a space-dependent diagonal matrix containing the shape functions  $S_{B;w;Y}(r_B)$  and  $S_{B;w;Z}(r_B)$ .  $\mathbf{v}_B(t)$  is a time-dependent vector consisting of the turbulence signals  $v_{B;Y}(t)$  and  $v_{B;Z}(t)$ , representing the in-plane and out-of-plane components of the excitation, respectively. The shape functions define the distribution of the fully coherent fluctuating wind signals over the length of the blade. One-point time signals for the fluctuating wind are derived in the global fixed reference frame (see Figure 3.1) from one-sided Kaimal turbulence spectra that depend on the frequency  $f$  in Hz [35]:

$$S_{R;YY}(f) = 4\sigma_{R;Y}^2 \frac{L_{R;Y}}{W_{R;Y}} \left(1 + 6f \frac{L_{R;Y}}{W_{R;Y}}\right)^{-\frac{5}{3}}, \quad (3.64)$$

and

$$S_{R;XX}(f) = 4\sigma_{R;X}^2 \frac{L_{R;X}}{W_{R;Y}} \left(1 + 6f \frac{L_{R;X}}{W_{R;Y}}\right)^{-\frac{5}{3}}. \quad (3.65)$$

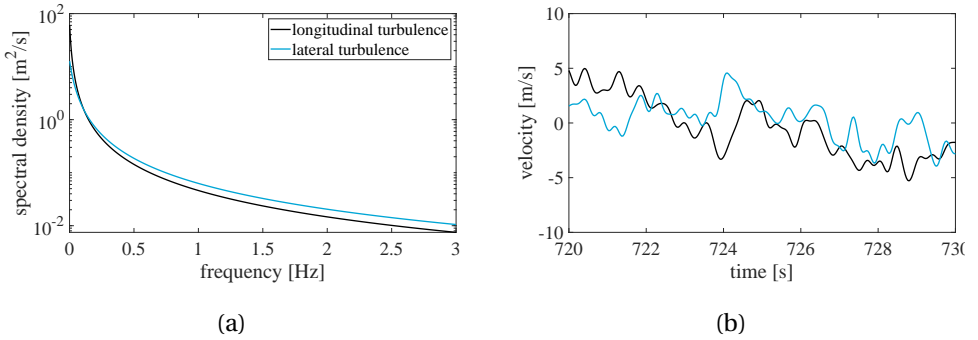


Figure 3.5: (a) Kaimal spectra for longitudinal and lateral turbulence, and (b) time frames of wind turbulence signals in longitudinal and lateral direction.

Here, it is assumed that the mean wind acts in the longitudinal  $Y_R$  direction, so that the mean velocity in the lateral  $X_R$  direction equals zero.  $\sigma_{R;Y}$  and  $\sigma_{R;X}$  represent the standard deviations of the turbulent wind velocity, and  $L_{R;Y}$  and  $L_{R;X}$  are turbulent length scales. Figure 3.5(a) visualizes these spectra for a mean wind velocity of 11.4 m/s, turbulence intensities of 10% and 8% in  $Y_R$  and  $X_R$  directions, respectively, and the following turbulence length scales:  $L_{R;Y} = 150$  m and  $L_{R;X} = 0.3L_{R;Y}$ . Moreover, it should be noted that the Kaimal spectra as defined by Eqs. (3.64) and (3.65) are valid only for frequencies larger than 0.02 Hz.

From these spectra, time signals are obtained by following a procedure described in [258], assuming independent random phase angle distributions in both directions. A time window of 10 s out of the turbulence signals with a total length of 1092 s is presented in Figure 3.5(b). Hereto, a cut-off frequency of 3.0 Hz and time steps of approximately 0.03 s were adopted. The time signals are applied for the analysis of both the stand-still blade (scenario i) and the rotating blade (scenario ii). In Section 3.2.5, it was explained that a correct analysis requires the rotational sampling of the turbulence spectra for generating the turbulence signals as experienced by the blade. Here, it is assumed that the  $Y_R$  wind turbulence represents the experienced turbulence in  $Y_B$  direction and the  $X_R$  turbulence the turbulence experienced in the rotating  $X_B$  direction. For a stand-still blade, pointing upwards, this assumption represents reality quite well, but for the rotating blade the frequency content of the experienced turbulence will be different. For instance, in the  $Y_R$  direction, the low-frequency energy content will diminish and be distributed over a sequence of peaks at each integer multiplication of the rotational frequency  $\Omega_{R;Y}$ . With respect to the spatial dependency of the turbulence, uniform distributions for  $S_{B;w;X}(r_B)$  and  $S_{B;w;Y}(r_B)$  are adopted.

It should be noted that with the direct derivation of the turbulent wind fields acting on the blade from the Kaimal spectra, the rotor-induced wind velocity is not accounted for. As a consequence, wind velocity acting on the blade of a rotating rotor is somewhat overestimated. Regarding the choice for the force fluctuations resulting from wind shear or tower shadowing could have been chosen for the analysis, alternatively. These sources of

aerodynamic excitation, however, only apply for the rotating blade. In order to compare the response from both scenarios, it was decided to apply the fluctuating wind signals, mimicking an ambient turbulence field.

## 3.4. RESULTS AND DISCUSSION

### 3.4.1. LINEARIZED INSTANTANEOUS AERODYNAMIC FORCING

In the following, the frequency response of the linearized models is analyzed, to visualize the differences in response to the instantaneous and the history-dependent force models, and to assess the coupling of the generalized coordinates and the relevance of the added damping. This analysis is elaborated on for both the stand-still blade (scenario i) and the rotating blade (scenario ii). Subsequently, the fully non-linear models are analyzed on the basis of the fluctuating wind signals in Section 3.4.3, where the level of non-linearity is assessed, as well as the the difference in response of the instantaneous and the history-dependent force models. In all analyses, a structural damping is added in the form of modal damping, accounting for 1.0% of the critical damping per considered mode (or generalized coordinate). Besides, all calculations employ a 48 node discretization of the blade, allowing the full application of the blade definition as given in [172].

Using the linearized equations for the instantaneous aerodynamic force model, the frequency responses for the two operational scenarios are determined. To this end, a drag coefficient of 0.01 is adopted. Regarding lift, the blade is assumed to be symmetric, i.e.,  $C_{B;L}^c(r_B) = 0$ . The angle of attack-dependent slope of the coefficient is defined in accordance with the thin aerofoil theory, implying that  $C_{B;L}^a(r_B) = \sin(\alpha_B(r_B, t))$ . For the air density a value of  $1.25 \text{ kg/m}^3$  is taken. The frequency response is derived on the basis of the harmonic inputs of either  $v_{B;Y}(t) = e^{2\pi i f t}$ , or  $v_{B;Z}(t) = e^{2\pi i f t}$ .

Figure 3.6 presents the amplitude of the blade tip deflection for the stand-still scenario (scenario i) – with Figures 3.6(a) and (b) representing the in-plane and out-of-plane deflections, respectively – and the rotating scenario (scenario ii) – where Figures 3.6(c) and (d), respectively, represent the in-plane and out-of-plane deflections. Each graph presents the amplitude of the displacement to both in-plane and out-of-plane excitation. This allows for assessing the extent of the coupling between the in-plane and out-of-plane motions of the blade. Furthermore, the dotted lines indicate the structural response in absence of the aerodynamic interaction, i.e., without added damping and modal coupling, resulting in a response that is independent of the structural motion.

Starting with the dotted lines, three peaks can be distinguished. These peaks correspond with the natural frequencies as identified in Section 3.1.4. In that section, it was also shown that for the stand-still blade (scenario i), the modal amplitudes of the first and third modes have the largest component in the in-plane direction, while the second mode is mostly pronounced in the out-of-plane direction. This observation is confirmed by the frequency-response graphs, where the opposite relation between the generalized coordinates and the direction of motion for the rotating blade (scenario ii) can be observed too. Clearly, the structural response curves for excitation without aerodynamic interaction visualize the directional coupling through the geometrical twist of the blade.

Considering next the frequency response when accounting for the aerodynamic interaction, the peaks can still be observed. The corresponding frequencies are lower, however,

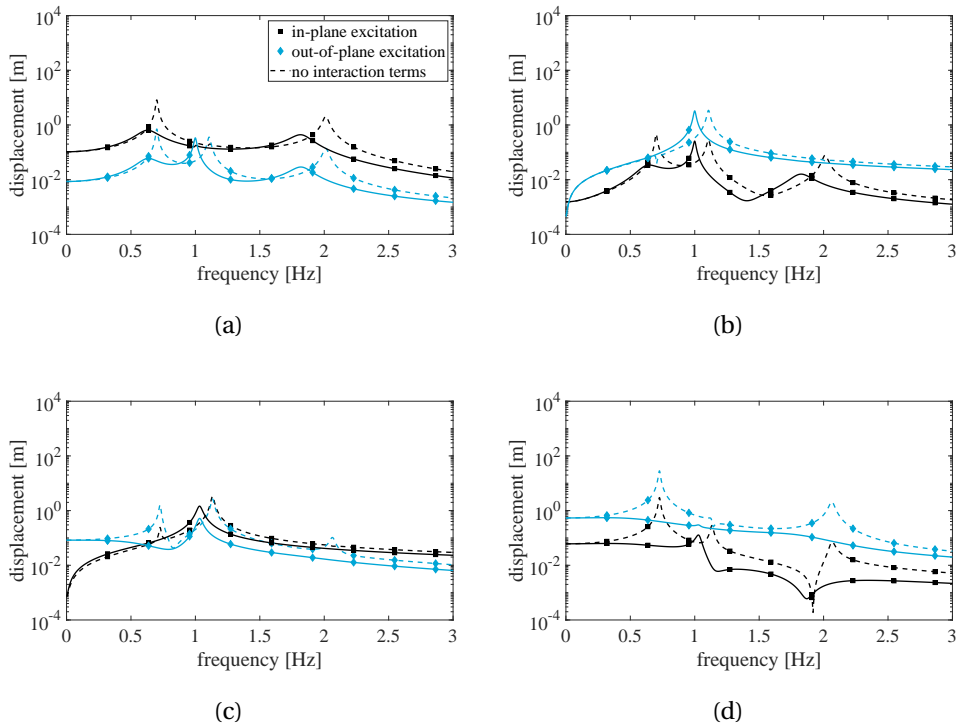


Figure 3.6: Amplitude of the blade tip deflection excited by a unit excitation, as predicted with the linearized instantaneous force model, (a) for a stand-still blade (scenario i) in in-plane direction and (b) in out-of-plane direction, and (c) for a rotating blade (scenario ii) in in-plane direction and (d) in out-of-plane direction. The dotted lines present the frequency responses in absence of aerodynamic interaction.

indicating the effect of the added damping and mass, as well as the influence of modal coupling. The magnitude of most peaks has decreased, again confirming the relevance of the added damping. When comparing the results of the rotating blade (scenario ii) to the stand-still blade (scenario i), it can be seen that the curves of the former are much smoother. This is a result of a larger added damping for the rotating blade, due to a much higher relative wind velocity. In Figure 3.6(d), the out-of-plane resonance peaks are completely absent. This curve clearly shows the influence of the added damping on the out-of-plane motion of a rotating blade. At the same time, though, the rotating blade does experience an amplified in-plane motion around the second natural frequency.

### 3.4.2. LINEARIZED HISTORY-DEPENDENT AERODYNAMIC FORCING

The history-dependent aerodynamic force model contains aerodynamic state variables that account for the separation of the flow in the case of sudden velocity changes. These aerodynamic state variables were derived from a double time-lag approximation of the Wagner's function, Eq. (3.24), containing the aspect ratio-dependent coefficients  $\Psi_{W;1}(r_B)$ ,

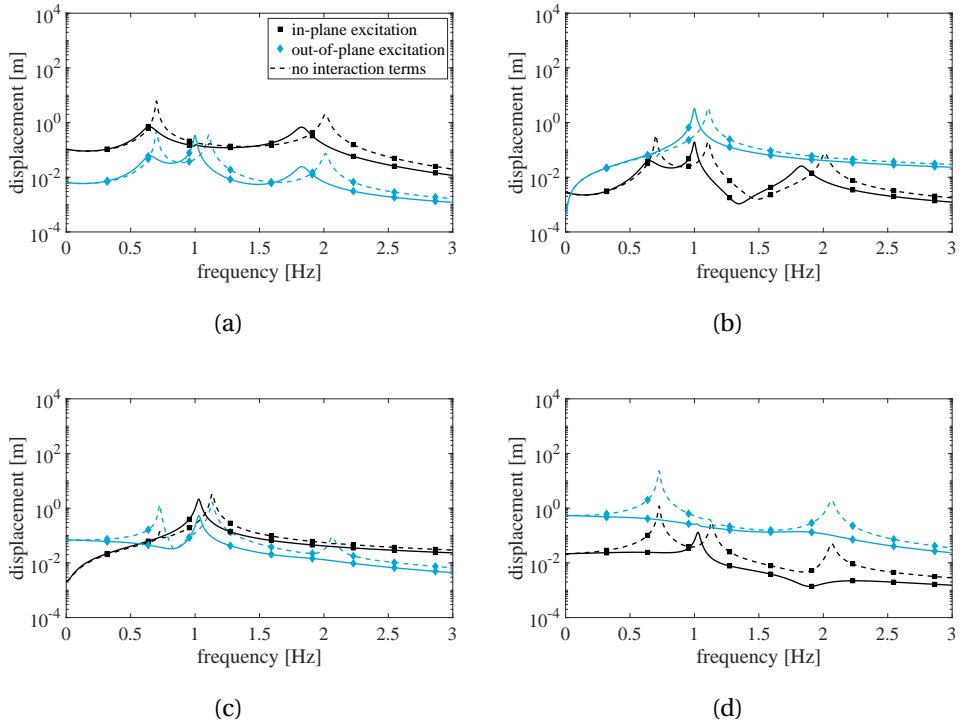


Figure 3.7: Amplitude of the blade tip deflection excited by a unit excitation, as predicted with the linearized history-dependent force model, (a) for a stand-still blade (scenario i) in in-plane direction and (b) in out-of-plane direction, and (c) for a rotating blade (scenario ii) in in-plane direction and (d) in out-of-plane direction. The dotted lines present the frequency responses in absence of aerodynamic interaction.

$\Psi_{W;2}(r_B)$ ,  $\eta_{W;1}(r_B)$  and  $\eta_{W;2}(r_B)$ . Numerical values of these coefficients for blade profiles are not available. Instead, the approximate values for thin plates from [212] are applied, the numerical values of which are presented in Table 3.2.

The frequency-response functions for both operational scenarios (scenario i and ii) are given in Figure 3.7. In general, the same conclusions can be drawn as for the analysis with the linearized instantaneous force model. The aerodynamic interaction affects the magnitudes of the frequency peaks, which occur at a lower frequency. In comparison to Figure 3.6, it can be noted that the shape of some peaks and dips differs somewhat. The main difference between the results of the analyses with the stationary and the history-dependent force models is visible in the directional coupling, and more specifically, in the response to a static excitation. Consider, for instance, Figures 3.6(a) and 3.7(a), or Figures 3.6(d) and 3.7(d). Such an excitation corresponds to a step excitation, as was discussed in Section 3.3.1. As soon as a new near wake equilibrium is established, the flow pattern round the blade remains undisturbed and the history-dependent force model should predict similar forces as the instantaneous force model. In Section 3.3.1, it was already demonstrated that both linearized models predict a different forcing as a result of a step excitation. Here, this finding is confirmed by the frequency-response graphs.

Table 3.2: Coefficients for the double time-lag approximation of the Wagner's function [212].

coefficient	numerical value [-]
$\Phi_{W;1}$	0.165
$\Phi_{W;2}$	0.335
$\eta_{W;1}$	0.045
$\eta_{W;2}$	0.300

### 3.4.3. NON-LINEAR AERODYNAMICS

As a final step, the extent of the non-linearity of the aerodynamic models is assessed. To this end, the blade tip response to the turbulent wind signals, as defined in Section 3.3.3, is evaluated. The results are presented in both time and frequency domain, where the former are obtained by means of an explicit Runge Kutta scheme. Concerning the frequency-domain representations, the power spectral densities of the finite time simulations are estimated on the basis of the fast-Fourier transform of the time series. These estimations are obtained from the squared amplitude spectra, divided by the length of the time signal.

Figure 3.8 presents a 10 s time window out of the blade tip response for the stand-still blade (scenario i) – with Figures 3.8(a) and (b) representing the in-plane and out-of-plane deflections, respectively – and the rotating blade (scenario ii) – where Figures 3.8(c) and (d), respectively, represent the in-plane and out-of-plane deflections. On average, the blade tip deflection of the stand-still blade (scenario i) is close to zero. This is in accordance with the expectations, since the drag contribution is very small and the blade is pitched such, that the lift force is minimized. It can be seen that the in-plane blade tip motion is governed by the first and the third natural frequencies, while the out-of-plane motion mainly takes place at the second natural frequency. This observation logically corresponds to the eigenanalysis as presented in Section 3.1.4. Due to the different orientation, in-plane blade tip motion of the the rotating blade (scenario ii) is



governed by the second mode of vibration. Again, this is in line with the results of the eigenanalysis. The rotating blade mainly deflects in negative in-plane direction and in positive out-of-plane direction. This perfectly agrees with the definition of the lift force in the global rotating frame of reference, see Figure 3.3, given that the flow is attached and the lift force is much larger than the drag force. The magnitude of the deflections of the rotating blade is in agreement with blade tip deflections found in previous studies. For instance, Hsu and Bazilevs [187] presented a blade tip deflection of 3 to 4 m to a constant wind velocity of 11.4 m/s and Li *et al.* [17] predicted a maximum out-of-plane blade tip deflection close to 8 m and an in-plane deflection up to 1 m, based on a turbulent wind field with an average wind velocity of 11.4 m/s. Both studies made use of the blade characteristics of the NREL 5MW turbine. In the original reference document, Jonkman *et al.* [172] presented blade tip deflections of approximately 5.5 m and 0.5 m, in the out-of-plane and in-plane directions, respectively, for a stationary wind of 11.4 m/s. These deflections are smaller than those obtained with the current model, due to the induced wind velocity, which is neglected here.

The blade tip deflections in Figure 3.8 are obtained with the four aerodynamic models. It is reasonable to expect that the non-linear history-dependent force model should provide the most accurate results. Taking this model as a benchmark, the results are now discussed in more detail. Considering first the stand-still blade (scenario i), it can be observed that all the different model predictions are similar in terms of frequency and phase. Deviations in vibration amplitudes, however, can clearly be distinguished. The different aerodynamic models tend to slightly overestimate the in-plane deflection, as predicted by the history-dependent force model – see Figure 3.8(b). On the other hand, in out-of-plane direction, the correspondence between the history-dependent and the instantaneous force models is very good. In general, these findings apply for the rotating blade (scenario ii) too, for which a good match between the instantaneous and the history-dependent force models is obtained. This match confirms the expectations based on the reduced-frequency analysis in Section 3.2.6. Furthermore, the predictions by the linearized instantaneous force model are relatively close to the results of both non-linear models. Only the linearized history-dependent force model is a bit off. In both in-plane and out-of-plane directions, Figures 3.8(c) and (d), a small deviation can be observed, whereas Figure 3.8(d) shows a general underprediction of the deflection peaks. The poorer performance of the linearized history-dependent force model was already expected after the analysis of the linearized models in Section 3.3.1, where it was shown that the linearized history-dependent force model converges to a different force after a step change in wind speed than the linearized instantaneous force model, see Eq. (3.56). The good performance of the linearized instantaneous force model for the rotating blade (scenario i), however, provides an interesting basis for further linearized analyses of such structural elements.

The power spectral density of the blade tip deflections for the stand-still blade (scenario i) is presented in Figure 3.9, and for the rotating blade (scenario ii) in Figure 3.10. These one-sided spectral densities are obtained from the complex-valued Fourier spectra, generated from the time series with the application of Fourier transformation. As a result of the random phase angle assumption in the derivation of the wind turbulence signals, the spectral densities have a noisy appearance. For this reason, a moving root mean

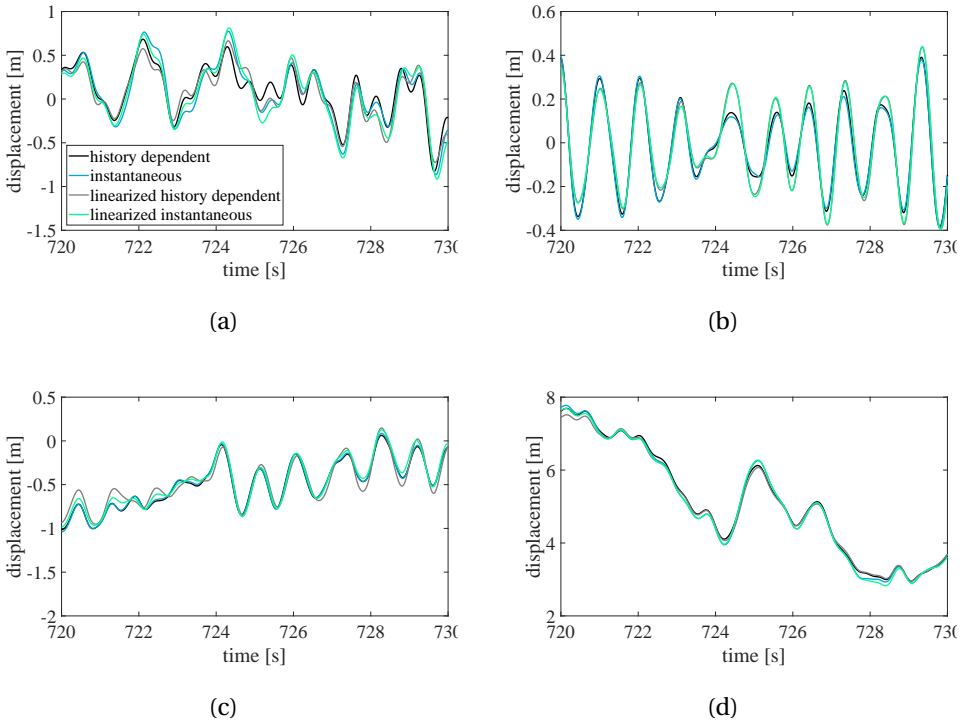


Figure 3.8: Blade tip response of a stand-still blade (scenario i), (a) in in-plane direction, and (b) in out-of-plane direction, and of a rotating blade (scenario ii), (c) in in-plane direction, and (d) in out-of-plane direction.

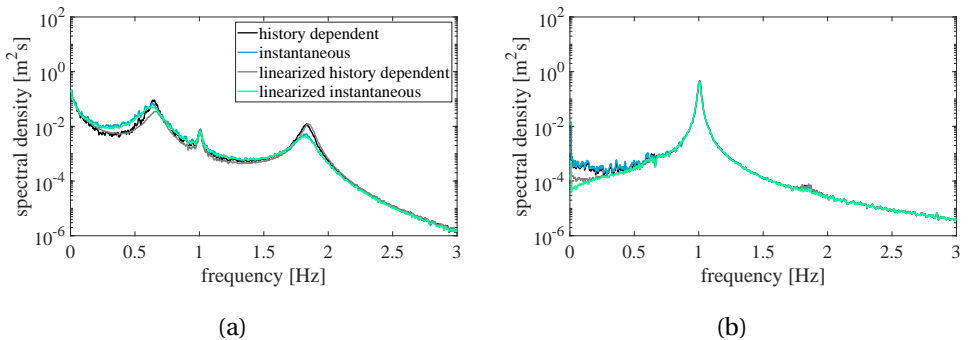


Figure 3.9: Estimated power spectral density of the blade tip deflection of a stand-still blade (scenario i), (a) in in-plane direction, and (b) in out-of-plane direction.

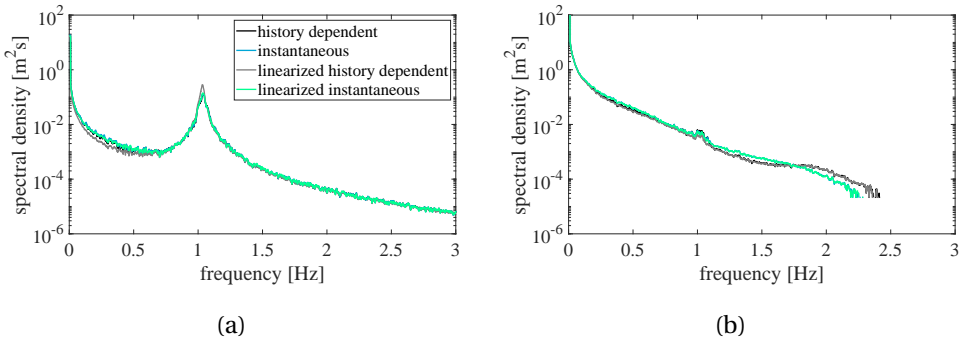


Figure 3.10: Estimated power spectral density of the blade tip deflection of a rotating blade (scenario ii), (a) in in-plane direction, and (b) in out-of-plane direction.

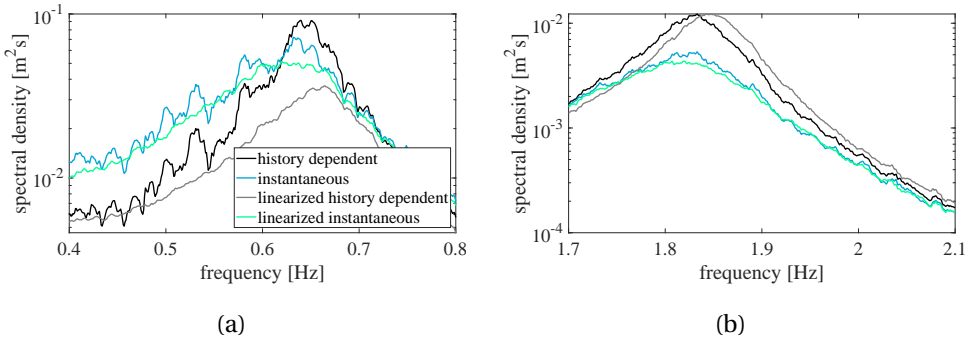


Figure 3.11: Close-up of the estimated power spectral density of the blade tip deflection of a stand-still blade (scenario i) in in-plane direction, at (a) the first natural frequency, and (b) the third natural frequency.

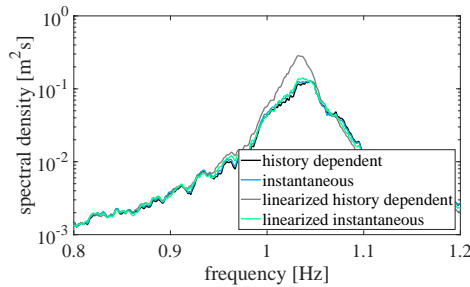


Figure 3.12: Close-up of the estimated power spectral density of the blade tip deflection of a rotating blade (scenario ii) in in-plane direction, at the second natural frequency.

square filter is applied to smooth out the power spectral densities.

In general, the shape of the spectral density distributions corresponds to the frequency-response functions, as derived on the basis of the linearized models in Section 3.4.1 and 3.4.2 and presented in Figures 3.6 and 3.7. The peaks at the natural frequencies are clearly visible, except for Figure 3.10(b), which shows the energy density of the blade tip deflection in out-of-plane direction for the rotating blade (scenario ii). In this case no peaks are visible – apart from a small disturbance at 1 Hz – as a result of the added damping.

When comparing the different aerodynamic models in Figures 3.9 and 3.10, no obvious differences in the locations and sizes of peaks can be distinguished. Only after zooming in, some deviations become visible. Consider, for instance, the in-plane deflection of the stand-still blade (scenario i). At the first and the third frequency, Figures 3.11(a) and (b), respectively, both instantaneous models predict the peak at a slightly lower frequency. Moreover, at the third natural frequency the instantaneous models predict a smaller peak, as can be seen in Figures 3.11(b). From this, the differences in the time response between the non-linear and the linearized models, as seen in Figure 3.8(a) can be explained quite well. The other most eye-catching difference is visible in the peak at the second natural frequency for in-plane motion of the rotating blade (scenario ii), Figure 3.12. Here, the linearized history-dependent force model clearly gives a larger peak at a slightly smaller frequency, explaining the difference in time response in Figure 3.8(c).

In summary, no remarkable differences between the response predictions with the instantaneous and the history-dependent force models have been observed. Most likely, this is related to the random nature of the excitation, due to which the influence of the delay in establishing the aerodynamic equilibrium is not pronounced in the time series of the blade tip displacement. On the basis of the reduced frequencies, see Section 3.2.6, it can be expected that for excitations containing energy at higher frequencies – for instance, corresponding to tower shadowing or wind shear – the difference in model performance is more pronounced. An analysis with rotationally-sampled turbulence spectra may amplify the effect of the history-dependent aerodynamics too.

After linearization, the instantaneous force model still predicts a response similar to the non-linear models. This especially applies for the rotating blade (scenario ii). The linearized history-dependent force model, on the other hand, provides the most deviating displacements. The explanation can be found in the choice linearize the force models around the mean wind speed, as a result of which the linearized aerodynamic state equations of the history-dependent force model result in a force prediction that differs from the other force models, and thus provide poorer predictions for the blade tip deflections in a turbulent wind field. This observation was substantiated in Section 3.3.1, where it was shown that the linearized history-dependent force model predicts deviating steady-state forces resulting from a step excitation, in comparison with the other models.

### 3.5. CONCLUSIONS

In this chapter, the aerodynamic interaction of a rotating blade with a turbulent wind field has been investigated. The aim was to assess the non-linear velocity and history dependency of such an interaction, as a preceding step towards the development of a

reduced rotor model for the engineering of offshore wind support structures. To this end, a blade with the structural characteristics of the NREL 5MW wind turbine was modelled, accounting for the twisted geometry and rotational effects. The blade was defined as a non-uniform Euler-Bernoulli beam, rigidly fixed to a hub and with lateral freedom of motion in two directions. The model explicitly incorporates the rotational velocity and the pitching of the blade, and demonstrates the directional coupling of the blade motion, as well as the effect of added damping and modal coupling through the non-linear aerodynamic interaction, accounting for the unsteadiness of the air flow.

With respect to the aerodynamic interaction, instantaneous and history-dependent force models were distinguished. The former was adopted for its simplicity, whereas the latter allowed for time delays in establishing the aerodynamic equilibrium in unsteady flows. To this end, two additional equations were required, expressing the aerodynamic state of the interaction process. By comparing the responses computed with the two different interaction models, the relevance of the history dependency could be assessed. The validity of the interaction models, however, is limited to attached-flow conditions, a requirement that can easily be met by pitching the blade. Moreover, both models possess a non-linear dependency on the relative wind velocity, and, in order to assess the significance of the non-linearity, two linearized models were derived on the basis of Taylor series expansions.

Results were presented for the blade tip deflection. Hereto, use was made of a reduced-order model, based on the first three modes of the free-vibrating blade. For the analyses, both a stand-still and a rotating blade were considered. With the linearized models, frequency-response functions were computed, clearly illustrating the combined directional and modal coupling. A difference between the linearized instantaneous and history-dependent force models was observed in the response to a step excitation, explained by a poor representation of the aerodynamic state equations after linearization. Furthermore, it was shown that due to the large contribution of the added damping for a rotating blade, some resonance peaks vanish.

Time-domain responses were computed from turbulent wind signals obtained from Kaimal turbulence spectra. These time signals and their frequency-domain representations showed a good correspondence between the predictions with the instantaneous and the history-dependent force models, especially for the rotating blade, implying little history dependency of the aerodynamic interaction. For the stand-still blade, the deviation between the responses to both interaction forces is larger, suggesting more history-dependent aerodynamics. This observation is confirmed by the reduced-frequency analysis, from which a more history-dependent interaction of the stand-still blade was expected. It was demonstrated that the results of the linearized instantaneous force model are in good correspondence with the non-linear interaction models, again especially for the rotating blade. This linearized model allows for an easy assessment of the added damping that results from the aerodynamic interaction. The results with the linearized history-dependent force model are somewhat off, which could be expected based on the linear frequency-response analysis. On this basis, the application of the linearized history-dependent model is not recommended.

It should be noted, that the results are computed for a mainly low-frequency turbulent excitation. The assessment of the reduced frequencies, however, suggested a

dominant instantaneous aerodynamic interaction for the rotating blade at low excitation frequencies. Excitation at higher frequencies, for instance through tower shadowing, can induce a more history-dependent aerodynamic interaction. Moreover, an assessment with the application of rotationally sampled turbulence spectra may show a higher degree of history dependency too.

The relevance of the results of the current chapter lie in the fact that the model allows for the prediction of the directionally coupled response of the blade, while accounting for modal coupling through the aerodynamic interaction. This allows for a much more accurate consideration of the added damping, which in the existing literature is commonly defined erroneously in terms of modal damping. Second, the good correspondence between the structural response obtained with the history-dependent and the instantaneous aerodynamic force models provides a good basis for the application of the latter, more simple model, to derive a reduced rotor model. Particularly the case of the rotating blade showed a good correspondence for the linearized instantaneous force model, which is of course the preferred model in terms of calculation time. Furthermore, the linearized instantaneous force model allowed for the extraction of an added damping matrix, with which straightforward dynamic analyses of a rotating wind turbine blade can be performed, and which can provide a basis for the definition of a reduced rotor model.

# 4

## STATE-INDEPENDENT APPARENT AERO-ELASTIC PROPERTIES

*The aerodynamic force on a wind turbine rotor depends on the motion of that wind turbine. For instance, in the fore-aft direction, the turbine experiences an aerodynamic resistance, which is widely considered as an apparent damping. Particularly for the structural analysis of offshore wind support structures, this apparent damping is of relevance, as it reduces the response to wave excitations. Furthermore, a change in orientation of the rotor – resulting from a tower deformation – is perceived as an apparent stiffness, and the non-circulatory lift force contributes to an apparent mass. This chapter presents closed-form state-independent expressions for these apparent aero-elastic properties, accounting for three-dimensional motions, obtained from a Taylor expansion of state-dependent aerodynamic force expressions, explicitly accounting for geometric and aeroelastic parameters, such as rotor eccentricity, rotational velocity, pitch angle, and lift and drag coefficients. The apparent properties are derived generically, allowing for differences in blade properties and spatial variations in the wind field. For the specific case of a rotor with identical blades, the expressions are explained and their relevance is visualized. The response of the NREL 5MW turbine with the UpWind monopile-based support structure is estimated and compared to response estimations obtained with an equivalent BLADED model. The estimated response shows good correspondence for turbulent wind conditions, provided that the yaw misalignment is not too large. In addition, a hybrid approach is presented, which combines the response-independent aerodynamic force from BLADED with the state-independent apparent aero-elastic properties presented in this chapter. The closed-form expressions for the apparent aero-elastic properties represent a valuable tool to assess and understand the interdependency between the response of a wind turbine and the aerodynamic excitation. Furthermore, the expressions are useful for the preliminary design of the foundations of wind turbines.*

---

This chapter represents an adaptation of Van der Male *et al.* [259], that was submitted for publication.

**T**HE aerodynamic force on a wind turbine rotor is a function of the relative wind velocity. This relative wind velocity is composed of the ambient and induced wind fields, the rotational velocity of the rotor and the structural motion, and depends, moreover, on the wake development behind the rotor. The flexible tower of a wind turbine allows for translational rotor motions, as well as structural rotations. The dependency of the aerodynamic force on the relative velocity is non-linear; hence, the aerodynamic force depends non-linearly on the structural motion. Concerning the structural motion, it is obvious that bending of the tower, either in the fore-aft or the side-to-side direction, results in both a deflection and a rotation of the tower top, while from a rotor perspective, both the fore-aft motion and the yaw motion, i.e., the rotation around the vertical tower axis, result in an out-of-plane structural velocity, i.e., a structural velocity perpendicular to the plane of rotation of the rotor. As a consequence, it can be stated that the aerodynamic forcing is affected by both the translational and rotational structural motions of the rotor. Since the aerodynamic force also depends on the rotational velocity of the rotor, this dependency is affected by the operational state of the turbine. Additionally, the eccentric positioning of the rotor with respect to the tower axis introduces an inertial coupling between the side-to-side and the yaw motions. Understanding the aerodynamic force-response interdependency is of particular relevance for the estimation of the force distribution in the foundation of the wind turbine. The mutual dependence between a force and a response is commonly referred to in terms of apparent damping and mass. Moreover, structural deformations affect the geometric orientation of the rotor plane with respect to the wind direction and subsequently, the aerodynamic forcing, resulting in an apparent stiffening, or apparent stiffness. For offshore wind turbines, the force distribution resulting from a wave excitation is affected by the aerodynamic interdependency too, as waves induce rotor motions and therefore aerodynamic excitations. As a result, the design of the foundation of offshore wind turbines requires a coupled analysis of the aerodynamic and hydrodynamic forces [9, 14].

The relation between the aerodynamic force and the fore-aft motion of the rotor has been addressed multiple times [49, 50, 52]. In these studies, the dependency has been expressed in terms of a damping coefficient, which is a function of the rotational velocity and the gradient of the lift coefficient of the aerofoils with respect to the angle of attack of the relative wind vector. Schafhirt and Muskulus [55] addressed the three-dimensional apparent damping by relating the decoupled support structure model to an integrated wind turbine model. The results of these studies have been derived with the assumption that the aerodynamic forcing reacts instantaneously to a change in the relative wind velocity, neglecting the history dependency of – or the memory effect on – the force-response relation. This assumption was shown to be acceptable at the level of a single blade in Chapter 3, where the aerodynamic coupling for in-plane and out-of plane blade vibrations was defined.

With the development of different aero-elastic software codes, the aerodynamic force-response interdependency has been accounted for to a greater extent. These models account for three-dimensional flow effects on the induced aerodynamic forcing [35, 40, 204]. Several researchers have presented the concepts behind the development of these codes [25, 230, 260, 261], and the results of an aero-elastic analysis with such a



tool [262]. These software codes do not allow for the application of aerodynamic models including memory effects [215, 219], which render the force-response interdependency more complicated. In Chapter 3, however, the analysis of the aerodynamic force on a flexible rotating blade connected to a fixed hub indicated the validity of the instantaneous model, particularly for a high rotational velocity. This finding is substantiated by the definition of the reduced frequency [182, 183], from which it can be derived that at the envisaged oscillation frequencies, the contribution of the history dependency is low. At a different level, the aerodynamic excitation of a wind turbine rotor has been modelled by means of vortex wake models [208] and computational fluid dynamics codes in combination with a multi-body dynamics code [17, 186, 187, 263]. The results of these studies are very valuable for the analysis of fully coupled fluid-structure interaction, but still require simplified analyses for validation. The need for simplified validation and modelling tools was already addressed in Van Kuik *et al.* [5]. In this respect, several studies have aimed at simplifying the support structure [12, 149, 155] and the soil-structure interaction [111, 117, 118] of offshore wind turbines. Zhang *et al.* [61] presented a simplified rotor model to investigate the control of lateral tower vibrations, using an active torque controller. Regarding the aerodynamic forcing, however, no closed-form expressions were presented.

When considering the dynamic response of offshore wind turbine foundations, it is not uncommon to assume the aerodynamic force and the structural response to be independent [49, 123, 152, 264, 265]. In most of these cases, the aerodynamic force is found from a separate rotor model, and multiple iterations are necessarily required to obtain an accurate response estimation. Future studies of this nature would benefit from the availability of closed-form relations, expressing the interdependency between the aerodynamic force and the structural response. A transparent analytical formulation of this mutual dependency would provide a valuable insight in the particular relevance of the different aero-elastic parameters, such as the rotational velocity, the pitch angle and the lift and drag coefficients. In addition, the expressions could prove to be a valuable tool in the design of wind turbine foundations, especially offshore – given the interaction between the wind and wave excitations, because the relevant aerodynamic force-response interdependency – in terms of apparent stiffness, damping and mass – can be accounted for, while a detailed rotor model can be omitted.

This chapter presents such closed-form expressions for the apparent stiffness, damping and mass for a wind turbine rotor. To this end, use is made of closed-form expressions of the aerodynamic force, which depend non-linearly on the structural response. Hence, the implicit apparent stiffness, damping and mass are state-dependent. By means of a first-order Taylor approximation of the aerodynamic force, the expressions are linearized with respect to the structural response, accounting for rotor motions and rotations in three directions. Since the aerodynamic force is defined in a global inertial frame of reference, forces in three directions and moments around three axes are distinguished. From these linearized expressions, state-independent apparent stiffness, damping and mass matrices are explicitly obtained.

The derivation of the apparent aero-elastic properties is done in a general manner with respect to the blade properties, implying that the matrices allow for the analysis of rotors with unequal blades. On the basis of the resulting expressions, the force-response

relation can be better understood. This already applied for the closed-form expressions that contain implicit state-dependent apparent aero-elastic properties, and specifically for the linearized state-independent expressions, provided that the aerodynamic force is approximated without loss of its validity. The results of Chapter 3 suggested that after such an approximation the force-response interdependency can still be predicted accurately.

As a starting point, the equations of motion of a rigid rotor fixed on a flexible tower top are derived, taking the rotor eccentricity into account. In addition, it is assumed that the rotational velocity is constant, implying that the resisting torque at the tower top always balances the aerodynamic torque acting on the rotor. The equations of motion are derived in the global inertial frame of reference, explicitly accounting for pseudo-force effects, such as Coriolis and centrifugal stiffening. Subsequently, the state-dependent aerodynamic force expressions are introduced, distinguishing lift, drag and inertia forces. The presented forces are valid for attached flow conditions, and it is assumed that memory effects can be neglected. After expanding the forces in terms of the structural motions, the state-independent apparent aero-elastic properties are presented. The terms of these expressions are assessed in more detail for the specific case of a rotor with identical blades and the resulting mean wind perpendicular to the rotor plane. The derived equations do not account for an active control system or particular drive-train dynamics. In Chapter 5, the drive-train will be added to the current model by distinguishing the rotational degrees of freedom of the rotor around its axis of rotation from the tower top motions. This addition will allow for a rotor with a varying speed rotation. Subsequently, simple control systems can be implemented, which relate this rotational velocity to the pitch angles of the blades or the resisting torque of the generator.

The analysis of the state-dependent force expressions for the specific case of identical blades allows for an assessment of the apparent stiffness, damping and mass contributions. Moreover, the contribution of the separate force components – lift, drag and inertia – can be visualized. In order to do so, the rotor properties of the NREL 5MW turbine are adopted [172]. As a validation of the state-independent force-response interdependency, the structural response to a turbulent wind signal is computed in the time domain and compared to the response derived with the force containing state-independent apparent aero-elastic properties. This comparison illustrates the degree of non-linearity of the adopted force expressions. Moreover, the response is compared with the simulation results obtained with the software package BLADED 4.6. This validation requires the definition of a tower and a foundation, for which use is made of the UpWind offshore wind support structure [173].

The derived closed-form expressions for the apparent stiffness, damping and mass can be applied for the coupling between a detailed rotor model and a model of the support structure. Given the explicit incorporation of the relevant aero-elastic parameters, such as rotor eccentricity, rotational velocity, pitch angle and lift and drag coefficients, the expressions allow for the further studying of operational concepts in relation to the foundation response. In this respect, the expressions have a practical potential, especially regarding the preliminary analysis of the fatigue damage for support structures of offshore wind turbines. Moreover, the force expressions provide a starting point for the further implementation of control aspects and drive-train dynamics.

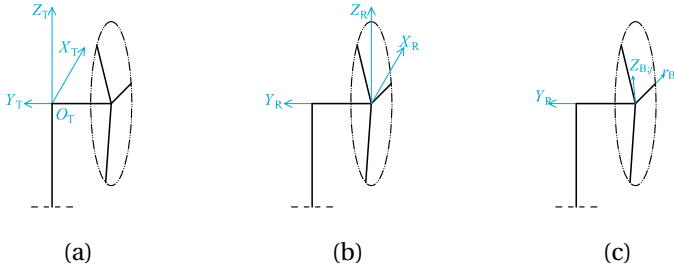


Figure 4.1: Schematic representation of the reference frames defining the turbine system, with (a) the global inertial reference frame, (b) the floating rotor reference frame, and (c) the rotating blade reference frames.

## 4.1. ROTOR MODEL

### 4.1.1. SYSTEM DEFINITION

In this chapter, the aerodynamic force on a wind turbine rotor in the inertial reference frame is defined in terms of matrix multiplications. This requires the definition of a turbine rotor on which the aerodynamic force acts, and, therefore, this rotor definition is presented first. The rotor model is obtained from Lagrange's equation and the derivation for wind turbine rotors is similar to the early work presented by Garrad and Quarton [266], which was employed in many subsequent works [267–269].

For the derivations presented in this chapter, use is made of the definition of a three-bladed rotor on a flexible tower. To define the turbine system, use is made primarily of three types of reference frame, which are illustrated in Figure 4.1. First, Figure 4.1(a) presents the global inertial  $X_T Y_T Z_T$  reference frame, with its origin  $O_T$  located at the intersection of the axis of rotation and the centre line of the tower. The support script 'T' indicates that the reference frame relates to the tower of the turbine system. Figure 4.1(b) depicts the rotor-fixed  $X_R Y_R Z_R$  floating reference frame, which connects to the hub of the rotor, and with the  $Y_R$  axis defining the axis of rotation, the  $X_R$  directed horizontally and the  $Z_R$  axis pointing in the vertical direction. The subscript 'R' refers to rotor and indicates that the reference frame relates to the rotor of the turbine. Both the orientation of the rotor-fixed reference frame and the location of its origin within the global inertial reference frame are affected by elastic deformations of the tower. In other words, the rotor-fixed reference frame floats within the global inertial reference frame. The orientation of each blade is defined by a blade-fixed  $r_{B;j} Y_{B;j} Z_{B;j}$  rotating reference frame – with 'B', which stands for blade, specifying that the reference frame relates to a blade, and the subscript  $j$  indicating the specific blade to which the reference frame relates. As shown in Figure 4.1(c), the axes  $Y_{B;j}$  coincide with the  $Y_R$  axis, and the  $r_{B;j}$  axes correspond with the longitudinal blade axes. The  $Z_{B;j}$  axes lie within the plane of rotation, perpendicular to the  $r_{B;j}$  axes.

To indicate within which reference system each vector, and its components, are defined, use is made of the superscripts 'f' and 'r', indicating that the specific vector is defined within the floating rotor reference frame, or a rotating blade reference frame.

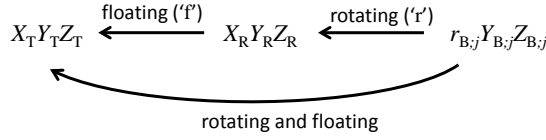


Figure 4.2: Definition of the relation between the different reference frames and the usage of the superscripts ‘f’ and ‘r’. The arrows indicated with respect to which reference frame a frame of reference is defined as floating or rotating.

No specific superscript is used to indicate that a vector is defined in the global inertial reference. Figure 4.2 illustrates the relation between the different reference frames and the usage of the superscripts.

Figure 4.3 presents the front view of a three-bladed rotor with radius  $R$ . The orbital angular velocity  $\Omega_R^f(t)$  characterizes the rotor rotation. As the rotor rotation  $\Omega_R^f(t)$  takes place around the  $Y_R$  axis, the magnitude of the rotational velocity is indicated by  $\Omega_{R;Y}^f(t)$ . The orientation of the  $Y_R$  within the global inertial reference frame is affected by the loads acting on the turbine system. For unloaded conditions, the tilt of the rotor introduces an inclination of the  $Y_R$  axis with respect to the  $Y_T$  axis.

The azimuth positions of the blades is given by  $\Psi_{B;j}^f(t)$ , for  $j = 1, 2, 3$

$$\Psi_{B;j}^f(t) = \int_0^t \Omega_{R;Y}^f(t) dt + \psi_{B;j}^f. \quad (4.1)$$

For equally spaced blades,  $\psi_{B;j}^f$  can be chosen as  $\frac{2}{3}(j-1)\pi$ . The rotor azimuth  $\Psi_R^f(t)$  is defined as the azimuth of the first blade, i.e., for  $j = 1$ . As indicated by the superscript ‘f’, both the rotor speed and the azimuth angle are defined in the rotor-fixed  $X_R Y_R Z_R$  frame of reference.

Having defined the rotor system within its frames of reference, the aero-elastic properties of the system can be introduced. Figure 4.4 distinguishes the rotor sub-system and the tower sub-system. Figure 4.4(a) illustrates the degrees of freedom of both sub-systems. The degrees of freedom vector  $\mathbf{v}_T(t)$ , defined at the tower top, describes the translation  $\mathbf{u}_T(t)$  and rotation  $\boldsymbol{\theta}_T(t)$  of the tower top within the global inertial reference frame. The translational motions –  $u_{T;X}(t)$ ,  $u_{T;Y}(t)$  and  $u_{T;Z}(t)$  – are from here on referred to as side-to-side, fore-aft and up-down, respectively, whereas the rotational motions –  $\theta_{T;X}(t)$ ,  $\theta_{T;Y}(t)$  and  $\theta_{T;Z}(t)$  – are referred to as tilting, rolling and torsion of the tower sub-system.

The degrees of freedom of the rotor sub-system, given by  $\mathbf{v}_R(t)$ , express the translation  $\mathbf{u}_R(t)$  and rotation  $\boldsymbol{\theta}_R(t)$  within the global inertial reference frame and are defined at the tower top as well. It should be noted that these degrees of freedom are defined in the global inertial reference frame. Within the rotor-fixed reference frame, the rotation  $\theta_{R;Y}^f(t)$  can be perceived as a perturbation of the rotor azimuth that corresponds with the mean rotor speed  $\bar{\Omega}_{R;Y}^f$ :

$$\Psi_R^f(t) = \bar{\Psi}_R^f(t) + \theta_{R;Y}^f(t), \quad (4.2)$$

where

$$\bar{\Psi}_R^f(t) = \bar{\Omega}_{R;Y}^f t. \quad (4.3)$$

The relation between the rotations  $\theta_{R;Y}^f(t)$  and  $\theta_{R;Y}(t)$  is defined mathematically in Section 4.1.2. Regarding the translational motions of the rotor sub-system and the rotational motions  $\theta_{R;X}(t)$  and  $\theta_{R;Z}(t)$ , similar definitions as for the tower sub-system are employed.

As illustrated by Figure 4.4, the tower sub-system is defined by the mass matrix  $\mathbf{M}_T$ , the stiffness matrix  $\mathbf{K}_T$  and the damping matrix  $\mathbf{C}_T$ . Moreover, the mass matrix  $\mathbf{M}_N$  – with ‘N’ indicating nacelle – represents the inertia of the nacelle components, including the drive-train, defined in the global inertial reference frame with respect to the tower top. The rotor system consists of the blades with the distributed masses  $m_{B,j}(r_{B,j})$ . The matrix  $\mathbf{M}_H$  represents the inertia of the hub defined with respect to the tower top. The tower representation by a six-degree-of-freedom system is adopted for reasons of simplicity. For the actual modelling of the tower-system, a model with many degrees of freedom is likely to be applied, for instance a finite-element beam model. The definition of the rotor sub-system allows for the application of such a model, as will be done in Section 4.5.

Figure 4.4(b) presents the external and internal forces acting on the rotor and tower sub-systems. The aerodynamic excitations on the rotor sub-system are expressed by the vector  $\mathbf{Q}_{R;A}(t)$ :

$$\mathbf{Q}_{R;A}(t) = \left[ \{\mathbf{F}_{R;A}(t)\}^T \quad \{\mathbf{T}_{R;A}(t)\}^T \right]^T, \quad (4.4)$$

with  $\mathbf{F}_{R;A}(t)$  containing the forces coinciding with the axes of the global inertial reference frame and  $\mathbf{T}_{R;A}(t)$  the moments about these axes. The subscript ‘A’ indicates that the forces represent aerodynamic excitations.

The forces  $F_{R;A;X}(t)$ ,  $F_{R;A;Y}(t)$  and  $F_{R;A;Z}(t)$  are from hereon referred to as the lateral, axial and vertical aerodynamic rotor forces. The moment  $T_{R;A;Y}(t)$  is referred to as the aerodynamic torque and concerning the moments  $T_{R;A;X}(t)$  and  $T_{R;A;Z}(t)$  – the definitions tilting and yawing are employed. The vector  $\mathbf{Q}_{T;E}(t)$  – with  $\mathbf{F}_{T;E}(t)$  and  $\mathbf{T}_{T;E}(t)$  – defines the external environmental excitation (‘E’) of the tower sub-system. At the interface between the two sub-systems, the force vector  $\mathbf{Q}_{R;DT}(t)$  represents the resistance from the drive-train (‘DT’) on the rotor and the force vector  $\mathbf{Q}_{T;DT}(t)$  from the the transfer between the rotor and tower sub-systems. For indirectly driven wind turbines, different drive-train torques act on the rotor and tower sub-systems.

The current model does not contain degrees of freedom which relate to the flexibility of the blades, implying that the blades are assumed to be rigid. The lowest natural frequency of the blades is generally multiple times higher than the natural frequencies corresponding to the first bending modes of the complete structure, implying that the interference of these modes is small. The energy of aerodynamic excitations from turbulence and hydrodynamic excitations – for offshore wind turbines – is mainly concentrated at frequencies much lower than the lowest natural frequencies of the blades. As a consequence, for these excitations, the response of the blades can be assumed to be predominantly quasi-static. The static stiffness of the blades affects the orientation of the aerodynamic inflow with respect to the blade cross-sections. This influence is not accounted for. Given that the deformation of the blades is sufficiently small, this effect is negligible. The quasi-static

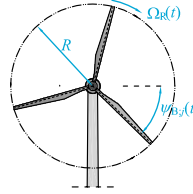


Figure 4.3: Front view of the three-bladed rotor.

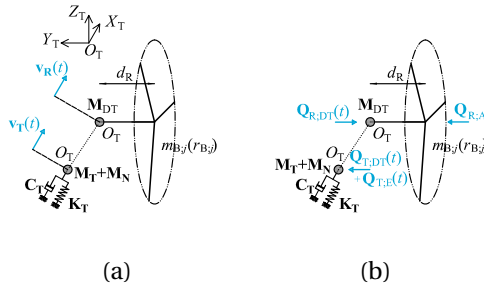


Figure 4.4: Schematic representation of the dynamic turbine system, sub-divided into the rotor and tower sub-systems, with (a) the degrees of freedom of the rotor and tower sub-systems, and (b) the external and internal forces acting on the rotor and tower sub-systems.

motion of flexible blades, however, affects the relative flow velocity, and subsequently the aerodynamic force on the blades, an effect which is neglected in this model.

#### 4.1.2. EQUATIONS OF MOTION

The equations of motion of the rigid rotor sub-system can be derived with the definition of the turbine rotor within both the global inertial reference frame and the moving blade reference frames. Starting point is the point  $\mathbf{x}_{B;j}^r$ , which is located on the  $j$ -th blade and defined in the corresponding  $r_{B;j} Y_R Z_{B;j}$  reference frame:

$$\mathbf{x}_{B;j}^r = [r_{B;j} \quad 0 \quad 0]^T. \quad (4.5)$$

The position of the corresponding point  $\mathbf{x}_{B;j}^f(t)$  in the rotor frame of reference is obtained with the application of the rotation matrix  $\mathbf{R}_{B;\bar{\Psi};j}(t)$ :

$$\mathbf{x}_{B;j}^f(t) = \mathbf{R}_{B;\bar{\Psi};j}(t) \mathbf{x}_{B;j}^r, \quad (4.6)$$

with

$$\mathbf{R}_{B;\bar{\Psi};j}(t) = \begin{bmatrix} \cos \bar{\Psi}_{B;j}^f(t) & 0 & \sin \bar{\Psi}_{B;j}^f(t) \\ 0 & 1 & 0 \\ -\sin \bar{\Psi}_{B;j}^f(t) & 0 & \cos \bar{\Psi}_{B;j}^f(t) \end{bmatrix}. \quad (4.7)$$

The blade azimuths  $\bar{\Psi}_{B;j}^f(t)$  define the positions on the basis of the mean rotor speed  $\bar{\Omega}_{R;Y}^f$ . The position vector  $\mathbf{x}_{B;j}^f(t)$  describes the time-varying blade position as a result of the rotor rotation only, and its time derivative is an important input for the state-independent force expressions, which are derived in Section 4.3.

Within the global inertial frame of reference, the vector  $\mathbf{x}_{B;j}(t)$  describes the deformed position of the  $j$ -th blade, and results from translations  $\mathbf{u}_R(t)$  and rotations  $\boldsymbol{\theta}_R(t)$  of the rotor sub-system:

$$\mathbf{x}_{B;j}(t) = \mathbf{d}_R + \mathbf{u}_R(t) + \mathbf{R}_{R;\theta}(t)\mathbf{x}_{B;j}^f(t), \quad (4.8)$$

where  $\mathbf{d}_R$  represents the eccentricity of the rotor plane with respect to the tower. The matrix  $\mathbf{R}_{R;\theta}(t)$  describes the total rotation after subsequent rotations  $\theta_{R;X}(t)$ ,  $\theta_{R;Y}(t)$  and  $\theta_{R;Z}(t)$  around the axes of the  $X_T Y_T Z_T$  reference frame. This matrix cannot be defined uniquely, since large rotations in a three-dimensional frame of reference are non-commutative [270]. The matrix  $\mathbf{R}_{R;\theta}(t)$  also relates the rotation vectors  $\boldsymbol{\theta}_R^f(t)$  and  $\boldsymbol{\theta}_R(t)$ , the former of which was used in Eq. (4.2):

$$\boldsymbol{\theta}_R(t) = \mathbf{R}_{R;\theta}(t)\boldsymbol{\theta}_R^f(t), \quad (4.9)$$

Defining the state vector  $\mathbf{S}_R(t)$  as

$$\mathbf{S}_R(t) = [\{\mathbf{v}_R(t)\}^T \quad \{\dot{\mathbf{v}}_R(t)\}^T \quad \{\ddot{\mathbf{v}}_R(t)\}^T]^T, \quad (4.10)$$

the Lagrangian  $L_R(\mathbf{S}_R(t))$  of the rotor sub-system can be expressed in terms of its kinetic energy:

$$L(\mathbf{S}_R(t)) = \frac{1}{2} \{\dot{\mathbf{v}}_R(t)\}^T \mathbf{M}_H \dot{\mathbf{v}}_R(t) + \sum_{j=1}^3 \int_{r_H}^R \frac{1}{2} \{\dot{\mathbf{x}}_{B;j}(t)\}^T m_{B;j}(r_{B;j}) \dot{\mathbf{x}}_{B;j}(t) dr_{B;j}, \quad (4.11)$$

where

$$\dot{\mathbf{x}}_{B;j}(t) = \dot{\mathbf{u}}_R(t) + \dot{\mathbf{R}}_{R;\theta}(t)\mathbf{x}_{B;j}^f(r_{B;j}, t) + \mathbf{R}_{R;\theta}(t)\dot{\mathbf{x}}_{B;j}^f(r_{B;j}, t), \quad (4.12)$$

and the kinetic energy of the blade is obtained after integration over the length of the blade, starting from the hub radius  $r_H$ .

With reference to Figure 4.4(b) and employing Hamilton's principle [148], the equations of motion of the rotor sub-system can be expressed as

$$\frac{d}{dt} \frac{\partial L(\mathbf{S}_R(t))}{\partial \dot{\mathbf{v}}_R(t)} - \frac{\partial L(\mathbf{S}_R(t))}{\partial \mathbf{v}_R(t)} = \mathbf{Q}_{R;A}(t) - \mathbf{Q}_{R;DT}(t). \quad (4.13)$$

These equations of motion depend non-linearly on the state  $\mathbf{S}_R(t)$ . With a first-order Taylor expansion of the nonlinear terms with respect to  $\mathbf{S}_R(t)$ , developed about the mean state  $\bar{\mathbf{S}}_R(t)$ , defined as

$$\bar{\mathbf{S}}_R = \{\mathbf{S}_R(t) = \bar{\mathbf{S}}_R(t)\}. \quad (4.14)$$

The linear approximation of the equations of motions can be expressed in terms of the perturbations  $\Delta \mathbf{v}_R(t)$  of  $\mathbf{v}_R(t)$  with respect to the mean  $\bar{\mathbf{v}}_R(t)$ :

$$\left[ \mathbf{M}_H + \sum_{j=1}^3 \mathbf{M}_{B;j}(t) \right] \Delta \ddot{\mathbf{v}}_R(t) + \sum_{j=1}^3 \mathbf{G}_{B;C;j}(t) \Delta \dot{\mathbf{v}}_R(t) + \sum_{j=1}^3 \mathbf{G}_{B;S;j}(t) \Delta \mathbf{v}_R(t) = \sum_{j=1}^3 \mathbf{Q}_{B;S;j}(t) + \mathbf{Q}_{R;A}(t) - \mathbf{Q}_{R;DT}(t). \quad (4.15)$$

The matrices  $\mathbf{M}_{B;j}(t)$  define the inertia of the rotating blades, and can be expressed as

$$\mathbf{M}_{B;j}(t) = \begin{bmatrix} \mathbf{M}_{B;uu;j}(t) & \mathbf{M}_{B;u\theta;j}(t) \\ \mathbf{M}_{B;\theta u;j}(t) & \mathbf{M}_{B;\theta\theta;j}(t) \end{bmatrix}, \quad (4.16)$$

with

$$\mathbf{M}_{B;uu;j}(t) = \mathbf{I}_{3 \times 3} \int_{r_H}^R m_{B;j}(r_{B;j}) dr_{B;j}, \quad (4.17)$$

$$\mathbf{M}_{B;u\theta;j}(t) = \{\mathbf{M}_{B;\theta u;j}(t)\}^T = \int_{r_H}^R m_{B;j}(r_{B;j}) \left[ \frac{\partial \{\dot{\mathbf{R}}_{R;\Delta\theta}(t) \mathbf{x}_{B;\bar{\theta};j}(t)\}}{\partial \{\dot{\theta}_R(t)\}} \right] \Big|_{\bar{\mathbf{s}}_R} dr_{B;j}, \quad (4.18)$$

and

$$\mathbf{M}_{B;\theta\theta;j}(t) = \frac{1}{2} \int_{r_H}^R m_{B;j}(r_{B;j}) \left[ \frac{\partial^2 \left\{ \{\dot{\mathbf{R}}_{R;\Delta\theta}(t) \mathbf{x}_{B;\bar{\theta};j}(r_{B;j}, t)\}^T \dot{\mathbf{R}}_{R;\Delta\theta}(t) \mathbf{x}_{B;\bar{\theta};j}(t) \right\}}{\partial \{\dot{\theta}_R(t)\}^2} \right] \Big|_{\bar{\mathbf{s}}_R} dr_{B;j}, \quad (4.19)$$

with the three by three identity matrix  $\mathbf{I}_{3 \times 3}$ .

The matrices  $\mathbf{G}_{B;C;j}(t)$  and  $\mathbf{G}_{B;S;j}(t)$  express the Coriolis effect and the centrifugal stiffening corresponding to tower top motions, respectively, and are obtained as

$$\mathbf{G}_{B;C;j}(t) = \begin{bmatrix} \mathbf{G}_{B;C;uu;j}(t) & \mathbf{G}_{B;C;u\theta;j}(t) \\ \mathbf{G}_{B;C;\theta u;j}(t) & \mathbf{G}_{B;C;\theta\theta;j}(t) \end{bmatrix}, \quad (4.20)$$

and

$$\mathbf{G}_{B;S;j}(t) = \begin{bmatrix} \mathbf{G}_{B;S;uu;j}(t) & \mathbf{G}_{B;S;u\theta;j}(t) \\ \mathbf{G}_{B;S;\theta u;j}(t) & \mathbf{G}_{B;S;\theta\theta;j}(t) \end{bmatrix}, \quad (4.21)$$

with

$$\mathbf{G}_{B;C;uu;j}(t) = \mathbf{0}_{3 \times 3}, \quad (4.22)$$

$$\begin{aligned} \mathbf{G}_{B;C;u\theta;j}(t) &= \int_{r_H}^R m_{B;j}(r_{B;j}) \left[ \frac{\partial \{\mathbf{R}_{R;\Delta\theta}(t) \dot{\mathbf{x}}_{B;\bar{\theta};j}(t)\}}{\partial \dot{\theta}_R(t)} \right] \Big|_{\bar{\mathbf{s}}_R} dr_{B;j} \\ &+ \int_{r_H}^R m_{B;j}(r_{B;j}) \left[ \left( \frac{d}{dt} \frac{\partial \{\mathbf{R}_{R;\Delta\theta}(t) \mathbf{x}_{B;\bar{\theta};j}(t)\}}{\partial \{\dot{\theta}_R(t)\}} \right) \right] \Big|_{\bar{\mathbf{s}}_R} dr_{B;j}, \end{aligned} \quad (4.23)$$



$$\begin{aligned} \mathbf{G}_{B;C;\theta u;j}(t) = & - \int_{r_H}^R m_{B;j}(r_{B;j}) \left[ \frac{\partial \left( \mathbf{R}_{R;\Delta\theta}(t) \dot{\mathbf{x}}_{B;\bar{\theta};j}(t) \right)}{\partial \dot{\boldsymbol{\theta}}_R(t)} \Bigg|_{\bar{S}_R} \right] dr_{B;j} \\ & + \int_{r_H}^R m_{B;j}(r_{B;j}) \left[ \left( \frac{d}{dt} \frac{\partial \left\{ \dot{\mathbf{R}}_{R;\Delta\theta}(t) \mathbf{x}_{B;\bar{\theta};j}(t) \right\}}{\partial \{\dot{\boldsymbol{\theta}}_R(t)\}} \right) \Bigg|_{\bar{S}_R} \right] dr_{B;j}, \end{aligned} \quad (4.24)$$

$$\mathbf{G}_{B;C;\theta\theta;j}(t) = \frac{1}{2} \int_{r_H}^R m_{B;j}(r_{B;j}) \left[ \left( \frac{d}{dt} \frac{\partial^2 \left\{ \dot{\mathbf{R}}_{R;\Delta\theta}(t) \mathbf{x}_{B;\bar{\theta};j}(r_{B;j}, t) \right\}^T \mathbf{R}_{R;\Delta\theta}(t) \mathbf{x}_{B;\bar{\theta};j}(t)}{\partial \{\dot{\boldsymbol{\theta}}_R(t)\}^2} \right) \Bigg|_{\bar{S}_R} \right] dr_{B;j}, \quad (4.25)$$

$$\mathbf{G}_{B;S;uu;j}(t) = \mathbf{G}_{B;S;\theta u;j}(t) = \mathbf{0}_{3 \times 3}, \quad (4.26)$$

$$\mathbf{G}_{B;S;u\theta;j}(t) = \int_{r_H}^R m_{B;j}(r_{B;j}) \left[ \left( \frac{d}{dt} \frac{\partial \left( \mathbf{R}_{R;\Delta\theta}(t) \dot{\mathbf{x}}_{B;\bar{\theta};j}(t) \right)}{\partial \dot{\boldsymbol{\theta}}_R(t)} \right) \Bigg|_{\bar{S}_R} \right] dr_{B;j}, \quad (4.27)$$

and

$$\mathbf{G}_{B;S;\theta\theta;j}(t) = \int_{r_H}^R m_{B;j}(r_{B;j}) \left[ \left( \frac{d}{dt} \frac{\partial^2 \left\{ \left( \dot{\mathbf{R}}_{R;\Delta\theta}(t) \mathbf{x}_{B;\bar{\theta};j}(t) \right)^T \mathbf{R}_{R;\Delta\theta}(t) \mathbf{x}_{B;\bar{\theta};j}(t) \right\}}{\partial \dot{\boldsymbol{\theta}}_R(t) \partial \dot{\boldsymbol{\theta}}_R(t)} \right) \Bigg|_{\bar{S}_R} \right] dr_{B;j}. \quad (4.28)$$

The matrix  $\mathbf{0}_{3 \times 3}$  represents the three by three null matrix.

The matrices  $\mathbf{G}_{B;C;j}(t)$  and  $\mathbf{G}_{B;S;j}(t)$  are asymmetric because of the description of the rotating blade elements in a fixed frame of reference and both matrices vanish if the rotor is not rotating. For a rotating rotor, the rotor sub-system matrices of Eq. (4.15) are time-dependent. It should be noted that the matrix  $\mathbf{G}_{B;S;\theta\theta;j}$  is susceptible to the assumed order of structural rotations, which defines the matrix  $\mathbf{R}_{R;\theta}(t)$  [270].

The vector  $\mathbf{Q}_{B;S;j}(t)$  represents the centrifugal stiffening and can be divided into the force vector  $\mathbf{F}_{B;S;j}(t)$  and the moment vector  $\mathbf{T}_{B;S;j}(t)$ :

$$\mathbf{Q}_{B;S;j}(t) = \left[ \left\{ \mathbf{F}_{B;S;j}(t) \right\}^T \quad \left\{ \mathbf{T}_{B;S;j}(t) \right\}^T \right]^T, \quad (4.29)$$

with

$$\mathbf{F}_{B;S;j}(t) = \int_{r_H}^R m_{B;j} \left[ \mathbf{R}_{R;\Delta\theta}(t) \ddot{\mathbf{x}}_{B;\bar{\theta};j}(t) \Bigg|_{\bar{S}_R} \right] dr_{B;j}, \quad (4.30)$$

and

$$\mathbf{T}_{B;S;j}(t) = - \int_{r_H}^R m_{B;j} \left[ \left( \frac{d}{dt} \frac{\partial \left\{ \dot{\mathbf{R}}_{R;\Delta\theta}(t) \mathbf{x}_{B;\bar{\theta};j}(t) \right\}^T \mathbf{R}_{R;\Delta\theta}(t) \mathbf{x}_{B;\bar{\theta};j}(t)}{\partial \{\dot{\boldsymbol{\theta}}_R(t)\}} \right) \Bigg|_{\bar{S}_R} \right] dr_{B;j}. \quad (4.31)$$

In deriving the system matrices, the matrix  $\mathbf{R}_{R;\theta}(t)$  is rewritten in terms of the matrix  $\mathbf{R}_{R;\bar{\theta}}$ , which expresses the rotation resulting from the mean deformation  $\bar{\boldsymbol{\theta}}_R$  and the matrix  $\mathbf{R}_{R;\Delta\theta}(t)$ , which corresponds to the perturbations  $\mathbf{R}_{R;\Delta\theta}(t)$ :

$$\mathbf{R}_{R;\theta}(t) = \mathbf{R}_{R;\Delta\theta}(t) \mathbf{R}_{R;\bar{\theta}}. \quad (4.32)$$

Furthermore, the vector  $\mathbf{x}_{B;\bar{\theta};j}(t)$  expresses the position of the point  $\mathbf{r}_{B;j}^f$  in the global inertial reference frame, accounting for the mean rotor deformations  $\bar{\boldsymbol{\theta}}_R$ :

$$\mathbf{x}_{B;\bar{\theta};j}(t) = \mathbf{R}_{R;\bar{\theta}} \mathbf{x}_{B;j}^r(\mathbf{X}_R(r_{B;j}), t). \quad (4.33)$$

Moreover, the small angle assumption for the perturbations  $\Delta\boldsymbol{\theta}_R(t)$  is adopted, allowing to approximate the matrix  $\mathbf{R}_{R;\Delta\theta}(t)$  as:

$$\mathbf{R}_{R;\Delta\theta}(t) \approx \mathbf{I}_{3 \times 3} + \Delta\bar{\boldsymbol{\theta}}_R(t), \quad (4.34)$$

where  $\Delta\bar{\boldsymbol{\theta}}_R(t)$  is the skew-symmetric maxtrix corresponding to the vector  $\Delta\boldsymbol{\theta}_R(t)$ .

If the three blades are identical, and the mean rotations  $\bar{\boldsymbol{\theta}}_R$  are assumed small, the rotor sub-system can be defined unambiguously in terms of the time-independent rotor matrices  $\mathbf{M}_R$ ,  $\mathbf{G}_{R;C}$  and  $\mathbf{G}_{R;S}$ :

$$[\mathbf{M}_H + \mathbf{M}_R(t)] \Delta\dot{\mathbf{v}}_R(t) + \mathbf{G}_{R;C}(t) \Delta\dot{\mathbf{v}}_R(t) + \mathbf{G}_{R;S}(t) \Delta\mathbf{v}_R(t) = \mathbf{Q}_{R;S}(t) + \mathbf{Q}_{R;A}(t) - \mathbf{Q}_{R;DT}(t), \quad (4.35)$$

of which the system matrices are defined as

$$\mathbf{M}_R = \sum_{j=1}^3 \mathbf{M}_{B;j}(t) = \begin{bmatrix} \mathbf{M}_{R;uu} & \mathbf{M}_{R;u\theta} \\ \mathbf{M}_{R;\theta u} & \mathbf{M}_{R;\theta\theta} \end{bmatrix}, \quad (4.36)$$

$$\mathbf{G}_{R;C} = \sum_{j=1}^3 \mathbf{G}_{B;C;j}(t) = \begin{bmatrix} \mathbf{0}_{3 \times 3} & \mathbf{0}_{3 \times 3} \\ \mathbf{0}_{3 \times 3} & \mathbf{G}_{R;C;\theta\theta} \end{bmatrix}, \quad (4.37)$$

and

$$\mathbf{G}_{R;S} = \sum_{j=1}^3 \mathbf{G}_{B;S;j}(t) = \mathbf{0}_{6 \times 6}, \quad (4.38)$$

where  $\mathbf{0}_{6 \times 6}$  is a  $6 \times 6$  null matrix, and

$$\mathbf{M}_{R;uu} = \int_{r_H}^R m_B(r_B) r_B \begin{bmatrix} \frac{3}{r_B} & 0 & 0 \\ 0 & \frac{3}{r_B} & 0 \\ 0 & 0 & \frac{3}{r_B} \end{bmatrix} dr_B, \quad (4.39)$$

$$\mathbf{M}_{R;u\theta} = \{\mathbf{M}_{R;u\theta}\}^T \int_{r_H}^R m_B(r_B) r_B \begin{bmatrix} 0 & 0 & 3 \frac{d_R}{r_B} \\ 0 & 0 & 0 \\ -3 \frac{d_R}{r_B} & 0 & 0 \end{bmatrix} dr_B, \quad (4.40)$$

$$\mathbf{M}_{R;\theta\theta} = \int_{r_H}^R m_B(r_B) r_B \begin{bmatrix} \frac{3}{2} r_B + 3 \frac{d_R^2}{r_B} & 0 & 0 \\ 0 & 3 r_B & 0 \\ 0 & 0 & \frac{3}{2} r_B + 3 \frac{d_R^2}{r_B} \end{bmatrix} dr_B, \quad (4.41)$$

and

$$\mathbf{G}_{R;C;\theta\theta} = \int_{r_H}^R m_B(r_B) \bar{\Omega}_R r_B \begin{bmatrix} 0 & 0 & 3r_B \\ 0 & 0 & 0 \\ -3r_B & 0 & 0 \end{bmatrix} dr_B. \quad (4.42)$$

It follows that, for the rotor with identical blades, the resulting centrifugal effect completely vanishes:

$$\mathbf{Q}_{R;S} = \sum_{j=1}^3 \mathbf{Q}_{B;S;j}(t) = \mathbf{0}_{6 \times 1}, \quad (4.43)$$

where  $\mathbf{0}_{6 \times 1}$  is a  $6 \times 1$  null vector. Since the blades are identical,  $r_{B;j}$  is replaced by  $r_B$  and  $m_{B;j}(r_{B;j})$  by  $m_B(r_B)$ .

With reference to Figure 4.4, the equations of motion of the tower sub-system can be defined straightforwardly:

$$[\mathbf{M}_T + \mathbf{M}_N] \ddot{\mathbf{v}}_T(t) + \mathbf{C}_T \dot{\mathbf{v}}_T(t) + \mathbf{K}_T \mathbf{v}_T(t) = \mathbf{Q}_{T;E}(t) + \mathbf{Q}_{T;DT}(t). \quad (4.44)$$

The turbine system is now described by the equations of motion of the tower sub-system, Eq. (4.44) and the rotor sub-system, Eq (4.15) or Eq. (4.35), with the degrees of freedom  $\mathbf{v}_T(t)$  and  $\mathbf{v}_R(t)$ , respectively, and the coupling forces  $\mathbf{Q}_{T;DT}(t)$  and  $\mathbf{Q}_{R;DT}(t)$ . Concerning translations, the motions of the rotor and tower sub-systems are equal and the forces  $\mathbf{F}_{T;DT}(t)$  and  $\mathbf{F}_{R;DT}(t)$  counteract each other, implying that the translations  $\mathbf{u}_T(t)$  and  $\mathbf{u}_R(t)$  are equal. The transfer of the torques is affected by the dynamic response of the drive train. Considering an indirect drive with rigid shafts, the torque transferred to the tower top balances the aerodynamic torque. If, in addition, a rigid yaw connection is assumed, the tilting and yawing rotations of rotor and tower top are equal, i.e.,  $\theta_{R;X}(t) = \theta_{T;X}(t)$  and  $\theta_{R;Z}(t) = \theta_{T;Z}(t)$ .

## 4.2. AERODYNAMIC EXCITATION

### 4.2.1. FORCE DEFINITIONS

In Section 4.1, the equations of motion of a rigid rotor on a flexible tower were derived. This model can now be used to derive the state-independent apparent mass, damping and stiffness of the rotor. To this end, an aerodynamic excitation model needs to be formulated. To allow for the analysis of wind turbine support structures, the apparent aero-elastic characteristics should be defined in the global inertial reference frame. As a basis, however, the aerodynamic forces need to be defined locally, using the local blade reference frames.

Figure 4.5(a) depicts a schematic cross-section of the  $j$ -th aerofoil, defined within the floating  $r_{B;j} Y_R Z_{B;j}$  reference frame. The local configuration of the aerofoil is indicated by the local floating  $r_{B;j} y_{B;j} z_{B;j}$  coordinate system, where the  $y_{B;j}$  and  $z_{B;j}$  axes correspond with the principal axes of the cross-section. The orientation of this local reference frame varies along the length of the blade, due to the twist angle  $\beta_{B;0;j}(r_{B;j})$  around the  $r_{B;j}$  axis. The time-varying pitch angle of the blades is given by  $\beta_{B;j}(r_{B;j}, t)$ . The subscript  $j$  and the dependency on  $r_{B;j}$  indicate that this pitch angle corresponds to a segmented individual blade pitching. For the derivations in this chapter, no control system is accounted for. As

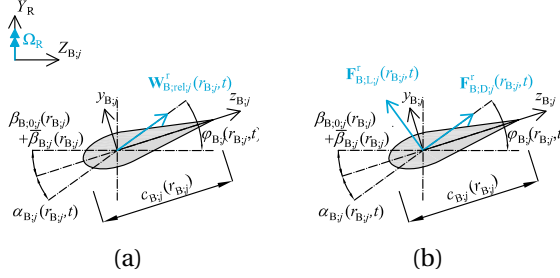


Figure 4.5: Aerodynamic configuration, with (a) the definition of the angle of attack with respect to the relative wind velocity vector, and (b) the definition of the drag and the lift forces.

4

a consequence, the perturbation of the pitch angle is neglected from here on, implying that  $\beta_{B;j}(r_{B;j}, t) = \bar{\beta}_{B;j}(r_{B;j})$ .

The force expressions are derived on the basis of a pitch angle corresponding to the mean pitch angle for the operational state under consideration, implying that no active pitch control is accounted for.  $c_{B;j}(r_{B;j})$  represents the chord width of the aerofoil of the  $j$ -th blade. The aerofoil is subjected to the relative wind velocity vector  $\mathbf{W}_{B;rel;j}^r(r_{B;j}, t)$ , which acts under an angle  $\alpha_{B;j}(r_{B;j}, t)$  – the angle of attack – with respect to the local rotating local  $z_{B;j}$  axis. It should be noted that the definition of the positive angles  $\beta_{0;j}(r_{B;j})$ ,  $\bar{\beta}_{B;j}(r_{B;j})$  and  $\alpha_{B;j}(r_{B;j}, t)$ , as indicated in Figure 4.5, contradicts the right-hand rule sign convention.

As a result of the relative wind velocity vector  $\mathbf{W}_{B;rel;j}^r(r_{B;j}, t)$ , the aerofoil experiences a lift and a drag force, the latter directed parallel to the wind vector and the former perpendicular to the wind vector. The configuration of these forces is depicted in Figure 4.5(b), from which it can be seen that the angle of attack defines the angle between the lift force and the local rotating  $y_{B;j}$  axis of the aerofoil. The angle of the lift force with respect to the axis of rotation is given by  $\varphi_{B;j}(r_{B;j}, t)$ .

With reference to Section 2.3, the quasi-stationary lift force  $\mathbf{F}_{B;L;j}^r(r_{B;j}, t)$  on the aerofoil is obtained as

$$\mathbf{F}_{B;L;j}^r(r_{B;j}, t) = \rho_{\text{air}} \left( \mathbf{W}_{B;rel;j}^r(r_{B;j}, t) \times \boldsymbol{\Gamma}_{B;b;j}^r(r_{B;j}, t) \right), \quad (4.45)$$

with

$$\boldsymbol{\Gamma}_{B;b;j}^r(r_{B;j}, t) = \frac{1}{2} c_{B;j}(r_{B;j}) C_{B;L}(r_{B;j}, t) \left| \mathbf{W}_{B;rel;j}^r(r_{B;j}, t) \right| \mathbf{e}_{B;r}^r, \quad (4.46)$$

where the lift coefficient is defined as

$$C_{B;L;j}(r_{B;j}, t) = C_{B;L;j}^\alpha(r_{B;j}) \sin \alpha_{B;j}(r_{B;j}, t) + C_{B;L;j}^c(r_{B;j}), \quad (4.47)$$

from which the  $\alpha$ -dependent and the camber-dependent force components,  $\mathbf{F}_{B;L;j}^{\alpha;r}(r_{B;j}, t)$  and  $\mathbf{F}_{B;L;j}^{c;r}(r_{B;j}, t)$ , can be defined as:

$$\mathbf{F}_{B;L;j}^{\alpha;r}(r_{B;j}, t) = \frac{1}{2} \rho_{\text{air}} c_{B;j}(r_{B;j}) C_{B;L;j}^\alpha \left( \{\bar{\beta}_{B;j}(r_{B;j})\}^T \mathbf{W}_{B;rel;j}^r(r_{B;j}, t) \right) \left( \mathbf{W}_{B;rel;j}^r(r_{B;j}, t) \times \mathbf{e}_{B;r}^r \right), \quad (4.48)$$

and

$$\mathbf{F}_{B;L;j}^{C;r}(r_{B;j}, t) = \frac{1}{2} \rho_{\text{air}} c_{B;j}(r_{B;j}) C_{B;L;j}^C \left| \mathbf{W}_{B;\text{rel};j}^r(r_{B;j}, t) \right| \left( \mathbf{W}_{B;\text{rel};j}^r(r_{B;j}, t) \times \mathbf{e}_{B;r}^r \right). \quad (4.49)$$

Considering the drag force, only skin friction is accounted for. This, because the current analysis is restricted to attached flows, implying that the angle of attack is relatively small, and the contribution of the pressure drag is negligible. Based on this assumption, the drag force  $\mathbf{F}_{B;D;j}^r(r_{B;j}, t)$  can be estimated by determining the viscous drag only:

$$\mathbf{F}_{B;D;j}^r(r_{B;j}, t) = \frac{1}{2} \rho_{\text{air}} c_{B;j}(r_{B;j}) C_{B;D;j}(r_{B;j}) \mathbf{W}_{B;\text{rel};j}^r(r_{B;j}, t) \left| \mathbf{W}_{B;\text{rel};j}^r(r_{B;j}, t) \right|, \quad (4.50)$$

with the aerofoil-dependent drag coefficient  $C_{B;D;j}(r_{B;j})$ .

In addition, an inertia force  $\mathbf{F}_{B;I;j}^r(r_{B;j}, t)$  can be accounted for. This force is aligned with the acceleration vector of the effective air flow field and is derived from:

$$\mathbf{F}_{B;I;j}^r(r_{B;j}, t) = \frac{1}{4} \rho_{\text{air}} \pi \{c_{B;j}(r_{B;j})\}^2 \mathbf{W}_{B;\text{rel};j}^r(r_{B;j}, t). \quad (4.51)$$

Given that the lift and drag coefficients are only known for flows perpendicular to the blade axis, the presented theory only allows for the derivations of the aerodynamic forces in the plane presented in Figure 4.5. Moreover, the presented force equations are in principle only valid for an instantaneous flow-force relation, implying that these expressions do not account for the loss of the aerodynamic equilibrium after a disturbance of the flow. In Chapter 2, it was shown that the aerodynamic force on a rotating blade in turbulent wind conditions can be approximated reasonably well with the current aerodynamic model.

#### 4.2.2. RELATIVE WIND VECTORS

The aerodynamic forces depend on the relative wind velocity  $\mathbf{W}_{B;\text{rel};j}^r(r_{B;j}, t)$ , normal to the longitudinal blade axes, implying that for each blade, the relative velocity vector needs to be defined in its moving frame of reference. The relative wind velocity describes the difference between the wind velocity at the rotor plane and the structural velocity. At the rotor plane, the wind velocity is expressed by the time-dependent velocity vector field  $\mathbf{W}_R(\mathbf{X}_T, t)$ , containing the lateral, axial and vertical velocity components. The derivation of the velocity field at the rotor plane requires an analysis of the inflow conditions, for instance on the basis of the momentum balance theory. This would allow for the definition of a static, equilibrium or dynamic wake, or a skewed wake in accordance with [40, 196]. Alternatively, the wake can be defined with the employment of vortex theory [197]. For more details, reference is made to Section 2.2. As a consequence,  $\mathbf{W}_R(\mathbf{X}_T, t)$  includes the axially and tangentially induced velocity fields, resulting from the rotor rotation.

Defining the position of a section of the  $j$ -th blade in the inertial reference frame as  $\mathbf{X}_{B;j}$ , the velocity field at this section can be expressed as  $\mathbf{W}_R(\mathbf{X}_{B;j}, t)$ . For non-homogeneous inflow conditions, this velocity field would represent the rotationally sampled inflow at the rotor plane. The structural velocity, including the rotational velocity, can be found from the time derivative of the position vector  $\mathbf{x}_{B;j}(t)$ , see Eq. (4.12). The relative wind velocity  $\mathbf{W}_{B;\text{rel};j}^r(r_{B;j}, t)$  can now be obtained from

$$\mathbf{W}_{B;\text{rel};j}^r(r_{B;j}, t) = \mathbf{\Xi} \left\{ \mathbf{R}_{B;\bar{\Psi};j}(t) \right\}^{-1} \left\{ \mathbf{R}_{R;\theta}(t) \right\}^{-1} \left\{ \mathbf{W}_R(\mathbf{X}_{B;j}, t) - \dot{\mathbf{x}}_{B;j}(t) \right\}. \quad (4.52)$$

The left multiplication with the matrix  $\Xi$  is applied to ensure that only the in-plane kinematics are accounted for. The matrix  $\Xi$  is defined as

$$\Xi = \begin{bmatrix} 0 & 0 & 0 \\ 0 & 1 & 0 \\ 0 & 0 & 1 \end{bmatrix}. \quad (4.53)$$

The inertia force requires the relative acceleration. This relative acceleration is defined as the acceleration of the wind velocity at the rotor plane, as experienced by a point on a rotating blade, minus the structural acceleration, both defined in the global rotating frames of reference.

### 4.2.3. GLOBAL AERODYNAMIC FORCES

Having defined the aerodynamic excitation within the floating blade reference frames, the resulting forces can be transformed to the inertial reference frame. After subsequent integration of these forces over the rotor plane, the total rotor force results. Since the blade forces also induce a moment around the tower top, the total rotor force consists of both a force and a moment component.

Denoting the total aerodynamic force  $\mathbf{F}_{B;A;j}^r(r_{B;j}, t)$  – with ‘A’ indicating the general aerodynamic nature of the force, and refers to either lift, drag, or inertia – in the local rotating blade frames of reference as the summation of the lift, drag and inertia forces, the aerodynamic force components in the inertial frame of reference  $\mathbf{F}_{B;A;j}(\mathbf{X}_{B;j}, t)$  can be obtained from

$$\mathbf{F}_{B;A;j}(\mathbf{X}_{B;j}, t) = \mathbf{R}_{R;\theta}(t) \mathbf{R}_{B;\Psi;j}(t) \mathbf{F}_{B;A;j}^r(r_{B;j}, t). \quad (4.54)$$

The moments around the origin tower top can subsequently be obtained from:

$$\mathbf{T}_{B;A;j}(\mathbf{X}_{B;j}, t) = (\mathbf{x}_{B;j}(\mathbf{X}_{B;j}, t) - \mathbf{u}_R(t)) \times \mathbf{F}_{B;A;j}(\mathbf{X}_{B;j}, t). \quad (4.55)$$

The total resulting aerodynamic rotor excitation  $\mathbf{Q}_{R;A}(t)$  can be found from integrating the separate blade contributions over the blade lengths and adding each contribution:

$$\mathbf{Q}_{R;A}(t) = \sum_{j=1}^3 \int_{r_H}^R \mathbf{Q}_{B;A;j}(\mathbf{X}_{B;j}, t) dr_{B;j}, \quad (4.56)$$

where the aerodynamic blade force  $\mathbf{Q}_{B;A;j}(\mathbf{X}_{B;j}, t)$  is defined as

$$\mathbf{Q}_{B;A;j}(\mathbf{X}_{B;j}, t) = [\mathbf{F}_{B;A;j}(\mathbf{X}_{B;j}, t) \quad \mathbf{T}_{B;A;j}(\mathbf{X}_{B;j}, t)]^T. \quad (4.57)$$

With the implementation of the relative-flow characteristics velocity and acceleration,  $\mathbf{W}_{B;rel;j}^r(r_{B;j}, t)$  and  $\dot{\mathbf{W}}_{B;rel;j}^r(r_{B;j}, t)$ , Eq. (4.56), with the aerodynamic force definitions presented in Section 4.2.1, represents a state-dependent expression for the aerodynamic force on the wind turbine rotor. It should be noted that the aerodynamic force on the turbine rotor is derived on the basis of two-dimensional force model and, therefore, does not account for three-dimensional effects such as tip and root losses, and wind velocity components parallel to the blade axes. The aerodynamic forces are now defined on the basis of the blade element theory. Combined with the actuator disc theory, the resulting wind velocity at the rotor plane are obtained [35]. On the basis of this approach, the aerodynamic forces on a wind turbine rotor are approximated in Sections 4.4 and 4.5.

## 4.3. APPARENT AERO-ELASTIC PROPERTIES

### 4.3.1. APPROXIMATION PROCEDURE

In Section 4.2, the state-independent aerodynamic excitation on a turbine rotor within the inertial reference frame was derived, see Eq. (4.56), with which an expression for the aerodynamic excitation of the rotor sub-system is obtained. The aerodynamic force expressions, presented in Section 4.2.1 relate the forcing and the structural motion in a non-linear manner. In other words, the force expressions contain apparent aero-elastic properties, introducing a state dependency with respect to the degrees of freedom  $\mathbf{v}_R(t)$  of the rotor sub-system. In this section, state-independent expressions of these apparent dynamics are derived. This derivation entails an approximation of the force expressions, by means of a first-order Taylor expansion with respect to  $\mathbf{v}_R(t)$  and its time derivatives, around the state  $\bar{\mathbf{S}}_R$  as given by Eq. (4.14), which was used earlier for the linearization of the equations of motion of the rotor sub-system too:

$$\begin{aligned} \mathbf{Q}_{B;A;j}(\mathbf{X}_{B;j}, t) \approx & \left[ \mathbf{Q}_{B;A;j}(\mathbf{X}_{B;j}, t) \Big|_{\bar{\mathbf{S}}_R} \right] + \left[ \frac{\partial \mathbf{Q}_{B;A;j}(\mathbf{X}_{B;j}, t)}{\partial \{\mathbf{v}_R(t)\}} \Big|_{\bar{\mathbf{S}}_R} \right] \Delta \mathbf{v}_R(t) \\ & + \left[ \frac{\partial \mathbf{Q}_{B;A;j}(\mathbf{X}_{B;j}, t)}{\partial \{\dot{\mathbf{v}}_R(t)\}} \Big|_{\bar{\mathbf{S}}_R} \right] \Delta \dot{\mathbf{v}}_R(t) + \left[ \frac{\partial \mathbf{Q}_{B;A;j}(\mathbf{X}_{B;j}, t)}{\partial \{\ddot{\mathbf{v}}_R(t)\}} \Big|_{\bar{\mathbf{S}}_R} \right] \Delta \ddot{\mathbf{v}}_R(t). \end{aligned} \quad (4.58)$$

The first term of Eq. (4.58) represents the force vector which is independent of the tower top motion. The remaining terms relate the aerodynamic force to  $\mathbf{v}_R(t)$ . The matrices within brackets are referred to as the state-independent apparent stiffness, damping and mass, respectively.

In the Sections 4.3.2 to 4.3.5, the components within brackets in Eq. (4.58) are presented for the lift, drag and inertia forces, separately. For these derivations, use is made of software for symbolic manipulations. In doing so, the orthonormality of the matrices  $\mathbf{R}_{B;\bar{\Psi};j}(t)$  and  $\mathbf{R}_{R;\bar{\theta}}(t)$  is recognized. Moreover, the inverse of the matrix  $\mathbf{R}_{R;\Delta\theta}(t)$  can be approximated as

$$\{\mathbf{R}_{R;\Delta\theta}(t)\}^{-1} \approx \mathbf{I}_{3 \times 3} - \Delta \bar{\boldsymbol{\theta}}_R(t). \quad (4.59)$$

### 4.3.2. STATE-INDEPENDENT AERODYNAMIC FORCE APPROXIMATIONS

The first term of Eq. (4.58) relates to the state-independent components of the aerodynamic excitation for the state  $\bar{\mathbf{S}}_R$ , and contains the mean components of both the aerodynamic forces and moments (see Eq. (4.57)):

$$\mathbf{Q}_{B;A;j}(\mathbf{X}_{B;j}, t) \Big|_{\bar{\mathbf{S}}_R} = \left[ \mathbf{F}_{B;A;j}(\mathbf{X}_{B;j}, t) \Big|_{\bar{\mathbf{S}}_R} \quad \mathbf{T}_{B;A;j}(\mathbf{X}_{B;j}, t) \Big|_{\bar{\mathbf{S}}_R} \right]^T. \quad (4.60)$$

The lift and drag force approximations can be expressed as

$$\begin{aligned} \mathbf{F}_{B;A;j}(\mathbf{X}_{B;j}, t) \Big|_{\bar{\mathbf{S}}_R} &= \frac{1}{2} \rho_{\text{air}} c_{B;j}(r_{B;j}) C_{B;A;j}(r_{B;j}) \cdot \\ & \left\{ \mathbf{A}_{B;A;j}(\mathbf{X}_{B;j}, t) \Xi \left\{ \mathbf{R}_{B;\bar{\Psi};j}(t) \right\}^T \left\{ \mathbf{R}_{R;\bar{\theta}} \right\}^T \left( \mathbf{W}_R(\mathbf{X}_{B;j}, t) - \dot{\mathbf{x}}_{B;\bar{\theta};j}(\mathbf{X}_{B;j}, t) \right) \right\}, \end{aligned} \quad (4.61)$$

whereas the state-independent moment vector around the tower top is obtained as

$$\begin{aligned} \mathbf{T}_{B;A;j}(\mathbf{X}_{B;j}, t) \Big|_{\bar{S}_R} &= \frac{1}{2} \rho_{\text{air}} c_{B;j}(r_{B;j}) C_{B;A;j}(r_{B;j}) \cdot \\ &\left\{ \tilde{\mathbf{x}}_{B;\bar{\theta};j}(\mathbf{X}_{B;j}, t) \mathbf{A}_{B;A;j}(\mathbf{X}_{B;j}, t) \Xi \left\{ \mathbf{R}_{B;\bar{\Psi};j}(t) \right\}^T \left\{ \mathbf{R}_{R;\bar{\theta}} \right\}^T \left( \mathbf{W}_R(\mathbf{X}_{B;j}, t) - \dot{\mathbf{x}}_{B;\bar{\theta};j}(\mathbf{X}_{B;j}, t) \right) \right\}, \end{aligned} \quad (4.62)$$

where  $C_{B;A;j}(r_{B;j})$  represents the aero-elastic coefficients  $C_{B;L;j}^\alpha(r_{B;j})$ ,  $C_{B;L;j}^C(r_{B;j})$  and  $C_{B;D;j}(r_{B;j})$ , respectively.  $\tilde{\mathbf{x}}_{B;\bar{\theta};j}(\mathbf{X}_{B;j}, t)$  is the skew-symmetric matrix of the vector  $\mathbf{x}_{B;\bar{\theta};j}(\mathbf{X}_{B;j}, t)$ , which accounts for the cross product in Eq. (4.55) to obtain the moment around the tower top delivered by the force. For the different aerodynamic forces – lift and drag – the matrix  $\mathbf{A}_{B;A;j}(\mathbf{X}_{B;j}, t)$  is obtained as

$$\begin{aligned} \mathbf{A}_{B;L;j}^\alpha(\mathbf{X}_{B;j}, t) &= \\ &-\mathbf{R}_{R;\bar{\theta}} \mathbf{R}_{B;\bar{\Psi};j}(t) \left\{ \tilde{\boldsymbol{\beta}}_{B;j}(r_{B;j}) \right\}^T \Xi \left\{ \mathbf{R}_{B;\bar{\Psi};j}(t) \right\}^T \left\{ \mathbf{R}_{R;\bar{\theta}} \right\}^T \left( \mathbf{W}_R(\mathbf{X}_{B;j}, t) - \dot{\mathbf{x}}_{B;\bar{\theta};j}(\mathbf{X}_{B;j}, t) \right) \tilde{\mathbf{e}}_{B;r}, \end{aligned} \quad (4.63)$$

$$\mathbf{A}_{B;L;j}^C(\mathbf{X}_{B;j}, t) = -\mathbf{R}_{R;\bar{\theta}} \mathbf{R}_{B;\bar{\Psi};j}(t) \Xi \left\{ \mathbf{R}_{B;\bar{\Psi};j}(t) \right\}^T \left\{ \mathbf{R}_{R;\bar{\theta}} \right\}^T \left( \mathbf{W}_R(\mathbf{X}_{B;j}, t) - \dot{\mathbf{x}}_{B;\bar{\theta};j}(\mathbf{X}_{B;j}, t) \right) \tilde{\mathbf{e}}_{B;r}. \quad (4.64)$$

and

$$\mathbf{A}_{B;D;j}(\mathbf{X}_{B;j}, t) = \mathbf{R}_{R;\bar{\theta}} \mathbf{R}_{B;\bar{\Psi};j}(t) \Xi \left\{ \mathbf{R}_{B;\bar{\Psi};j}(t) \right\}^T \left\{ \mathbf{R}_{R;\bar{\theta}} \right\}^T \left( \mathbf{W}_R(\mathbf{X}_{B;j}, t) - \dot{\mathbf{x}}_{B;\bar{\theta};j}(\mathbf{X}_{B;j}, t) \right), \quad (4.65)$$

where  $\tilde{\mathbf{e}}_{B;r}$  is the skew-symmetric matrix of the unit vector  $\mathbf{e}_{B;r}^T$ , defining the longitudinal axis of the  $j$ -th blade in its local frame of reference.

The state-independent approximations of the inertia force and moment are obtained as

$$\begin{aligned} \mathbf{F}_{B;I;j}(\mathbf{X}_{B;j}, t) \Big|_{\bar{S}_R} &= \frac{1}{4} \rho_{\text{air}} \pi \left\{ c_{B;j}(r_{B;j}) \right\}^2 \cdot \\ &\mathbf{R}_{R;\bar{\theta}} \mathbf{R}_{B;\bar{\Psi};j}(t) \Xi \left\{ \dot{\mathbf{R}}_{B;\bar{\Psi};j}(t) \right\}^T \left\{ \mathbf{R}_{R;\bar{\theta}} \right\}^T \left( \mathbf{W}_R(\mathbf{X}_{B;j}, t) - \dot{\mathbf{x}}_{B;\bar{\theta};j}(\mathbf{X}_{B;j}, t) \right) \\ &-\mathbf{R}_{R;\bar{\theta}} \mathbf{R}_{B;\bar{\Psi};j}(t) \Xi \left\{ \mathbf{R}_{B;\bar{\Psi};j}(t) \right\}^T \left\{ \mathbf{R}_{R;\bar{\theta}} \right\}^T \ddot{\mathbf{x}}_{B;\bar{\theta};j}(\mathbf{X}_{B;j}, t), \end{aligned} \quad (4.66)$$

and

$$\begin{aligned} \mathbf{T}_{B;I;j}(\mathbf{X}_{B;j}, t) \Big|_{\bar{S}_R} &= \frac{1}{4} \rho_{\text{air}} \pi \left\{ c_{B;j}(r_{B;j}) \right\}^2 \cdot \\ &\tilde{\mathbf{x}}_{B;\bar{\theta};j}(\mathbf{X}_{B;j}, t) \mathbf{R}_{R;\bar{\theta}} \mathbf{R}_{B;\bar{\Psi};j}(t) \Xi \left\{ \dot{\mathbf{R}}_{B;\bar{\Psi};j}(t) \right\}^T \left\{ \mathbf{R}_{R;\bar{\theta}} \right\}^T \left( \mathbf{W}_R(\mathbf{X}_{B;j}, t) - \dot{\mathbf{x}}_{B;\bar{\theta};j}(\mathbf{X}_{B;j}, t) \right) \\ &-\tilde{\mathbf{x}}_{B;\bar{\theta};j}(\mathbf{X}_{B;j}, t) \mathbf{R}_{R;\bar{\theta}} \mathbf{R}_{B;\bar{\Psi};j}(t) \Xi \left\{ \mathbf{R}_{B;\bar{\Psi};j}(t) \right\}^T \left\{ \mathbf{R}_{R;\bar{\theta}} \right\}^T \ddot{\mathbf{x}}_{B;\bar{\theta};j}(\mathbf{X}_{B;j}, t). \end{aligned} \quad (4.67)$$



The presented force expressions allow for the approximation of the aerodynamic force on the tower top without the contribution of the apparent stiffness, mass and damping. The expressions present the forces along the length of the blades within the global inertial frame of reference.

### 4.3.3. STATE-INDEPENDENT APPARENT STIFFNESS APPROXIMATIONS

The second term of Eq. (4.58) relates the aerodynamic force to the structural deformation of the tower top. The matrix  $\left. \frac{\partial \mathbf{Q}_{B;A;j}(\mathbf{X}_{B;j},t)}{\partial \{\mathbf{v}_R(t)\}} \right|_{\bar{s}_R}$  expresses the state-independent apparent stiffness, which can be subdivided for the different aerodynamic forces and moments related to either the tower top deflection  $\mathbf{u}_R(t)$ , or the rotation  $\boldsymbol{\theta}_R(t)$ :

$$\left. \frac{\partial \mathbf{Q}_{B;A;j}(\mathbf{X}_{B;j},t)}{\partial \mathbf{v}_R(t)} \right|_{\bar{s}_R} = \begin{bmatrix} \left. \frac{\partial \mathbf{F}_{B;A;j}(\mathbf{X}_{B;j},t)}{\partial \mathbf{u}_R(t)} \right|_{\bar{s}_R} & \left. \frac{\partial \mathbf{F}_{B;A;j}(\mathbf{X}_{B;j},t)}{\partial \boldsymbol{\theta}_R(t)} \right|_{\bar{s}_R} \\ \left. \frac{\partial \mathbf{T}_{B;A;j}(\mathbf{X}_{B;j},t)}{\partial \mathbf{u}_R(t)} \right|_{\bar{s}_R} & \left. \frac{\partial \mathbf{T}_{B;A;j}(\mathbf{X}_{B;j},t)}{\partial \boldsymbol{\theta}_R(t)} \right|_{\bar{s}_R} \end{bmatrix}. \quad (4.68)$$

The apparent stiffness resulting from lateral deformations equals zero for all force components:

$$\left. \frac{\partial \mathbf{F}_{B;A;j}(\mathbf{X}_{B;j},t)}{\partial \mathbf{u}_R(t)} \right|_{\bar{s}_R} = \left. \frac{\partial \mathbf{T}_{B;A;j}(\mathbf{X}_{B;j},t)}{\partial \mathbf{u}_R(t)} \right|_{\bar{s}_R} = \mathbf{0}_{3 \times 3}. \quad (4.69)$$

A rotation of the tower top affects the orientation of the wind inflow on the rotor plane. Moreover, the orientation of the aerodynamic forces on the different blade sections within the global inertial reference frame is affected. As a consequence, the apparent stiffness matrices  $\left. \frac{\partial \mathbf{F}_{B;A;j}(\mathbf{X}_{B;j},t)}{\partial \boldsymbol{\theta}_R(t)} \right|_{\bar{s}_R}$  and  $\left. \frac{\partial \mathbf{T}_{B;A;j}(\mathbf{X}_{B;j},t)}{\partial \boldsymbol{\theta}_R(t)} \right|_{\bar{s}_R}$  contain non-zero entries. For the lift and drag forces, these matrices are obtained as

$$\begin{aligned} \left. \frac{\partial \mathbf{F}_{B;A;j}(\mathbf{X}_{B;j},t)}{\partial \boldsymbol{\theta}_R(t)} \right|_{\bar{s}_R} &= \frac{1}{2} \rho_{\text{air}} c_{B;j}(r_{B;j}) C_{B;A;j}(r_{B;j}) \cdot \\ &\left[ (\mathbf{A}_{B;A;j}(\mathbf{X}_{B;j},t) + \mathbf{B}_{B;A;j}(\mathbf{X}_{B;j},t)) \Xi \left\{ \mathbf{R}_{B;\bar{\Psi};j}(t) \right\}^T \left\{ \mathbf{R}_{R;\bar{\theta}} \right\}^T \tilde{\mathbf{W}}_{B;j}(\mathbf{X}_{B;j},t) - \tilde{\mathbf{q}}_{B;A;j}(\mathbf{X}_{B;j},t) \right], \end{aligned} \quad (4.70)$$

and

$$\begin{aligned} \left. \frac{\partial \mathbf{T}_{B;A;j}(\mathbf{X}_{B;j},t)}{\partial \boldsymbol{\theta}_R(t)} \right|_{\bar{s}_R} &= \frac{1}{2} \rho_{\text{air}} c_{B;j}(r_{B;j}) C_{B;A;j}(r_{B;j}) \left[ \tilde{\mathbf{x}}_{B;\bar{\theta};j}(\mathbf{X}_{B;j},t) \right. \\ &\left. \left\{ (\mathbf{A}_{B;A;j}(\mathbf{X}_{B;j},t) + \mathbf{B}_{B;A;j}(\mathbf{X}_{B;j},t)) \Xi \left\{ \mathbf{R}_{B;\bar{\Psi};j}(t) \right\}^T \left\{ \mathbf{R}_{R;\bar{\theta}} \right\}^T \tilde{\mathbf{W}}_{B;j}(\mathbf{X}_{B;j},t) - \tilde{\mathbf{q}}_{B;A;j}(\mathbf{X}_{B;j},t) \right\} \right. \\ &\left. + \tilde{\mathbf{q}}_{B;A;j}(\mathbf{X}_{B;j},t) \tilde{\mathbf{x}}_{B;\bar{\theta};j}(\mathbf{X}_{B;j},t) \right]. \end{aligned} \quad (4.71)$$

$\tilde{\mathbf{W}}_R(\mathbf{X}_{B;j}, t)$  is the skew-symmetric matrix of the vector  $\mathbf{W}_R(\mathbf{X}_{B;j}, t)$ , and  $\tilde{\mathbf{q}}_{B;A;j}(\mathbf{X}_{B;j}, t)$  is the skew-symmetric matrix of the vector  $\bar{\mathbf{q}}_{B;A;j}(\mathbf{X}_{B;j}, t)$ :

$$\bar{\mathbf{q}}_{B;A;j}(\mathbf{X}_{B;j}, t) = \mathbf{A}_{B;A;j}(\mathbf{X}_{B;j}, t) \Xi \left\{ \mathbf{R}_{B;\Psi;j}(t) \right\}^T \left\{ \mathbf{R}_{R;\bar{\theta}} \right\}^T \left[ \mathbf{W}_R(\mathbf{X}_{B;j}, t) - \dot{\mathbf{x}}_{B;\bar{\theta};j}(\mathbf{X}_{B;j}, t) \right]. \quad (4.72)$$

For the different lift and drag forces, the matrix  $\mathbf{B}_{B;A;j}(\mathbf{X}_{B;j}, t)$  is given by

$$\mathbf{B}_{B;L;j}^\alpha(\mathbf{X}_{B;j}, t) = -\mathbf{R}_{R;\bar{\theta}} \mathbf{R}_{B;\Psi;j}(t) \tilde{\mathbf{e}}_{B;T} \Xi \left\{ \mathbf{R}_{B;\Psi;j}(t) \right\}^T \left\{ \mathbf{R}_{R;\bar{\theta}} \right\}^T \left( \mathbf{W}_R(\mathbf{X}_{B;j}, t) - \dot{\mathbf{x}}_{B;\bar{\theta};j}(\mathbf{X}_{B;j}, t) \right) \left\{ \boldsymbol{\beta}_{B;j}(r_{B;j}) \right\}^T, \quad (4.73)$$

$$\mathbf{B}_{B;L;j}^c(\mathbf{X}_{B;j}, t) = -\mathbf{R}_{R;\bar{\theta}} \mathbf{R}_{B;\Psi;j}(t) \tilde{\mathbf{e}}_{B;T} \Xi \left\{ \mathbf{R}_{B;\Psi;j}(t) \right\}^T \left\{ \mathbf{R}_{R;\bar{\theta}} \right\}^T \left( \mathbf{W}_R(\mathbf{X}_{B;j}, t) - \dot{\mathbf{x}}_{B;\bar{\theta};j}(\mathbf{X}_{B;j}, t) \right) \frac{\left\{ \Xi \left\{ \mathbf{R}_{B;\Psi;j}(t) \right\}^T \left\{ \mathbf{R}_{R;\bar{\theta}} \right\}^T \left( \mathbf{W}_R(\mathbf{X}_{B;j}, t) - \dot{\mathbf{x}}_{B;\bar{\theta};j}(\mathbf{X}_{B;j}, t) \right) \right\}^T}{\left| \Xi \left\{ \mathbf{R}_{B;\Psi;j}(t) \right\}^T \left\{ \mathbf{R}_{R;\bar{\theta}} \right\}^T \left( \mathbf{W}_R(\mathbf{X}_{B;j}, t) - \dot{\mathbf{x}}_{B;\bar{\theta};j}(\mathbf{X}_{B;j}, t) \right) \right|^2}, \quad (4.74)$$

and

$$\mathbf{B}_{B;D;j}(\mathbf{X}_{B;j}, t) = \mathbf{R}_{R;\bar{\theta}} \mathbf{R}_{B;\Psi;j}(t) \frac{\left\{ \Xi \left\{ \mathbf{R}_{B;\Psi;j}(t) \right\}^T \left\{ \mathbf{R}_{R;\bar{\theta}} \right\}^T \left( \mathbf{W}_R(\mathbf{X}_{B;j}, t) - \dot{\mathbf{x}}_{B;\bar{\theta};j}(\mathbf{X}_{B;j}, t) \right) \right\}^T}{\left| \Xi \left\{ \mathbf{R}_{B;\Psi;j}(t) \right\}^T \left\{ \mathbf{R}_{R;\bar{\theta}} \right\}^T \left( \mathbf{W}_R(\mathbf{X}_{B;j}, t) - \dot{\mathbf{x}}_{B;\bar{\theta};j}(\mathbf{X}_{B;j}, t) \right) \right|^2}. \quad (4.75)$$

The apparent stiffness resulting from structural rotations for the inertia force is obtained as

$$\left. \frac{\partial \mathbf{F}_{B;I;j}(\mathbf{X}_{B;j}, t)}{\partial \boldsymbol{\theta}_R(t)} \right|_{\bar{S}_R} = \frac{1}{4} \rho_{\text{air}} \pi \left\{ c_{B;j}(r_{B;j}) \right\}^2 \cdot \left[ \mathbf{R}_{R;\bar{\theta}} \mathbf{R}_{B;\Psi;j}(t) \Xi \left\{ \dot{\mathbf{R}}_{B;\Psi;j}(t) \right\}^T \left\{ \mathbf{R}_{R;\bar{\theta}} \right\}^T \tilde{\mathbf{W}}_{B;j}(r_{B;j}) - \tilde{\mathbf{q}}_{B;I;j}(\mathbf{X}_{B;j}, t) \right], \quad (4.76)$$

and

$$\left. \frac{\partial \mathbf{T}_{B;I;j}(\mathbf{X}_{B;j}, t)}{\partial \boldsymbol{\theta}_R(t)} \right|_{\bar{S}_R} = \frac{1}{4} \rho_{\text{air}} \pi \left\{ c_{B;j}(r_{B;j}) \right\}^2 \cdot \left[ \dot{\mathbf{x}}_{B;\bar{\theta};j} \left\{ \mathbf{R}_{R;\bar{\theta}} \mathbf{R}_{B;\Psi;j}(t) \Xi \left\{ \dot{\mathbf{R}}_{B;\Psi;j}(t) \right\}^T \left\{ \mathbf{R}_{R;\bar{\theta}} \right\}^T \tilde{\mathbf{W}}_{B;j}(r_{B;j}) - \tilde{\mathbf{q}}_{B;I;j}(\mathbf{X}_{B;j}, t) \right\} + \tilde{\mathbf{q}}_{B;L;j} \dot{\mathbf{x}}_{B;\bar{\theta};j} \right]. \quad (4.77)$$

The matrix  $\tilde{\mathbf{q}}_{B;I;j}(\mathbf{X}_{B;j}, t)$  is the skew-symmetric matrix from the vector  $\mathbf{q}_{B;I;j}(\mathbf{X}_{B;j}, t)$ :

$$\mathbf{q}_{B;I;j}(\mathbf{X}_{B;j}, t) = \mathbf{R}_{R;\bar{\theta}} \mathbf{R}_{B;\Psi;j}(t) \Xi \left\{ \dot{\mathbf{R}}_{B;\Psi;j}(t) \right\}^T \left\{ \mathbf{R}_{R;\bar{\theta}} \right\}^T \left( \mathbf{W}_R(\mathbf{X}_{B;j}, t) - \dot{\mathbf{x}}_{B;\bar{\theta};j}(\mathbf{X}_{B;j}, t) \right) - \mathbf{R}_{R;\bar{\theta}} \mathbf{R}_{B;\Psi;j}(t) \Xi \left\{ \mathbf{R}_{B;\Psi;j}(t) \right\}^T \left\{ \mathbf{R}_{R;\bar{\theta}} \right\}^T \dot{\mathbf{x}}_{B;\bar{\theta};j}(\mathbf{X}_{B;j}, t). \quad (4.78)$$

Contrarily to translations, structural rotations do affect the resulting aerodynamic force on the turbine rotor. As a result of tilting or yawing rotations, the axial wind velocity at the rotor plane changes. The matrix  $\bar{\mathbf{W}}_R(\mathbf{X}_{B;j}, t)$  accounts for the changing orientation of the wind inflow on the rotor plane. The matrix  $\bar{\mathbf{q}}_{B;A;j}(\mathbf{X}_{B;j}, t)$  relates to the changing orientation of the aerodynamic forces in the global inertial reference frame.

#### 4.3.4. STATE-INDEPENDENT APPARENT DAMPING APPROXIMATIONS

The state-independent apparent damping is obtained as the matrix  $\left. \frac{\partial \mathbf{Q}_{B;A;j}(\mathbf{X}_{B;j}, t)}{\partial \{\bar{\mathbf{v}}_R(t)\}} \right|_{\bar{\mathbf{s}}_R}$  in the third term of Eq. (4.58). This matrix relates the velocity of the tower top motion to the aerodynamic forces on the rotor. Similar to the state-independent apparent stiffness matrix, the apparent damping is subdivided for the different aerodynamic forces and moments and for the tower top velocity  $\bar{\mathbf{u}}_R(t)$  and rotational velocity  $\bar{\boldsymbol{\theta}}_R(t)$ :

$$\left. \frac{\partial \mathbf{Q}_{B;A;j}(\mathbf{X}_{B;j}, t)}{\partial \bar{\mathbf{v}}_R(\mathbf{X}_{B;j}, t)} \right|_{\bar{\mathbf{s}}_R} = \begin{bmatrix} \left. \frac{\partial \mathbf{F}_{B;A;j}(\mathbf{X}_{B;j}, t)}{\partial \bar{\mathbf{u}}_R(t)} \right|_{\bar{\mathbf{s}}_R} & \left. \frac{\partial \mathbf{F}_{B;A;j}(\mathbf{X}_{B;j}, t)}{\partial \bar{\boldsymbol{\theta}}_R(t)} \right|_{\bar{\mathbf{s}}_R} \\ \left. \frac{\partial \mathbf{T}_{B;A;j}(\mathbf{X}_{B;j}, t)}{\partial \bar{\mathbf{u}}_R(t)} \right|_{\bar{\mathbf{s}}_R} & \left. \frac{\partial \mathbf{T}_{B;A;j}(\mathbf{X}_{B;j}, t)}{\partial \bar{\boldsymbol{\theta}}_R(t)} \right|_{\bar{\mathbf{s}}_R} \end{bmatrix}, \quad (4.79)$$

for which the sub-matrices for the lift and drag forces can be expressed as

$$\left. \frac{\partial \mathbf{F}_{B;A;j}(\mathbf{X}_{B;j}, t)}{\partial \bar{\mathbf{u}}_R(t)} \right|_{\bar{\mathbf{s}}_R} = \frac{1}{2} \rho_{\text{air}} c_{B;j}(r_{B;j}) C_{B;A;j}(r_{B;j}) \cdot \left[ -(\mathbf{A}_{B;A;j}(\mathbf{X}_{B;j}, t) + \mathbf{B}_{B;A;j}(\mathbf{X}_{B;j}, t)) \Xi \left\{ \mathbf{R}_{B;\bar{\Psi};j}(t) \right\}^T \left\{ \mathbf{R}_{R;\bar{\theta}} \right\}^T \right], \quad (4.80)$$

$$\left. \frac{\partial \mathbf{T}_{B;A;j}(\mathbf{X}_{B;j}, t)}{\partial \bar{\mathbf{u}}_R(t)} \right|_{\bar{\mathbf{s}}_R} = \frac{1}{2} \rho_{\text{air}} c_{B;j}(r_{B;j}) C_{B;A;j}(r_{B;j}) \cdot \left[ -\tilde{\mathbf{x}}_{B;\bar{\theta};j}(\mathbf{X}_{B;j}, t) (\mathbf{A}_{B;A;j}(\mathbf{X}_{B;j}, t) + \mathbf{B}_{B;A;j}(\mathbf{X}_{B;j}, t)) \Xi \left\{ \mathbf{R}_{B;\bar{\Psi};j}(t) \right\}^T \left\{ \mathbf{R}_{R;\bar{\theta}} \right\}^T \right], \quad (4.81)$$

$$\left. \frac{\partial \mathbf{F}_{B;A;j}(\mathbf{X}_{B;j}, t)}{\partial \bar{\boldsymbol{\theta}}_R(t)} \right|_{\bar{\mathbf{s}}_R} = \frac{1}{2} \rho_{\text{air}} c_{B;j}(r_{B;j}) C_{B;A;j}(r_{B;j}) \cdot \left[ (\mathbf{A}_{B;A;j}(\mathbf{X}_{B;j}, t) + \mathbf{B}_{B;A;j}(\mathbf{X}_{B;j}, t)) \Xi \left\{ \mathbf{R}_{B;\bar{\Psi};j}(t) \right\}^T \left\{ \mathbf{R}_{R;\bar{\theta}} \right\}^T \tilde{\mathbf{x}}_{B;\bar{\theta};j}(\mathbf{X}_{B;j}, t) \right], \quad (4.82)$$

and

$$\left. \frac{\partial \mathbf{T}_{B;A;j}(\mathbf{X}_{B;j}, t)}{\partial \bar{\boldsymbol{\theta}}_R(t)} \right|_{\bar{\mathbf{s}}_R} = \frac{1}{2} \rho_{\text{air}} c_{B;j}(r_{B;j}) C_{B;A;j}(r_{B;j}) \cdot \left[ \tilde{\mathbf{x}}_{B;\bar{\theta};j}(\mathbf{X}_{B;j}, t) (\mathbf{A}_{B;A;j}(\mathbf{X}_{B;j}, t) + \mathbf{B}_{B;A;j}(\mathbf{X}_{B;j}, t)) \Xi \left\{ \mathbf{R}_{B;\bar{\Psi};j}(t) \right\}^T \left\{ \mathbf{R}_{R;\bar{\theta}} \right\}^T \tilde{\mathbf{x}}_{B;\bar{\theta};j}(\mathbf{X}_{B;j}, t) \right]. \quad (4.83)$$

The state-independent apparent damping matrices from the inertia force are obtained as

$$\left. \frac{\partial \mathbf{F}_{B;l;j}(\mathbf{X}_{B;j}, t)}{\partial \dot{\mathbf{u}}_R(t)} \right|_{\bar{s}_R} = \frac{1}{4} \rho_{\text{air}} \pi \{c_{B;j}(r_{B;j})\}^2 \left[ -\mathbf{R}_{R;\bar{\theta}} \mathbf{R}_{B;\bar{\Psi};j}(t) \Xi \left\{ \dot{\mathbf{R}}_{B;\bar{\Psi};j}(t) \right\}^T \left\{ \mathbf{R}_{R;\bar{\theta}} \right\}^T \right], \quad (4.84)$$

$$\left. \frac{\partial \mathbf{T}_{B;l;j}(\mathbf{X}_{B;j}, t)}{\partial \dot{\mathbf{u}}_R(t)} \right|_{\bar{s}_R} = \frac{1}{4} \rho_{\text{air}} \pi \{c_{B;j}(r_{B;j})\}^2 \left[ \tilde{\mathbf{x}}_{B;\bar{\theta};j}(\mathbf{X}_{B;j}, t) \mathbf{R}_{R;\bar{\theta}} \mathbf{R}_{B;\bar{\Psi};j}(t) \Xi \left\{ \dot{\mathbf{R}}_{B;\bar{\Psi};j}(t) \right\}^T \left\{ \mathbf{R}_{R;\bar{\theta}} \right\}^T \right], \quad (4.85)$$

$$\begin{aligned} \left. \frac{\partial \mathbf{F}_{B;l;j}(\mathbf{X}_{B;j}, t)}{\partial \dot{\theta}_R(t)} \right|_{\bar{s}_R} &= \frac{1}{4} \rho_{\text{air}} \pi \{c_{B;j}(r_{B;j})\}^2 \cdot \\ &\left[ \mathbf{R}_{R;\bar{\theta}} \mathbf{R}_{B;\bar{\Psi};j}(t) \Xi \left\{ \mathbf{R}_{B;\bar{\Psi};j}(t) \right\}^T \left\{ \mathbf{R}_{R;\bar{\theta}} \right\}^T \left( \tilde{\mathbf{W}}_{B;j}(\mathbf{X}_{B;j}, t) + \tilde{\mathbf{x}}_{B;\bar{\theta};j}(\mathbf{X}_{B;j}, t) \right) \right. \\ &\left. + \mathbf{R}_{R;\bar{\theta}} \mathbf{R}_{B;\bar{\Psi};j}(t) \Xi \left\{ \dot{\mathbf{R}}_{B;\bar{\Psi};j}(t) \right\}^T \left\{ \mathbf{R}_{R;\bar{\theta}} \right\}^T \tilde{\mathbf{x}}_{B;\bar{\theta};j}(\mathbf{X}_{B;j}, t) \right], \end{aligned} \quad (4.86)$$

and

$$\begin{aligned} \left. \frac{\partial \mathbf{T}_{B;l;j}(\mathbf{X}_{B;j}, t)}{\partial \dot{\theta}_R(t)} \right|_{\bar{s}_R} &= \frac{1}{4} \rho_{\text{air}} \pi \{c_{B;j}(r_{B;j})\}^2 \cdot \\ &\left[ \tilde{\mathbf{x}}_{B;\bar{\theta};j}(\mathbf{X}_{B;j}, t) \mathbf{R}_{R;\bar{\theta}} \mathbf{R}_{B;\bar{\Psi};j}(t) \Xi \left\{ \mathbf{R}_{B;\bar{\Psi};j}(t) \right\}^T \left\{ \mathbf{R}_{R;\bar{\theta}} \right\}^T \left( \tilde{\mathbf{W}}_{B;j}(\mathbf{X}_{B;j}, t) + \tilde{\mathbf{x}}_{B;\bar{\theta};j}(\mathbf{X}_{B;j}, t) \right) \right. \\ &\left. + \tilde{\mathbf{x}}_{B;\bar{\theta};j}(\mathbf{X}_{B;j}, t) \mathbf{R}_{R;\bar{\theta}} \mathbf{R}_{B;\bar{\Psi};j}(t) \Xi \left\{ \dot{\mathbf{R}}_{B;\bar{\Psi};j}(t) \right\}^T \left\{ \mathbf{R}_{R;\bar{\theta}} \right\}^T \tilde{\mathbf{x}}_{B;\bar{\theta};j}(\mathbf{X}_{B;j}, t) \right]. \end{aligned} \quad (4.87)$$

#### 4.3.5. STATE-INDEPENDENT APPARENT MASS APPROXIMATIONS

The last term of Eq. (4.58) contains the apparent mass matrix  $\left. \frac{\partial \mathbf{Q}_{B;A;j}(\mathbf{X}_{B;j}, t)}{\partial \{\dot{\mathbf{v}}_R(t)\}} \right|_{\bar{s}_R}$  which relates the structural accelerations to the aerodynamic force on the wind turbine rotor. Distinguishing the aerodynamic force and moment on the tower top, and the lateral and rotational tower top accelerations, this matrix can be subdivided as follows:

$$\left. \frac{\partial \mathbf{Q}_{B;A;j}(\mathbf{X}_{B;j}, t)}{\partial \dot{\mathbf{v}}_R(\mathbf{X}_{B;j}, t)} \right|_{\bar{s}_R} = \begin{bmatrix} \left. \frac{\partial \mathbf{F}_{B;A;j}(\mathbf{X}_{B;j}, t)}{\partial \dot{\mathbf{u}}_R(t)} \right|_{\bar{s}_R} & \left. \frac{\partial \mathbf{F}_{B;A;j}(\mathbf{X}_{B;j}, t)}{\partial \dot{\theta}_R(t)} \right|_{\bar{s}_R} \\ \left. \frac{\partial \mathbf{T}_{B;A;j}(\mathbf{X}_{B;j}, t)}{\partial \dot{\mathbf{u}}_R(t)} \right|_{\bar{s}_R} & \left. \frac{\partial \mathbf{T}_{B;A;j}(\mathbf{X}_{B;j}, t)}{\partial \dot{\theta}_R(t)} \right|_{\bar{s}_R} \end{bmatrix}. \quad (4.88)$$

For the lift and drag force components, no apparent mass contribution is obtained, since these forces as defined in Section 4.2.1 do not depend on structural accelerations. The apparent mass resulting from the inertia force can be expressed as

$$\left. \frac{\partial \mathbf{F}_{B;l;j}(\mathbf{X}_{B;j}, t)}{\partial \dot{\mathbf{u}}_R(t)} \right|_{\bar{s}_R} = \frac{1}{4} \rho_{\text{air}} \pi \{c_{B;j}(r_{B;j})\}^2 \left[ -\mathbf{R}_{R;\bar{\theta}} \mathbf{R}_{B;\bar{\Psi};j}(t) \Xi \left\{ \mathbf{R}_{B;\bar{\Psi};j}(t) \right\}^T \left\{ \mathbf{R}_{R;\bar{\theta}} \right\}^T \right], \quad (4.89)$$

$$\left. \frac{\partial \mathbf{T}_{B,i;j}(\mathbf{X}_{B;j}, t)}{\partial \bar{\mathbf{u}}_R(t)} \right|_{\bar{s}_R} = \frac{1}{4} \rho_{\text{air}} \pi \{c_{B;j}(r_{B;j})\}^2 \left[ \tilde{\mathbf{x}}_{B;\bar{\theta};j}(\mathbf{X}_{B;j}, t) \mathbf{R}_{R;\bar{\theta}} \mathbf{R}_{B;\bar{\Psi};j}(t) \Xi \left\{ \mathbf{R}_{B;\bar{\Psi};j}(t) \right\}^T \left\{ \mathbf{R}_{R;\bar{\theta}} \right\}^T \right], \quad (4.90)$$

$$\left. \frac{\partial \mathbf{F}_{B,i;j}(\mathbf{X}_{B;j}, t)}{\partial \bar{\theta}_R(t)} \right|_{\bar{s}_R} = \left[ \mathbf{R}_{R;\bar{\theta}} \mathbf{R}_{B;\bar{\Psi};j}(t) \Xi \left\{ \mathbf{R}_{B;\bar{\Psi};j}(t) \right\}^T \left\{ \mathbf{R}_{R;\bar{\theta}} \right\}^T \tilde{\mathbf{x}}_{B;\bar{\theta};j}(\mathbf{X}_{B;j}, t) \right], \quad (4.91)$$

and

$$\left. \frac{\partial \mathbf{T}_{B,i;j}(\mathbf{X}_{B;j}, t)}{\partial \bar{\theta}_R(t)} \right|_{\bar{s}_R} = \frac{1}{4} \rho_{\text{air}} \pi \{c_{B;j}(r_{B;j})\}^2 \cdot \left[ \tilde{\mathbf{x}}_{B;\bar{\theta};j}(\mathbf{X}_{B;j}, t) \mathbf{R}_{R;\bar{\theta}} \mathbf{R}_{B;\bar{\Psi};j}(t) \Xi \left\{ \mathbf{R}_{B;\bar{\Psi};j}(t) \right\}^T \left\{ \mathbf{R}_{R;\bar{\theta}} \right\}^T \tilde{\mathbf{x}}_{B;\bar{\theta};j}(\mathbf{X}_{B;j}, t) \right]. \quad (4.92)$$

With the apparent mass expressions for the inertia force and moment, all closed-form expressions for the state-independent apparent stiffness, damping and mass have been presented in this section. Combined within Eq. (4.58), and subsequently applied in Eq. (4.56), these expressions constitute the approximation of the non-linear aerodynamic excitation of a rotating wind turbine rotor. The individual matrices define the blade force components and therefore allow for differences in the aerodynamic force per blade.

## 4.4. APPARENT PROPERTIES OF AN ISOTROPIC ROTOR

### 4.4.1. ROTOR DEFINITION AND OPERATIONAL STATE

The aerodynamic force approximations, presented in Section 4.3, have been derived for each blade separately, and are hence necessarily time dependent. In deriving the total rotor force, on the basis of Eq. (4.56), differences between the blades – both geometrically and aero-elastically – can be accounted for. Therefore, it can be stated that the presented force matrices are valid in a general sense, provided that the attached flow condition is met, and the instantaneous aerodynamic force model is sufficiently accurate.

To elucidate the physical significance of the derived matrices, in this section the complete rotor matrices are presented for the particular case of a rotor with identical blades, implying that the geometric and aero-elastic blade properties are independent of the blade number  $j$ . Moreover, the wind field at the rotor plane is assumed to be axial, uniform and positive. If, in addition, a static wake model is assumed, the induced velocity field is not affected by time variations of the airflow, and the resulting velocity field at the rotor plane can be expressed as:

$$\mathbf{W}_R(\mathbf{X}_B, t) = \begin{bmatrix} 0 & W_{R;Y}(\mathbf{X}_B, t) & 0 \end{bmatrix}^T. \quad (4.93)$$

To illustrate the relevance of the separate force components, the forces on the rotor of the NREL 5MW turbine are derived for a wind velocity of 15.0 m/s. The rotational velocity in this operational state is 12.1 rpm, and the full-span pitch angle is 10.45 degrees. For this equilibrium state, the values of the aero-elastic lift and drag coefficients are readily available from any aero-elastic code, and presented here in Table 4.1 for each aerofoil

of the NREL 5MW turbine and in Figure 4.6(a) as a function of the relative blade radius. Figure 4.6(b) presents the axial and tangential induction coefficients for the described operational conditions. The components of the incident velocity in the rotor plane – the wind and rotor speeds – are depicted in Figure 4.6(c). Figure 4.6(d) presents the angle of attack along the blade length, where the transition from attached to separated flows is indicated at an approximated angle of 8 degrees. For small radii, the angle of attack is zero, because of the circular cross section of the blades. It is shown that up to circa 30% of the blade length separation of flow may occur for the adopted operational state. With the assumed attached flow conditions, the lift force in this range is overestimated, whereas the drag force is underestimated. Towards the centre of rotation, however, the effective inflow velocity decreases, and the contributions of the blade section forces are of minor relevance, compared to the section forces towards the blade tips.

Table 4.1: Aero-elastic coefficients of the NREL 5MW turbine aerofoils for small angles of attack.

aerofoil	lift coefficient $C_L^c$ [-]	slope of lift coefficient $C_L^\alpha$ [-]	drag coefficient $C_D$ [-]
NACA64	0.442	6.003	0.0052
DU21	0.521	6.205	0.0057
DU25	0.444	6.446	0.0065
DU30	0.288	7.333	0.0087
DU35	0.196	7.184	0.0094
DU40	0.137	7.489	0.0113

#### 4.4.2. APPARENT STIFFNESS FOR AN ISOTROPIC ROTOR

As addressed in Section 4.3, structural translations do not affect the resulting aerodynamic force on the rotor. On the other hand, structural rotations were shown to affect the forces on the rotor and, subsequently, the tower sub-system. The reason for this is twofold. First, as a result of a rotation of the rotor plane, the projection of the wind field on the rotor plane changes. This effect is expressed through the matrix  $\tilde{\mathbf{W}}_R(\mathbf{X}_{B;j}, t)$  in Eq. (4.68). Secondly, a structural rotation of the rotor affects the orientation of the blade forces in the global inertial frame of reference, and, as a consequence, the resulting rotor forces too. With a reference to the same equations, this effect is expressed through the matrix  $\tilde{\mathbf{Q}}_{B;A;j}(\mathbf{X}_{B;j}, t)$ . These force effects are visible in the apparent stiffness matrices, derived for the operational conditions defined in Section 4.4.1 and with the application of Eqs. (4.56) and (4.57).

Apart from the contributions to the lateral and vertical rotor forces, structural rotations affect the moments around the tower top. Here, again, two effects can be distinguished. First, due to the rotor eccentricity, a structural rotation introduces an additional moment around the tower top. A second contribution results from a change in orientation of the aerodynamic torque, or the resulting moment around the axis of rotation of the rotor. As a result of a tilting rotation, the aerodynamic torque  $T_{B;Y;j}^f(r_{B;j}, t)$  around the rotational axis of the rotor can be decomposed into components around the  $Y_T$  and the  $Z_T$  axes in the global inertial reference frame, i.e., a yawing and a rolling moment. The same

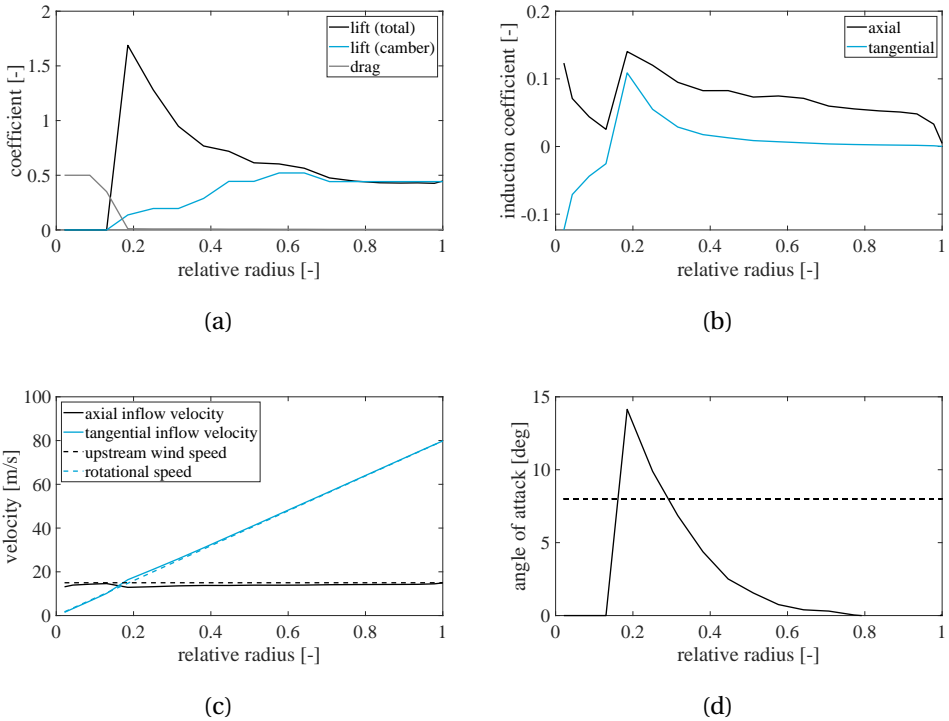


Figure 4.6: Operational conditions, with (a) the aero-elastic coefficients for lift and drag, (b) the axial and tangential induction coefficients, (c) the resulting axial and tangential inflow velocities in the rotor plane, where the dashed lines indicate the upstream wind velocity and the rotational speed, and (d) the angle of attack, for which dashed line indicates the assumed limit for attached flow conditions.

applies for a yawing rotation, which induces an additional tilting moment at the tower top, because of the changed orientation of the rotor plane.

Figure 4.7 illustrates the apparent stiffness matrix for the given operational state. As shown in Figure 4.7(a), the sensitivity of the rotor forces to structural rotations results mainly from the lift force, with the  $\alpha$ -dependent lift force providing the largest contribution, while the sensitivity of the rotor moments, depicted in Figure 4.7(b) almost completely results from the  $\alpha$ -dependent lift force only.

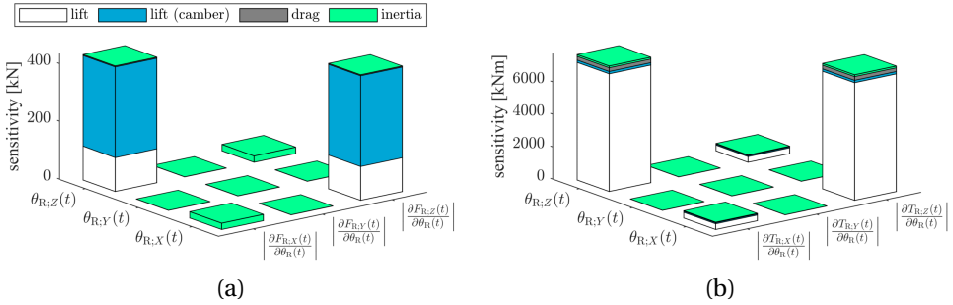


Figure 4.7: Apparent stiffness for the turbine system for the given operational state, with (a) the rotor force sensitivities, and (b) the rotor moment sensitivities. The diagrams show the superposition of the absolute values of the force sensitivities.

#### 4.4.3. APPARENT DAMPING FOR AN ISOTROPIC ROTOR

The matrices relating the structural velocities to the aerodynamic force can be considered as apparent damping matrices, and the entries represent what in literature is often referred to as aerodynamic damping [50]. Particularly for rotating turbines, this damping contribution is a very relevant component of the dynamic characteristics of a wind turbine, with damping ratios of about 4% of the critical damping of the first turbine mode [49].

The extent to which the different aerodynamic force components affect the overall aerodynamic damping is visualized in Figure 4.8. This figure provides insight in the sensitivity of the rotor forces to the structural velocities. The sensitivity of the rotor forces to the translational motions is depicted in Figure 4.8(a). This figure shows that for the given operational conditions the sensitivity to the fore-aft motion is dominant, and moreover, that the  $\alpha$ -dependent lift force mainly contributes to apparent damping. The magnitude of the sensitivity of the  $\alpha$ -dependent lift force to the fore-aft motion corresponds with the aerodynamic damping as defined in previous studies [49, 50, 52].

Given the relevance for the analysis of support structures of offshore wind turbines, the apparent damping matrix for the isotropic rotor relating the translational rotor motions to the  $\alpha$ -dependent and the camber-dependent lift forces are presented in full:



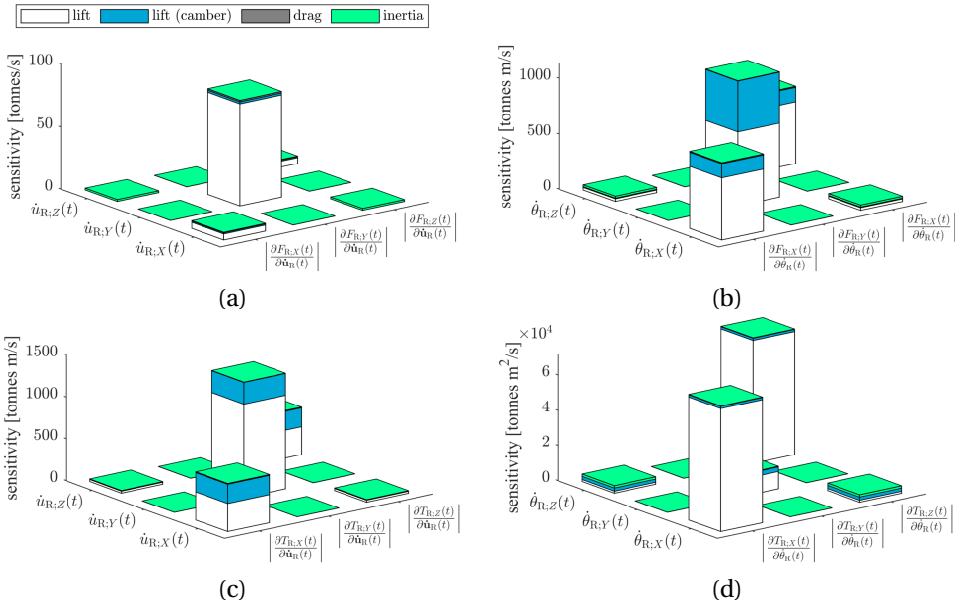


Figure 4.8: Sensitivity of the rotor forces to structural motions, with (a) the rotor force sensitivity to translational motions, (b) the rotor force sensitivity to rotational motions, (c) the rotor force sensitivity to translational motions, and (d) the rotor moment sensitivity to rotational motions. The diagrams show the superposition of the absolute values of the force sensitivities.

$$\left. \frac{\partial \mathbf{F}_{R;L}^\alpha(t)}{\partial \bar{\mathbf{u}}_R(t)} \right|_{S_{R;0}} = \frac{3}{2} \int_{r_H}^R \rho_{\text{air}} c_B(r_B) C_{B;L}^\alpha(r_B) \sin(\beta_{B;0}(r_B) + \bar{\beta}(r_B)) \begin{bmatrix} -\frac{1}{2} \bar{W}_{R;Y}(\mathbf{X}_B) & 0 & 0 \\ 0 & 0 & 0 \\ 0 & 0 & -\frac{1}{2} \bar{W}_{R;Y}(\mathbf{X}_B) \end{bmatrix} dr_B \quad (4.94)$$

$$+ \frac{3}{2} \int_{r_H}^R \rho_{\text{air}} c_B(r_B) C_{B;L}^\alpha(r_B) \cos(\beta_{B;0}(r_B) + \bar{\beta}(r_B)) \begin{bmatrix} 0 & 0 & 0 \\ 0 & -\bar{\Omega}_{R;Y} r_B & 0 \\ 0 & 0 & 0 \end{bmatrix} dr_B,$$

and

$$\left. \frac{\partial \mathbf{F}_{R;L}^c(t)}{\partial \bar{\mathbf{u}}_R(t)} \right|_{S_{R;0}} = \frac{3}{2} \int_{r_H}^R \frac{\rho_{\text{air}} c_B(r_B) C_L^c(r_B)}{|\bar{\mathbf{W}}_{B;\text{eff}}^r(r_B)|} \bar{\Omega}_{R;Y} r_B \bar{W}_{R;Y}(\mathbf{X}_B) \begin{bmatrix} \frac{1}{2} & 0 & 0 \\ 0 & -1 & 0 \\ 0 & 0 & \frac{1}{2} \end{bmatrix} dr_B. \quad (4.95)$$

The matrices are obtained for the state  $S_{R;0}$ , for which the mean deformations  $\bar{\mathbf{v}}_R$  are assumed to be zero. The diagonal entries of the matrices in Eq. (4.94) are negative, implying that the apparent damping is positive. Eq. (4.95), however, contains positive entries on its diagonal. Positive entries indicate a negative damping and could induce structural instabilities. Nonetheless, with reference to Figure 4.8, the contributions from the camber dependent lift force are much smaller than the contributions from the  $\alpha$ -dependent lift force, and the overall apparent damping from the diagonal entries is positive.

Considering the sensitivity of the rotor forces to the rotational velocities, presented in Figure 4.8(b), the strongest interdependency is observed between the axial force and the rotor azimuth perturbation. In fact, this motion can be seen as an additional rotational velocity of the rotor  $\bar{\Omega}_{R;Y}$ . The sensitivity of the lateral and vertical forces to the rotational tilting and yawing velocities, respectively, is considerable too. In comparison, the associated cross-coupling sensitivities, however, are shown to be negligibly small. The apparent damping mainly results from the  $\alpha$ -dependent lift force, though the contribution of the camber to the total lift force cannot be neglected here. The matrix entries from both the  $\alpha$ -dependent and the camber-dependent lift forces have been computed as follows:

$$\left. \frac{\partial \mathbf{F}_{R;L}^\alpha(t)}{\partial \bar{\boldsymbol{\theta}}_R(t)} \right|_{S_{R;0}} = \frac{3}{2} \int_{r_H}^R \rho_{\text{air}} c_B(r_B) C_{B;L}^\alpha(r_B) \sin(\beta_{B;0}(r_B) + \bar{\beta}(r_B)) \bar{\Omega}_{R;Y} r_B^2 \begin{bmatrix} -\frac{1}{2} & 0 & -\frac{1}{2} \frac{\bar{W}_{R;Y}(\mathbf{X}_B) dr_B}{\bar{\Omega}_{R;Y} r_B^2} \\ 0 & -2 & 0 \\ \frac{1}{2} \frac{\bar{W}_{R;Y}(\mathbf{X}_B) dr_B}{\bar{\Omega}_{R;Y} r_B^2} & 0 & -\frac{1}{2} \end{bmatrix} dr_B$$

$$+ \frac{3}{2} \int_{r_H}^R \rho_{\text{air}} c_B(r_B) C_{B;L}^\alpha(r_B) \cos(\beta_{B;0}(r_B) + \bar{\beta}(r_B)) \bar{W}_{R;Y}(\mathbf{X}_B) r_B \mathbf{I}_{3 \times 3} dr_B, \quad (4.96)$$

and

$$\begin{aligned} \left. \frac{\partial \mathbf{F}_{R;L}^c(t)}{\partial \mathbf{u}_R(t)} \right|_{S_{R;0}} &= \frac{3}{2} \int_{r_H}^R \rho_{\text{air}} c_B(r_B) C_{B;L}^c(r_B) \left| \bar{\mathbf{W}}_{R;\text{eff}}^r(r_B) \right| \begin{bmatrix} \frac{1}{2} r_B & 0 & 0 \\ 0 & r_B & 0 \\ 0 & 0 & \frac{1}{2} r_B \end{bmatrix} dr_B \\ &+ \frac{3}{2} \int_{r_H}^R \frac{\rho_{\text{air}} c_B(r_B) C_{B;L}^c(r_B)}{\left| \bar{\mathbf{W}}_{R;\text{eff}}^r(r_B) \right|} \begin{bmatrix} \frac{1}{2} \{\bar{W}_{R;Y}(\mathbf{X}_B)\}^2 r & 0 & \frac{1}{2} \bar{\Omega}_{R;Y} r_B \bar{W}_{R;Y}(\mathbf{X}_B) d_R \\ 0 & \bar{\Omega}_{R;Y}^2 r_B^3 & 0 \\ -\frac{1}{2} \bar{\Omega}_{R;Y} r_B \bar{W}_{R;Y}(\mathbf{X}_B) d_R & 0 & \frac{1}{2} \{\bar{W}_{R;Y}(\mathbf{X}_B)\}^2 r_B \end{bmatrix} dr_B, \end{aligned} \quad (4.97)$$

A similar pattern is observed in the sensitivity of the rotor moments to the translational velocities, Figure 4.8(c). The strongest interdependency is observed for the aerodynamic torque and the fore-aft velocity, while also the mutual dependencies between the tilting and yawing moments to the lateral and vertical velocities, respectively, are substantial. Cross-coupling contributions can again be considered as absent, and despite the main contribution to the apparent damping from the  $\alpha$ -dependent lift force, the effect of the camber cannot be neglected. The matrix entries from both the  $\alpha$ -dependent and the camber-dependent lift forces are computed as follows:

$$\begin{aligned} \left. \frac{\partial \mathbf{T}_{R;L}^\alpha(t)}{\partial \mathbf{u}_R(t)} \right|_{S_{R;0}} &= \\ &\frac{3}{2} \int_{r_H}^R \rho_{\text{air}} c_B(r_B) C_{B;L}^\alpha(r_B) \sin(\beta_{B;0}(r_B) + \bar{\beta}(r_B)) \bar{\Omega}_{R;Y} r_B^2 \begin{bmatrix} 1 & 0 & \frac{1}{2} \frac{\bar{W}_{R;Y}(\mathbf{X}_B) d_R}{\bar{\Omega}_{R;Y} r_B^2} \\ 0 & 1 & 0 \\ -\frac{1}{2} \frac{\bar{W}_{R;Y}(\mathbf{X}_B) d_R}{\bar{\Omega}_{R;Y} r_B^2} & 0 & 1 \end{bmatrix} dr_B \\ &+ \frac{3}{2} \int_{r_H}^R \rho_{\text{air}} c_B(r_B) C_{B;L}^\alpha(r_B) \cos(\beta_{B;0}(r_B) + \bar{\beta}(r_B)) \bar{W}_{R;Y}(\mathbf{X}_B) r_B \begin{bmatrix} -\frac{1}{2} & 0 & 0 \\ 0 & -2 & 0 \\ 0 & 0 & -\frac{1}{2} \end{bmatrix} dr_B, \end{aligned} \quad (4.98)$$

and

$$\begin{aligned} \left. \frac{\partial \mathbf{T}_{R;L}^c(t)}{\partial \mathbf{u}_R(t)} \right|_{S_{R;0}} &= \frac{3}{2} \int_{r_H}^R \rho_{\text{air}} c_B(r_B) C_{B;L}^c(r_B) \left| \bar{\mathbf{W}}_{R;\text{eff}}^r(r_B) \right| \begin{bmatrix} -\frac{1}{2} r_B & 0 & 0 \\ 0 & -r_B & 0 \\ 0 & 0 & -\frac{1}{2} r_B \end{bmatrix} dr_B \\ &+ \frac{3}{2} \int_{r_H}^R \frac{\rho_{\text{air}} c_B(r_B) C_{B;L}^c(r_B)}{\left| \bar{\mathbf{W}}_{R;\text{eff}}^r(r_B) \right|} \begin{bmatrix} -\frac{1}{2} \bar{\Omega}_{R;Y}^2 r_B^3 & 0 & -\frac{1}{2} \bar{\Omega}_{R;Y} r_B \bar{W}_{R;Y}(\mathbf{X}_B) d_R \\ 0 & -\bar{W}_{R;Y}(\mathbf{X}_B) r_B & 0 \\ \frac{1}{2} \bar{\Omega}_{R;Y} r_B \bar{W}_{R;Y}(\mathbf{X}_B) d_R & 0 & -\frac{1}{2} \bar{\Omega}_{R;Y}^2 r_B^3 \end{bmatrix} dr_B. \end{aligned} \quad (4.99)$$

As shown in Figure 4.8(d), the sensitivity of the aerodynamic torque to a perturbation of the rotational velocity is much smaller than the sensitivity of the tilting and yawing moments to the tilting and yawing motions, respectively. This indicates a relatively strong damping of the yaw and tilt motions of the turbine rotor. This apparent damping almost

completely results from the  $\alpha$ -dependent lift force, which is given as

$$\left. \frac{\partial \mathbf{T}_{R:L}^\alpha(t)}{\partial \tilde{\boldsymbol{\theta}}_R(t)} \right|_{S_{R;0}} = \frac{3}{2} \int_{r_H}^R \left\{ \rho_{\text{air}} c_B(r_B) C_{B:L}^\alpha(r_B) \sin(\beta_{B;0}(r_B) + \bar{\beta}(r_B)) \bar{W}_{R;Y}(\mathbf{X}_B) d_R^2 \begin{bmatrix} -\frac{1}{2} & 0 & \frac{3}{2} \frac{\bar{\Omega}_{R;Y} r_B^2 d_R}{\bar{W}_{R;Y}(\mathbf{X}_B) d_R^2} \\ 0 & -1 & 0 \\ -\frac{3}{2} \frac{\bar{\Omega}_{R;Y} r_B^2 d_R}{\bar{W}_{R;Y}(\mathbf{X}_B) d_R^2} & 0 & -\frac{1}{2} \end{bmatrix} \right. \\ \left. + \rho_{\text{air}} c_B(r_B) C_{B:L}^\alpha(r_B) \cos(\beta_{B;0}(r_B) + \bar{\beta}(r_B)) \begin{bmatrix} -\frac{1}{2} \bar{\Omega}_{R;Y} r_B^3 & 0 & -\frac{3}{2} \bar{W}_{R;Y}(\mathbf{X}_B) r_B d_R \\ 0 & 0 & 0 \\ \frac{3}{2} \bar{W}_{R;Y}(\mathbf{X}_B) r_B d_R & 0 & -\frac{1}{2} \bar{\Omega}_{R;Y} r_B^3 \end{bmatrix} \right\} d r_B. \quad (4.100)$$

The apparent damping contributions from the camber-dependent lift force result from

$$\left. \frac{\partial \mathbf{T}_{R:L}^c(t)}{\partial \tilde{\boldsymbol{\theta}}_R(t)} \right|_{S_{R;0}} = \frac{3}{2} \int_{r_H}^R \rho_{\text{air}} c_B(r_B) C_{B:L}^c(r_B) \left| \bar{\mathbf{W}}_{R;\text{eff}}^T(r_B) \right| \begin{bmatrix} 0 & 0 & -\frac{3}{2} r_B d_R \\ \frac{3}{2} r_B d_R & 0 & 0 \end{bmatrix} d r_B \\ + \frac{3}{2} \int_{r_H}^R \frac{\rho_{\text{air}} c_B(r_B) C_{B:L}^c(r_B)}{\left| \bar{\mathbf{W}}_{R;\text{eff}}^T(r_B) \right|} \bar{\Omega}_{R;Y} r_B \bar{W}_{R;Y}(\mathbf{X}_B) \begin{bmatrix} -\frac{1}{2} (r_B^2 - d_R^2) & 0 & 0 \\ 0 & r_B^2 & 0 \\ 0 & 0 & -\frac{1}{2} (r_B^2 - d_R^2) \end{bmatrix} d r_B. \quad (4.101)$$

The apparent damping matrices from the camber-dependent lift and the drag forces contain negative diagonal entries relating the rotation of the rotor to the moments on the tower top. As shown in Figure 4.8(d), these contributions are much smaller than the positive contributions from the  $\alpha$ -dependent lift force, indicating that these negative contributions to the damping of the system don't induce structural instabilities. No relevant cross-couplings are observed in Figure 4.8(d).

#### 4.4.4. APPARENT MASS FOR AN ISOTROPIC ROTOR

The inertia force contains a dependency on the structural acceleration. The corresponding state-dependent matrix can be considered as an apparent inertia matrix. For the operational conditions presented in Section 4.4.1, and with the application of Eqs. (4.56), (4.57) and (4.88) – separating the contributions terms related to  $\dot{\mathbf{u}}_R(t)$  and  $\ddot{\boldsymbol{\theta}}_R(t)$ , Figure 4.9 visualizes the magnitude of the terms of Eqs. (4.89) to (4.92). The magnitude of the diagonal entries of Eqs. (4.89) and (4.92) are shown in Figure 4.9(a) and (d), while Figure 4.9(b) and (c) show the extent of the cross-coupling of Eqs. (4.90) and (4.91). The magnitude of the entries of Eqs. (4.89) to (4.92) is small compared to the actual mass and mass moment of inertia of the NREL 5MW rotor. This apparent mass matrix can therefore be expected to be of limited relevance for the dynamic response of this wind turbine.

## 4.5. TURBINE RESPONSE ANALYSIS

### 4.5.1. TURBINE DEFINITION

In the previous sections, apparent stiffness, damping and mass matrices have been derived, which allow for the analysis of the aerodynamic excitation of a wind turbine

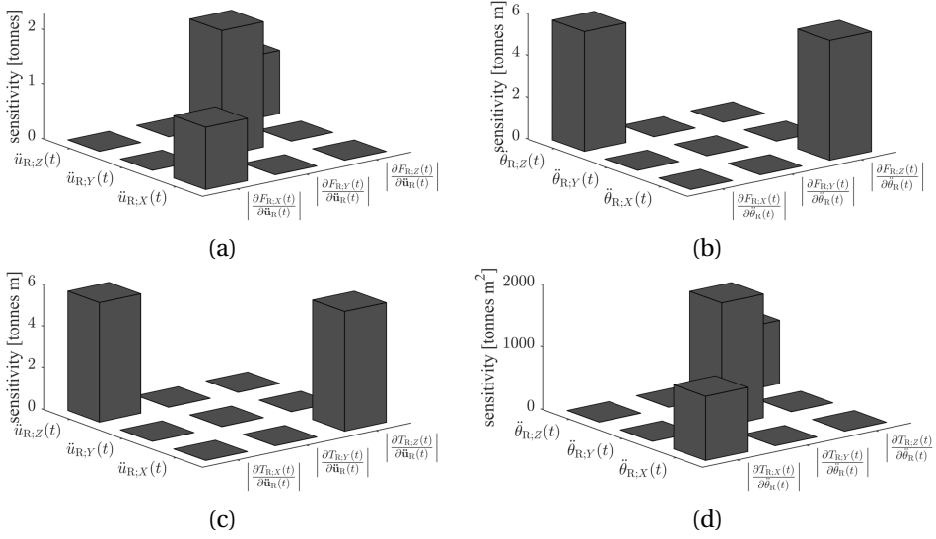


Figure 4.9: Sensitivity of the rotor forces to structural accelerations, with (a) the rotor force sensitivity to translational accelerations, (b) the rotor force sensitivity to rotational accelerations, (c) the rotor force sensitivity to translational accelerations, and (d) the rotor moment sensitivity to rotational accelerations. The diagrams show the absolute values of the force sensitivities.

rotor on a flexible support structure. These matrices were derived for a rotor with rigid blades and are valid for attached flow conditions. In this section, the response of a wind turbine is calculated with the application of the presented matrices, and compared to the response computed with the non-linear state-dependent aerodynamic rotor force expressions as defined in Section 4.2. Moreover, simulations with the aero-elastic software BLADED 4.6 are used to validate the estimated response with the state-dependent and the state-independent simulation approaches.

To predict the structural response of a wind turbine on the basis of these simulation approaches, the UpWind support structure [173] is modelled by means of the finite-element method, allowing for both bending, extensional and torsional deformations, employing the work presented in [271, 272]. This offshore support structure – consisting of a 6 m diameter monopile with an embedded length of 24m and a water depth of 25m – is chosen, as it suits the NREL 5MW turbine. The structure is modelled geometrically linearly with 34 Timoshenko beam elements, containing six degrees of freedom per node (warping is not accounted for). The soil is modelled as a Winkler foundation, representing the stiffness properties of sand. The dynamic properties of the rotor are implemented by means of Eqs. (4.36) to (4.38), for which it was assumed that the rotor blades are identical. The resulting finite-element model replaces the matrices  $\mathbf{M}_T$  and  $\mathbf{K}_T$  of Figure 4.3.

The first six undamped natural frequencies of the modelled turbine are presented in Table 4.2 and the corresponding mode shapes are depicted in Figure 4.10. These dynamic properties are derived for a wind velocity of 15.0 m/s, i.e., the operational conditions are the same as defined in Section 4.4.1. The natural frequencies of the first fore-aft and side-to-side bending modes, which correspond with [173], are similar. This suggests that

the asymmetry introduced by the rotor eccentricity, resulting in a coupling between the side-to-side and torsional motions, is small on the scale of the complete turbine. The similarity between the modes can also be observed in the mode shapes, as shown in Figure 4.10. Here, however, a coupling between the side-to-side bending modes – mode 1, 3 and 6 - and the tower torsion, or yawing mode – mode 5 – is visible. The irregularities in the mode shapes result from the stiffness variation along the length of the turbine structure.

The undamped natural frequencies and the corresponding mode shapes of the first six modes were presented in Table 4.2 and Figure 4.10. The state-independent force expressions introduce an apparent mass and damping, which vary with the operational conditions of the turbine. The effect of the apparent mass on the first six natural frequencies is illustrated in Figure 4.11(a), for two upstream wind speeds, i.e., 6 m/s and 15 m/s. As a result of the apparent mass from the inertia force, the natural frequencies of these modes decreases slightly, with the largest reduction of 2% for mode 5, whereas the first four modes show a reduction of less than 0.5%. Both the wind speed and the rotational speed of the turbine are of negligible influence on the natural frequencies, since both considered operational conditions lead to almost the same reductions.

The contribution of the apparent, or aerodynamic damping to the modal damping of the first six modes, obtained from the real part of the corresponding natural frequencies, is depicted in Figure 4.11(b). The damping ratios are presented as a function of the wind speed and, therefore, implicitly of the operational conditions of the turbine. The highest damping ratios are obtained for the torsional mode. Furthermore, the fore-aft modes generate a higher amount of damping than the side-to-side modes. It is shown that the apparent damping does relate to the operational state, as the damping ratios enhance initially with the increasing rotational speed, after which the damping stabilizes for above rated wind speeds. The small decrease in damping in this wind range is caused by the increasing pitch of the blades to ensure a constant aerodynamic torque.

In the following, Section 4.5.2 describes the BLADED reference model that is used for the validation of the predicted response with the state-dependent and state-independent simulation approaches. Afterwards, the specific analysis approach is addressed in more detail in Section 4.5.3. Section 4.5.4 considers the aerodynamic forces on a rotor mounted on a rigid tower, implying that only the response-independent aerodynamic forces are covered. Dynamic analyses of the aerodynamic excitation are subsequently addressed in Sections 4.5.5 and 4.5.6, which consider the response to a sudden step change in the upstream wind velocity and a turbulent upstream wind velocity, respectively. At the end of Section 4.5.6, misaligned inflow conditions are considered.

#### 4.5.2. BLADED REFERENCE MODEL

To validate the results of the numerical simulation with the model presented in Section 4.5.1, a turbine model with similar properties is created with the software package BLADED 4.6, from here on referred to as BLADED. The turbine is defined as stall-regulated with a constant rotor speed, to ensure a similar behaviour. For numerical simulations, BLADED represents the support structure by a set of attachment modes and constraint modes, effectively employing a sub-structuring technique.

Table 4.3 presents the frequencies corresponding with the six attachment modes.

Table 4.2: First six undamped natural frequencies of the modelled turbine.

mode	frequency [Hz]	description
1	0.269	first side-to-side bending mode
2	0.270	first fore-aft bending mode
3	1.36	second side-to-side bending mode
4	1.40	second fore-aft bending mode
5	1.88	first torsion mode
6	3.02	third side-to-side mode

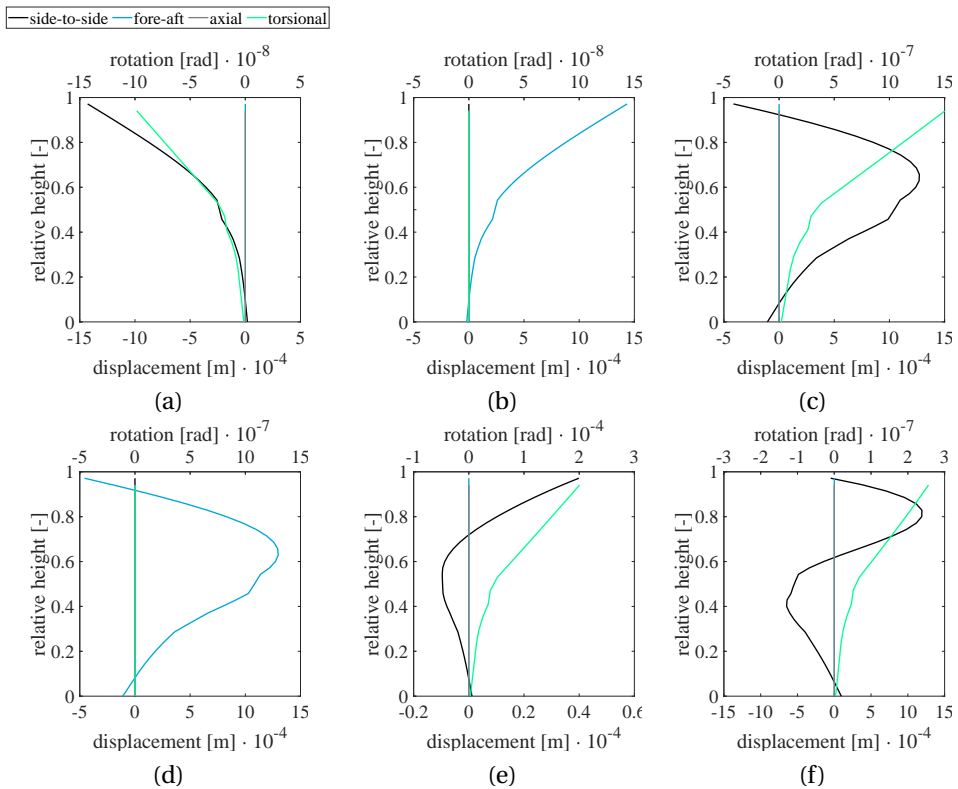


Figure 4.10: First six mode shapes of the modelled undamped turbine for a wind speed of 15.0 m/s, with (a) the first side-to-side bending mode, (b) the first fore-aft bending mode, (c) the second side-to-side bending mode, (d) the second fore-aft bending mode, (e) the first torsion mode, and (f) the third side-to-side mode.

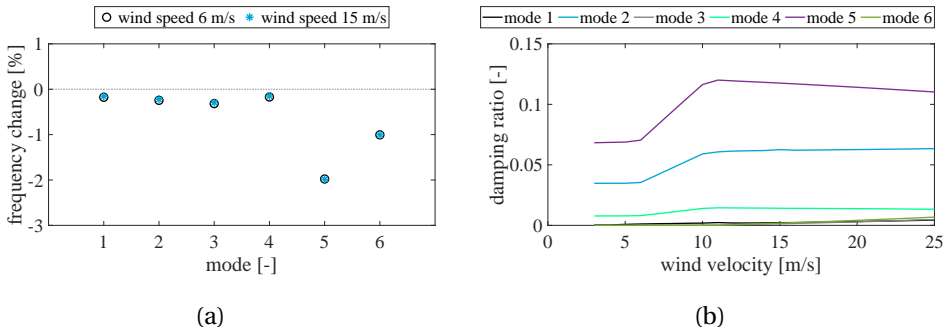


Figure 4.11: Effect of the state-independent forces on the dynamic characteristics of the turbine, with (a) the change in the first six natural frequencies for two operational states, and (b) the damping ratios of the first six modes as a function of the upstream wind velocity.

BLADED bases these mode shapes on the deformation shape resulting from a concentrated load or moment at the tower top. Hence, these modes are obtained from the stiffness properties only. The frequencies of the two translational attachment modes are relatively close to the first side-to-side and fore-aft natural frequencies from the finite-element model. The other attachment modes correspond to very different frequencies than the natural frequencies of Table 4.2. Simulating an analysis with BLADED with a similar dynamic performance as the six-mode approximation of the finite-element model requires the inclusion of a large number of constraint modes. Alternatively, the BLADED model can be reduced to the first two attachment modes only, implying that the model cannot predict resonance response for higher modes. The BLADED model that is adopted for validation purposes accounts for these first two attachment modes, i.e., modes 1 and 2 of Table 4.3, only.

Table 4.3: Six attachment mode frequencies of the BLADED model.

mode	frequency [Hz]	description
1	0.275	side-to-side translational attachment mode
2	0.276	fore-aft translational attachment mode
3	1.89	torsional attachment mode
4	1.91	side-to-side rotational attachment mode
5	2.07	fore-aft rotational attachment mode
6	9.08	up-down attachment mode

#### 4.5.3. ANALYSIS APPROACH

The turbine response analysis comprises the simulated response of the finite-element model with either the state-independent or the state-dependent aerodynamic apparent aero-elastic properties of the aerodynamic force. The predicted response is subsequently validated with the BLADED model presented in Section 4.5.2. As indicated in Section 4.5.2,



the BLADED turbine is modelled as constant speed and stall-regulated, as the force expressions presented in Section 4.3 do not account for a torque or pitch controller either.

The presented aerodynamic force expressions with state-independent apparent aero-elastic properties distinguish the response-independent and the response-dependent force components, i.e., the force components that relate to the response of the turbine structure. This distinction allows to adopt the response-independent force from BLADED, which can be obtained from the simulation of a rotor on a rigid tower. The combined analysis, where BLADED is used to find the response-independent force components and the state-independent force expressions for the response-dependent forces, is referred to as the hybrid analysis procedure.

Table 4.4 summarizes the four simulation approaches and indicates how the flow conditions and the apparent aero-elastic properties of the aerodynamic forcing are accounted for. As indicated, only the BLADED and the hybrid simulation approaches account for separation of the flow. Since the hybrid approach uses the state-independent aero-elastic properties as derived in Section 4.3.2, a separation of the flow can only be accounted for as a part of the response-independent aerodynamic forcing. The state-independent simulation approach, subsequently, is similar to the hybrid approach, with the exception that only attached flow conditions are captured. In the same way, the state-dependent approach is similar to the simulations fully based on BLADED.

Table 4.4: Overview of the four simulation approaches.

description	flow conditions	apparent properties	structural model
BLADED	flow separation possible	state-dependent	two attachment modes
hybrid	flow separation possible*	state-independent	six normal modes
state-independent	attached flow	state-independent	six normal modes
state-dependent	attached flow	state-dependent	six normal modes

\*restricted to the response-independent force components only.

The response analysis requires a modelling of the inflow conditions as well, with which the axially and tangentially induced velocity fields can be determined. For the current analysis, static wake conditions are adopted. The induction coefficients that give expression to the induced velocity fields, are determined with BLADED and subsequently employed in the state-independent, state-dependent and the hybrid analysis procedures.

Regarding the computational procedure, a Galerkin decomposition is applied. As indicated in Table 4.4, the BLADED simulation approach uses the first two attachment modes of the BLADED reference model to obtain the dynamic response. The other simulation approaches employ the finite-element model described in Section 4.5.1, which is subsequently reduced on the basis of the first six normal modes of the unloaded and undamped structure, reducing the number of degrees of freedom for the numerical solver from 208 to six. As a consequence, the BLADED simulations only capture fore-aft and side-to-side motions corresponding with the first attachment modes, whereas the other simulations also allow for motions described by the second fore-aft bending mode, the second and third side-to-side bending modes and the first torsional mode.

#### 4.5.4. FORCE ANALYSIS OF A ROTOR ON A RIGID TOWER

The response-independent aerodynamic force components can be determined with a rigid tower analysis. The resulting thrust force and the aerodynamic torque are determined as a function of the wind speed with both the state-independent model and the BLADED model, see Figure 4.12. The upstream wind is uniform and directed in the global  $Y_T$  direction. For each wind speed, the state-independent analysis uses the inflow conditions, as well as the operational conditions in terms of the rotational speed and the pitch angle, as obtained from BLADED. It should be noted that the state-dependent force expressions will give the same forces for this rigid tower analysis as the state-independent force expressions.

For both the thrust force, Figure 4.12(a), and the aerodynamic torque, Figure 4.12(b), the curves obtained from the state-independent analysis and the BLADED analysis compare well. Apart from the wind speeds close to the cut-out wind velocity the BLADED model predicts a somewhat higher thrust force and aerodynamic torque. For above-rated wind speeds, the aerodynamic torque should be independent of the wind speed, as is correctly obtained from the BLADED model. The state-independent model, however, predicts an aerodynamic torque that slightly increases with the wind speed.

The differences between the calculated thrust and torque results from the attached-flow assumption, which was adopted for the derivation of the state-independent force expressions, whereas the BLADED model allows for flow separation. As a consequence, an offset between the estimated deformations of the tower top in the dynamic analysis (Sections 4.5.5 and 4.5.6) between the BLADED and hybrid simulations – on the one hand – and the state-dependent and state-independent simulations – on the other hand – is to be expected.

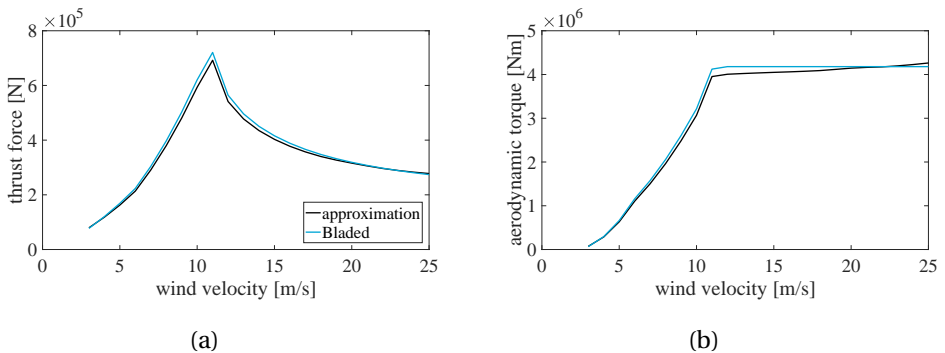


Figure 4.12: Aerodynamic forcing as a function of the upstream wind speed on a rotor with a rigid tower, with (a) the thrust force, and (b) the aerodynamic torque.

#### 4.5.5. RESPONSE ANALYSIS TO A STEP CHANGE IN THE UPSTREAM WIND VELOCITY

The response to a step change in the uniform upstream wind speed provides insight in the structural behaviours as obtained with the different analysis procedures. To analyze these

behaviours, a uniform wind speed of 15 m/s is applied, which after 30 s changes abruptly to 16 m/s. This wind speed signal is illustrated by Figure 4.13. The inflow conditions are based on the static wake assumption, the induced wind field of which is determined for the initial wind speed. Moreover, tip and root loss effects are not accounted for. For each analysis, the initial conditions are chosen such, that no transient response occurs at the start of the simulation.

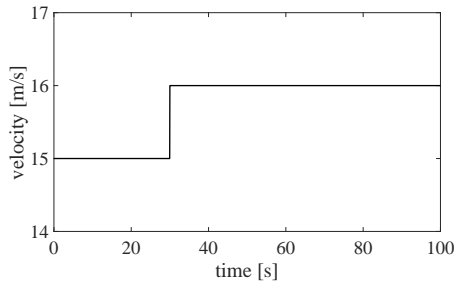


Figure 4.13: Time signal of the uniform upstream wind speed with a step change from 15 m/s to 16 m/s after 30 s.

The tower top deflections resulting from this wind signal are depicted in Figure 4.14, where Figure 4.14(a) presents the fore-aft motion primarily resulting from the thrust force, and Figure 4.14(b) the side-to-side motion resulting from the aerodynamic torque. Both figures present the response from the BLADED simulation, as well as the hybrid, the state-independent and the state-dependent simulations.

Considering first the fore-aft deflections, Figure 4.14(a), the tower top deformation takes place in the positive direction, which coincides with the direction of the wind. The figure shows a difference in the initial deformations for the different simulations; the smallest deformation for the state-independent and state-dependent simulations, a slightly larger deformation for the BLADED simulation and the largest deflection for the hybrid simulation. The cause for this difference can partly be found in the mean force components, as depicted in Figure 4.12(a), which showed that BLADED predicts a higher thrust force for a constant upstream wind speed of 15 m/s than the state-independent approach, and likewise the state-dependent approach. As a consequence, the BLADED and hybrid simulations give a larger initial deflection, whereas the deflections obtained from the state-independent and the state-dependent simulations are equal. The difference between the BLADED and hybrid simulations can be explained in addition by the difference in the first fore-aft natural frequencies, which is larger for the BLADED model. As a consequence, the stiffness of the corresponding modal equation of motion is larger as well, resulting in the smaller deflection.

After the change in wind speed, a transient fore-aft response is induced, which almost completely damps out for all simulations during the remainder of the 100 s simulations. Apart from the different deflections for which each simulation finds its equilibrium, no obvious differences between the fore-aft responses is observed, apart from a small phase

difference between the BLADED simulation and the other three simulations, which again is explained by the difference in the first fore-aft natural frequencies. As the transient responses of the different simulations show a similar pattern, it can be inferred that both the separation of the flow and the state dependency of the apparent aero-elastic properties do not affect the estimated fore-aft motions much.

The side-to-side deflections, presented in Figure 4.14(b) take place in the positive direction as well. The displacement results from the aerodynamic moment around the rotor axis, which results in a positive deflection in the global  $X_T$  direction (see Figure 4.3(b)). The side-to-side motions also show an increase in deflection after the wind speed change, the transient response of which initially damps out quickly. Within the range from 40 s to 60 s, all simulations show an increase in the amplitude of the side-to-side deflection, which subsequently damps out at a much slower rate. This behaviour is explained by the coupling of the first and second modes through the aerodynamic damping, an effect which is smallest for the linearized hybrid and state-independent simulations. With the exception of the BLADED simulation, which only describes fore-aft and side-to-side motions, the side-to-side response signals also have a small higher frequency contribution, which results from the second side-to-side bending mode of vibration of the wind turbine.

The hybrid and the state-independent simulations show a smaller amplitude of oscillation after 50 s than the BLADED and the state-dependent simulations. An explanation can primarily be found in the contribution of the higher-order contributions of the apparent aero-elastic properties. Neglecting the state-dependency of these properties, as is done for the hybrid and the state-independent simulations, results in an underestimation of the amplitude of oscillation of the side-to-side motion.

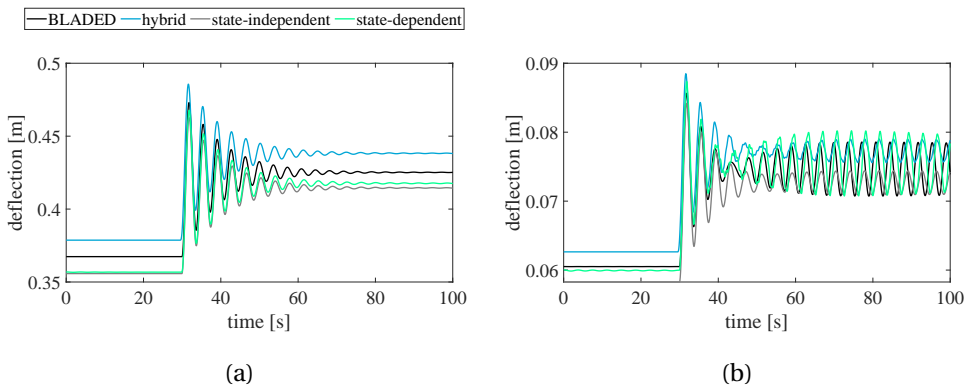


Figure 4.14: Tower top response to a step change in the upstream wind speed, with (a) the fore-aft motion, and (b) the side-to-side motion.

#### 4.5.6. RESPONSE ANALYSIS TO A TURBULENT WIND VARIATION

The turbine models are now applied to compute the time response to a turbulent wind excitation. To this end a time representation of a turbulent wind signal of 1000 s at all

locations of the rotor plane is obtained from a single-point Kaimal turbulence spectrum for a mean wind velocity of 15.0 m/s with a turbulence intensity of 15.7% and a longitudinal turbulence length scale of 340.2 m. Figure 4.15(a) presents a 100 s window of this turbulent wind signal, while the corresponding estimated power spectral density is depicted in Figure 4.15(b).

The power spectral density is estimated from the squared amplitude spectrum of the finite time series, obtained from the fast-Fourier transform, divided by the duration of the time signal. The shape of the Kaimal spectrum can easily be recognized. The time signal presented in the former shows a varying wind with a non-zero mean value. This can be explained from the fact that only a relatively short part of the complete time signal is presented. The statistical properties of the turbulent wind are presented in Table 4.5.

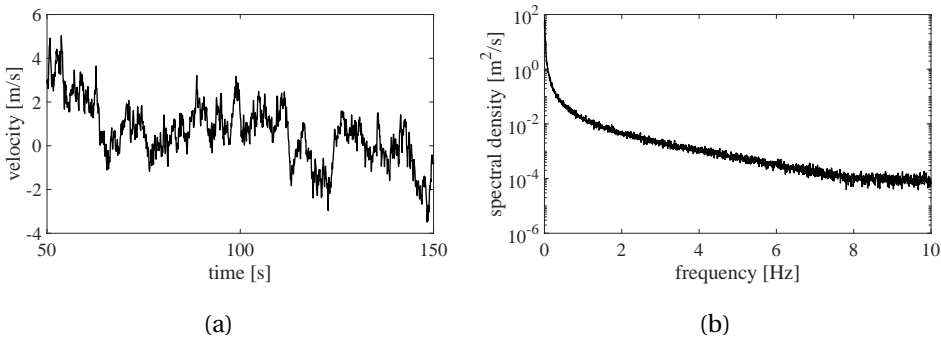


Figure 4.15: Turbulent component of the aerodynamic excitation corresponding to a mean wind velocity of 15.0 m/s, with (a) the time-domain representation, and (b) the estimated power spectral density of the turbulence signal.

Table 4.5: Statistical characteristics of the turbulence signal.

minimum [m/s]	maximum [m/s]	mean [m/s]	standard deviation [m/s]
11.5	20.5	16.3	1.47

In computing the response to the turbulent wind, spatial variations of the turbulence are neglected. As a consequence, a rotational sampling of the turbulence does not introduce higher-frequency components into the excitation signal. Moreover, the induced velocity field at the rotor plane is defined on the basis of the static wake model, implying that it relates to the mean wind velocity component only, and tip and root loss effects are neglected.

Figure 4.16 presents the fore-aft response to the turbulent wind input, distinguishing the time-domain response and the power spectral density of the response, Figure 4.16(a) and (b), respectively. To smooth out the power spectral densities, a moving root mean square filter has been applied. The time signals show a good match between the reference BLADED model on the one hand, and the hybrid, state-independent and state-dependent models on the other hand. This match is confirmed in the frequency domain, where for all simulations a single peak can be observed, which corresponds with the first mode of

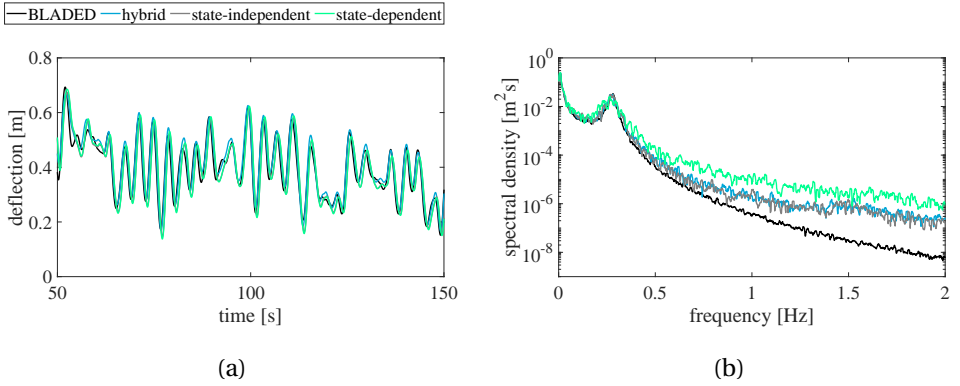


Figure 4.16: Fore-aft motion of the tower top, with (a) the time-domain representations, and (b) the estimated power spectral densities.

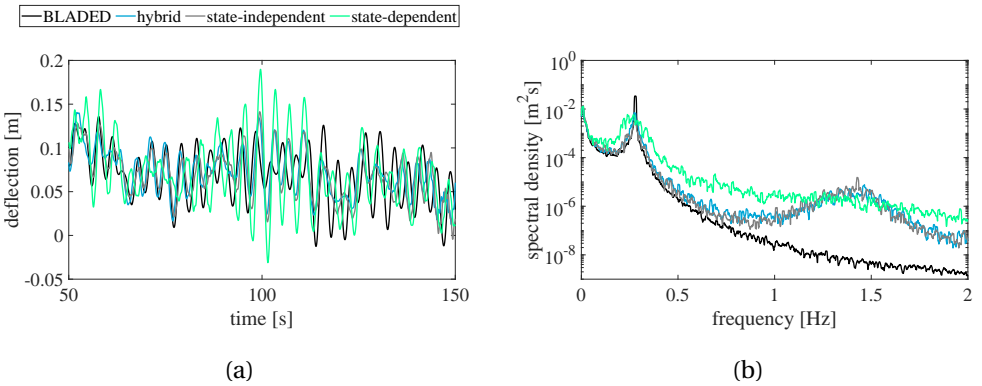


Figure 4.17: Side-to-side motion of the tower top, with (a) the time-domain representations, and (b) the estimated power spectral densities.

Table 4.6: Comparative values of the fore-aft tower top motion.

simulation	minimum [m]	maximum [m]	mean [m]	standard deviation [m]
BLADED	-0.292	0.795	0.361	0.166
hybrid	-0.305	0.807	0.371	0.170
state-independent	-0.253	0.803	0.356	0.166
state-dependent	-0.262	0.818	0.353	0.174

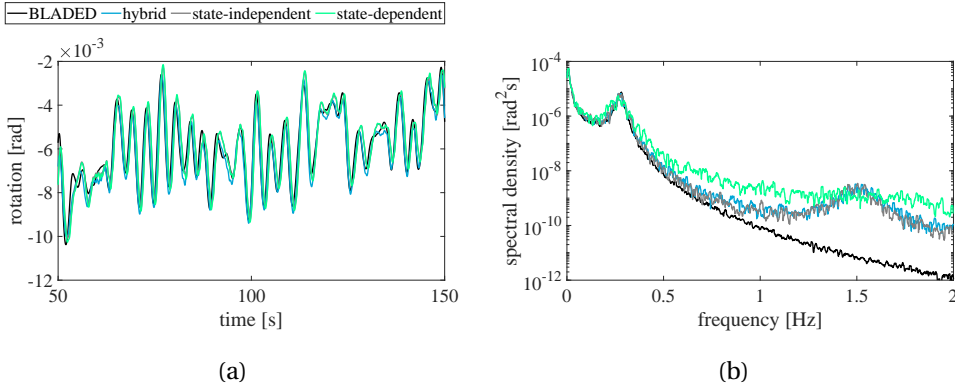


Figure 4.18: Tilting motion of the tower top, with (a) the time-domain representations, and (b) the estimated power spectral densities.

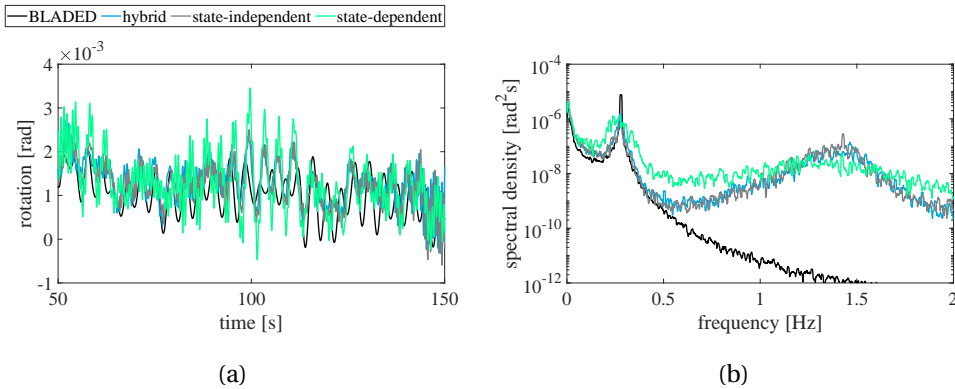


Figure 4.19: Rolling of the tower top, with (a) the time-domain representations, and (b) the estimated power spectral densities.

Table 4.7: Comparative values of the side-to-side tower top motion.

simulation	minimum [m]	maximum [m]	mean [m]	standard deviation [m]
BLADED	-0.0932	0.226	0.0624	0.0516
hybrid	-0.107	0.188	0.0644	0.0448
state-independent	-0.114	0.179	0.0598	0.0427
state-dependent	-0.116	0.215	0.0628	0.0586

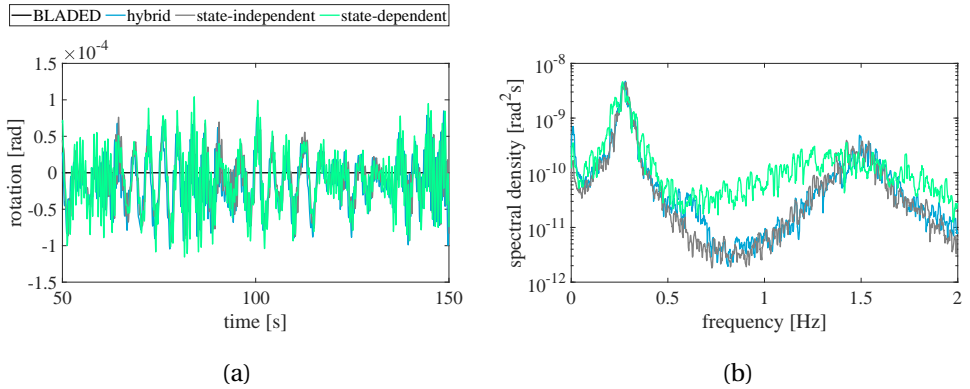


Figure 4.20: Torsional motion of the tower top, with (a) the time-domain representations, and (b) the estimated power spectral densities.

vibration. The order of magnitude of the presented deflections compares well to results presented in [208, 273].

The side-to-side response is presented in Figure 4.17, again showing the response in the time and frequency domains, Figure 4.17(a) and (b), respectively. Compared to the fore-aft motions, the side-to-side motions show a larger variation in the time domain between the simulations, with the largest amplitudes within the presented time window resulting from the state-dependent analysis. The power spectral densities all show a clear peak, at the frequency of the first vibrational mode. The shape of the peak of the state-dependent simulation is broader, indicating a higher amount of damping. The hybrid and state-independent simulations show a second peak, corresponding with the second side-to-side mode of vibration. The BLADED simulation does not show this peak, as the BLADED model only contains the first two attachment modes. In the frequency-domain response of the state-dependent simulation, the peak cannot be distinguished either, implying that the higher-order damping of the second side-to-side mode is substantial.

Figures 4.18, 4.19 and 4.20 show the rolling, tilting and torsional motions of the tower top, respectively. Each of the figures distinguishes a response representation in the time and frequency domain. In both these representations, couplings of the fore-aft and side-to-side motions can be observed. Considering first the tilting response in the time domain, Figures 4.18(a), a similarity with the fore-aft response signal can clearly be observed, see Figure 4.16(a). This similarity can be explained by the coupling of the tower top rotation around the global  $X_T$  axis with the deflection in the global  $Y_T$  direction through the structural model. The rotation takes place in the negative direction, because for low-frequency excitations a positive deflection in the global  $Y_T$  direction results in a negative rotation around the global  $X_T$  axis. When comparing the tilting motion of different simulations in the time-domain, the differences are small. In the frequency-domain, however, the hybrid and state-independent simulations show the peak at the natural frequency corresponding to the second side-to-side mode, as was also observed



for the side-to-side motion, see Figure 4.17(b).

The coupling between the torsional and rolling motions is even stronger, as can be concluded from Figure 4.19, where Figure 4.19(a) shows a high-frequency component in the time signals and Figure 4.19(b) a peak at the natural frequency of the second side-to-side bending mode, which is only one order of magnitude smaller than the peak at the natural frequency of the first side-to-side mode. In the time-domain, the state-dependent simulation shows a larger variation than the other simulations. This variation was observed for the side-to-side motion too, see Figure 4.17(a). Also in the results of the analysis of the step change in the upstream wind velocity, Section 4.5.5, these larger amplitude of the oscillations obtained with the state-dependent simulation approach were observed, which were explained by the contribution of the higher-order contributions of the apparent aero-elastic properties.

The amplitude of the torsional motion, Figure 4.20(a) is much smaller than the amplitude of the other rotations, because the energy level in the excitation signal at the corresponding natural frequency is lower. Again, the torsional motion in the BLADED simulation is absent, as the model does not contain modes that allow for torsion. The other simulations estimated a very similar response in torsion, as is confirmed by the frequency-domain representation, Figure 4.20(b). In the frequency-domain, the coupling with the side-to-side motion is again clearly illustrated.

Tables 4.6 and 4.7 summarize the main statistical properties of the fore-aft and side-to-side motions as obtained with the four different simulation approaches. The tables compare the minimum and maximum deflections during the 1000 s response, as well as the mean and the standard deviation. The presented values show a good agreement of the different approaches. As was already observed from the responses to the step excitation, the BLADED and hybrid simulations show a slightly larger mean fore-aft deformation, resulting from the larger mean thrust force. Concerning the standard deviations of the fore-aft motions, which provides an indication for the differences between predictions of the fatigue damage, only small differences are obtain. In a relative sense, these differences are larger for the side-to-side motions. In absolute terms, the standard deviations of the side-to-side motion are much smaller than the standard deviations of the fore-aft motion, implying that the contribution to the fatigue damage accumulation will be much smaller as well.

Table 4.8: Components of the mean wind velocity in the lateral and axial directions for different misalignment angles.

misalignment [deg]	mean wind in $X_T$ direction [m/s]	mean wind in $Y_T$ direction [m/s]
7.5	1.96	14.9
15.0	3.88	14.5
22.5	5.74	13.9

The derived expressions for the state-dependent and the state-independent aerodynamic interaction, in Sections 4.2 and 4.3, allow for three-dimensional inflow conditions, implying that, for instance, the turbine loads resulting from a yaw misalignment can be estimated. To illustrate the accuracy of the predicted tower motions for yawed loading

conditions, Table 4.8 presents three scenarios with a misalignment angle of 7.5, 15.0 and 22.3 degrees respectively. The table also indicates, for a mean wind speed of 15.0 m/s, the lateral and axial components of the wind with respect to the rotor plane, the wind speeds in the global  $X_T$  and  $Y_T$  directions, respectively.

To understand the impact of the misalignment on the aerodynamic force distribution, the effects of the axial and lateral velocity components are considered separately. As a consequence of the misalignment, the axial wind speed decreases, resulting in an overall reduction of the angle of attack along the blades of the rotor. This smaller angle of attack induces a lower distributed lift force and subsequently a lower aerodynamic torque and thrust force. On average, the tower top deflections, both fore-aft and side-to-side will reduce. In addition, the lower axial wind speed reduces the length over which separation of the flow will take place. Hence, the differences between the response estimations of the BLADED and hybrid simulations – on the one hand – with the state-independent and the state-dependent simulations – on the other hand – will be smaller.

The lateral wind speed, which is introduced with the misalignment, results into a time-varying in-plane flow velocity as experienced by each separate blade, which varies with the rotational frequency of the rotor. Consequently, the angle of attack of each blade varies with this same frequency as well. For three-bladed rotors, this variation in the angle of attack of the individual blades results in harmonic components in the tilting and yawing moments, with a frequency of three times the rotor frequency, i.e., the blade-passing frequency.

As a second result of the time-varying angle of attack, separation of flow will take place over a larger radius of the blades, for which the linear relation between the angle of attack and the lift force is no longer valid. The BLADED simulations account for this non-linear relation in an instantaneous manner. This will reflect in higher-order harmonic components in the aerodynamic forcing. The response-independent aerodynamic force components of the hybrid simulations allow for separation of the flow, whereas the apparent aero-elastic properties are based on assumed attached-flow conditions. The state-independent and state-dependent simulations are fully based on the assumption of attached flows. On this basis, it can be expected that misaligned inflows will show larger differences between the response estimations of the BLADED and hybrid simulations – on the one hand – with the state-independent and the state-dependent simulations – on the other hand.

The tower top displacements for the misaligned load scenarios are presented in Figures 4.21 and 4.22, distinguishing the fore-aft and side-to-side tower top responses in the time- and frequency-domain, respectively. Considering first the time signals of the fore-aft tower top deflections, a general agreement between the estimated motions can be observed, see Figures 4.21(a), (c) and (e). Because of the reduction of the axial wind speeds, the overall fore-aft deflections decrease with the increase of the misalignment angle. As expected, the difference between the BLADED and hybrid simulations, and the state-independent and the state-dependent simulations enhances with the increase in misalignment angle.

The side-to-side motions show stronger variations between the estimated responses, see Figures 4.21(b), (d) and (f), also when compared with the side-to-side motions of the aligned loading scenario of Figure 4.17(a). This larger variation, which was also seen in

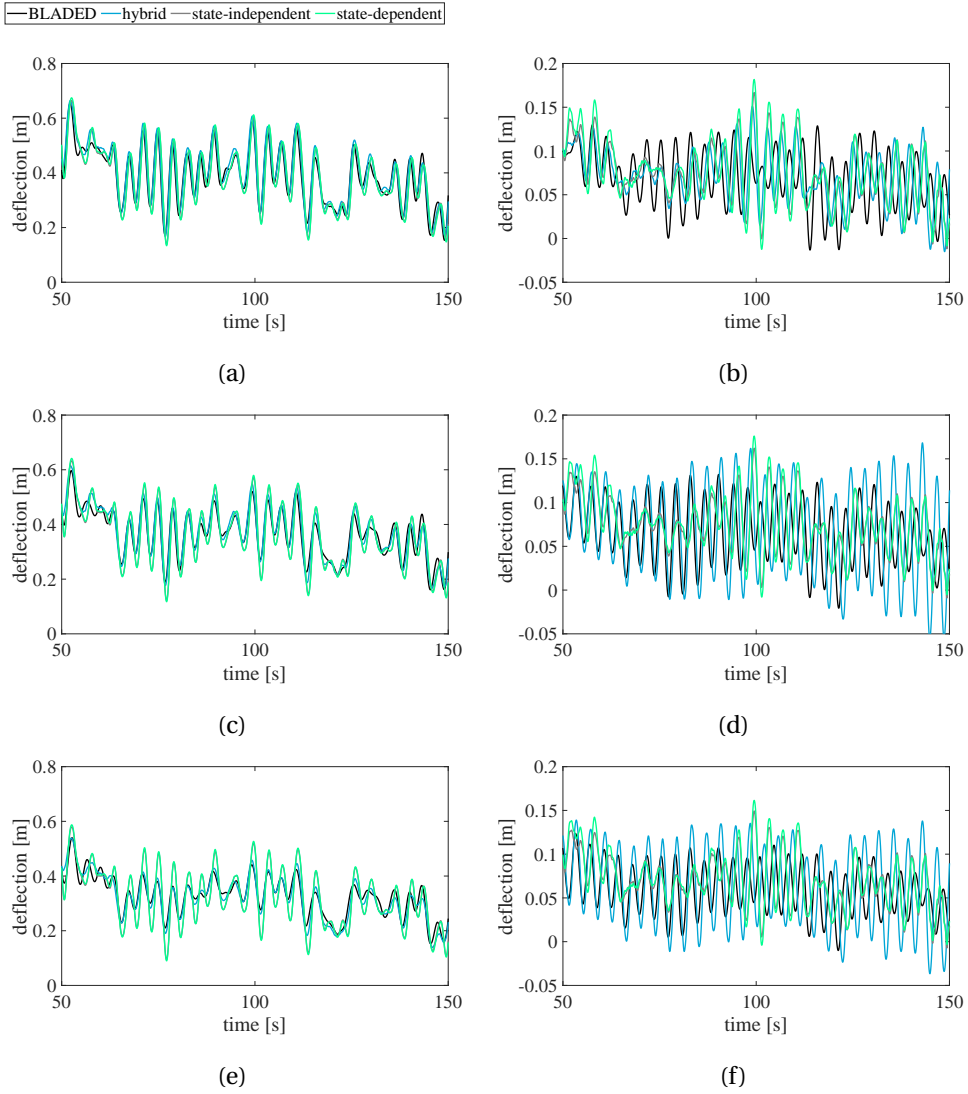


Figure 4.21: Time-domain representations of the tower top deflections for the yaw-misalignment load scenarios of Table 4.8, with (a) the fore-aft deformation for a misalignment angle of 7.5 degrees, (b) the side-to-side deformation for a misalignment angle of 7.5 degrees, (c) the fore-aft deformation for a misalignment angle of 15.0 degrees, (d) the side-to-side deformation for a misalignment angle of 15.0 degrees, (e) the fore-aft deformation for a misalignment angle of 22.5 degrees, and (f) the side-to-side deformation for a misalignment angle of 22.5 degrees.

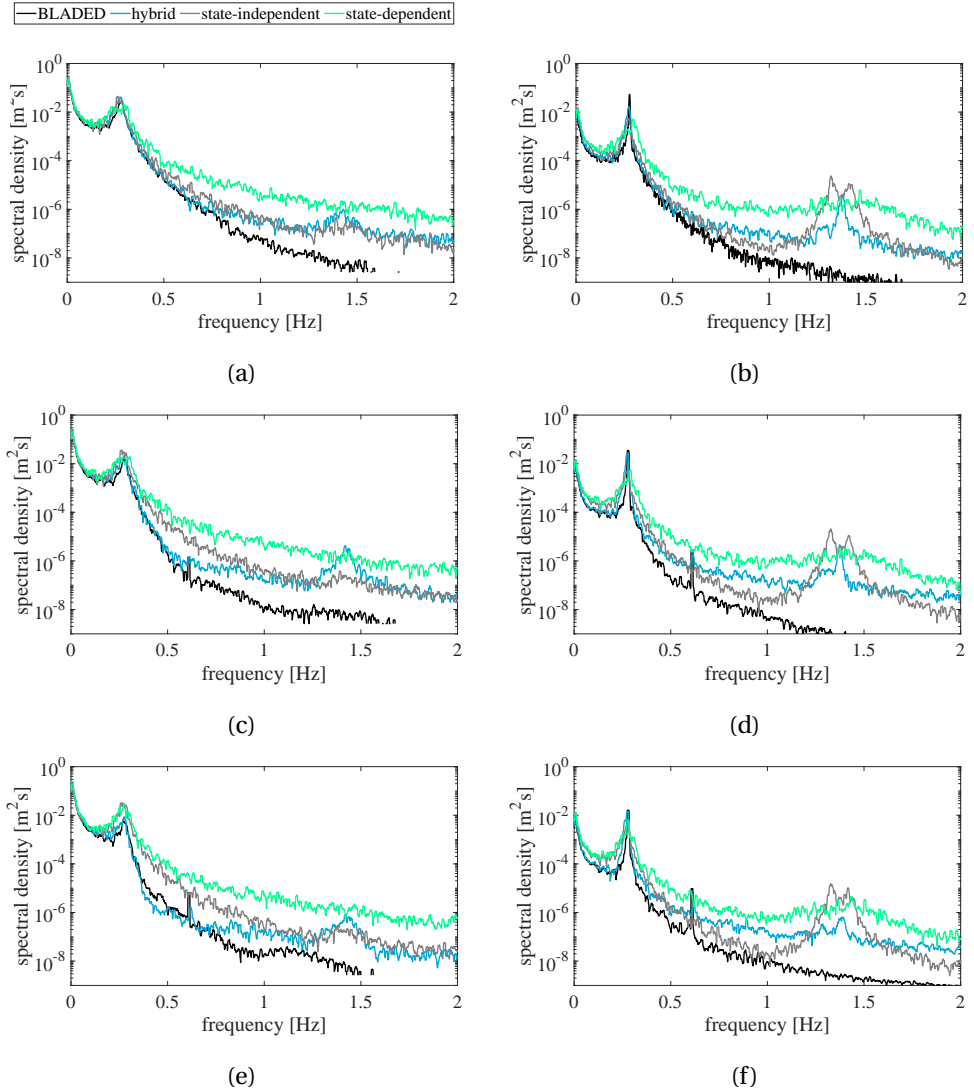


Figure 4.22: Estimated power spectral densities of the tower top deflections for the yaw-misalignment load scenarios of Table 4.8, with (a) the fore-aft deformation for a misalignment angle of 7.5 degrees, (b) the side-to-side deformation for a misalignment angle of 7.5 degrees, (c) the fore-aft deformation for a misalignment angle of 15.0 degrees, (d) the side-to-side deformation for a misalignment angle of 15.0 degrees, (e) the fore-aft deformation for a misalignment angle of 22.5 degrees, and (f) the side-to-side deformation for a misalignment angle of 22.5 degrees.

the analyses of the step change in the upstream wind velocity and the axial turbulent wind, is mainly expressed in the amplitude of the oscillations, whereas no clear effect of the different misalignment angles on the dominant frequency of oscillation can be observed.

In the frequency domain, the fore-aft tower top motions obtained with a different misalignment angle, see Figures 4.22(a), (c) and (e), are similar to the motion obtained with the aligned inflow, Figure 4.16(b). One difference can be observed at the frequency corresponding to the second fore-aft mode of vibration, at which the hybrid simulation shows a small peak. The BLADED simulation does not show peak at this frequency, since the structural model is represented by the first two modes of vibration only. A second difference is visible at the blade-passing frequency, approximately 0.61 Hz, where the BLADED and hybrid simulations develop a small peak with the increasing misalignment angle, resulting from the separation of the flow along parts of the blade radii.

This peak at the blade-passing frequency is more visible in the frequency-domain representation of the side-to-side tower top motions, see Figures 4.22(b), (d) and (f). The more dominant peaks, however can be observed at the frequencies corresponding to the first side-to-side and the second fore-aft and side-to-side modes of vibration. In this respect, the figures are comparable to Figure 4.17(b), which contained the frequency-domain representation of the side-to-side tower top motion for the aligned inflow conditions, with the exception that due to the yaw misalignment the second fore-aft mode is excited too.

Overall, the resemblance between the fore-aft response simulations for the different misalignment angles provides a good basis for the application of the apparent mass, damping and stiffness matrices to model the aerodynamic interaction with the rotor. The estimated side-to-side motions, however, show larger distinctions, especially for the misalignment angles of 15 and 22.5 degrees. Still, for practical design situations, a maximum misalignment angle for normal operations of 8 degrees is prescribed [15], which is close to the analyzed case with 7.5 degrees misalignment, and for which the resemblance in the estimated side-to-side motions is best. On top of this, it should be noted that the current simulations were run without a control algorithm, with which the flow separation resulting from the wind speed fluctuations can be mitigated. It is expected that the implementation of a control algorithm will increase the agreement between the estimated responses even further.

## 4.6. CONCLUSIONS

This chapter presented the derivation of transparent closed-form expressions for the state-dependent aerodynamic excitation of a wind turbine rotor – comprising lift, drag and inertia force components. These expressions relate the structural motion of the turbine tower to the aerodynamic excitation and allow for the simulation of the structural response of a wind turbine tower to a time-dependent aerodynamic excitation. By means of a first-order Taylor approximation, closed-form state-independent apparent stiffness, damping and mass matrices are extracted from the state-dependent force. These expressions are derived in a general manner and allow, therefore, for differences in blade geometries and spatial variations in the aerodynamic excitation. Additionally, the effect of a camber of the blade aerofoils on the aerodynamic forcing is explicitly taken into

account.

In deriving the closed-form expressions, the blades of the rotor were assumed to be rigid. Furthermore, attached-flow conditions were adopted, a requirement which in general can be met over the largest part of the blades by choosing the right rotational velocity and pitch angle. Active control was not accounted for in the model, implying that the rotational velocity and the pitch angle do not respond to velocity changes in the aerodynamic excitation.

For the particular case of a rotor with identical blades and a perfect alignment of the mean wind component, the contribution of the separate aerodynamic force components was visualized for a regular operational state of the NREL 5MW rotor. The mean force components – the aerodynamic thrust and torque – were compared with the forces obtained with the aero-elastic software *BLADED* 4.6., and a good overall agreement was shown. The observed differences could be related to the separation of the flow. Furthermore, the visualization allowed for an assessment of the force-response sensitivity to the different structural motions. The matrices that relate the structural velocities to the aerodynamic forces give insight in the aerodynamic damping of the rotating rotor. The large damping of the fore-aft and yaw motions was illustrated, the former of which being in correspondence with expressions available in literature.

The last part of the chapter addressed the numerical validation of the presented model by comparing the response estimations obtained with the state-independent and the state-dependent simulation approaches, with the response obtained within *BLADED*. A fourth approach, which was referred to as the hybrid simulation approach, combined the response-independent aerodynamic forces from *bladed* with the response-dependent terms of the state-independent simulation approach. Estimated tower top motions were presented for a step change in the upstream wind velocity, and aligned and misaligned turbulent inflow conditions. Concerning the fore-aft tower top motions, all simulations showed a good agreement. The side-to-side motions illustrated the contributions of flow separation and the higher-order terms of the response-dependent aerodynamic force to the aerodynamic interaction with the rotor.

With the application of the state-independent matrix expressions, a wind turbine can be modelled with the inclusion of the coupling of the structural motions through the aerodynamic forces. This way, the force-response interdependency can be assessed and understood, while the detailed modelling of a wind turbine rotor is avoided. In addition, the matrices provide direct insight in the implications of geometric and aero-elastic parameters, such as the rotor eccentricity, rotational velocity, pitch angle, and the lift and drag coefficients, as well as the extent of the coupling of the structural motions through the aerodynamic forcing. Moreover, the matrices allow for the further implementation of rotor control and drive-train dynamics. The expressions presented in this chapter can be adopted for the preliminary design of the foundations of wind turbines. Especially for offshore wind turbines, these expressions allow for a transparent analysis of the coupled aerodynamic and hydrodynamic excitations.

# 5

## A WIND AND WAVE-EXCITED PITCH-REGULATED OFFSHORE WIND TURBINE

*The response of offshore wind turbines to wave excitations is known to be affected considerably by the apparent damping of aerodynamic force, implying that the structural analysis of offshore wind support structures requires a representation of the apparent system properties of this force. The application of the state-independent expressions for the apparent system properties of the aerodynamic force potentially leads to a quicker structural assessment in the preliminary design phase of offshore wind support structures, provided that the estimated response to simultaneous wind and wave excitations is sufficiently accurate. This chapter assesses the accuracy of the method with the state-independent apparent aero-elastic properties in comparison with response estimations obtained with the aero-elastic software BLADED 4.6. Moreover, drive-train and control sub-systems are included, allowing for the analysis of modern pitch-regulated variable-speed wind turbines and the contribution to the state-independent aero-elastic properties defined. In assessing the accuracy of the proposed method, simulations with both aligned and misaligned wind-wave conditions are performed, focussing on the performance of the implemented pitch controller. The results show that the method with state-independent aero-elastic properties gives accurate results, in comparison with BLADED, provided that the controller response is governed by the aerodynamic excitation.*

OFFSHORE wind turbines are exposed to simultaneous wind-wave excitations. For the design, the statistical variation of both environmental excitations needs to be covered adequately, resulting in a vast amount of load simulations. These load simulations should not only represent the expected correlated combinations of wind and wave conditions, but also the directional distributions of both. The integrated design approach, as described in Section 1.1, aims to capture the so-called aero-hydro-servo-elasticity of the complete system, so that the dynamic response of the structure as a whole can be captured sufficiently accurately. The decoupled approach, on the other hand, see Section 1.1, focusses on the modelling of a specific sub-system, whereas the remaining structural components are represented in a simplified manner. The approach aims to capture only the most relevant mechanical behaviour of these simplified components.

For the preliminary design stage, the use of an integrated design model already requires a relatively high level of detail. Combined with the large amount of simulations, little opportunity to process optimizations remains. A decoupled approach may be preferred at this stage, as it leaves more freedom in defining the properties of the separate sub-systems [11]. The question remains what level of detail of these sub-systems is required, in order to obtain an acceptable representation of the system as a whole.

When considering the decoupled modelling of a support structure, the representation of the rotor, drive-train and nacelle should include the relevant mass and damping characteristics. Whereas the mass properties are usually available, concerning the damping, typically only the fore-aft aerodynamic damping is accounted for. Especially for misaligned load cases, a three-dimensional damping representation is required. Misaligned waves excite the side-to-side motion, which is coupled with the torsional motion. Side-to-side motion is limitedly damped, and this damping is often neglected. Yawing motion of the rotor generates a large aerodynamic damping and necessitates a more extensive representation of the aerodynamic damping.

Moreover, the advancing control strategies of wind turbines affect the dynamic characteristics of the system as a whole [274]. In the above-rated regime, this control system regulates the pitch angle of the rotor blades. By pitching the blades, perturbations of the aerodynamic torque are mitigated, so that the rotor speed remains constant. A decoupled model that estimates the aerodynamic excitation of the foundation of a wind turbine, requires a representation of the force mitigating effect of the controller contributions.

The representation of the aerodynamic damping for the decoupled modelling of offshore wind support structures has received significant attention in research. Several studies derived closed-form expressions for the fore-aft damping [50–52], the relevance of which was illustrated by Kühn [49]. Valamanesh and Myers [51] addressed the side-to-side damping of the aerodynamic interaction as well. Other studies suggested the use of an integrated model to obtain the numerical values of the load case-specific damping characteristics, usually in terms of a modal damping ratio [49, 152], which is commonly defined for the first mode of vibration only [47, 48].

A more extensive approach was presented by Schafhirt and Muskulus [55], who estimated the separate damping contributions for the translational and rotational motions of the support structure, from an integrated turbine model. In Chapter 4 of the current work, closed-form expressions for the coupled three-dimensional aerodynamic damping were



presented, assuming attached-flow conditions and linearizing the aerodynamic excitation with respect to the structural kinematics. These closed-form expressions were validated by a comparison with simulations with the aero-elastic software BLADED 4.6 for the NREL 5MW turbine with the UpWind monopile support structure [172, 173]. However, the applicability was not demonstrated for simultaneous misaligned wind-wave excitations of an offshore wind turbine. Moreover, an improved performance can be expected with the inclusion of a representation of the control system of the turbine.

Basic controller concepts for wind turbines are PI and PID controllers [275, 276]. For the below-rated regime, the controller aims at the optimization of the tip speed ratio by adjusting the generator torque, whereas in the above-rated regime, the pitch angle of the blades is controlled, keeping the power output constant, with the input provided by the measured generator speed [31, 172]. Apart from power limitation, the control system serves as well the suppression of the loads [30], for instance by employing the pitch controller to mitigate the oscillations of the support structure [56]. Individual pitch control systems, which affect the pitch angle of each blade separately offer the possibility to reduce asymmetric loads on the rotor plane, for instance resulting from altitudinal wind speed variations [57–59]. In this regard, Fischer *et al.* [60] and Zhang *et al.* [61] studied the application of active generator torque and individual pitch controllers for the mitigation of side-to-side tower oscillations.

The implementation of a control system requires a representation of the drive-train of the wind turbine as well, as the rotor and generator rotations need recognition as separate degrees of freedom. In modelling the drive-train dynamics, numerous studies have aimed at the suppression of torsional oscillations. To this end, Geng *et al.* [277] adopted a two-mass model, accounting for the mass moments of inertia of the wind turbine rotor and the generator, a model which was employed to demonstrate an active-damping strategy. Ritto *et al.* [278] proposed a methodology for the optimization of rotor-bearing systems, based on the dynamic response, making use of a probabilistic drive-train model, whereas Licari *et al.* [279] considered a three-mass model of a drive-train model, considering both shaft and blade flexibilities. Other researchers focussed on the modelling of alternative drive-train systems, such as the direct-driven turbine and turbines with a fluid power transmission [29, 280]. An overview of the trends in drive-train design and the varying modelling strategies was provided by Struggl *et al.* [281].

The current chapter addresses the response estimation with a decoupled support structure model to simultaneous misaligned wind and wave excitations, using the state-independent apparent aero-elastic properties defined in Chapter 4, with the purpose to illustrate their applicability for preliminary design purposes. Whereas in Chapter 4 the turbine was modelled as fixed-speed, here a pitch-regulated variable speed turbine is considered, requiring an extension of the model with drive-train and controller representations. With the primary focus on the pitch controller, the linear contributions of the controller to the aerodynamic forcing are presented, from which, on the basis of a PID controller expression, additional apparent aero-elastic properties are identified.

The inclusion of a pitch controller requires the adoption of a time-dependent pitch angle and rotational velocity of the rotor. In addition, a drive-train needs to be defined, which decouples the rotor rotation from that of the wind turbine tower. For a drive-train with flexible shafts, the rotations of both the rotor and the generator can be distinguished

as degrees of freedom. In Section 5.1, the turbine model of Chapter 4 is extended with drive-train and control sub-systems, resulting in an indirect coupling between the azimuth deviation of the rotor and the tower top motion. The state-independent apparent aero-elastic properties that relate to the pitch controller are then presented in Section 5.2, after defining the coefficients of the linear force contributions of collective pitching actions. Subsequently, Section 5.3 addresses the performance of the proposed modelling approach, using the state-independent apparent aero-elastic properties to represent the aerodynamic excitation, now including the representation of a control system. In this regard, use is made of the properties of the NREL 5MW turbine with the UpWind monopile support structure [172, 173].

The response to combined wind and wave excitations is estimated and compared with response estimated with a similar BLADED model. As in Chapter 4, the response is estimated with a hybrid and a state-dependent approach too, the former consisting of a response-independent force estimation by BLADED, in combination with the state-independent force expressions, which account for the response-dependency of the aerodynamic force, and the latter of a non-linear response-dependent force representation. The BLADED and the state-dependent approaches differ in the sense that BLADED accounts for flow separation for large angles of attack, whereas the state-dependent approach assumes linear relations between the lift and drag coefficients and the angle of attack, or in other words, attached flow conditions.

With the analysis of simultaneous wind and wave excitations, the focus is fully on the offshore application of wind turbines. The comparison of the simulation approaches provides insight in the applicability of the state-independent, or, alternatively, the hybrid analysis approach to estimate the support structure response. In the definition of the model, both pitch and torque controller sub-systems are addressed. Given the state-independent definition of the apparent aerodynamic properties, these approaches are believed to be most promising for preliminary design purposes of support structures of offshore wind turbines.

## 5.1. MODEL DEFINITION

### 5.1.1. TURBINE SYSTEM DEFINITION

The derivations presented in this section are based on the three-bladed rotor as presented in Section 4.1, which was defined within the global inertial  $X_T Y_T Z_T$  reference frame, the floating rotor-fixed  $X_R Y_R Z_R$  reference frame and the blade-fixed  $r_{B;j} Y_{B;j} Z_{B;j}$  reference frames. Whereas the turbine system in Section 4.1 was only divided into tower-nacelle and rotor sub-systems, here, the additional drive-train and control sub-systems, required for the implementation of the pitch controller, are defined in addition.

The dynamic model which is adopted to describe this turbine system is depicted in Figure 5.1. Figure 5.1(a) presents the dynamic properties which are accounted for, and the degrees of freedom of the system. In the following sections, the four sub-systems are described in more detail. The consideration of these sub-systems as a part of the turbine system requires the definition of a force transfer. Regarding the interfaces between these sub-systems, reference is made to Figure 5.1(b), which presents the interaction forces required for the definition of the equations of motion of the separate sub-systems.

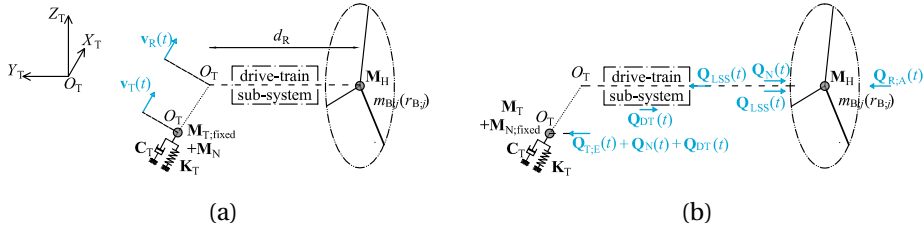


Figure 5.1: Definition of the model characteristics, with (a) the dynamic properties and the degrees of freedom of the system and (b) the external forces and the interface forces between the sub-systems. The drive-train sub-system is considered in detail in Figure 5.2

### ROTOR SUB-SYSTEM

Compared with the rotor sub-system definition of Section 4.1, the rotor speed is now time varying. The time-dependent rotational velocity of the rotor can be expressed as a superposition of the mean rotational velocity  $\bar{\Omega}_{R;Y}^f$  and the variational rotational velocity  $\Delta\Omega_{R;Y}^f(t)$ :

$$\Omega_{R;Y}^f(t) = \bar{\Omega}_{R;Y}^f + \Delta\Omega_{R;Y}^f(t). \quad (5.1)$$

The cumulative azimuth deviation of the rotor, with respect to the mean, can be expressed in terms of  $\Delta\Psi_{R;Y}^f(t)$ :

$$\Delta\Psi_{R;Y}^f(t) = \int_0^t \Delta\Omega_{R;Y}^f(t) dt. \quad (5.2)$$

The rotor azimuth corresponding with the mean rotational velocity  $\bar{\Omega}_{R;Y}^f$  is indicated as  $\bar{\Psi}_{R;Y}^f(t)$ .

The motion of the rotor sub-system in the global inertia reference frame is described by the six-component deformation vector  $\Delta\mathbf{v}_R(t)$ , composed of the translation vector  $\Delta\mathbf{u}_R(t)$ , and the rotation vector  $\Delta\boldsymbol{\theta}_R(t)$ . In the moving rotor reference frame, the rotational degrees of freedom of the rotor consist of the rotations  $\Delta\theta_{R;X}^f(t)$  and  $\Delta\theta_{R;Z}^f(t)$  and the azimuth deviation around the  $Y_R$  axis:

$$\Delta\boldsymbol{\theta}_R^f(t) = \begin{bmatrix} \Delta\theta_{R;X}^f(t) \\ \Delta\Psi_{R;Y}^f(t) \\ \Delta\theta_{R;Z}^f(t) \end{bmatrix}. \quad (5.3)$$

The matrix  $\mathbf{R}_{R;\theta}(t)$  defines the transformation from the rotor reference frame to the inertial reference frame:

$$\Delta\boldsymbol{\theta}_R(t) = \mathbf{R}_{R;\theta}(t)\Delta\boldsymbol{\theta}_R^f(t). \quad (5.4)$$

Following the same procedure as in Section 4.3, the linearized system of equations of

motion for the rotor sub-system can be defined:

$$\begin{aligned} \left[ \mathbf{M}_H + \sum_{j=1}^3 \mathbf{M}_{B;j}(t) \right] \Delta \ddot{\mathbf{v}}_R(t) + \sum_{j=1}^3 \mathbf{C}_{B;j}(t) \Delta \dot{\mathbf{v}}_R(t) + \sum_{j=1}^3 \mathbf{K}_{B;j}(t) \Delta \mathbf{v}_R(t) = \\ \sum_{j=1}^3 \mathbf{Q}_{B;j}(t) + \mathbf{Q}_{R;A}(t) - \mathbf{Q}_N(t) - \mathbf{Q}_{LSS}(t). \end{aligned} \quad (5.5)$$

Here, the rotational degrees of freedom are approximated as:

$$\Delta \boldsymbol{\theta}_R(t) \approx \begin{bmatrix} \Delta \theta_{R;X}(t) \\ \Delta \Psi_{R;Y}^f(t) \\ \Delta \theta_{R;Z}(t) \end{bmatrix} \quad (5.6)$$

On the right-hand side of Eq. (5.5),  $\mathbf{Q}_N(t)$  contains the force components that are transferred directly through the bearings of the low-speed shaft to the nacelle and, subsequently the tower.  $\mathbf{Q}_{LSS}(t)$  contains the torque that is transferred to the gearbox through the low-speed shaft.

#### DRIVE-TRAIN SUB-SYSTEM

The drive-train sub-system describes the dynamic force balance between the torque on the low-speed shaft and the electro-magnetic generator torque,  $T_{LSS;Y}^f(t)$  and  $T_{G;Y}^f(t)$ , respectively (see Figure 5.1). As the axis of rotation corresponds with the  $Y_R$  axis of the rotor, the system is defined in the floating rotor reference frame. Assuming an indirect drive, the drive-train consists of a low-speed shaft, connected the hub to the rotor and a high-speed shaft which connects to the generator. The low-speed and high-speed shafts are coupled through the gearbox, of which the gearbox ratio  $N_{DT}$  defines ratio of the torques of the drive-train shafts. In the dynamic modelling of the drive-train for global response analysis, the shafts are commonly assumed to be massless. Moreover, an effective stiffness  $K_{DT}$  and damping  $C_{DT}$  are included, where ‘DT’ refers to drive-train. Regarding the degrees of freedom, the azimuth deviations of the rotor and the generator can be distinguished, where the latter is expressed by  $\Delta \Psi_{G;Y}^f(t)$  and is obtained from the integration of the generator speed deviation  $\Delta \Omega_{G;Y}^f(t)$  over time, similar to Eq. (5.2). This definition of the drive-train model corresponds with models, previously reported in [61, 279], and is depicted in Figure 5.2, with Figure 5.2(a) presenting the dynamic properties and the degrees of freedom, and Figure 5.2(b) the torque transfer.

The equations of motion of the rotor sub-system, Eq. (5.5), contain the dynamic equilibrium of the rotor mass moment of inertia with the difference between the aerodynamic torque and the torque of the low-speed shaft. Introducing a friction between the low-speed shaft and the shaft bearing, expressed by the coefficient  $\mu_{DT}$ , the equation of motion of the low-speed shaft can be expressed as

$$C_{DT} \left( \Delta \dot{\Psi}_{R;Y}^f(t) - \frac{\Delta \dot{\Psi}_{G;Y}^f(t)}{N_{DT}} \right) + K_{DT} \left( \Delta \Psi_{R;Y}^f(t) - \frac{\Delta \Psi_{G;Y}^f(t)}{N_{DT}} \right) = (1 - \mu_{DT}) T_{LSS;Y}^f(t). \quad (5.7)$$

The friction-component of the aerodynamic torque,  $\mu_{DT} T_{LSS;Y}^f(t)$ , is transferred through the bearing to the nacelle.

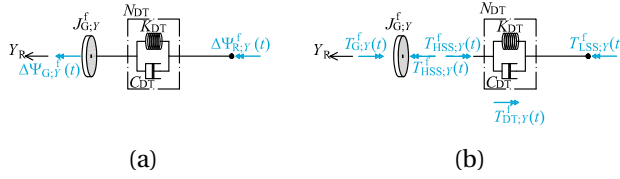


Figure 5.2: Schematic representation of the drive-train sub-system within the floating rotor reference frame, with (a) the rotational degrees of freedom of the low-speed and high-speed shafts, and (b) the transmission of the aerodynamic torque through the drive-train to the tower fixed-nacelle components.

The equation of motion of the high-speed shaft, including the generator inertia, is obtained as

$$J_{G;Y}^f \Delta\ddot{\Psi}_{G;Y}^f(t) + C_{DT} \left( \frac{\Delta\dot{\Psi}_{G;Y}^f(t)}{N_{DT}^2} - \frac{\Delta\dot{\Psi}_{R;Y}^f(t)}{N_{DT}} \right) + K_{DT} \left( \frac{\Delta\Psi_{G;Y}^f(t)}{N_{DT}^2} - \frac{\Delta\Psi_{R;Y}^f(t)}{N_{DT}} \right) = -T_{G;Y}^f(t). \quad (5.8)$$

Summation of Eqs. (5.7) and (5.8), after multiplication of the latter with the gearbox ratio  $N_{DT}$ , results in the global balance equation of the drive-train sub-system:

$$N_{DT} J_{G;Y}^f \Delta\ddot{\Psi}_{G;Y}^f(t) = (1 - \mu_{DT}) T_{LSS;Y}^f(t) - N_{DT} T_{G;Y}^f(t). \quad (5.9)$$

Moreover, after defining the torque of the high-speed shaft  $T_{HSS;Y}^f(t)$  in terms of the generator acceleration and the generator torque,

$$T_{HSS;Y}^f(t) = J_{G;Y}^f \Delta\ddot{\Psi}_{G;Y}^f(t) + T_{G;Y}^f(t), \quad (5.10)$$

the low-speed and high-speed torques can be related in terms of the gearbox ratio:

$$T_{HSS;Y}^f(t) = (1 - \mu_{DT}) \frac{\pm T_{LSS;Y}^f(t)}{N_{DT}}. \quad (5.11)$$

The sign difference, ‘ $\pm$ ’, indicates whether the gearbox contains an even or odd number of stages.

The total torque transferred through the drive-train to the nacelle, which is defined as  $T_{HSS;Y}^f(t)$ , is composed of the low-speed shaft friction, the summation of the gearbox torques and the generator torque on the stator:

$$T_{DT;Y}^f(t) = \mu_{DT} T_{LSS;Y}^f(t) + \left\{ (1 - \mu_{DT}) T_{LSS;Y}^f(t) \mp T_{HSS;Y}^f(t) \right\} \pm T_G^f(t), \quad (5.12)$$

which, after substitution of Eq. (5.8) turns into

$$T_{DT;Y}^f(t) = T_{LSS;Y}^f(t) \mp J_{G;Y}^f \Delta\ddot{\Psi}_{G;Y}^f(t). \quad (5.13)$$

In absence of an acceleration of the rotor, the aerodynamic torque is transmitted in full to the top of the tower. In case of a time-varying aerodynamic torque, only a fraction of the torque deviation is transferred, as the varying torque will primarily result in an acceleration of the rotor sub-system.

### TOWER-NACELLE SUB-SYSTEM

The tower-nacelle sub-system is defined by the mass matrices  $\mathbf{M}_T$  and  $\mathbf{M}_{N;\text{fixed}}$ , and the damping and stiffness matrices  $\mathbf{C}_T$  and  $\mathbf{K}_T$ .  $\mathbf{M}_{N;\text{fixed}}$  is the nacelle inertia matrix, containing the inertias of the tower-fixed nacelle components, and therefore not including the mass moment of inertia of the drive-train components around the rotor axis  $Y_R$ . For reasons of convenience, the sub-system characteristics are lumped at  $O_T$ . The motion of the tower top is described by the six-component deformation vector  $\Delta\mathbf{v}_T(t)$ , composed of the translation vector  $\Delta\mathbf{u}_T(t)$  and the rotation vector  $\Delta\boldsymbol{\theta}_T(t)$ :

$$[\mathbf{M}_T + \mathbf{M}_{N;\text{fixed}}] \Delta\ddot{\mathbf{v}}_T(t) + \mathbf{C}_T \Delta\dot{\mathbf{v}}_T(t) + \mathbf{K}_T \Delta\mathbf{v}_T(t) = \mathbf{Q}_{T;E}(t) + \mathbf{Q}_N(t) + \mathbf{Q}_{DT}(t). \quad (5.14)$$

The translations of the tower top are fully coupled to the translation of the rotor sub-system, implying that

$$\Delta\mathbf{u}_T(t) = \Delta\mathbf{u}_R(t). \quad (5.15)$$

Within the reference frame of the rotor, the rotations around the  $X_R$  and  $Z_R$  axes of the rotor and tower-nacelle sub-systems are equal as well. The rotations around the  $Y_R$  axis are coupled through the transferred drive-train force vector  $\mathbf{Q}_{DT}(t)$ . The external forces acting on the tower are represented by the effective force vector  $\mathbf{Q}_{T;E}(t)$ . Among others, this vector contains forces resulting from the aerodynamic drag and, in the case of offshore wind turbines, hydrodynamic impacts.

### CONTROLLER SUB-SYSTEM

For below-rated wind velocities, the control sub-system of a variable speed pitch-regulated wind turbine aims at power optimization. To this end, the magnitude of the generator torque  $T_{G;Y}^f(t)$  is controlled, based on the measured magnitude of the rotational velocity of the high-speed shaft  $\Omega_{G;Y}^f(t)$ . For a given operational state of the turbine, the magnitude of the generator torque can be defined as  $\bar{T}_{G;Y}^f$ . A perturbation of the operational conditions yields a variation of the generator torque  $\Delta T_{G;Y}^f(t)$ , to optimize the power output by maintaining a constant optimal tip-speed ratio of the rotor. For the below-rated regime, the generator torque can be defined as

$$T_{G;Y}^f(t) = \bar{T}_{G;Y}^f + \Delta T_{G;Y}^f(t). \quad (5.16)$$

In the above-rated regime, the turbine should operate such, that the generator torque remains constant, i.e.,  $T_{G;Y}^f(t) = \bar{T}_{G;Y}^f$ . This can be achieved with the implementation of a collective full-span pitch control system, which relates a change in the generator rotational velocity to an adjustment in the pitch angle of the rotor blades. For a certain operational state, the pitch angle can be defined as the superposition of its mean and a variation:

$$\beta_R^r(t) = \bar{\beta}_R^r + \Delta\beta_R^r(t), \quad (5.17)$$

where  $\bar{\beta}_R^r$  and  $\Delta\beta_R^r(t)$  are the mean pitch angle and the corresponding perturbation, respectively. The collective angle  $\beta_R^r(t)$  expresses the pitch angles  $\beta_{B;j}^r(t)$  of the individual

blades, and relates, for that reason, to the rotating blade reference frames, indicated by the superscript 'r'.

Concerning the equations of motion describing the control sub-system, the below and above-rated regimes are distinguished. For below-rated wind velocities, the generator torque should be set proportional to the square of the measured rotational speed of the high speed shaft [30]:

$$T_{G;Y}^f(t) = G_{G;P} \left\{ \dot{\Psi}_{G;Y}^f(t) \right\}^2. \quad (5.18)$$

The proportionality coefficient  $G_{G;P}$  is defined on the basis of the air density, rotor diameter, gearbox ratio and the tip-speed ratio that maximizes the power output.

For a given operational state with the mean generator torque  $\bar{T}_{G;Y}^f$  and corresponding high-speed shaft velocity  $\bar{\Omega}_{G;Y}^f$ , the variation of the generator torque  $\Delta T_{G;Y}^f(t)$ , resulting from a rotational velocity perturbation  $\Delta \dot{\Psi}_{G;Y}^f(t)$ , can be approximated as

$$T_{G;Y}^f(t) \approx T_{G;Y}^f(t) \Big|_{\dot{\Psi}_{G;Y}^f(t)=\bar{\Omega}_{G;Y}^f} + \left[ \frac{\partial T_{G;Y}^f(t)}{\partial \dot{\Psi}_{G;Y}^f(t)} \Big|_{\dot{\Psi}_{G;Y}^f(t)=\bar{\Omega}_{G;Y}^f} \right] \Delta \dot{\Psi}_{G;Y}^f(t), \quad (5.19)$$

which can be re-formulated as

$$T_{G;Y}^f(t) \approx \bar{T}_{G;Y}^f + G_{G;P} \bar{\Omega}_{G;Y}^f \Delta \dot{\Psi}_{G;Y}^f(t), \quad (5.20)$$

from which it follows that

$$\Delta T_{G;Y}^f(t) \approx G_{G;P} \bar{\Omega}_{G;Y}^f \Delta \dot{\Psi}_{G;Y}^f(t). \quad (5.21)$$

This approximation is based on the assumption that  $\Delta \dot{\Psi}_{G;Y}^f(t)$  is much smaller than  $\bar{\Omega}_{G;Y}^f$ .

For the above-rated regime, the pitch controller aims keeping a constant generator torque. A PID controller relates the variation of the generator speed to an adjusted pitch angle in the following manner:

$$\Delta \beta_{R}^r(t) = G_{\beta;D} \Delta \dot{\Psi}_{G;Y}^f(t) + G_{\beta;P} \Delta \dot{\Psi}_{G;Y}^f(t) + G_{\beta;I} \Delta \Psi_{G;Y}^f(t), \quad (5.22)$$

or, for rigid drive-trains,

$$\Delta \beta_{R}^r(t) = N_{DT} G_{\beta;D} \Delta \dot{\Psi}_{R;Y}^f(t) + N_{DT} G_{\beta;P} \Delta \dot{\Psi}_{R;Y}^f(t) + N_{DT} G_{\beta;I} \Delta \Psi_{R;Y}^f(t), \quad (5.23)$$

where  $G_{\beta;D}$ ,  $G_{\beta;P}$  and  $G_{\beta;I}$  are the differential, proportional and integral gains of the pitch control, respectively.

The aerodynamic torque  $T_{R;A;Y}^f(t)$  is a function of the collective pitch  $\beta_R^r(t)$ , and its first and second time derivatives. If the optimal pitch angle for a given operational state is defined as  $\bar{\beta}_R$ , the first-order Taylor approximation of the aerodynamic torque with respect to the collective pitch can be expressed as

$$\begin{aligned} T_{R;A;Y}^f(t) \approx T_{R;A;Y}^f(t) \Big|_{\beta_R^r(t)=\bar{\beta}_R} + \left[ \frac{\partial T_{R;A;Y}^f(t)}{\partial \beta_R^r(t)} \Big|_{\beta_R^r(t)=\bar{\beta}_R} \right] \Delta \beta_R^r(t) \\ + \left[ \frac{\partial T_{R;A;Y}^f(t)}{\partial \dot{\beta}_R^r(t)} \Big|_{\beta_R^r(t)=\bar{\beta}_R} \right] \Delta \dot{\beta}_R^r(t) + \left[ \frac{\partial T_{R;A;Y}^f(t)}{\partial \ddot{\beta}_R^r(t)} \Big|_{\beta_R^r(t)=\bar{\beta}_R} \right] \Delta \ddot{\beta}_R^r(t). \end{aligned} \quad (5.24)$$

Eq. (5.24) serves as a basis for the derivation of the pitch-dependent aerodynamic force components, which are presented in Section 5.2.

### 5.1.2. SYSTEM OF EQUATIONS OF MOTION

The system of equations of motion of the turbine system, as defined by Figure 5.1, can now be composed of the equations of motions of the different sub-systems. Starting with the rotor sub-system, the motion is described by Eq. (5.5). This expression is derived for three-bladed rotors, and is valid for both isotropic and anisotropic systems, i.e., a rotor with identical or different blades. The rotor sub-system transfers the aerodynamic torque  $T_{R;A;Y}^f(t)$  to the drive-train subsystem, while the remaining forces are transferred directly to the tower-fixed nacelle components.

The motion of the drive-train is described by Eqs. (5.7) and (5.8), which only accounts for the motions of the low-speed and high-speed-shafts,  $\Delta\Psi_{R;Y}^f(t)$  and  $\Delta\Psi_{G;Y}^f(t)$ . Here, an indirect-drive with a gearbox is adopted. With a gearbox ratio  $N_{DT} = 1$ , the system can be applied to describe a direct-drive transmission too. It is assumed that part of the mechanical torque can be transferred to the bedplate directly. To this end, the friction coefficient  $\mu_{DT}$  is introduced.

The tower sub-system is represented by the mass matrices  $\mathbf{M}_T$  and  $\mathbf{M}_{N;fixed}$ , and the stiffness and damping matrices  $\mathbf{K}_T$  and  $\mathbf{C}_T$ , with which the motion of the tower top can be described. The matrix  $\mathbf{M}_{N;fixed}$  contains the inertias of the tower-fixed nacelle components. The motion is expressed by Eq. (5.14), where the external forcing on the tower is given by  $\mathbf{Q}_{T;E}(t)$ . This forcing represents the environmental actions on the tower, for instance the aerodynamic drag or hydrodynamic impacts for offshore wind turbines. The remaining forces on the tower top are internal forces, required to describe the transfer of the aerodynamic forcing through the drive-train and the nacelle.

For the control of the power output and the aerodynamic torque, the control sub-system has been defined. The control of the generator torque for the below-rated regime is given by Eq. (5.18), a linearization of which is given by Eq. (5.20). For the above-rated regime a pitch controller becomes active. Eq. (5.22) presents a PID-controller for the full-span collective pitch  $\beta_R^f(t)$ .

In the derivation of the equations of motion, the small angle assumption was adopted for the deformations of the system. As a consequence, the axis of rotation of the rotor approximately coincides with the global inertial  $Y_T$  axis of the turbine system. With the inclusion of a geometrical tilt, this assumption would be violated to a certain extent, and the transformation from the global inertial reference frame to the floating frame of reference becomes more cumbersome.

## 5.2. EXTENSION OF THE STATE-INDEPENDENT APPARENT AERO-ELASTIC PROPERTIES

### 5.2.1. INFLUENCE OF PITCH ACTIONS ON THE AERODYNAMIC EXCITATION

In Section 5.1, the equations of motion of a turbine with a rigid rotor on a flexible tower were derived. The aerodynamic excitation of the rotor was expressed as  $\mathbf{Q}_{R;A}(t)$ , consisting of forces and moments, defined in the global inertial reference frame. As described in Section 4.2, the aerodynamic excitation is obtained from the integration of the aerodynamic forces acting along the length of the blades. These aerodynamic forces are a function of the pitch angle  $\beta_R^f(t)$ , both through the angle of attack, and through its influence on the relative inflow velocity.



In accordance with Figure 2.9(a), the attack  $\alpha_{B;j}^r(r_{B;j}, t)$  adheres to the following definition:

$$\sin \alpha_{B;j}^r(r_{B;j}, t) = \frac{W_{B;rel;y;j}^r(r_{B;j}, t)}{|W_{B;rel;j}^r(r_{B;j}, t)|}, \quad (5.25)$$

with  $W_{B;rel;y;j}^r(r_{B;j}, t)$  representing the magnitude of the relative wind velocity in the local  $y_{B;j}$  direction (it could be argued that the superscript 'r' is superfluous for variables defined in the local blade reference frames):

$$W_{B;rel;y;j}^r(r_{B;j}, t) = \left\{ \beta_{B;j}^r(r_{B;j}, t) \right\}^T W_{B;rel;j}^r(r_{B;j}, t). \quad (5.26)$$

The vector  $\beta_{B;j}^r(r_{B;j}, t)$  expresses the orientation of the aerofoil as a result of the geometrical twist  $\beta_{B;0;j}^r(r_{B;j})$  and the blade pitch angle  $\beta_{B;j}^r(r_{B;j}, t)$ :

$$\beta_{B;j}^r(r_{B;j}, t) = \begin{bmatrix} 0 \\ \cos \left( \beta_{B;0;j}^r(r_{B;j}) + \beta_{B;j}^r(r_{B;j}, t) \right) \\ -\sin \left( \beta_{B;0;j}^r(r_{B;j}) + \beta_{B;j}^r(r_{B;j}, t) \right) \end{bmatrix}. \quad (5.27)$$

For a full-span collective pitch control system, the pitch angle of the blades can be described by Eq. (5.17). Subsequently, the vector  $\beta_{B;j}^r(r_{B;j}, t)$  can be replaced by the following multiplication:

$$\beta_{B;j}^r(r_{B;j}, t) = \mathbf{R}_{R;\beta}(t) \beta_{B;0}^r(r_{B;j}), \quad (5.28)$$

where  $\mathbf{R}_{R;\beta}(t)$  and  $\beta_{B;0}^r(r_{B;j})$  are given by

$$\mathbf{R}_{R;\beta}(t) = \begin{bmatrix} 1 & 0 & 0 \\ 0 & \cos \beta_R^r(t) & -\sin \beta_R^r(t) \\ 0 & \sin \beta_R^r(t) & \cos \beta_R^r(t) \end{bmatrix}, \quad (5.29)$$

and

$$\beta_{B;0;j}^r(r_{B;j}) = \begin{bmatrix} 0 \\ \cos \beta_{B;0;j}^r(r_{B;j}) \\ -\sin \beta_{B;0;j}^r(r_{B;j}) \end{bmatrix}. \quad (5.30)$$

With the application of the thin aerofoil theory, and assuming that the inflow velocity is constant over the length of the aerofoil chord  $c_{B;j}(r_{B;j})$ , the relative wind velocity  $W_{B;rel;j}^r(r_{B;j}, t)$  can be obtained from (see Section 2.3)

$$W_{B;rel;j}^r(r_{B;j}, t) = W_{B;j}^r(r_{B;j}, t) - \dot{\mathbf{x}}_{B;j}^r(r_{B;j}, t) - \left( \frac{1}{2} b(r_{B;j}) - z_\beta(r_{B;j}) \right) \left( \mathbf{e}_{B;z}^r \times \dot{\beta}_R^r(t) \right). \quad (5.31)$$

The third term of Eq. (5.31) results from the additional velocity at the third-quarter chord point, induced by a pitch action.  $z_\beta(r_{B;j})$  specifies the location of the pitch axis on the

chord line of the aerofoil, as indicated in Figure 5.3 and  $\mathbf{e}_{B;z}^r$  is the unit vector defining the local  $z_{B;j}$  axis. The figure also illustrates the pitch action  $\beta_R^r(t)$ :

$$\beta_R^r(t) = \begin{bmatrix} 0 \\ \cos \beta_R^r(t) \\ -\sin \beta_R^r(t) \end{bmatrix}. \quad (5.32)$$

The lift and drag force definitions are based on a uniform inflow velocity over the chord length of the aerofoil. For a cambered aerofoil, the inflow velocity normal to the camber line varies over the length of the chord. Concerning the definition of the lift force, this is accounted for by means of the  $C_{L;j}^c(r_{B;j})$  coefficient. The pitching of a blade results in a varying relative velocity over the length of the chord. It can be shown that the effective angle of attack for the quasi-static lift force on a thin aerofoil should be determined at the three-quarter chord point.

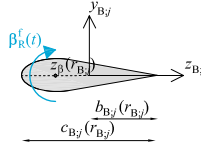


Figure 5.3: Schematic representation of an aerofoil, indicating the location  $z_\beta(r_{B;j})$  of the pitch axis.

When considering the viscous drag force on an aerofoil, a variation of the flow velocity over the length of the chord affects the development of the boundary layer. Such a flow variation may result from a pitch action, but since pitching only induces velocities normal to the chord of the aerofoil, it is not believed that this affects the effective drag coefficient much, even more, because for small angles of attack, the drag coefficient of an aerofoil is virtually independent of this angle. It does remain a question which relative inflow velocity should be adopted for the estimation of the viscous drag on a pitching aerofoil. At this stage, it is assumed that the velocity  $\mathbf{W}_{B;rel;j}^r(r_{B;j}, t)$ , which is determined at the three-quarter chord point, is also applicable for the estimation of the viscous drag force. The definition of the quasi-static drag force on a pitching aerofoil requires an analysis of the corresponding boundary layer development.

The inertia force requires the relative acceleration. This relative acceleration is defined as the acceleration of the wind particles at the rotor plane, as experienced by a point on a rotating blade, minus the structural acceleration, both defined in the global rotating frames of reference and plus the acceleration induced by pitch actions:

$$\dot{\mathbf{W}}_{B;rel;j}^r(r_{B;j}, t) = \dot{\mathbf{W}}_{B;j}^r(r_{B;j}, t) - \ddot{\mathbf{x}}_{B;j}^r(r_{B;j}, t) + \mathbf{W}_{B;eff}^r(r_{B;j}, t) \times \dot{\beta}_R^r(t) - z_\beta(r_{B;j}) \left( \mathbf{e}_{B;z}^r \times \ddot{\beta}_R^r(t) \right). \quad (5.33)$$

With the implementation of the angle of attack and relative-flow formulations, provided by Eqs. (5.25), (5.31) and (5.33), the aerodynamic forcing explicitly depends on the pitch action  $\Delta\beta_R^r(t)$  that relates the pitch angle of the blades and the rotational speed of the rotor in the above-rated regime.

### 5.2.2. APPROXIMATION PROCEDURE

In Chapter 4, the aerodynamic force expressions with state-independent apparent aero-elastic properties for the state vector  $\mathbf{S}_R(t)$  – which consists of the rotor degrees of freedom  $\mathbf{v}_R(t)$ , and its first and second time derivatives – were defined. Apart from the rotor degrees of freedom, the aerodynamic excitation is affected by the control parameters  $\Delta\beta_R^f(t)$  and  $\Delta T_{G;Y}^f(t)$ . Concerning the generator torque, the approximation given by Eq. (5.19) can be adopted straightforwardly in the below-rated regime, for which the pitch angle variation is absent. In the above-rated regime, the aerodynamic excitation depends non-linearly on the pitch angle variation, which itself is governed by the pitch controller, defined by Eq. (5.22) or (5.23).

The state vector  $\mathbf{S}_{R;\beta}(t)$  contains the collective pitch angle of the rotor and its time derivatives:

$$\mathbf{S}_{R;\beta}(t) = [\beta_R^f(t) \quad \dot{\beta}_R^f(t) \quad \ddot{\beta}_R^f(t)]. \quad (5.34)$$

The state-independent force expressions corresponding with the state vector  $\mathbf{S}_R(t)$  were obtained by means of a Taylor approximation of the aerodynamic blade force vector  $\mathbf{Q}_{B;A;j}(r_{B;j}, t)$  around the mean state  $\bar{S}_R$ . Following the same procedure, the force components that relate to the components of the state vector  $\mathbf{S}_{R;\beta}(t)$  can be obtained, adopting the mean state  $\bar{S}_{R;\beta}$ :

$$\bar{S}_{R;\beta} = \{\mathbf{S}_{R;\beta}(t) = \bar{S}_{R;\beta}\}. \quad (5.35)$$

Similar to Eq. (5.24), which concerned the pitch actions affecting the aerodynamic torque  $T_{R;A}^f(t)$  only, the aerodynamic force vector  $\mathbf{Q}_{R;A}(t)$  can be expanded with respect to the pitch actions around the states  $\bar{S}_R$  and  $\bar{S}_{R;\beta}$ :

$$\begin{aligned} \mathbf{Q}_{R;A}(t) \approx & \mathbf{Q}_{R;A}(t) \Big|_{\bar{S}_R, \bar{S}_{R;\beta}} + \left[ \frac{\partial \mathbf{Q}_{R;A}(t)}{\partial \beta_R^f(t)} \Big|_{\bar{S}_R, \bar{S}_{R;\beta}} \right] \Delta\beta_R^f(t) \\ & + \left[ \frac{\partial \mathbf{Q}_{R;A}(t)}{\partial \dot{\beta}_R^f(t)} \Big|_{\bar{S}_R, \bar{S}_{R;\beta}} \right] \Delta\dot{\beta}_R^f(t) + \left[ \frac{\partial \mathbf{Q}_{R;A}(t)}{\partial \ddot{\beta}_R^f(t)} \Big|_{\bar{S}_R, \bar{S}_{R;\beta}} \right] \Delta\ddot{\beta}_R^f(t). \end{aligned} \quad (5.36)$$

In the following sections, the forcing expressions that correspond to the control parameters of the state vector  $\mathbf{S}_{R;\beta}(t)$  are presented for the lift, drag and inertia forces, separately. For the derivations, use was made of software for symbolic manipulations. In doing so, blade pitching actions were described in terms of two subsequent rotations:

$$\mathbf{R}_{R;\beta}(t) = \mathbf{R}_{R;\Delta\beta}(t)\mathbf{R}_{R;\hat{\beta}}, \quad (5.37)$$

where for small pitch action, the matrix  $\mathbf{R}_{R;\Delta\beta}(t)$  can be approximated as (see Section 4.3)

$$\mathbf{R}_{R;\Delta\beta}(t) \approx \mathbf{I}_{3 \times 3} + \Delta\tilde{\boldsymbol{\beta}}_R(t). \quad (5.38)$$

$\Delta\tilde{\boldsymbol{\beta}}_R(t)$  is the skew-symmetric matrix of the vector  $\Delta\boldsymbol{\beta}_R^f(t)$ :

$$\Delta\boldsymbol{\beta}_R^f(t) = \begin{bmatrix} 0 \\ \cos \Delta\beta_R^f(t) \\ -\sin \Delta\beta_R^f(t) \end{bmatrix}. \quad (5.39)$$

### 5.2.3. PITCH ANGLE-RELATED STATE-INDEPENDENT EXPRESSIONS OF THE AERODYNAMIC FORCE

With the inclusion of a control system that regulates the pitch angle of the blades, the aerodynamic force expressions have become dependent on the time-varying pitch angle, and the velocity and acceleration of the pitch actions. Following the approximation procedure of Section 5.2.2, state-independent force expressions that relate the aerodynamic forcing and the pitch actions can be derived.

Considering the different aerodynamic forces, the  $\alpha$ -dependent lift force depends on the actual pitch angle, as it affects the angle of attack along the blade. All aerodynamic forces depend on the pitch velocity, through the relative inflow velocity at each blade section, Eq. (5.31), and only the inertia force depends on the acceleration of the pitch angle variations through the relative inflow acceleration, Eq. (5.33). Similar to Section 4.3, the coefficient vectors of the pitch-related state-independent terms of the aerodynamic force are now presented, starting with the pitch angle-dependency of the  $\alpha$ -dependent lift force:

$$\left. \frac{\partial \mathbf{Q}_{B;L;j}^{\alpha}(r_{B;j}, t)}{\partial \beta_R^f(t)} \right|_{\bar{s}_R, \bar{s}_{R;\beta}} = \begin{bmatrix} \left. \frac{\partial \mathbf{F}_{B;j}^{\alpha}(r_{B;j}, t)}{\partial \beta_R^f(t)} \right|_{\bar{s}_R, \bar{s}_{R;\beta}} \\ \left. \frac{\partial \mathbf{T}_{B;j}^{\alpha}(r_{B;j}, t)}{\partial \beta_R^f(t)} \right|_{\bar{s}_R, \bar{s}_{R;\beta}} \end{bmatrix}, \quad (5.40)$$

with

$$\left. \frac{\partial \mathbf{F}_{B;L;j}^{\alpha}(r_{B;j}, t)}{\partial \beta_R^f(t)} \right|_{\bar{s}_R, \bar{s}_{R;\beta}} = \frac{1}{2} \rho_{\text{air}} c_{B;j}(r_{B;j}) C_{L;j}^{\alpha}(r_{B;j}) \left[ \mathbf{D}_{B;L;j}^{\alpha}(r_{B;j}, t) \right], \quad (5.41)$$

and

$$\left. \frac{\partial \mathbf{T}_{B;L;j}^{\alpha}(r_{B;j}, t)}{\partial \beta_R^f(t)} \right|_{\bar{s}_R, \bar{s}_{R;\beta}} = \frac{1}{2} \rho_{\text{air}} c_{B;j}(r_{B;j}) C_{L;j}^{\alpha}(r_{B;j}) \left[ \tilde{\mathbf{x}}_{B;\bar{\theta};j}(r_{B;j}, t) \mathbf{D}_{B;L;j}^{\alpha}(r_{B;j}, t) \right], \quad (5.42)$$

where the vector  $\mathbf{D}_{B;L;j}^{\alpha}(r_{B;j}, t)$  is obtained as

$$\begin{aligned} \mathbf{D}_{B;L;j}^{\alpha}(r_{B;j}, t) &= \mathbf{R}_{R;\bar{\theta}} \mathbf{R}_{B;\Psi;j}(t) \tilde{\mathbf{e}}_{B;t}^f \Xi \left\{ \mathbf{R}_{B;\Psi;j}(t) \right\}^T \left\{ \mathbf{R}_{R;\bar{\theta}} \right\}^T \left( \mathbf{W}_R(\mathbf{X}_{B;j}, t) - \dot{\mathbf{x}}_{B;\bar{\theta};j}(\mathbf{X}_{B;j}, t) \right) \\ &\Xi \left\{ \mathbf{R}_{B;\Psi;j}(t) \right\}^T \left\{ \mathbf{R}_{R;\bar{\theta}} \right\}^T \left( \mathbf{W}_R(\mathbf{X}_{B;j}, t) - \dot{\mathbf{x}}_{B;\bar{\theta};j}(\mathbf{X}_{B;j}, t) \right)^T \tilde{\boldsymbol{\beta}}_{B;\bar{\beta};0}^f(r_{B;j}). \end{aligned} \quad (5.43)$$

Following the same procedure, the matrices for the pitch velocity for the different aerodynamic forces can be derived. Adopting the subscript 'A' to refer to represent the different aerodynamic forces:

$$\left. \frac{\partial \mathbf{Q}_{B;A;j}(r_{B;j}, t)}{\partial \beta_R^f(t)} \right|_{\bar{s}_R, \bar{s}_{R;\beta}} = \begin{bmatrix} \left. \frac{\partial \mathbf{F}_{B;A;j}(r_{B;j}, t)}{\partial \beta_R^f(t)} \right|_{\bar{s}_R, \bar{s}_{R;\beta}} \\ \left. \frac{\partial \mathbf{T}_{B;A;j}(r_{B;j}, t)}{\partial \beta_R^f(t)} \right|_{\bar{s}_R, \bar{s}_{R;\beta}} \end{bmatrix}, \quad (5.44)$$

the force expressions for the lift and drag forces are obtained as follows:

$$\left. \frac{\partial \mathbf{F}_{B;A;j}(r_{B;j}, t)}{\partial \beta_R^f(t)} \right|_{\bar{S}_R, \bar{S}_{R;\beta}} = \frac{1}{2} \rho_{\text{air}} C_{B;j}(r_{B;j}) C_{B;A;j}(r_{B;j}) \cdot \left[ (\mathbf{A}_{B;A;j}(r_{B;j}, t) + \mathbf{B}_{B;A;j}(r_{B;j}, t)) \left\{ \left( \frac{1}{2} b(r_{B;j}) - z_\beta(r_{B;j}) \right) \mathbf{e}_{B;z}^f \tilde{\boldsymbol{\beta}}_{B;\beta;0}(r_{B;j}) \right\} \right] \left. \frac{d(\boldsymbol{\beta}_R^f(t))}{d\beta_R^f(t)} \right|_{\bar{S}_{R;\beta}}, \quad (5.45)$$

and

$$\left. \frac{\partial \mathbf{T}_{B;A;j}(r_{B;j}, t)}{\partial \beta_R^f(t)} \right|_{\bar{S}_R, \bar{S}_{R;\beta}} = \frac{1}{2} \rho_{\text{air}} C_{B;j}(r_{B;j}) C_{B;A;j}(r_{B;j}) \left[ \tilde{\mathbf{x}}_{B;\bar{\theta};j}(r_{B;j}, t) (\mathbf{A}_{B;A;j}(r_{B;j}, t) + \mathbf{B}_{B;A;j}(r_{B;j}, t)) \left( \frac{1}{2} b(r_{B;j}) - z_\beta(r_{B;j}) \right) \mathbf{e}_{B;z}^f \tilde{\boldsymbol{\beta}}_{B;\beta;0}(r_{B;j}) \right] \left. \frac{d(\boldsymbol{\beta}_R^f(t))}{d\beta_R^f(t)} \right|_{\bar{S}_{R;\beta}}, \quad (5.46)$$

where  $C_{B;A;j}(r_{B;j})$  represents the aerodynamic coefficient of either the  $\alpha$ -dependent or the camber-dependent lift forces, or the drag force. The same applies for the  $\mathbf{A}_{B;A;j}(r_{B;j}, t)$  and  $\mathbf{B}_{B;A;j}(r_{B;j}, t)$  matrices, the expressions of which are provided in Section 4.3. The presented expressions contain a dependency on the derivative of the pitch vector  $\boldsymbol{\beta}_R^f(t)$ , given by Eq. (5.27) with respect to the collective pitch angle  $\beta_R^f(t)$ , for the state  $\bar{S}_{R;\beta}$ :

$$\left. \frac{d(\boldsymbol{\beta}_R^f(t))}{d\beta_R^f(t)} \right|_{\bar{S}_{R;\beta}} = \begin{bmatrix} 0 \\ -\sin \bar{\beta}_R^r \\ -\cos \bar{\beta}_R^r \end{bmatrix}. \quad (5.47)$$

From the apparent inertia force, a pitch speed-dependent force component can be obtained as well, containing the following expression:

$$\left. \frac{\partial \mathbf{Q}_{B;l;j}(r_{B;j}, t)}{\partial \beta_R^f(t)} \right|_{\bar{S}_R, \bar{S}_{R;\beta}} = \begin{bmatrix} \left. \frac{\partial \mathbf{F}_{B;l;j}(r_{B;j}, t)}{\partial \beta_R^f(t)} \right|_{\bar{S}_R, \bar{S}_{R;\beta}} \\ \left. \frac{\partial \mathbf{T}_{B;l;j}(r_{B;j}, t)}{\partial \beta_R^f(t)} \right|_{\bar{S}_R, \bar{S}_{R;\beta}} \end{bmatrix}, \quad (5.48)$$

with

$$\left. \frac{\partial \mathbf{F}_{B;l;j}(r_{B;j}, t)}{\partial \beta_R^f(t)} \right|_{\bar{S}_R, \bar{S}_{R;\beta}} = -\frac{1}{4} \rho_{\text{air}} \pi \{C_{B;j}(r_{B;j})\}^2 \cdot \left[ \mathbf{R}_{R;\bar{\theta}} \mathbf{R}_{B;\Psi;j}(t) \boldsymbol{\Xi} \{ \mathbf{R}_{B;\Psi;j}(t) \}^T \{ \mathbf{R}_{R;\bar{\theta}} \}^T \left( \tilde{\mathbf{W}}_R(\mathbf{X}_{B;j}, t) - \tilde{\mathbf{x}}_{B;\bar{\theta};j}(\mathbf{X}_{B;j}, t) \right) \tilde{\boldsymbol{\beta}}_{B;\beta;0}(r_{B;j}) \right] \left. \frac{d(\boldsymbol{\beta}_R^f(t))}{d\beta_R^f(t)} \right|_{\bar{S}_{R;\beta}}, \quad (5.49)$$

and

$$\begin{aligned} \left. \frac{\partial \mathbf{T}_{B;l;j}(r_{B;j}, t)}{\partial \beta_R^l(t)} \right|_{\bar{s}_R, \bar{s}_{R;\beta}} &= -\frac{1}{4} \rho_{\text{air}} \pi \{c_{B;j}(r_{B;j})\}^2 \cdot \\ &\quad \left[ \tilde{\mathbf{x}}_{B;\bar{\theta};j}(\mathbf{X}_{B;j}, t) \mathbf{R}_{R;\bar{\theta}} \mathbf{R}_{B;\Psi;j}(t) \Xi \{\mathbf{R}_{B;\Psi;j}(t)\}^T \left\{ \mathbf{R}_{R;\bar{\theta}} \right\}^T \right. \\ &\quad \left. \left( \tilde{\mathbf{W}}_R(\mathbf{X}_{B;j}, t) - \tilde{\mathbf{x}}_{B;\bar{\theta};j}(\mathbf{X}_{B;j}, t) \right) \tilde{\boldsymbol{\beta}}_{B;\bar{\beta};0}(r_{B;j}) \right] \left. \frac{d(\beta_R^l(t))}{d\beta_R^l(t)} \right|_{\bar{s}_R, \bar{s}_{R;\beta}}. \end{aligned} \quad (5.50)$$

The dependency of the apparent inertia force on the acceleration of the pitch action can be expressed as

$$\left. \frac{\partial \mathbf{Q}_{B;l;j}(r_{B;j}, t)}{\partial \beta_R^l(t)} \right|_{\bar{s}_R, \bar{s}_{R;\beta}} = \left[ \begin{array}{c} \left. \frac{\partial \mathbf{F}_{B;l;j}(r_{B;j}, t)}{\partial \beta_R^l(t)} \right|_{\bar{s}_R, \bar{s}_{R;\beta}} \\ \left. \frac{\partial \mathbf{T}_{B;l;j}(r_{B;j}, t)}{\partial \beta_R^l(t)} \right|_{\bar{s}_R, \bar{s}_{R;\beta}} \end{array} \right], \quad (5.51)$$

for which the following expressions are obtained:

$$\left. \frac{\partial \mathbf{F}_{B;l;j}(r_{B;j}, t)}{\partial \Delta \beta_R^l(t)} \right|_{\bar{s}_R, \bar{s}_{R;\beta}} = \frac{1}{4} \rho_{\text{air}} \pi \{c_{B;j}(r_{B;j})\}^2 z_{B;\beta;j}(r_{B;j}) \mathbf{R}_{R;\bar{\theta}} \mathbf{R}_{B;\Psi;j}(t) \tilde{\mathbf{e}}_{B;z}^r \tilde{\boldsymbol{\beta}}_{B;\bar{\beta};0}(r_{B;j}) \left. \frac{d(\beta_R^l(t))}{d\beta_R^l(t)} \right|_{\bar{s}_R, \bar{s}_{R;\beta}}, \quad (5.52)$$

and

$$\begin{aligned} \left. \frac{\partial \mathbf{T}_{B;l;j}(r_{B;j}, t)}{\partial \Delta \beta_R^l(t)} \right|_{\bar{s}_R, \bar{s}_{R;\beta}} &= \frac{1}{4} \rho_{\text{air}} \pi \{c_{B;j}(r_{B;j})\}^2 \cdot \\ &\quad z_{B;\beta;j}(r_{B;j}) \tilde{\mathbf{x}}_{B;\bar{\theta};j}(\mathbf{X}_{B;j}, t) \mathbf{R}_{R;\bar{\theta}} \mathbf{R}_{B;\Psi;j}(t) \tilde{\mathbf{e}}_{B;z}^r \tilde{\boldsymbol{\beta}}_{B;\bar{\beta};0}(r_{B;j}) \left. \frac{d(\beta_R^l(t))}{d\beta_R^l(t)} \right|_{\bar{s}_R, \bar{s}_{R;\beta}}. \end{aligned} \quad (5.53)$$

Following the approximation procedure given by Eq. (5.36), the coefficient vectors of the pitch-related state-independent terms of the aerodynamic force have been derived and presented in this section. With the application of the pitch controller defined in Section 5.1.1, and the implementation in the drive-train sub-system of Section 5.1.1, the apparent aero-elastic properties are now extended with the drive-train and pitch control dynamics.

#### 5.2.4. IMPLEMENTATION OF DRIVE-TRAIN AND PITCH-CONTROL DYNAMICS IN TERMS OF APPARENT AERO-ELASTIC PROPERTIES

In Chapter 4, the apparent aero-elastic properties for a constant-speed wind turbine rotor were presented. In the current chapter, the wind turbine model has been extended with a drive-train sub-system, as a consequence of which the aerodynamic torque is no longer transferred in full to the tower top (see Eqs. (5.13)). This implies that the apparent aero-elastic properties for the rotor cannot straightforwardly be applied to a decoupled

support structure model. Moreover, the system has been extended with a control subsystem, which, for above-rated conditions, relates the rotational degree of freedom of the generator  $\Delta\Psi_{G;Y}^f(t)$  to the collective pitch angle of the blades.

Starting with the latter, and assuming a rigid drive-train, for which the rotational speed of the generator can be expressed in terms of the rotor speed, i.e.,  $\dot{\Psi}_{G;Y}^f(t) = N_{DT}\dot{\Psi}_{R;Y}^f(t)$ , the pitch angle variation can be related to the rotor rotation through Eq. (5.22). Accordingly, the forcing term of the  $\alpha$ -dependent lift force that relates to the pitch angle deviation  $\Delta\beta_R^f(t)$ , which contains the coefficient vector provided by Eq. (5.40), can be rewritten as

$$\begin{aligned} & \left[ \frac{\partial \mathbf{Q}_{B;L;j}^\alpha(r_{B;j}, t)}{\partial \beta_R^f(t)} \Big|_{\bar{s}_R, \bar{s}_{R;\beta}} \right] \Delta\beta_R^f(t) = \\ N_{DT} & \left[ \frac{\partial \mathbf{Q}_{B;L;j}^\alpha(r_{B;j}, t)}{\partial \beta_R^f(t)} \Big|_{\bar{s}_R, \bar{s}_{R;\beta}} \right] \left( G_{\beta;D} \Delta\dot{\Psi}_{R;Y}^f(t) + G_{\beta;P} \Delta\Psi_{R;Y}^f(t) + G_{\beta;I} \Delta\Psi_{R;Y}^f(t) \right). \end{aligned} \quad (5.54)$$

Recognizing that this expression contains coefficients that relate to either the azimuth deviation, the rotor speed or the rotor acceleration, the corresponding coefficients can – apart from their sign – be perceived as apparent stiffness, damping or mass. In a similar way, the coefficients of the forcing terms that relate to the pitch velocity and acceleration, Eqs. (5.44), (5.48) and (5.51), can be interpreted as apparent aero-elastic properties as well. From these expressions, however, also forcing terms relating to the second and third-order time derivatives of the rotor speed – relating to the jerk and jounce of the rotation – are obtained. For rigid bodies, no forces are associated to these terms in the theory of classical mechanics.

Regarding the drive-train, the torque  $T_{DT;Y}^f(t)$  that acts on the tower top was derived in Section 5.1.1, with Eq. (5.13) presenting the transferred torque through the drive-train. Employing the relation between the low-speed shaft and high-speed shaft torques, Eq. (5.11), Eq. (5.13) can be re-written as

$$T_{DT;Y}^f(t) = \pm \frac{N_{DT}}{1-\mu_{DT}} T_{HSS;Y}^f(t) \mp J_{G;Y}^f \Delta\ddot{\Psi}_{G;Y}^f(t), \quad (5.55)$$

where  $T_{HSS;Y}^f(t)$  can be replaced by Eq. (5.10):

$$T_{DT;Y}^f(t) = \pm \frac{N_{DT}}{1-\mu_{DT}} \left( J_{G;Y}^f \Delta\ddot{\Psi}_{G;Y}^f(t) + T_{G;Y}^f(t) \right) \mp J_{G;Y}^f \Delta\dot{\Psi}_{G;Y}^f(t), \quad (5.56)$$

which can be re-formulated as

$$T_{DT;Y}^f(t) = \pm \frac{N_{DT}}{1-\mu_{DT}} T_{G;Y}^f(t) \pm \left( \frac{N_{DT}}{1-\mu_{DT}} \mp 1 \right) J_{G;Y}^f \Delta\dot{\Psi}_{G;Y}^f(t) \quad (5.57)$$

for rigid drive-trains,  $\Psi_{G;Y}^f(t) = N_{DT}\Psi_{R;Y}^f(t)$ . Using this relation, the transferred torque can be expressed as

$$T_{DT;Y}^f(t) = \pm \frac{N_{DT}}{1-\mu_{DT}} T_{G;Y}^f(t) \pm N_{DT} \left( \frac{N_{DT}}{1-\mu_{DT}} \mp 1 \right) J_{G;Y}^f \Delta\dot{\Psi}_{R;Y}^f(t). \quad (5.58)$$

The transferred torque is presented as a function of the rotor acceleration, the coefficient of which can be perceived as an apparent inertia. This transferred inertia, however, is

a fraction of the inertia of the rotor, and is even zero for direct-driven turbines, i.e., for  $N_{DT} = 1$ . For below-rated wind speeds, the generator torque and the rotor acceleration are controlled by the torque controller. For above-rated wind speeds, on the other hand, the generator torque is constant and the rotor acceleration is minimized by the pitch controller. As a consequence, the transferred torque is almost constant and, in other words, the contribution of the apparent mass corresponding to the rotor acceleration will be small.

## 5.3. TURBINE RESPONSE ANALYSIS

### 5.3.1. TURBINE DEFINITION

For the analyses presented in this section, use is made of the turbine properties of the NREL 5MW turbine and the UpWind monopile foundation, the global dynamic properties of which were already discussed in Sections 4.4 and 4.5. For the current analyses, the model is extended with the drive-train and control sub-systems, based on the equations of motion presented in Section 5.1. The adopted numerical values for the modelling of these sub-systems are presented in Table 5.1.

Table 5.1: Adopted numerical values for the drive-train and control sub-systems [172].

property	numerical value
rated generator torque	43.094 kNm
generator inertia	534.116 kgm <sup>2</sup>
gearbox ratio	97
proportional gain	0.008449 s
integral gain	0.004457

The drive-train is modelled as rigid, meaning that the relation between the rotor and generator speeds is defined by the gearbox ratio:

$$J_{DT;Y}^f(t) = J_{R;Y}^f(t) + N_{DT}^2 J_{G;Y}^f, \quad (5.59)$$

where

$$J_{R;Y}^f(t) = J_{H;Y}^f + \sum_{j=1}^3 J_{B;Y;j}^f(t). \quad (5.60)$$

contains the mass moments of inertia of the hub and the blades,  $J_{H;Y}^f$  and  $J_{B;Y;j}^f(t)$ , respectively, defined around the  $Y_R$  axis. Assuming an isotropic rotor, the mass moment of inertia of the rotor is time-independent, i.e.,  $J_{R;Y}^f(t) = J_{R;Y}^f$ .

The analyses in this section only concern the above-rated regime, implying that only the control-subsystem regulates the pitch angle of the blades only. To this end, the PI controller defined by Jonkman *et al.* [172] is adopted, the gains of which are presented in Table 5.1. Moreover, the generator torque is constant in time and equals its rated value. Friction losses between the mechanical components of the drive-train and the bearings are neglected, i.e.,  $\mu_{DT} = 0$ . Regarding the modelling of the near wake, the dynamic inflow model presented in Section 2.2 is adopted.



In the following, first the performance of the pitch sub-system is illustrated. To this end, the rotor speed and pitch angle variations resulting from both a step change in wind speed and a turbulent wind, accounting for the rotor azimuth degree of freedom only, are estimated and compared with a equivalent BLADED simulations. Subsequently, the tower top response of the complete turbine system is estimated for simultaneous wind and wave excitations. In this regard, both aligned and misaligned load cases are distinguished, the latter with a misalignment angle of 45 degrees. First, the tower top motions are determined for a load case consisting of a constant wind and a regular wave, whereas subsequently simultaneous irregular wave and turbulent wind excitations are considered.

As the purpose of the presented turbine response analyses is to provide insight in the accuracy of the aerodynamic interaction with state-independent apparent aero-elastic properties, in comparison with a state-dependent formulation of the interaction, as well as the relevance of the force contribution from aerodynamic flow separation, the modelling of the hydrodynamic forces acting on the turbine tower is kept rather simple. For the modelling of the waves, use is made of Airy's linear wave theory, whereas the hydrodynamic drag and inertia forces are obtained from Morison's equation, where the structural motion, velocity and acceleration, is assumed to be much smaller than the kinematics of the wave particles. The adopted drag and inertia coefficients are assumed constant in time and along the length of the foundation, and equal 1.0 and 2.0, respectively. Marine growth is not accounted for.

In accordance with Chapter 4, the BLADED simulations include the first two attachment modes of the turbine. These modes are similar to the first two normal modes of the system. The other simulations include the first six normal modes of vibrations, and, as a consequence, account for the torsional motion of the system too. The first, third, fifth and sixth normal modes contain a coupling between the side-to-side and the torsional motions, which is not accounted for by BLADED either.

### 5.3.2. PERFORMANCE OF THE PITCH CONTROL SUB-SYSTEM

As a first analysis, the accuracy of the approximated pitch controller is illustrated for both the step change in the upstream wind velocity and the turbulent wind signal that were applied in Chapter 4 as well. To this end, the rigid drive-train including the pitch controller is modelled separately, i.e., containing the rotor azimuth deviation  $\Delta\Psi_{R,Y}^f(t)$  as a degree of freedom only. The calculated response is compared with a BLADED simulation of a similar model, which does account for separation of the flow.

The step change in the upstream wind velocity comprises a constant wind speed of 15 m/s, which abruptly changes to 16 m/s after 30 s. Figure 5.4 shows the evolution of the rotational speed and the collective pitch angle of both simulations. The rotational speed in Figure 5.4(a) shows a steep increase in velocity after 30 s, beyond which the rotational speed converges quickly to the original value corresponding to the above-rated regime. The overall picture from both simulations is very similar. Only right after 30 s, the BLADED simulation attains a slightly higher peak rotational speed.

Concerning the blade pitching, Figure 5.4(b), a rapid change in the pitch angle takes place after 30 s. Both simulations show a different value to which the blade pitches, both before and after the step change in wind speed. The step size of the pitch angle variations,

however, is similar. The differences between the simulations can be attributed to the flow separation along parts of the blades, which only the BLADED simulation accounts for. As a consequence, a small difference in the time-varying aerodynamic torque is calculated, which results in a different setting value and variation of the pitch angle. This also explains the initial variation in rotational speed and pitch angle of the BLADED simulation.

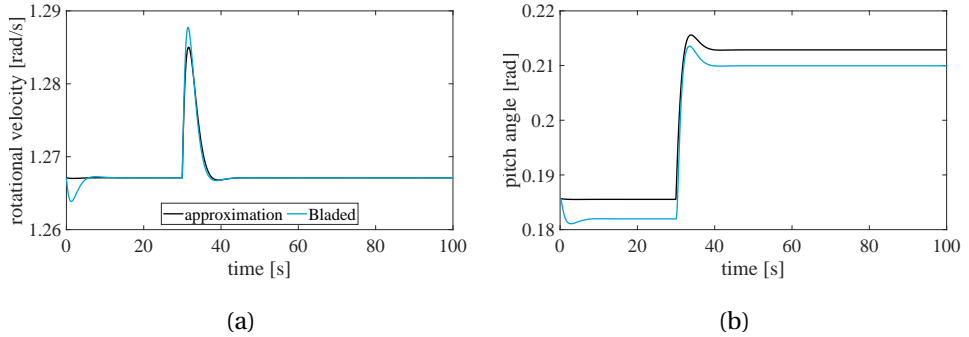


Figure 5.4: Pitch controller response to a step change in the upstream wind speed, with (a) the rotational velocity, and (b) the collective blade pitch angle.

Figure 5.5 presents the response of the controller sub-system to a turbulent wind signal, distinguishing again the rotational velocity and the pitch angle variation, Figures 5.5(a) and (b), respectively. For the presented time window, the differences between both simulations are small. To give more insights in the actual differences, the main statistical values of both simulations are presented in Tables 5.2 and 5.3. These values are obtained from a simulation of 300 s. For both control parameters, the minimum, maximum and mean values are almost equal. The standard deviations are very similar as well, with the BLADED simulation resulting in slightly higher values. Hence, for these simulations, the impact of the separation of the flow, which is accounted for by BLADED is of minor importance.

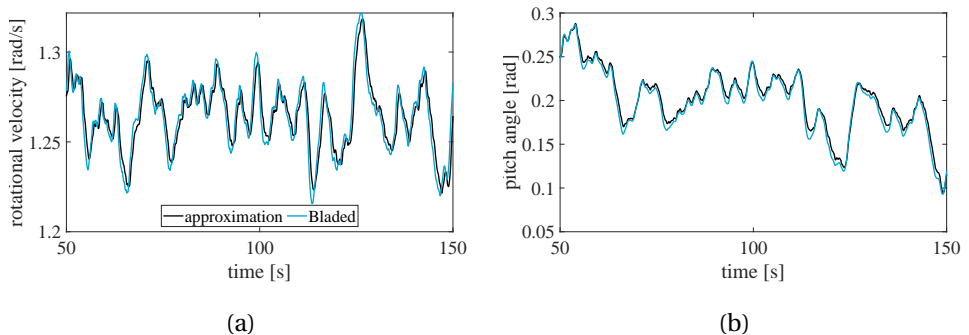


Figure 5.5: Pitch controller response to a turbulent wind speed, with (a) the rotational velocity, and (b) the collective blade pitch angle.

Table 5.2: Comparative statistical values of the rotor velocity variation resulting from a turbulent wind.

simulation	minimum [rad/s]	maximum [rad/s]	mean [rad/s]	standard deviation [rad/s]
BLADED	1.22	1.34	1.27	0.0212
approximation	1.22	1.34	1.27	0.0191

Table 5.3: Comparative statistical values of the pitch angle variation resulting from a turbulent wind.

simulation	minimum [rad]	maximum [rad]	mean [rad]	standard deviation [rad]
BLADED	0.0927	0.305	0.215	0.0378
approximation	0.0947	0.299	0.218	0.0361

### 5.3.3. ANALYSIS OF SIMULTANEOUS WIND AND WAVE EXCITATIONS

The response of an operating wind turbine to a wave excitation is affected by the aerodynamic interaction. This section addresses to what extent this relation can be captured by the aerodynamic force with state-independent apparent aero-elastic properties. To this end, first the tower top response to a regular wave and a constant wind is analyzed, as in this manner the effect of the time-varying waves is isolated, as the structural motion is wave-induced only. The analysis is restricted to the above-rated regime, for which the pitch controller is active, and a constant wind speed of 15 m/s is adopted. The regular wave elevation is defined in correspondence with the UpWind study, with a wave height of 2.8 m and a wave period of 6.79 s, as illustrated in Figure 5.6(a).

The second analysis considers an irregular wave and a turbulent wind. The irregular wave is defined from a sea state defined by a JONSWAP spectrum with a significant wave height of 2.8 m and a peak period of 6.07 s. Figure 5.6(a) shows a 100 s window of the irregular-wave elevation with a total length of 300 s, Figure 5.6(b) presents the corresponding estimated power spectral density, obtained from the squared amplitude spectrum of the finite time signal, divided by the duration. The statistical properties of the irregular wave signal are presented in Table 5.4. Concerning the turbulent wind, the same signal of Section 4.5 is adopted. For both environmental scenarios, an aligned and misaligned load case is considered, the latter with a misalignment angle of 45 degrees. None of the load cases includes a yaw misalignment of the wind direction with respect to the rotor plane.

Table 5.4: Statistical values of the irregular sea surface elevation.

minimum [m]	maximum [m]	mean [m]	standard deviation [m]
-2.29	2.32	$-4.61 \cdot 10^{-4}$	0.822

### TURBINE RESPONSE TO A CONSTANT WIND SPEED AND A REGULAR WAVE

Figure 5.7 presents the estimated tower top response to an aligned constant wind and a regular wave, distinguishing the BLADED, hybrid, state-independent and state-dependent approaches. The fore-aft and side-to-side motions are depicted in Figure 5.7(a) and

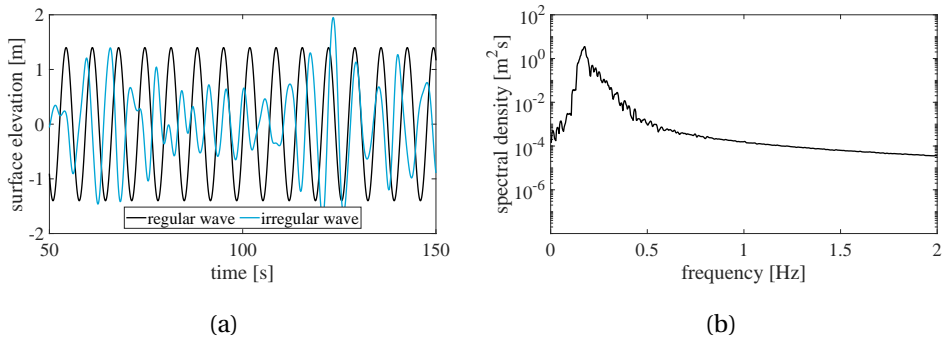


Figure 5.6: Sea surface elevation of the waves at the centre of the monopile foundation, with (a) the time-domain representation of both the regular and the irregular waves, and (b) the estimated power spectral density of the irregular wave.

(b) respectively. The tower top motion takes place almost exclusively in the fore-aft direction. The governing frequency of the motion corresponds with the wave frequency, approximately 0.15 Hz, which is lower than the first natural frequency of the system. Only small differences between the amplitudes of the different simulations can be observed.

In side-to-side direction, the motion possesses a non-zero mean, resulting from the aerodynamic forces that are transferred to the support structure. From the state-independent apparent aero-elastic properties, this coupling can be recognized in the added damping matrices, see Section 4.4. As a result of this coupling, both the first fore-aft and side-to-side modes of vibration are excited. The mean deformation in the side-to-side direction of the BLADED simulations differs from the other simulations because of the different modal basis. Concerning the side-to-side oscillations, the beating phenomenon can be observed, because the natural frequencies of both motions are very closely spaced. In the fore-aft response, this behaviour cannot be observed, as here the motion is governed by the hydrodynamic excitation. Figure 5.7(b) shows a different beating frequency for the BLADED simulation than for the other simulations. This difference can again be explained by the small difference between the modal bases.

Tables 5.5 and 5.6 present the statistical values of the fore-aft and side-to-side tower top motions, allowing for a comparison of the modelling approaches over the full simulation length. Despite the difference in the mean in the side-to-side direction for the BLADED simulation the obtained values are very similar. Concerning the standard deviations, the BLADED and state-dependent simulations resulted in values about 9 to 10% larger than for the other simulation approaches. Using the standard deviation as a measure for fatigue, the BLADED and the state-dependent simulations will result in the largest damage. Regarding the side-to-side vibrations, the standard deviations of the different simulations are very small, with the smallest value from the BLADED simulation.

The motions presented in Figure 5.7 are wave-induced. In Section 5.3.2, the performance of the control system to a wind excitation only was illustrated. Here, Figure 5.8 shows the behaviour of the control parameters for the different simulation approaches. Figure 5.8(a) clearly shows an oscillating rotational speed of the rotor for the BLADED

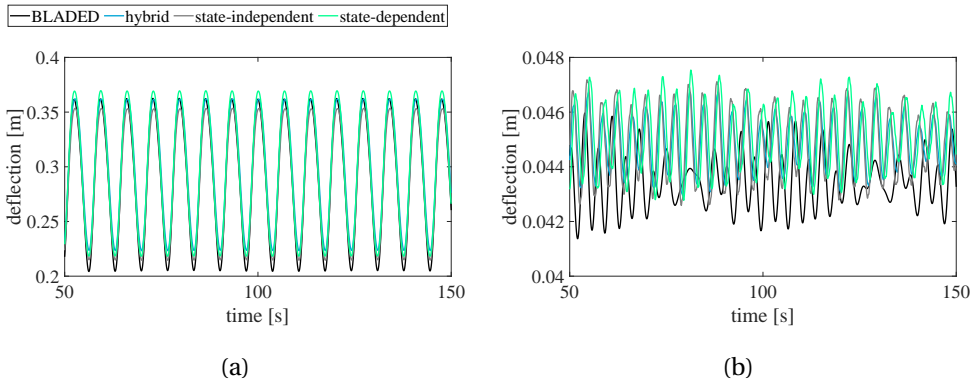


Figure 5.7: Tower top response to an aligned constant wind speed and a regular wave, with (a) the fore-aft motion, and (b) the side-to-side motion.

Table 5.5: Comparative values of the fore-aft tower top motion resulting from a constant wind and a regular wave with a misalignment angle of zero degrees.

simulation	minimum [m]	maximum [m]	mean [m]	standard deviation [m]
BLADED	0.202	0.380	0.289	0.0549
hybrid	0.218	0.378	0.297	0.0496
state-independent	0.206	0.373	0.288	0.0497
state-dependent	0.211	0.396	0.296	0.0543

Table 5.6: Comparative values of the side-to-side tower top motion resulting from a constant wind and a regular wave with a misalignment angle of zero degrees.

simulation	minimum [m]	maximum [m]	mean [m]	standard deviation [m]
BLADED	0.0411	0.0463	0.0435	$0.920 \cdot 10^{-3}$
hybrid	0.0428	0.0469	0.0443	$1.06 \cdot 10^{-3}$
state-independent	0.0423	0.0473	0.0444	$1.37 \cdot 10^{-3}$
state-dependent	0.0424	0.0479	0.0446	$1.38 \cdot 10^{-3}$

and the state-dependent simulations, whereas the oscillation for the hybrid and state-independent approaches is barely visible on this scale. A similar patterns can be observed for the pitch angle variation, see Figure 5.8(a). This lack of response is caused by the decoupling of the control behaviour with the implementation of the pitch angle-related state-independent expressions of the aerodynamic force as presented in Section 5.2.3. As a consequence, the control system does not respond to wave-induced motions.

Figure 5.8 presents the torque  $T_{DT,Y}^f(t)$ , which is transferred through the drive-train to the tower sub-system. With reference to Eq. (5.58), the variation of this torque relates to the rotor acceleration, which is negligibly small for the hybrid and state-independent simulation approaches. As a consequence, the transferred torque is constant in time. For the BLADED and state-dependent simulations, an oscillating variation of the transferred torque can be observed. Given the similarity between the side-to-side tower top motions, see Figure 5.7(b), it can be inferred that the impact of these oscillations on the structural motions is small. The side-to-side motion is mainly induced by the lateral force that results from the tilting motion of the rotor due to the wave excitation. The occurrence of this lateral force was addressed in Section 4.4.

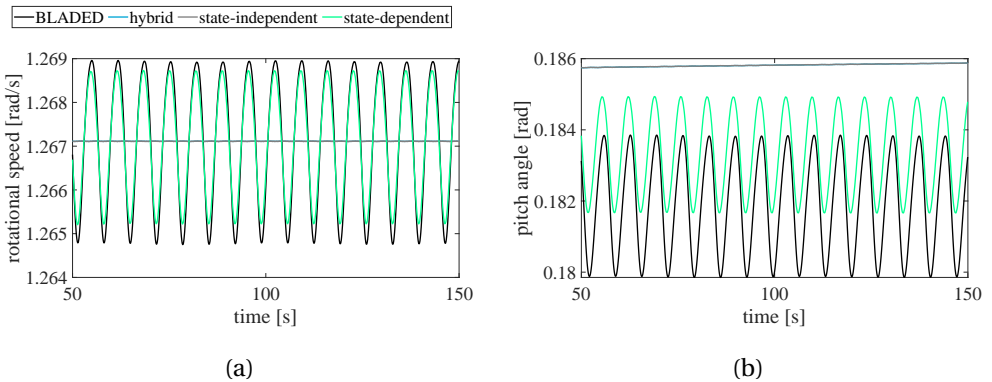


Figure 5.8: Control response to an aligned constant wind speed and a regular wave, with (a) the rotor speed, and (b) the collective pitch angle.

With the application of a wind-wave misalignment, the deflection in the fore-aft direction reduces somewhat, whereas in the side-to-side direction a direct wave-induced motion takes place. These effects are visible in Figure 5.10, which presents the tower top motion in the fore-aft and side-to-side directions, Figure 5.10(a) and (b), respectively, for the misalignment of 45 degrees. With the direct wave-induced excitation in the side-to-side-direction, the beating phenomenon is now only visible to a much smaller degree, compared with the aligned wind-wave simulation of Figure 5.7(b).

Again a small difference between the amplitudes of vibration between the different simulation approaches can be observed, with the largest deflections resulting from the BLADED simulation. In this respect, more insight is provided by Tables 5.7 and 5.8. These tables show that the standard deviations of the fore-aft and side-to-side motions are of

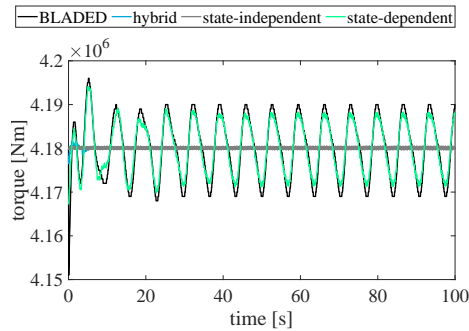


Figure 5.9: Torque transferred from the drive-train to the tower top for an aligned constant wind speed and a regular wave.

the same order of magnitude. When focussing on the standard deviations of the fore-aft motion of the different simulations, again the largest values are obtained with the BLADED and state-dependent simulations, which are 8 to 9% larger than the standard deviations of the hybrid and state-independent simulations. In side-to-side direction, the difference between the motions are very small and the smallest standard deviation is obtained with the BLADED simulation.

From the performed aligned and misaligned simulations combining a constant wind and a regular wave, it can be concluded that the overall response in both the fore-aft and side-to-side directions is similar for the different simulation approaches. The small deviations result from the different modal bases, the activation of the control system – the contribution of which is marginal for the hybrid and the state-independent simulations – and the higher-order contributions to the aerodynamic force. With respect to the latter, the effect of flow separation for large angles of attack was tested with BLADED and can be shown to be of minor importance.

#### TURBULENT WIND AND IRREGULAR WAVES

The next analysis concerns the response analysis to a turbulent wind and irregular wave excitation. Similar to the case with a constant wind and regular wave, the load case is addressed for both aligned and misaligned directionalities, the latter with a misalignment angle of 45 degrees. Figure 5.11 presents the fore-aft tower top response, both in the time and frequency domain, Figures 5.11 (a) and (b), respectively. Within the presented 100 s window, the differences in mean and amplitude of the motions estimated with the different simulation approaches are very small. This is confirmed by the power spectral density of the simulated signals, which is obtained from a simulation length of 300 s. To smooth out the power spectral densities, a moving root mean square filter has been applied. All signals show a distinguished peak at the first fore-aft natural frequency of the system. With the exception of the BLADED simulation, as the BLADED model contained only two modes of vibration, a small second peak can be observed at the natural frequency corresponding to the second fore-aft mode.

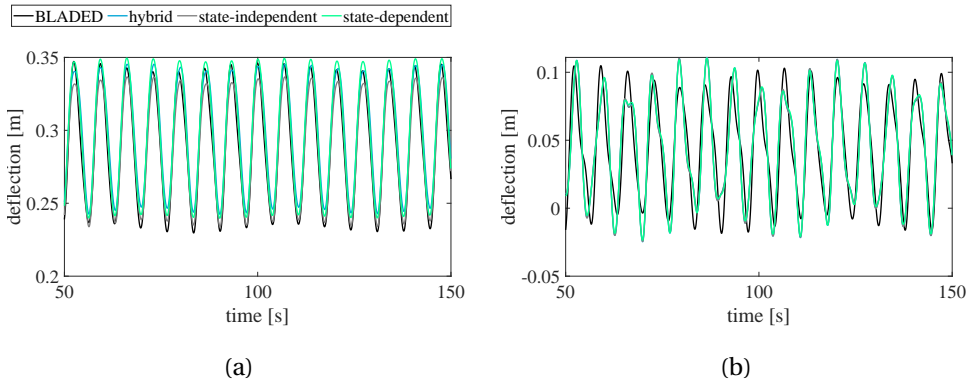


Figure 5.10: Tower top response to a misaligned constant wind speed and a regular wave, with (a) the fore-aft motion, and (b) the side-to-side motion.

5

Table 5.7: Comparative values of the fore-aft tower top motion resulting from a constant wind and a regular wave with a misalignment angle of 45 degrees.

simulation	minimum [m]	maximum [m]	mean [m]	standard deviation [m]
BLADED	0.227	0.357	0.289	0.0383
hybrid	0.242	0.352	0.297	0.0352
state-independent	0.231	0.348	0.288	0.0353
state-dependent	0.235	0.366	0.296	0.0386

Table 5.8: Comparative values of the side-to-side tower top motion resulting from a constant wind and a regular wave with a misalignment angle of 45 degrees.

simulation	minimum [m]	maximum [m]	mean [m]	standard deviation [m]
BLADED	-0.0211	0.109	0.0435	0.0362
hybrid	-0.0259	0.117	0.0443	0.0379
state-independent	-0.0259	0.117	0.0444	0.0379
state-dependent	-0.0252	0.117	0.0446	0.0379



The small differences between the simulations are confirmed by Table 5.9, which presents the minimum, maximum and mean deflections, as well as the standard deviations of the different simulations. Even though the differences, in absolute terms, are small, the hybrid and the state-independent simulations underestimate the fore-aft motion with respect to the BLADED and state-dependent simulations. The difference in standard deviation is 19 to 23%.

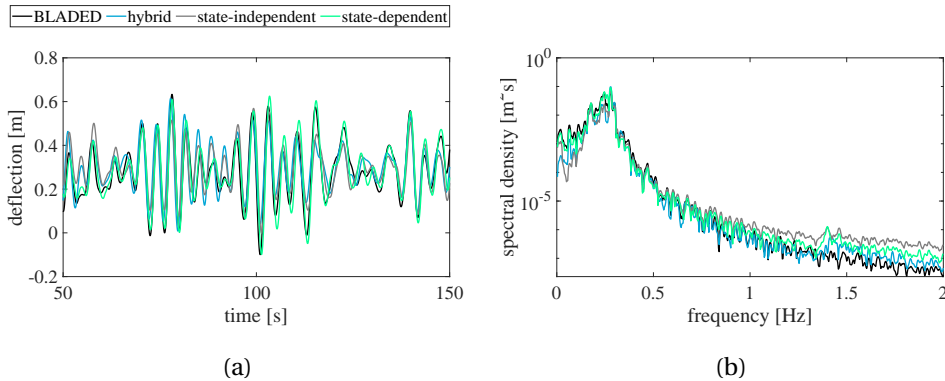


Figure 5.11: Fore-aft response of the tower top to an a turbulent wind and an irregular wave with a misalignment angle of zero degrees, with (a) the time-domain representations, and (b) the estimated power spectral densities.

simulation	minimum [m]	maximum [m]	mean [m]	standard deviation [m]
BLADED	-0.191	0.724	0.270	0.147
hybrid	$-0.505 \cdot 10^{-3}$	0.630	0.294	0.120
state-independent	-0.0346	0.613	0.304	0.115
state-dependent	-0.146	0.664	0.274	0.150

Table 5.9: Comparative values of the fore-aft tower top motion resulting from a turbulent wind and an irregular wave with a misalignment angle of zero degrees.

As was observed before for the simulations with a constant wind and a regular wave – see Figure 5.7(b), the aligned wind-wave excitation introduces vibrations with a non-zero mean in the side-to-side direction, see Figure 5.12. Within the presented time window, Figure 5.12(a), it can be seen that the BLADED and the state-dependent simulations result in the largest amplitudes of vibration. The dominant frequency of the different motions is very similar, as is confirmed by Figure 5.12(b), which presents the estimated spectral densities of the side-to-side motions. All simulations are governed by the first side-to-side mode of vibration, whereas a small contribution of the second side-to-side mode is present too.

The comparison of the statistical properties of the different estimated side-to-side motions, see Table 5.10, shows the largest amplitudes of vibration result from the BLADED

simulation. This is best illustrated by the standard deviations, of which BLADED result is 36% larger than estimated with the state-dependent simulation approach. In absolute terms, however, the standard deviations of the side-to-side-motion can be perceived as small (an order of magnitude smaller than the standard deviations of the fore-aft motion).

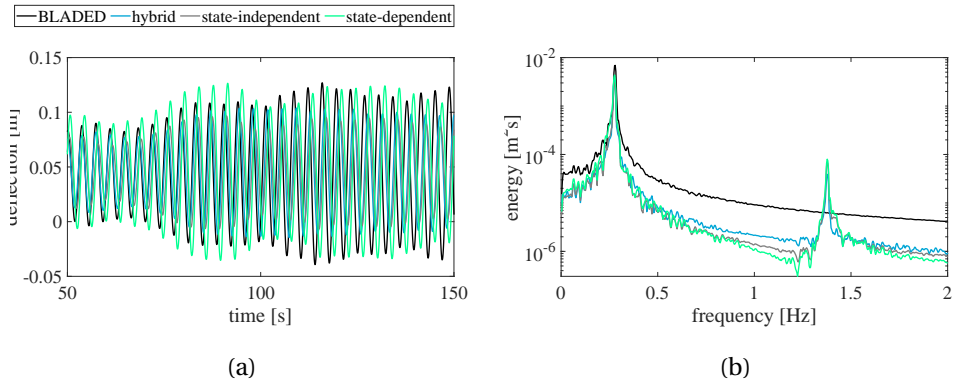


Figure 5.12: Side-to-side response of the tower top to a turbulent wind and an irregular wave with a misalignment angle of zero degrees, with (a) the time-domain representations, and (b) the estimated power spectral densities.

Table 5.10: Comparative values of the side-to-side tower top motion resulting from a turbulent wind and an irregular wave with a misalignment angle of zero degrees.

simulation	minimum [m]	maximum [m]	mean [m]	standard deviation [m]
BLADED	-0.0828	0.170	0.0436	0.0553
hybrid	-0.0145	0.104	0.0449	0.0277
state-independent	-0.0681	0.097	0.0448	0.0248
state-dependent	-0.0354	0.126	0.0451	0.0355

Regarding the response of the control system, Figure 5.13 presents the rotor speed and the pitch angle variation, Figure 5.13(a) and (b), respectively, of the different simulation approaches. Within the presented time window, the response patterns are very similar. The BLADED simulation, however, is shown to give the largest variation in the rotor speed, seemingly indicating a somewhat poorer performance of the pitch-control system. From a comparison with Figure 5.5(a), however, it can be inferred that the rotor speed of the BLADED simulation approach and, to a somewhat smaller extent, the state-dependent approach is affected by the wave excitation, an effect which is not included in the hybrid and state-independent simulation approaches. As a consequence, the latter two approaches underestimate the variation in rotor speed and pitch angle, and, at the same time estimate smaller standard deviations of the fore-aft and side-to-side motions.

The consequence of the difference in the estimated rotor speed can also be assessed from the transferred torque through the drive-train to the tower top, see Figure 5.14.

The variations in torque result from the acceleration of the rotor. Overall, the estimated torque of the four simulation approaches is very similar, since the variation in rotor speed is governed by the aerodynamic force. The BLADED simulation, however, contains the largest peaks, implying a larger acceleration of the rotor sub-system. The larger transferred torque of the BLADED simulation also serves as an explanation for the larger standard deviation of the side-to-side tower top motion, see Table 5.10.

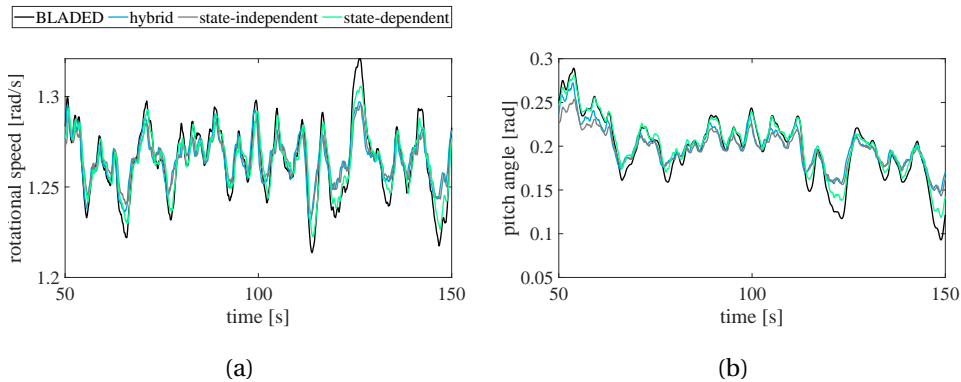


Figure 5.13: Control response to an aligned constant wind speed and a regular wave, with (a) the rotational rotor speed, and (b) the collective pitch angle.

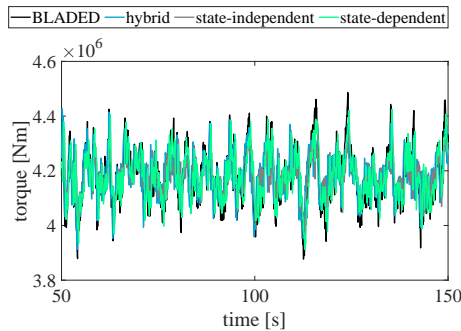


Figure 5.14: Torque transferred from the drive-train to the tower top for an aligned constant wind speed and a regular wave.

With the introduction of the misalignment between the wind and waves, the fore-aft response as depicted in Figure 5.15 is obtained. Within the presented window, the time-domain response in Figure 5.15(a) shows a deviation between the BLADED simulation and the other simulations. This deviation is confirmed by the power spectral densities of

Figure 5.15(a), for which the largest peak at the first fore-aft natural frequency is obtained for the BLADED simulation. Also the statistical values of the simulations, as presented in Table 5.11, show a larger variation in vibration, in terms of standard deviation, for the BLADED simulation.

In the side-to-side direction, the BLADED simulation shows the smallest amplitudes of vibration, see Figure 5.16(a). As illustrated in Figure 5.16(b), this vibration is governed by the first side-to-side mode of vibration, but the peak frequency of the wave spectrum, see Figure 5.6(b) can clearly be distinguished too. Regarding the standard deviations, the order of magnitude of the vibrations in the fore-aft and side-to-side directions is similar – compare Tables 5.11 and 5.12. Unlike the results of the previous analyses, the BLADED simulation gives the least conservative standard deviation of the oscillation amplitudes.

From the turbulent wind and irregular wave analysis, it can be concluded that the overall picture of the response obtained with the different simulation approaches is similar, especially when the results are considered in the frequency domain. The largest relative differences are obtained for the side-to-side motions, for both the aligned and the misaligned analyses, which can be explained by the much lower aerodynamic damping, activated in that direction.

The application of the hybrid or state-independent simulation approaches, which require lower computational costs and provide insights in the aerodynamic interaction through the state-independent apparent interaction matrices does not by default result in both accurate and conservative response predictions, when compared with the results from the BLADED simulations. This is partly explained by the difference in modal properties that were accounted for in the BLADED simulations. Other sources are found in the attached flow assumption and the linearization of the aerodynamic interaction with respect to the state parameters. Regarding the attached flow assumption, it should be mentioned that BLADED assumes instantaneous stall, whereas the actual stalling is a dynamic and history-dependent process, reducing the validity of the aero-elastic modelling of the BLADED simulation approach.

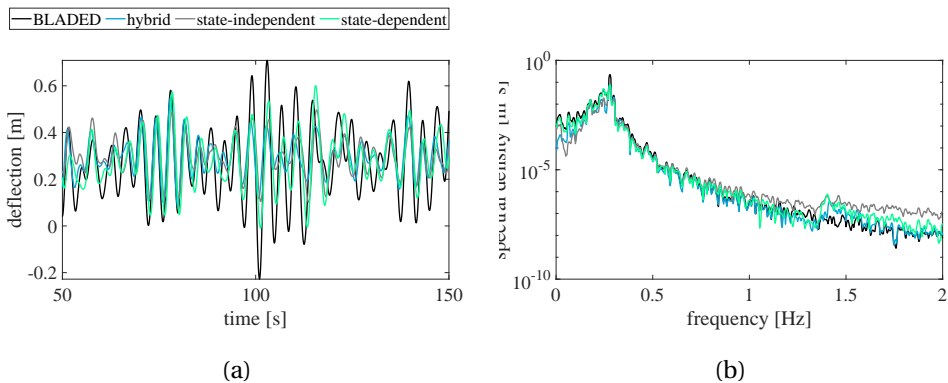


Figure 5.15: Fore-aft response of the tower top to a turbulent wind and an irregular wave with a misalignment angle of 45 degrees, with (a) the time-domain representations, and (b) the estimated power spectral densities.

Table 5.11: Comparative values of the fore-aft tower top motion resulting from a turbulent wind and an irregular wave with a misalignment angle of 45 degrees.

simulation	minimum [m]	maximum [m]	mean [m]	standard deviation [m]
BLADED	-0.228	0.709	0.264	0.156
hybrid	-0.0177	0.633	0.294	0.110
state-independent	-0.0166	0.582	0.304	0.103
state-dependent	-0.103	0.649	0.275	0.130

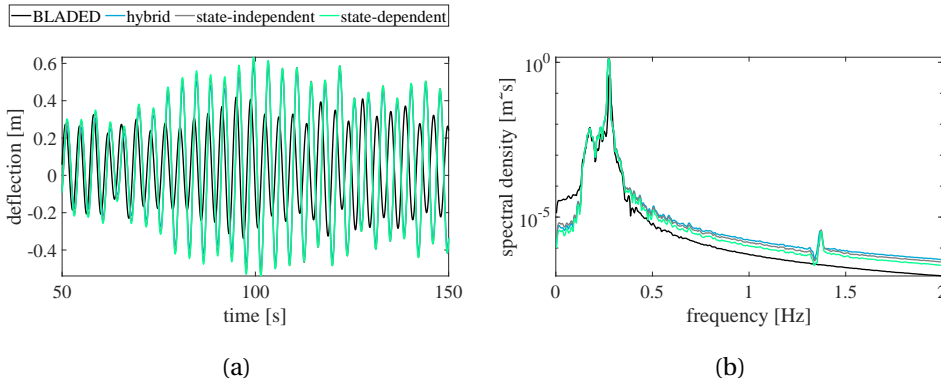


Figure 5.16: Side-to-side response of the tower top to a turbulent wind and an irregular wave with a misalignment angle of 45 degrees, with (a) the time-domain representations, and (b) the estimated power spectral densities.

Table 5.12: Comparative values of the side-to-side tower top motion resulting from a turbulent wind and an irregular wave with a misalignment angle of 45 degrees.

simulation	minimum [m]	maximum [m]	mean [m]	standard deviation [m]
BLADED	-0.419	0.338	0.0441	0.150
hybrid	-0.570	0.660	0.0446	0.277
state-independent	-0.574	0.664	0.0446	0.282
state-dependent	-0.536	0.636	0.0449	0.266

## 5.4. CONCLUSIONS

In this chapter, a decoupled support structure model of an offshore wind turbine was defined to predict the response to simultaneous wind and wave excitations. To this end, use was made of the model presented in Chapter 4, which was extended with drive-train and control sub-systems. These extensions were implemented to include the mitigating effect of the pitch controller on the loads in the above-rated operating regime.

After the implementation of the drive-train and control sub-systems, closed-form expressions for the state-dependent aerodynamic force were presented. Subsequently, additional the state-independent apparent aerodynamic properties were extracted, with the application of a first-order Taylor approximation. In deriving the closed-form expressions, the blades of the rotor were assumed to be rigid, whereas both flexible and rigid structural properties for the drive-train were considered. Furthermore, attached-flow conditions were adopted, a requirement which in general can be met over the largest part of the blades by choosing the right rotational velocity and pitch angle.

The response of an offshore wind turbine with the properties of the NREL 5MW turbine and the UpWind monopile-based support structure, were estimated with both the state-dependent and state-independent force expressions. A BLADED 4.6 model was used to validate the predicted responses. Moreover, a hybrid simulation approach was adopted, which combines the response-independent aerodynamic force from BLADED with the force contributions associated with the state-independent apparent aero-elastic properties.

As a first analysis, the performance of the pitch control sub-system was illustrated for both constant and turbulent wind conditions, assuming a rigid support structure. It was shown that the predicted response with the state-independent simulation approach shows a very similar behaviour as the BLADED response. Differences primarily result from the attached flow assumption, which is not used by BLADED.

Regarding the analysis of simultaneous wind and wave excitations, both a constant wind with a regular wave, and a turbulent wind with an irregular wave was considered. Moreover, the effect of a wind wave misalignment of 45 degrees is considered. Both the fore-aft and the side-to-side tower top responses are presented for the four simulation approaches. Overall, the response predictions obtained with those four simulation procedures show good agreement. Adopting the BLADED simulation as a reference, however, none of the other simulation approaches can be considered to be conservative. If the state-independent or the hybrid approaches are to be adopted for design purposes, a small underestimation of the tower top oscillations should be accounted for. Nevertheless, the application of these approaches potentially reduces the computational costs required for the preliminary design of offshore wind support structures substantially. In addition, the insights, provided by the closed-form expressions for the apparent aero-elastic properties of the aerodynamic interaction, potentially allow for quicker design optimizations in the preliminary design stage of offshore wind support structures, as the contributions of the apparent aero-elastic properties, in particular the aerodynamic damping, are explicitly obtained.

An important explanation of the differences between the tower top motions obtained with the four simulation approaches relates to the extent with which the control system is activated by wave excitations. The BLADED and state-independent simulation approaches contain a stronger coupling between the wave-induced motions and the controller response. As a consequence, both the rotor speed and the pitch angle react differently to the excitation than for the hybrid and state-independent simulation approaches. This difference was illustrated mostly for the constant wind combined with a regular wave load case, since here the control system is activated by wave-induced motions only. If the wind speed variations govern the controller behaviour, the differences in estimated

response becomes less obvious.

Other differences between the predicted responses can partially be explained in terms of flow separation and higher-order apparent aero-elastic properties. The largest variations were observed for the side-to-side motions, for which a much smaller aerodynamic damping is activated, and especially for the misaligned wave excitation. In this respect, the separation of the flow, which is accounted for by the BLADED approach, provides an explanation for the observed differences. This flow separation, however, is modelled instantaneously, whereas the actual process requires a dynamic formulation, reducing the validity of the aero-elastic modelling of the BLADED simulation approach.

Another contribution to the difference was attributed to the different modal properties. The BLADED model included only the first two attachment modes, which describe the deformation shape resulting from a point load at the tower top. The predicted corresponding natural frequencies differ slightly from the frequencies corresponding to the first two normal modes. The other simulation approaches used the first six normal modes, with which it was demonstrated that the second side-to-side mode does provide a contribution to the dynamic response of the wind turbine system.

The presented results only account for a pitch controller. The equations for a torque controller have been presented in this chapter, but were not used for the analyses. Special attention is required, however, for the transition between the torque and pitch controller, for close to rated wind speeds. A sharp transition between these controller systems is known to result in overshoots of both loads and motions, which is avoided by an earlier activation of the pitch controller, i.e., an activation at below-rated wind speeds. The model presented in this chapter, however, does not include a transition between the torque and pitch controllers, let alone an overlap between both controller regimes. To account for this transition, an extension of the model is required, for which a formulation linearized with respect to the state variables most likely will not be sufficient.





# 6

## CONCLUSIONS

FOR the preliminary design of offshore wind turbines, the turbine and the support structure<sup>1</sup> are generally considered separately, the former by a turbine manufacturer and the latter by an offshore contractor. Commercial interests provide a primary reason for this approach, as well as the specific engineering expertise of the different parties. The separated modelling approach, however, requires multiple design iterations, which significantly slow down the design process and does not leave time for design optimization and differentiation within a wind farm.

Speeding up the preliminary design phase requires the sharing of the relevant coupling characteristics between the different design teams. For instance, the sub-structure can be represented by a so-called ‘super element’, which describes both the dynamic stiffness and the interface force for the frequency range of interest (see Section 1.4). On the other hand, the decoupled design of the support structure should capture the wave-induced aerodynamic interaction of the rotor, which is perceived as an apparent damping.

With the focus on the latter, the current industry practice adopts an additional damping in terms of a modal damping ratio, provided by the turbine manufacturer, which concerns the fore-aft motion of the wind turbine only. This damping ratio is only valid for the first fore-aft mode of vibration and cannot be adopted for other modes. This implies that the damping of the side-to-side and the yawing motions is not accounted for. Moreover, the provided damping does not explicitly give insight in the effect of the operational state parameters – wind speed and rotational speed, or the contributions from the control system.

The research objective of this work was the definition of an apparent damping matrix for the aerodynamic force on a wind turbine rotor. Such a matrix should describe the three-dimensional damping, including the couplings between different motions and the resulting aerodynamic forces. The main question that was addressed concerned the extent to which the coupling between an operating turbine and its support structure can be captured by an added damping matrix.

---

<sup>1</sup>Strictly speaking, the interface is usually between the tower and the sub-structure (see Section 1.1).

The derivation of an apparent damping matrix for the rotor as a whole first required an extensive analysis of the aerodynamic force on the wind turbine blades, which is known to depend non-linearly on the structural response. To this end, Chapter 3 defined a model of a rotating blade with the properties of the NREL 5MW turbine, and the blade motions in a turbulent wind field were estimated with both an instantaneous and a history-dependent aerodynamic force model. From a comparison of the response estimations of both models, and their linearized representations (with respect to the structural motion), it was inferred that the blade response of an operating wind turbine in a turbulent wind field can be estimated sufficiently accurately with the linearized instantaneous force model. Furthermore, the results indicated that in the out-of-plane blade direction a substantial apparent damping is mobilized, allowing to describe the blade motion quasi-statically. The apparent damping for the motion within the plane of rotation is smaller and a dynamic contribution to the response can be distinguished in the blade motion.

As a next step, a model of a rigid turbine rotor on a flexible tower was presented in Chapter 4, describing motions and rotations in 3D. Using the instantaneous force model, closed-form expressions for the state-dependent aerodynamic force on the rotor were presented. With the application of a Taylor expansion, the state-independent apparent dynamic properties of the force were obtained, including an added damping matrix which explicitly depends on the operational state of the turbine and which describes the damping coupling between the side-to-side and the yawing motions.

The contribution of the apparent dynamic properties was illustrated for an isotropic rotor with an above-rated operational state, and the couplings were visualized. In this respect, the high apparent damping associated with yawing motion and the aero-elastic coupling between the side-to-side and the yawing motion of the turbine were of particular relevance. The performance of the force model with the state-independent apparent dynamic properties was demonstrated for the NREL 5 MW turbine with the UpWind monopile support structure. In this respect load cases with a step change in the wind speed and a turbulent wind were considered, the latter also with a yaw misalignment. The response estimations were compared with simulations of a similar model, which was created with the aero-elastic software BLADED 4.6. Moreover, a hybrid simulation approach was defined, which combines the aerodynamic force of the BLADED model on a rigid tower with the presented state-independent apparent dynamic properties.

The comparison of the response estimations with the different approaches showed a good match of the tower top motions. Only for very large yaw misalignments (larger than 15 degrees), the quality of the estimations with the state-independent properties dropped. In practical design, however, yaw misalignments larger than 8 degrees are not considered for most design load cases. The accurate response prediction with the state-independent apparent dynamic properties provides a good basis to include the response-dependency of the aerodynamic force for the preliminary design of the support structure. With the application of the hybrid simulation approach, the response of the control system to the wind speed variations can be captured as well.

Concerning the control system, the potential benefit of the linearization of the aerodynamic force with respect to the control parameters – the generator torque and the pitch angle – was recognized. To this end, Chapter 5 presented an extension of the turbine model, by defining drive-train and control sub-systems. Restricting the further analyses

to the above-rated regime, the linear force contributions of a collective pitch-system were presented, from which additional apparent dynamic properties could be identified. A comparison of this linearized control system with BLADED showed a good match.

The final analysis concerned the tower top response of the offshore wind turbine to simultaneous wind and wave excitations. In this respect, regular waves were combined with a constant wind speed and the load from a irregular wave with a turbulent wind excitation. For both scenarios, both aligned and misaligned wind and wave loads were considered, where a misalignment angle of 45 degrees was applied for the wave excitation. The misalignment imposes a side-to-side excitation of the turbine system, which, due to the limited amount of apparent aerodynamic damping, induces a significant side-to-side deflection of the tower top.

In comparing the results obtained with the four simulation approaches – using BLADED, force expressions with state-dependent or state-independent apparent dynamic properties, or the hybrid approach – a good correspondence between the tower top motions was obtained, especially in the fore-aft direction. It was demonstrated, however, that the hybrid and state-independent simulation approaches contain a weaker coupling between the wave-induced motions and the controller response. Nevertheless, the controller behaviour is governed by the variations in the wind speed and the effect of this weaker coupling was less pronounced in the analyses with a turbulent wind and a irregular sea. Observed differences in the side-to-side response were primarily explained by the assumption of attached flow, whereas the BLADED simulations allow for separation of the flow at the blades. As a consequence, the response estimations with BLADED deviate somewhat from the other response predictions. The assumption of attached flow can be defended, however, by the limited validity of the flow separation, which is modelled in BLADED as instantaneous. A more correct description would account for the dynamic and history-dependent characteristics of the boundary layer of the blades. To date, the computational costs of the inclusion of these effects affect the efficiency of the preliminary design stage to a large extent.

The overall conclusions of this work is that the apparent aerodynamic damping for a rotor of a wind turbine can be defined in closed form and state-independently, accounting for motions in three directions and cross-couplings between motions and resisting forces. The resulting damping matrix allows for a linearized response analysis of a support structure of a wind and wave-excited offshore wind turbine, including the response-mitigating actions of a pitch-control system. The estimated response shows a good correspondence with results obtained with BLADED and the presented approach offers opportunities for application in the preliminary design phase of offshore wind support structures.

The results presented in this work provide a good basis for the further development of the state-independent apparent dynamic properties, and in particular the added aerodynamic damping. This development first off all concerns some of the assumptions that were made, in order to assess the potential of the method. Second, some extensions could be explored, to broaden the perspective of practical application.

As a first extension, the inclusion of blade modes could be considered, as in the derivation of the apparent dynamic properties, rigid blades were assumed. In Chapter 3, however, it was shown that the out-of-plane motion is strongly damped and only quasi-

static response is to be expected. On the other hand, the in-plane motion is damped to a much smaller extent. This motion is known to introduce rotor speed oscillations, which results in variations of the thrust force and the moment transferred through the drive-train to the tower top.

Second, the analysis of the wind and wave-excited offshore wind turbine only accounted for a pitch-control system in the above-rated operational regime. In this respect, the work demonstrated the performance of the linearized pitch controller. In the below-rated regime, a torque-control system will be active, as presented in Chapter 5. It can be expected that the accuracy of the linearized torque controller will be similar to that of the linearized pitch controller, as long as the wind speed variations are not too large. Since the torque controller is active at below-rated wind speeds, the standard deviation of the wind speed fluctuations is generally smaller, which confirms the expected accuracy of the response prediction.

A more challenging extension concerns the possibility to assess transitions in the controller response, for instance for wind speeds close to cut-in, and, especially, around rated. For wind speeds in these transition regions, the application of the state-independent apparent dynamic properties cannot be expected to provide accurate response estimations. As an alternative, however, the controller response can be pre-determined with a separate drive-train model. The obtained pitch-angle and generator-torque variations can then be implemented as input for the simulations of the complete turbine system. As demonstrated in Chapter 5, this approach can be successful if the controller response is governed by the wind speed fluctuations. The accuracy of this method should be validated for a variety of load cases. Provided that the obtained accuracy is acceptable, the suggested approach potentially allows for response simulations in the frequency domain.

The presented method with state-independent apparent system properties of the aerodynamic force assumed attached flow conditions along the blades of the rotor. With the assumption of a homogeneous turbulent inflow, flow separation only occurs towards the hub of the rotor, and contributes only limitedly to the overall aerodynamic forcing. Moreover, if the response-independent aerodynamic force is obtained with an aero-elastic tool such as *BLADED*, a method which was presented in Chapter 4 as the hybrid approach, the force contribution resulting from flow separation can even be captured in part. The implementation of the pitch-control system in Chapter 5 demonstrated the successful mitigation of flow separations, even after linearizing the force contribution of the pitch controller around the mean pitch angle. Nevertheless, the performance of the pitch controller is known to deteriorate for non-homogeneous turbulent inflow conditions, or additional aerodynamic load phenomena such as tower shadow, leading to flow separation over longer stretches of the blades. The performance of the presented simulation approach requires a validation with respect to these more realistic aerodynamic load conditions.

The performance of the method with state-independent apparent dynamic properties was demonstrated for the NREL 5MW turbine. The presented approaches can be adopted to estimate the apparent dynamic properties for larger turbines (10+ MW). The validity of the assumptions, however, should be checked. Regarding the larger turbines, the tip speed ratio will be smaller, leading to larger inflow angles and potentially flow separation over longer stretches. Blade frequencies may also shift with respect to the current turbine,

leading to different dynamic interactions.

As a final recommendation, and along the same line, the method should be assessed for novel support structure concepts. Larger turbines and deeper waters may require different support structure concepts, such as lattice towers and floating structures, introducing different modes and frequencies of vibration. As an example, the frequency of the first torsion mode of a turbine on a full-lattice support structure could be much closer to the frequencies of the first bending modes of the wind turbine (compared to a monopile-based support structure), offering the potentially high aerodynamic damping of the yawing motion of the turbine as a mitigation of the side-to-side motion of the system. The possible benefits of the aerodynamic damping for novel support structure concepts can easily be explored with the application of the presented approach.



## REFERENCES

- [1] P. Van der Male, M. Vergassola, and K. N. van Dalen, *Decoupled modelling approaches for environmental interactions with monopile-based offshore wind support structures*, *Energies* **13** (2020).
- [2] WindEurope, *Offshore Wind in Europe - Key Trends and Statistics 2018*, Tech. Rep. (WindEurope, Brussels, Belgium, 2019).
- [3] C. Dickens, *Great Expectations* (Chapman & Hall, UK, 1861).
- [4] E. Lozano-Minguez, A. J. Kolios, and F. P. Brennan, *Multi-criteria assessment of offshore wind turbine support structures*, *Renewable Energy* **11**, 2831 (2011).
- [5] G. A. M. Van Kuik, J. Peinke, R. Nijssen, D. Lekou, J. Mann, J. N. Sørensen, C. Ferreira, J. W. van Wingerden, D. Schlipf, P. Gebraad, H. Polinder, A. Abrahamsen, G. J. W. van Bussel, J. D. Sørensen, P. Tavner, C. L. Bottasso, M. Muskulus, D. Matha, H. J. Lindeboom, S. Degraer, O. Kramer, S. Lehnhoff, M. Sonnenschein, P. E. Sørensen, R. W. Künneke, P. E. Morthorst, and K. Skytte, *Long-term research challenges in wind energy – a research agenda by the European Academy of Wind Energy*, *Wind Energy Science* **1**, 1 (2016).
- [6] E. Topham and D. McMillan, *Sustainable decommissioning of an offshore wind farm*, *Renewable energy* **102**, 470 (2017).
- [7] DNVGL-ST-0126, *Support Structures for Wind Turbines*, Tech. Rep. (DNVGL, Oslo, Norway, 2016).
- [8] M. Seidel, *Design of support structures for offshore wind turbines–interfaces between project owner, turbine manufacturer, authorities and designer*, *Stahlbau* **79**, 631 (2010).
- [9] M. Seidel, S. Voormeeren, and J. B. Van der Steen, *State-of-the-art design processes for offshore wind turbine support structures*, *Stahlbau* **85**, 583 (2016).
- [10] L. Arany, S. Bhattacharya, J. Macdonald, and S. J. Hogan, *Design of monopiles for offshore wind turbines in 10 steps*, *Soil Dynamics and Earthquake Engineering* **92**, 126 (2017).
- [11] P. Passon and K. Branner, *Load calculation methods for offshore wind turbine foundations*, *Ships and Offshore Structures* **9**, 433 (2014).
- [12] P. L. C. Van der Valk and D. J. Rixen, *Substituting internal forces for blocked forces or free interface displacements in substructured simulations*, in *Topics in Experimental Dynamic Substructuring*, Vol. 2 (Springer, New York, New York, 2014) pp. 77–96.

- [13] M. Muskulus and S. Schaffhirt, *Design optimization of wind turbine support structures - a review*, *Journal of Ocean and Wind Energy* **1**, 12 (2014).
- [14] F. Vorpahl, H. Schwarze, T. Fischer, M. Seidel, and J. Jonkman, *Offshore wind turbine environment, loads, simulation, and design*, *Wiley Interdisciplinary Reviews: Energy and Environment* **2**, 548 (2013).
- [15] DNVGL-ST-0437, *Loads and site conditions for wind turbines*, Tech. Rep. (DNVGL, Oslo, Norway, 2016).
- [16] P. Van der Male and E. Lourens, *Operational vibration-based response estimation for offshore wind lattice structures*, in *Structural Health Monitoring and Damage Detection, Proceedings of the 33rd IMAC, A Conference and Exposition on Structural Dynamics*, Vol. 7 (Springer International Publishing, Orlando, FL, 2015).
- [17] Y. Li, A. M. Castro, T. Sinokrot, W. Prescott, and P. M. Carrica, *Coupled multi-body dynamics and CFD for wind turbine simulation including explicit wind turbulence*, *Renewable Energy* **76**, 338 (2015).
- [18] S. Schløer, B. T. Paulsen, and H. Bredmose, *Application of CFD based wave loads in aeroelastic calculations*, in *ASME 2014 33rd International Conference on Ocean, Offshore and Arctic Engineering* (Citeseer, 2014).
- [19] B. Devolder, P. Rauwoens, and P. Troch, *Application of a buoyancy-modified  $k$ - $\omega$  SST turbulence model to simulate wave run-up around a monopile subjected to regular waves using openFOAM®*, *Coastal Engineering* **125**, 81 (2017).
- [20] W. G. Versteijlen, K. N. van Dalen, A. V. Metrikine, and L. Hamre, *Assessing the small-strain soil stiffness for offshore wind turbines based on in situ seismic measurements*, *Journal of Physics: Conference Series* **524** (2014).
- [21] E. Kementzetzidis, S. Corciulo, W. G. Versteijlen, and F. Pisanó, *Geotechnical aspects of offshore wind turbine dynamics from 3d non-linear soil-structure simulations*, *Soil Dynamics and Earthquake Engineering* **120**, 181 (2019).
- [22] M. Seidel, M. Von Mutius, P. Rix, and D. Steudel, *Integrated analysis of wind and wave loading for complex support structures of offshore wind turbines*, in *Conference Proceedings Offshore Wind 2005* (Copenhagen, Denmark, 2005).
- [23] D. Kaufer, N. Cosack, C. Böker, M. Seidel, and M. Kühn, *Integrated analysis of the dynamics of offshore wind turbines with arbitrary support structures*, in *European Wind Energy Conference* (Marseille, France, 2009).
- [24] A. Morató, S. Sriramula, N. Krishnan, and J. Nichols, *Ultimate loads and response analysis of a monopile supported offshore wind turbine using fully coupled simulation*, *Renewable energy* **101**, 126 (2017).
- [25] J. Jonkman and M. L. Buhl Jr., *FAST User's Guide*, Technical Report NREL/EL-500-38230 (National Renewable Energy Laboratory, Golden, Colorado, 2005).



- [26] P. Van der Male, *Preliminary design of offshore wind turbine support structures – the importance of proper mode shape estimation*, in *Proceedings of EWEA Conference 2013* (Vienna, Austria, 2013).
- [27] K. A. Abhinav and N. Saha, *Coupled hydrodynamic and geotechnical analysis of jacket offshore wind turbine*, *Soil Dynamics and Earthquake Engineering*, 66 (2015).
- [28] S. Bisoi and S. Haldar, *Design of monopile supported offshore wind turbine in clay considering dynamic soil-structure interaction*, *Soil Dynamics and Earthquake Engineering*, 103 (2015).
- [29] A. Jarquin Laguna, *Modeling and analysis of an offshore wind turbine with fluid power transmission for centralized electricity generation*, *Journal of Computational and Nonlinear Dynamics* **10**.
- [30] E. A. Bossanyi, *The design of closed loop controllers for wind turbines*, *Wind Energy*, 149 (2000).
- [31] M. H. Hansen, A. D. Hansen, T. J. Larsen, S. Øye, P. Sørensen, and P. Fuglsang, *Control design for a pitch-regulated, variable speed wind turbine*, Tech. Rep. (2005).
- [32] T. Theodorsen, *General theory of aerodynamic instability and the mechanism of flutter*, Report 496 (National Advisory Committee for Aeronautics, Langley Field, Virginia, 1935).
- [33] H. Wagner, *Über die Entstehung des dynamischen Auftriebes von Tragflügeln*, *ZAMM-Journal of Applied Mathematics and Mechanics/Zeitschrift für Angewandte Mathematik und Mechanik* **5**, 17 (1925).
- [34] J. F. Manwell, J. G. McGowan, and A. L. Rogers, *Wind energy explained: Theory, design and application* (Wiley, West Sussex, United Kingdom, 2002).
- [35] T. Burton, N. Jenkins, D. Sharpe, and E. Bossanyi, *Wind Energy Handbook*, 2nd ed. (Wiley, West Sussex, United Kingdom, 2011).
- [36] M. O. L. Hansen, *Aerodynamics of wind turbines* (Routledge, 2015).
- [37] D. A. Peters, D. D. Boyd, and C. J. He, *Finite-state induced-flow model for rotors in hover and forward flight*, *Journal of the American Helicopter Society* **34**, 5 (1989).
- [38] W. Yu, C. Simao Ferreira, G. A. M. van Kuik, and D. Baldacchino, *Verifying the blade element momentum method in unsteady, radially varied, axisymmetric loading using a vortex ring model*, *Wind Energy* **20**, 269 (2017).
- [39] W. Yu, C. Simao Ferreira, and G. A. M. van Kuik, *The dynamic wake of an actuator disc undergoing transient load: A numerical and experimental study*, *Renewable energy* **132**, 1402 (2019).
- [40] J. G. Leishman, *Challenges in modelling the unsteady aerodynamics of wind turbines*, *Wind Energy* **5**, 85 (2002).

- [41] E. Branlard, *Wind Turbine Aerodynamics and Vorticity-Based Methods, Fundamentals and Recent Applications*, Research Topics in Wind Energy, Vol. 7 (Springer International Publishing, 2017).
- [42] J. N. Sorensen and W. Z. Shen, *Numerical modeling of wind turbine wakes*, Journal of Fluids Engineering **124**, 393 (2002).
- [43] J. N. Sørensen, R. F. Mikkelsen, D. S. Henningson, S. Ivanell, S. Sarmast, and S. J. Andersen, *Simulation of wind turbine wakes using the actuator line technique*, Philosophical Transactions of the Royal Society A: Mathematical, Physical and Engineering Sciences **373** (2015).
- [44] W. Z. Shen, J. H. Zhang, and J. N. Sørensen, *The actuator surface model: a new navier–stokes based model for rotor computations*, Journal of solar energy engineering **131** (2009).
- [45] T. Kim, S. Oh, and K. Yee, *Improved actuator surface method for wind turbine application*, Renewable Energy **76**, 16 (2015).
- [46] J. M. O'Brien, T. M. Young, D. C. O'Mahoney, and P. C. Griffin, *Horizontal axis wind turbine research: A review of commercial CFD, FE codes and experimental practices*, Progress in Aerospace Sciences **92**, 1 (2017).
- [47] S. Bisoi and S. Haldar, *Dynamic analysis of offshore wind turbine in clay considering soil–monopile–tower interaction*, Soil Dynamics and Earthquake Engineering **63**, 19 (2014).
- [48] L. Ziegler, S. Voormeeren, S. Schafhirt, and M. Muskulus, *Design clustering of offshore wind turbines using probabilistic fatigue load estimation*, Renewable Energy **91**, 425 (2016).
- [49] M. J. Kühn, *Dynamics and Design Optimisation of Offshore Wind Energy Conversion Systems*, Ph.D. thesis, Delft University Wind Energy Research Institute (2001).
- [50] A. D. Garrad, *Forces and dynamics of horizontal axis wind turbines*, in *Wind Energy Conversion Systems*, edited by L. Freris (Prentice Hall, Englewood Cliffs, New Jersey, 1990) Chap. 5, pp. 119–144.
- [51] V. Valamanesh and A. T. Myers, *Aerodynamic damping and seismic response of horizontal axis wind turbine towers*, Journal of Structural Engineering **140** (2014).
- [52] D. Cerda Salzmänn and J. Van der Tempel, *Aerodynamic damping in the design of support structures for offshore wind turbines*, in *Proceedings of the Copenhagen Offshore Conference* (Copenhagen, Denmark, 2005).
- [53] X. Liu, C. Lu, G. Li, A. Godbole, and Y. Chen, *Effects of aerodynamic damping on the tower load of offshore horizontal axis wind turbines*, Applied energy **204**, 1101 (2017).

- [54] M. C. Ong, E. E. Bachynski, and O. D. Økland, *Dynamic responses of jacket-type offshore wind turbines using decoupled and coupled models*, *Journal of Offshore Mechanics and Arctic Engineering* **139** (2017).
- [55] S. Schafhirt and M. Muskulus, *Decoupled simulations of offshore wind turbines with reduced rotor loads and aerodynamic damping*, *Wind Energy Science* **3**, 25 (2018).
- [56] E. A. Bossanyi, *Wind turbine control for load reduction*, *Wind Energy*, 229 (2003).
- [57] E. A. Bossanyi, *Individual blade pitch control for load reduction*, *Wind Energy: An International Journal for Progress and Applications in Wind Power Conversion Technology* **6**, 119 (2003).
- [58] E. A. Bossanyi, *Further load reductions with individual pitch control*, *Wind Energy: An International Journal for Progress and Applications in Wind Power Conversion Technology* **8**, 481 (2005).
- [59] K. Selvam, S. Kanev, J. W. van Wingerden, T. van Engelen, and M. Verhaegen, *Feedback-feedforward individual pitch control for wind turbine load reduction*, *International Journal of Robust and Nonlinear Control: IFAC-Affiliated Journal* **19**, 72 (2009).
- [60] T. Fischer, P. Rainey, E. Bossanyi, and M. Kühn, *Study on control concepts suitable for mitigation of loads from misaligned wind and waves on offshore wind turbines supported on monopiles*, *Wind Engineering* **5**, 561 (2011).
- [61] Z. Zhang, S. R. K. Nielsen, F. Blaabjerg, and D. Zhou, *Dynamics and control of lateral tower vibrations in offshore wind turbines by means of active generator torque*, *Energies* **7**, 7746 (2014).
- [62] G. G. Stokes, *On the theory of oscillatory waves*, *Transactions of the Cambridge Philosophical Society* **8**, 441 (1847).
- [63] R. G. Dean, *Stream function representation of nonlinear ocean waves*, *Journal of Geophysical Research* **70**, 4561 (1965).
- [64] L. H. Holthuijsen, *Waves in oceanic and coastal waters* (Cambridge university press, Cambridge, UK, 2007).
- [65] A. R. Henderson and M. B. Zaaijer, *Hydrodynamic loading on offshore wind turbine support structures*, *Engineering Integrity* **25**, 24 (2014).
- [66] P. Agarwal and L. Manuel, *Incorporating irregular nonlinear waves in coupled simulation and reliability studies of offshore wind turbines*, *Applied Ocean Research* **33**, 215 (2011).
- [67] J. N. Sharma and R. G. Dean, *Second-order directional seas and associated wave forces*, *Society of Petroleum Engineers Journal* **21**, 129 (1981).

- [68] E. Marino, C. Lugni, and C. Borri, *A novel numerical strategy for the simulation of irregular nonlinear waves and their effects on the dynamic response of offshore wind turbines*, *Computer Methods in Applied Mechanics and Engineering* **255**, 275 (2013).
- [69] J. R. Morison, M. P. O'Brien, J. W. Johnson, and S. A. Schaaf, *The force exerted by surface waves on piles*, *Journal of Petroleum Technology* **189**, 149 (1950).
- [70] T. Sarpkaya, *Wave forces on offshore structures* (Cambridge University Press, 2014).
- [71] R. C. MacCamy and R. A. Fuchs, *Wave forces on piles: A diffraction theory*, Tech. Rep. (Corps of Engineers, 1954).
- [72] B. M. Sumer and J. Fredsøe, *Hydrodynamics Around Cylindrical Structures*, Advanced Series on Ocean Engineering, Vol. 26 (World Scientific, 2006).
- [73] H. Liu, L. Zhang, H. Chen, W. Zhang, and M. Liu, *Wave diffraction by vertical cylinder with multiple concentric perforated walls*, *Ocean Engineering* **166**, 242 (2018).
- [74] J. H. Vugts, *Handbook of Bottom Founded Offshore Structures. Part 1. General Features of Offshore Structures and Theoretical Background* (Eburon, Delft, The Netherlands, 2013).
- [75] E. E. Bachynski, M. Thys, and V. Delhaye, *Dynamic response of a monopile wind turbine in waves: Experimental uncertainty analysis for validation of numerical tools*, *Applied Ocean Research* **89**, 96 (2019).
- [76] N. D. P. Barltrop and A. J. Adams, *Dynamics of Fixed Marine Structures*, 3rd ed. (Butterworth-Heinemann, Oxford, United Kingdom, 1991).
- [77] M. Birkinshaw, W. J. Easson, C. A. Greated, and R. M. Webb, *Breaking wave design: a case history*, *Proceedings of the Institution of Civil Engineers* **85**, 415 (1988).
- [78] N. G. Jacobsen, D. R. Fuhrman, and J. Fredsøe, *A wave generation toolbox for the open-source cfd library: Openfoam®*, *International Journal for numerical methods in fluids* **70**, 1073 (2012).
- [79] M. Alagan Chella, H. Bihs, D. Myrhaug, and M. Muskulus, *Breaking characteristics and geometric properties of spilling breakers over slopes*, *Coastal Engineering* **95**, 4 (2015).
- [80] E. Marino, C. Borri, and C. Lugni, *Influence of wind-waves energy transfer on the impulsive hydrodynamic loads acting on offshore wind turbines*, *Journal of Wind Engineering and Industrial Aerodynamics* **99**, 767 (2011).
- [81] W. Mo, A. Jensen, and P. L.-F. Liu, *Plunging solitary wave and its interaction with a slender cylinder on a sloping beach*, *Ocean Engineering* **74**, 48 (2013).

- [82] H. Xiao and W. Huang, *Three-dimensional numerical modeling of solitary wave breaking and force on a cylinder pile in a coastal surf zone*, *Journal of Engineering Mechanics* **141** (2014).
- [83] M. Alagan Chella, H. Bihs, D. Myrhaug, and M. Muskulus, *Breaking solitary waves and breaking wave forces on a vertically mounted slender cylinder over an impermeable sloping seabed*, *Journal of Ocean Engineering and Marine Energy* **3**, 1 (2017).
- [84] E. Marino, C. Borri, and U. Peil, *A fully nonlinear wave model to account for breaking wave impact loads on offshore wind turbines*, *Journal of Wind Engineering and Industrial Aerodynamics* **99**, 483 (2011).
- [85] E.-S. Chan, H.-F. Cheong, and B.-C. Tan, *Laboratory study of plunging wave impacts on vertical cylinders*, *Coastal Engineering* **25**, 87 (1995).
- [86] H. Bredmose, P. Slabiak, L. Sahlberg-Nielsen, and F. Schlütter, *Dynamic excitation of monopiles by steep and breaking waves: experimental and numerical study*, in *ASME 2013 32nd International Conference on Ocean, Offshore and Arctic Engineering* (Citeseer, 2013).
- [87] H. Hendrikse and T. S. Nord, *Dynamic response of an offshore structure interacting with an ice floe failing in crushing*, *Marine Structures* **65**, 271 (2019).
- [88] D. S. Sodhi, *An ice-structure interaction model*, in *Studies in Applied Mechanics*, Vol. 42 (Elsevier, 1995) pp. 57–75.
- [89] M. Määttänen, *Numerical model for ice-induced vibration load lock-in and synchronization*, in *Proceedings of the 14th International Symposium on Ice, Potsdam/New York/Usa*, Vol. 2 (1998) pp. 923–930.
- [90] T. Kärnä, K. Kamesaki, and H. Tsukuda, *A numerical model for dynamic ice-structure interaction*, *Computers & structures* **72**, 645 (1999).
- [91] H. Hendrikse and A. V. Metrikine, *Interpretation and prediction of ice induced vibrations based on contact area variation*, *International Journal of Solids and Structures* **75**, 336 (2015).
- [92] H. Hendrikse, G. Ziemer, and C. C. Owen, *Experimental validation of a model for prediction of dynamic ice-structure interaction*, *Cold Regions Science and Technology* **151**, 345 (2018).
- [93] T. Willems and H. Hendrikse, *Coupled simulation of ice-structure interaction of offshore wind turbines in BHawC using VANILLA*, in *25th International Conference on Port and Ocean engineering under Arctic Conditions* (2019).
- [94] M. Seidel and H. Hendrikse, *Analytical assessment of sea ice-induced frequency lock-in for offshore wind turbine monopiles*, *Marine Structures* **60**, 87 (2018).
- [95] L. C. Reese and W. F. Van Impe, *Single piles and pile groups under lateral loading*, 2nd ed. (CRC Press, 2011).

- [96] H. Matlock, *Correlations for design of laterally loaded piles in soft clay*, Offshore Technology in Civil Engineering's Hall of Fame Papers from the Early Years , 77 (1970).
- [97] W. R. Cox, L. C. Reese, and B. R. Grubbs, *Field testing of laterally loaded piles in sand*, in *Proceedings of the Sixth Annual Offshore Technology Conference, OTC* (Houston, Texas, 1974) pp. 459–472.
- [98] L. C. Reese, W. R. Cox, and F. D. Koop, *Analysis of laterally loaded piles in sand*, in *Proceedings of the Sixth Annual Offshore Technology Conference, OTC* (Houston, Texas, 1974) pp. 473–484.
- [99] C. T. Leth, S. P. H. Sørensen, R. T. Klinkvort, A. H. Augustesen, L. B. Ibsen, and O. Hededal, *A snapshot of present research at aau and dtu on large-diameter piles in coarse-grained materials*, in *The Nordic Geotechnical Meeting* (Dansk Geoteknisk Forening, 2012) pp. 491–498.
- [100] M. Shadlou and S. Bhattacharya, *Dynamic stiffness of monopiles supporting offshore wind turbine generators*, Soil Dynamics and Earthquake Engineering , 15 (2016).
- [101] S. P. H. Sørensen, L. B. Ibsen, and A. H. Augustesen, *Effects of diameter on initial stiffness of p-y curves for large-diameter piles in sand*, in *Numerical Methods in Geotechnical Engineering* (CRC Press, 2010) pp. 923–928.
- [102] D. Kallehave, C. L. Thilsted, M. Liingaard, *et al.*, *Modification of the api py formulation of initial stiffness of sand*, in *Offshore site investigation and geotechnics: integrated technologies-present and future* (Society of Underwater Technology, 2012).
- [103] G. T. Houlsby, C. N. Abadie, W. J. A. P. Beuckelaers, and B. W. Byrne, *A model for nonlinear hysteretic and ratcheting behaviour*, International Journal of Solids and Structures **120**, 67 (2017).
- [104] H. Y. Liu, J. A. Abell, A. Diambra, and F. Pisanò, *Modelling the cyclic ratcheting of sands through memory-enhanced bounding surface plasticity*, Géotechnique **69**, 783 (2019).
- [105] S. Schafhirt, A. M. Page, G. R. Eiksund, and M. Muskulus, *Influence of soil parameters on the fatigue lifetime of offshore wind turbines with monopile support structure*, Energy Procedia **94**, 347 (2016).
- [106] M. Achmus, Y.-S. Kuo, and K. Abdel-Rahman, *Behavior of monopile foundations under cyclic lateral load*, Computers and Geotechnics **36**, 725 (2009).
- [107] M. Damgaard, M. Bayat, L. V. Andersen, and L. B. Ibsen, *Assessment of the dynamic behaviour of saturated soil subjected to cyclic loading from offshore monopile wind turbine foundations*, Computers and Geotechnics **61**, 116 (2014).
- [108] R. J. Jardine, A. Puech, and K. H. Andersen, *Cyclic loading of offshore piles: potential effects and practical design*, in *7th Int. Conf. on Offshore Site Investigations and Geotechnics: Integrated Geotechnologies–Present and Future* (2012).

- [109] F. Pisanò and K. Gavin, *General report for tc209: Offshore geotechnics*, in *19th International Conference on Soil Mechanics and Geotechnical Engineering* (2017).
- [110] S. C. Dutta and R. Roy, *A critical review on idealization and modeling for interaction among soil–foundation–structure system*, *Computers and Structures*, 1579 (2002).
- [111] M. B. Zaaijer, *Foundation modelling to assess dynamic behaviour of offshore wind turbines*, *Applied Ocean Research* **28**, 45 (2006).
- [112] S. Bhattacharya and S. Adhikari, *Experimental validation of soil-structure interaction of offshore wind turbines*, *Soil Dynamics and Earthquake Engineering* **31**, 805 (2011).
- [113] L. V. Andersen, M. J. Vahdatirad, M. T. Sichani, and J. D. Sørensen, *Natural frequencies of wind turbines on monopile foundations in clayey soils—a probabilistic approach*, *Computers and Geotechnics* **43**, 1 (2012).
- [114] M. Damgaard, V. Zania, L. V. Andersen, and L. B. Ibsen, *Effects of soil–structure interaction on real time dynamic response of offshore wind turbines on monopiles*, *Engineering Structures* **75**, 388 (2014).
- [115] J. Häfele, C. Hübler, C. G. Gebhardt, and R. Rolfes, *An improved two-step soil-structure interaction modeling method for dynamical analyses of offshore wind turbines*, *Applied Ocean Research* **55**, 141 (2016).
- [116] Varun, D. Assimaki, and G. Gazetas, *A simplified model for lateral response of large diameter caisson foundations—linear elastic formulation*, *Soil Dynamics and Earthquake Engineering* **29**, 268 (2009).
- [117] W. G. Versteijlen, A. V. Metrikine, and K. N. van Dalen, *A method for identification of an effective Winkler foundation for large-diameter offshore wind turbine support structures based on in-situ measured small-strain soil response and 3D modelling*, *Engineering Structures* **124**, 221 (2016).
- [118] W. G. Versteijlen, J. M. de Oliveira Barbosa, K. N. van Dalen, and A. V. Metrikine, *Dynamic soil stiffness for foundation piles: Capturing 3D continuum effects in an effective, non-local 1D model*, *International Journal of Solids and Structures* (2017).
- [119] S. Corciulo, O. Zanolì, and F. Pisanò, *Transient response of offshore wind turbines on monopiles in sand: role of cyclic hydro–mechanical soil behaviour*, *Computers and Geotechnics* **83**, 221 (2017).
- [120] S. Corciulo, O. Zanolì, and F. Pisanò, *Supporting the engineering analysis of offshore wind turbines through advanced soil-structure 3d modelling*, in *ASME 2017 36th International Conference on Ocean, Offshore and Arctic Engineering* (American Society of Mechanical Engineers, 2017).
- [121] L. Andersen, *Assessment of lumped-parameter models for rigid footings*, *Computers & structures* **88**, 1333 (2010).

- [122] M. Damgaard, L. B. Ibsen, L. V. Andersen, and J. K. F. Andersen, *Cross-wind modal properties of offshore wind turbines identified by full scale testing*, *Journal of Wind Engineering and Industrial Aerodynamics* **116**, 94 (2013).
- [123] W. Carswell, J. Johansson, F. Løvholt, S. Arwade, C. Madshus, D. J. DeGroot, and A. T. Myers, *Foundation damping and the dynamics of offshore wind turbine monopiles*, *Renewable Energy*, 724 (2015).
- [124] M. Achmus, C. T. Akdag, and K. Thieken, *Load-bearing behavior of suction bucket foundations in sand*, *Applied Ocean Research* **43**, 157 (2013).
- [125] J. H. Zhang, Z. Y. Chen, and F. Li, *Three dimensional limit analysis of suction bucket foundations*, *Ocean Engineering* **37**, 790 (2010).
- [126] P. Zhang, K. Xiong, H. Ding, and C. Le, *Anti-liquefaction characteristics of composite bucket foundations for offshore wind turbines*, *Journal of Renewable and Sustainable Energy* **6** (2014).
- [127] M. Van Wijngaarden, P. Meijers, T. Raaijmakers, R. de Jager, and K. Gavin, *Gravity based foundations for offshore wind turbines: Cyclic loading and liquefaction*, in *International Conference on Offshore Mechanics and Arctic Engineering*, Vol. 51302 (American Society of Mechanical Engineers, 2018).
- [128] M. L. Buhl, A. D. Wright, and K. G. Pierce, *Wind turbine design codes: A comparison of the structural response*, in *American Society of Mechanical Engineers (ASME) Wind Energy Symposium*, AIAA 2000-0022 (Reno, Nevada, 2000).
- [129] P. Passon, M. Kühn, S. Butterfield, J. Jonkman, T. Camp, and T. J. Larsen, *OC3 - benchmark exercise of aero-elastic offshore wind turbine codes*, in *Journal of Physics: Conference Series*, Vol. 75 (IOP Publishing, 2007).
- [130] F. R. Vorpahl, A. Van Wingerde, M. Blunk, H.-G. Busmann, S. Kleinhansl, M. Bolton, M. Bolon, C. Böker, D. Kaufer, J. Azcona, J. Martinez, and X. Munduate, *Validation of a finite element based simulation approach for offshore wind turbines within IEA Wind Annex XXIII - simulation challenges and results for a 5-MW turbine on a tripod substructure*, in *The Nineteenth International Offshore and Polar Engineering Conference* (International Society of Offshore and Polar Engineers, 2009).
- [131] J. Jonkman and W. Musial, *Offshore Code Comparison Collaboration (OC3) for IEA Task 23 Offshore Wind Technology and Deployment*, Tech. Rep. (National Renewable Energy Laboratory, 2010).
- [132] W. Popko, F. Vorpahl, A. Zuga, M. Kohlmeier, J. Jonkman, A. Robertson, T. J. Larsen, A. Yde, K. Sætertrø, K. M. Okstad, J. Nichols, T. A. Nygaard, Z. Gao, D. Manolas, K. Kim, Q. Yu, W. Shi, H. Park, A. Vásquez-Rojas, J. Dubois, D. Kaufer, P. Thomassen, M. J. de Ruyter, J. M. Peeringa, H. Zhiwen, and H. von Waaden, *Offshore Code Comparison Collaboration Continuation (OC4), Phase 1 - Results of coupled simulations of an offshore wind turbine with jacket support structure*, in *The Twenty-second International Offshore and Polar Engineering Conference* (International Society of Offshore and Polar Engineers, 2012).



- [133] F. Vorpahl, M. Strobel, J. M. Jonkman, T. J. Larsen, P. Passon, and J. Nichols, *Verification of aero-elastic offshore wind turbine design codes under IEA Wind Task XXIII*, *Wind Energy* **17**, 519 (2014).
- [134] A. N. Robertson, F. F. Wendt, J. M. Jonkman, W. Popko, F. Vorpahl, C. T. Stansberg, E. E. Bachynski, I. Bayati, F. Beyer, J. B. de Vaal, R. Harries, A. Yamaguchi, H. Shin, B. Kim, T. van der Zee, P. Bozonnet, B. Aguilo, R. Bergua, J. Qvist, W. Qijun, X. Chen, M. Guerinel, Y. Tu, H. Yutong, R. Li, and L. Bouy, *OC5 project phase I: Validation of hydrodynamic loading on a fixed cylinder*, Technical Report NREL/CP-5000-63567 (National Renewable Energy Laboratory, Golden, Colorado, 2015).
- [135] A. N. Robertson, F. Wendt, J. M. Jonkman, W. Popko, M. Borg, H. Bredmose, F. Schlutter, J. Qvist, R. Bergua, R. Harries, A. Yde, T. A. Nygaard, J. B. de Vaal, L. Oggiano, P. Bozonnet, L. Bouy, C. Barrera Sanchez, R. Guancho García, E. E. Bachynski, Y. Tu, I. Bayati, F. Borisade, H. Shin, T. van der Zee, and M. Guerinel, *Oc5 project phase ib: validation of hydrodynamic loading on a fixed, flexible cylinder for offshore wind applications*, *Energy Procedia* **94**, 82 (2016).
- [136] M. H. Hansen, K. Thomsen, P. Fuglsang, and T. Knudsen, *Two methods for estimating aeroelastic damping of operational wind turbine modes from experiments*, *Wind Energy* **9**, 179 (2006).
- [137] W. G. Versteijlen, A. V. Metrikine, J. S. Hoving, E. Smid, and W. E. de Vries, *Estimation of the vibration decrement of an offshore wind turbine support structure caused by its interaction with soil*, in *Proceedings of the EWEA Offshore 2011 Conference* (Amsterdam, The Netherlands, 2011).
- [138] R. Osgood, G. Bir, H. Mutha, B. Peeters, M. Luczak, and G. Sablon, *Full-scale modal wind turbine tests: comparing shaker excitation with wind excitation*, in *Structural Dynamics and Renewable Energy, Volume 1* (Springer, 2011) pp. 113–124.
- [139] M. Damgaard, J. K. F. Andersen, L. B. Ibsen, and L. V. Andersen, *Natural frequency and damping estimation of an offshore wind turbine structure*, in *The Twenty-second International Offshore and Polar Engineering Conference* (International Society of Offshore and Polar Engineers, 2012).
- [140] R. Shirzadeh, C. Devriendt, M. A. Bidakhvidi, and P. Guillaume, *Experimental and computational damping estimation of an offshore wind turbine on a monopile foundation*, *Journal of Wind Engineering and Industrial Aerodynamics* **120**, 96 (2013).
- [141] C. Devriendt, P. Jordaens, G. de Sitter, and P. Guillaume, *Damping estimation of an offshore wind turbine on a monopile foundation*, *IET Renewable Power Generation* **7**, 401 (2013).
- [142] C. Devriendt, W. Weijtjens, M. El-Kafafy, and G. De Sitter, *Monitoring resonant frequencies and damping values of an offshore wind turbine in parked conditions*, *IET Renewable Power Generation* **8**, 433 (2014).

- [143] R. Shirzadeh, W. Weijtjens, P. Guillaume, and C. Devriendt, *The dynamics of an offshore wind turbine in parked conditions: a comparison between simulations and measurements*, *Wind Energy* **18**, 1685 (2015).
- [144] W. G. Versteijlen, F. W. Renting, P. L. C. van der Valk, J. Bongers, K. N. van Dalen, and A. V. Metrikine, *Effective soil-stiffness validation: Shaker excitation of an in-situ monopile foundation*, *Soil Dynamics and Earthquake Engineering* **102**, 241 (2017).
- [145] A. M. Page, V. Næss, J. B. De Vaal, G. R. Eiksund, and T. A. Nygaard, *Impact of foundation modelling in offshore wind turbines: Comparison between simulations and field data*, *Marine Structures* **64**, 379 (2019).
- [146] D. Rudolph, T. Raaijmakers, and C. J. Stam, *Time-dependent scour development under combined current and wave conditions—hindcast of field measurements*, in *Proceedings Fourth International Conference on Scour and Erosion ICSE*, Vol. 4 (2008) pp. 340–347.
- [147] T. Raaijmakers and D. Rudolph, *Time-dependent scour development under combined current and waves conditions—laboratory experiments with online monitoring technique*, in *Proceedings Fourth International Conference on Scour and Erosion ICSE*, Vol. 4 (2008) pp. 152–161.
- [148] L. Meirovitch, *Computational Methods in Structural Dynamics* (Sijthoff & Noordhoff, Alphen aan den Rijn, The Netherlands, 1980).
- [149] S. N. Voormeeren, P. L. C. van der Valk, B. P. Noriter, D. Molenaar, and D. J. Rixen, *Accurate and efficient modeling of complex offshore wind turbine support structures using augmented superelements*, *Wind Energy* **7**, 1035 (2014).
- [150] P. Passon and K. Branner, *Condensation of long-term wave climates for the fatigue design of hydrodynamically sensitive offshore wind turbine support structures*, *Ships and Offshore Structures* **11**, 142 (2016).
- [151] A. Halfpenny, *Dynamic analysis of both on and offshore wind turbines in the frequency domain*, Ph.D. thesis, University of London (1998).
- [152] J. Van der Tempel, *Design of Support Structures for Offshore Wind Turbines*, Ph.D. thesis, Delft University Wind Energy Research Institute (2006).
- [153] D. de Klerk, D. J. Rixen, and S. N. Voormeeren, *General framework for dynamic substructuring: history, review and classification of techniques*, *AIAA journal* **46**, 1169 (2008).
- [154] P. L. C. Van der Valk and S. N. Voormeeren, *An overview of modeling approaches for complex offshore wind turbine support structures*, *Proceedings of the ISMA2012-USD2012*, Leuven, Belgium, Sept, 17 (2012).
- [155] D. J. Rixen and P. L. C. van der Valk, *An impulse based substructuring approach for impact analysis and load case simulations*, *Journal of Sound and Vibration* **26**, 7174 (2013).

- [156] M. Seidel, *Wave induced fatigue loads*, Stahlbau **83**, 535 (2014).
- [157] P. Passon, *Damage equivalent wind–wave correlations on basis of damage contour lines for the fatigue design of offshore wind turbines*, Renewable energy **81**, 723 (2015).
- [158] J. Velarde and E. E. Bachynski, *Design and fatigue analysis of monopile foundations to support the dtu 10 mw offshore wind turbine*, Energy Procedia **137**, 3 (2017).
- [159] J. Häfele, C. Hübler, C. G. Gebhardt, and R. Rolfes, *A comprehensive fatigue load set reduction study for offshore wind turbines with jacket substructures*, Renewable Energy **118**, 99 (2018).
- [160] L. E. Stieng and M. Muskulus, *Reducing the number of load cases for fatigue damage assessment of offshore wind turbine support structures using a simple severity-based sampling method*, Wind Energy Science **3**, 805 (2018).
- [161] D. Zwick and M. Muskulus, *The simulation error caused by input loading variability in offshore wind turbine structural analysis*, Wind Energy **18**, 1421 (2015).
- [162] K. Müller and P. W. Cheng, *Validation of uncertainty in iec damage calculations based on measurements from alpha ventus*, Energy Procedia **94**.
- [163] C. Hübler, C. G. Gebhardt, and R. Rolfes, *Methodologies for fatigue assessment of offshore wind turbines considering scattering environmental conditions and the uncertainty due to finite sampling*, Wind Energy **21**, 1092 (2018).
- [164] C. Hübler, W. Weijtjens, C. G. Gebhardt, R. Rolfes, and C. Devriendt, *Validation of improved sampling concepts for offshore wind turbine fatigue design*, Energies **12**.
- [165] L. E. Borgman, *Random hydrodynamic forces on objects*, The Annals of Mathematical Statistics, 37 (1967).
- [166] L. E. Borgman, *Spectral analysis of ocean wave forces on piling*, Journal of the Waterways and Harbors Division, Proceedings of ASCE **2**, 129 (1967).
- [167] A. Naess and S. C. S. Yim, *Stochastic response of offshore structures excited by drag forces*, Journal of engineering mechanics **122**, 442 (1996).
- [168] A. Kareem, *Nonlinear wind velocity term and response of compliant offshore structures*, Journal of Engineering Mechanics **110**, 1573 (1984).
- [169] A. Kareem, J. Shao, and Tognarelli, *Surge response statistics of tension leg platforms under wind and wave loads: a statistical quadratization approach*, Probabilistic Engineering Mechanics **10**, 225 (1995).
- [170] A. Kareem, M. A. Tognarelli, and K. R. Gurley, *Modeling and analysis of quadratic term in the wind effects on structures*, Journal of Wind Engineering and Industrial Aerodynamics **74–76**, 1101 (1998).

- [171] L. Carassale and A. Kareem, *Modeling nonlinear systems by Volterra series*, Journal of Engineering Mechanics **136**, 801 (2010).
- [172] J. Jonkman, S. Butterfield, W. Musial, and S. G., *Definition of a 5-MW reference wind turbine for offshore system development*, Technical Report NREL/TP-500-38060 (National Renewable Energy Laboratory, Golden, Colorado, 2009).
- [173] W. E. de Vries, N. K. Vemula, P. Passon, T. Fischer, D. Kaufer, D. Matha, B. Schmidt, and F. Vorpahl, *UpWind WP4 D4.2.8 Final Report WP4.2: Support Structure Concepts for Deep Water*, Tech. Rep. (UpWind, 2011).
- [174] L. Sartori, F. Bellini, A. Croce, and C. L. Bottasso, *Preliminary design and optimization of a 20MW reference wind turbine*, in *Journal of Physics: Conference Series*, Vol. 1037 (IOP Publishing, 2018).
- [175] H. Rahimi, J. G. Schepers, W. Z. Shen, N. Ramos García, M. S. Schneider, D. Micallef, C. Simao Ferreira, E. Jost, L. Klein, and I. Herráez, *Evaluation of different methods for determining the angle of attack on wind turbine blades with CFD results under axial inflow conditions*, Renewable Energy **125**, 866 (2018).
- [176] M. Sessarego, J. Feng, N. Ramos-García, and S. G. Horcas, *Design optimization of a curved wind turbine blade using neural networks and an aero-elastic vortex method under turbulent inflow*, Renewable Energy **146**, 1524 (2020).
- [177] J. N. Sørensen, *General Momentum Theory for Horizontal Axis Wind Turbines*, Research Topics in Wind Energy, Vol. 4 (Springer International Publishing, 2016).
- [178] J. Katz and A. Plotkin, *Low-Speed Aerodynamics*, 2nd ed. (Cambridge university press, 2001).
- [179] J. D. Anderson Jr., *Fundamentals of Aerodynamics* (McGraw-Hill, New York, New York, 2011).
- [180] P. G. Saffman, *Vortex Dynamics* (Cambridge University Press, New York, New York, 1995).
- [181] W. Johnson, *Helicopter Theory*, 1st ed. (Dover Publications, New York, New York, 1994).
- [182] J. G. Leishman, *Principles of Helicopter Aerodynamics*, 2nd ed. (Cambridge University Press, New York, New York, 2006).
- [183] J. R. Wright and J. E. Cooper, *Introduction to Aircraft Aeroelasticity and Loads* (Wiley, West Sussex, United Kingdom, 2007).
- [184] R. L. Bisplinghoff, H. Ashley, and R. L. Halfman, *Aeroelasticity* (Dover Publications, Inc., Mineola, NY, 1955).
- [185] Y. C. Fung, *An Introduction to the Theory of Aeroelasticity* (Dover Publications, Inc., New York, NY, 1993).

- [186] Y. Bazilevs, M.-C. Hsu, I. Akkerman, S. Wright, K. Takizawa, B. Henicke, T. Speilman, and T. E. Tezduyar, *3d simulation of wind turbine rotors at full scale. Part I: Geometry modeling and aerodynamics*, International Journal for Numerical Methods in Fluids **65**, 207 (2011).
- [187] M. Hsu and Y. Bazilevs, *Fluid-structure interaction modeling of wind turbines: simulating the full machine*, Computational Mechanics **50**, 821 (2012).
- [188] K. Takizawa, T. E. Tezduyar, S. Mcintyre, N. Kostov, R. Kolesar, and C. Habluetzel, *Space-time vms computation of wind-turbine rotor and tower aerodynamics*, Computational Mechanics **53**, 1 (2014).
- [189] H. Glauert, *Airplane propellers*, in *Aerodynamic theory* (Springer, 1935) pp. 169–360.
- [190] G. A. M. Van Kuik, J. N. Sørensen, and V. L. Okulov, *Rotor theories by Professor Joukowsky: momentum theories*, Progress in Aerospace Sciences **73**, 1 (2015).
- [191] W. Kinner, *Die kreisförmige Tragfläche auf potentialtheoretischer Grundlage*, Ingenieur-Archiv **8**, 47 (1937).
- [192] M. Joglekar and R. Loewy, *An actuator-disc analysis of helicopter wake geometry and the corresponding blade response*, Tech. Rep. (University of Rochester, 1970).
- [193] G. J. W. Van Bussel, *The aerodynamics of horizontal axis wind turbine rotors explored with asymptotic expansion methods*, Ph.D. thesis, Delft University of Technology (1995).
- [194] E. T. Whittaker and G. N. Watson, *A Course of Modern Analysis*, 3rd ed. (Cambridge University Press, 1920).
- [195] K. W. Mangler and H. B. Squire, *The induced velocity field of a rotor*, Aeronautical Research Council Reports and Memoranda **2642** (1950).
- [196] D. M. Pitt and D. A. Peters, *Theoretical prediction of dynamic inflow derivatives*, Vertica **5**, 21 (1981).
- [197] R. P. Coleman, A. M. Feingold, and C. W. Stempin, *Evaluation of the induced-velocity field of an idealized helicopter rotor*, Report L5E10 (National Advisory Committee for Aeronautics, Langley Field, Virginia, 1945).
- [198] G. H. Gaonkar and D. Peters, *Review of dynamic inflow modeling for rotorcraft flight dynamics*, Vertica **12**, 213 (1988).
- [199] D. A. Peters, J. A. Morillo, and A. M. Nelson, *New developments in dynamic wake modeling for dynamic applications*, Journal of the American Helicopter Society **48**, 120 (2003).
- [200] V. L. Okulov, J. N. Sørensen, and D. H. Wood, *The rotor theories by professor joukowsky: Vortex theories*, Progress in aerospace sciences **73**, 19 (2015).

- [201] A. Betz, *Schraubenpropeller mit geringstem Energieverlust*, Gottinger Nachrichten , 193 (1919).
- [202] E. Branlard and M. Gaunaa, *Cylindrical vortex wake model: right cylinder*, Wind Energy **18**, 1973 (2015).
- [203] E. Branlard and M. Gaunaa, *Cylindrical vortex wake model: skewed cylinder, application to yawed or tilted rotors*, Wind Energy **19**, 345 (2016).
- [204] M. O. L. Hansen, J. N. Sørensen, S. Voutsinas, N. Sørensen, and H. A. Madsen, *State of the art in wind turbine aerodynamics and aeroelasticity*, Progress in Aerospace Sciences **42**, 285 (2006).
- [205] T. Wang and F. N. Coton, *A high resolution tower shadow model for downwind wind turbines*, Journal of Wind Engineering and Industrial Aerodynamics **89**, 873 (2001).
- [206] G. C. Gebhardt, S. Preidikman, and J. C. Massa, *Numerical simulations of the aerodynamic behavior of large horizontal-axis wind turbines*, International Journal of Hydrogen Energy **35**, 6005 (2010).
- [207] G. C. Gebhardt, S. Preidikman, M. H. Jörgensen, and J. C. Massa, *Non-linear aeroelastic behavior of large horizontal-axis wind turbines: A multibody system approach*, International Journal of Hydrogen Energy **37**, 14719 (2012).
- [208] G. C. Gebhardt and B. A. Rocchia, *Non-linear aeroelasticity: An approach to compute the response of three-blade large-scale horizontal-axis wind turbines*, Renewable Energy **66**, 494 (2014).
- [209] G. Magnus, *Über die Abweichung der Geschosse, und: Über eine auffallende Erscheinung bei rotirenden Körpern*, Annalen der Physik **164**, 1 (1853).
- [210] I. E. Garrick, *On some reciprocal relations in the theory of non-stationary flows*, (1938).
- [211] R. T. Jones, *Operational treatment of the nonuniform-lift theory in airplane dynamics*, Report 667 (National Advisory Committee for Aeronautics, Langley Field, Virginia, 1938).
- [212] R. T. Jones, *The unsteady lift of a wing of finite aspect ratio*, Report 681 (National Advisory Committee for Aeronautics, Langley Field, Virginia, 1940).
- [213] T. H. Von Karman, *Airfoil theory for non-uniform motion*, Journal of the Aeronautical Sciences **5**, 379 (1938).
- [214] W. R. Sears and B. O. Sparks, *On the reaction of an elastic wing to vertical gusts*, Journal of the Aeronautical Sciences **9**, 64 (1941).
- [215] B. G. Van der Wall and J. G. Leishman, *On the influence of the time-varying flow velocity on unsteady aerodynamics*, Journal of the American Helicopter Society **39**, 25 (1994).

- [216] J. M. Greenberg, *Airfoil in sinusoidal motion in a pulsating stream*, Report 1326 (National Advisory Committee for Aeronautics, Langley Field, Virginia, 1947).
- [217] S. B. R. Kottapalli, *Unsteady aerodynamics of oscillating airfoils with inplane motions*, American Helicopter Society, Journal **30**.
- [218] J. G. Leishman and T. S. Beddoes, *A semi-empirical model for dynamic stall*, Journal of the American Helicopter Society **34**, 3 (1989).
- [219] M. H. Hansen, M. Gaunaa, and H. A. Madsen, *A Beddoes-Leishman type dynamic stall model in state-space and indicial formulations*, Tech. Rep. Risø -R-1354(EN) (Risø National Laboratory, Roskilde, Denmark, 2004).
- [220] S. Gupta and J. G. Leishman, *Dynamic stall modelling of the s809 aerofoil and comparison with experiments*, Wind Energy: An International Journal for Progress and Applications in Wind Power Conversion Technology **9**, 521 (2006).
- [221] J. W. Larsen, S. R. K. Nielsen, and S. Krenk, *Dynamic stall model for wind turbine airfoils*, Journal of Fluids and Structures **23**, 959 (2007).
- [222] A. O. St. Hilaire, F. O. Carta, M. R. Fink, and W. D. Jepson, *Influence of Sweep on the Aerodynamic Loading of an Oscillating NACA 0012 Aerofoil – Volume 1*, Tech. Rep. (1979).
- [223] A. O. St. Hilaire and F. O. Carta, *Analysis of unswept and swept wing chordwise pressure data from an oscillating NACA 0012 airfoil experiment – Volume 1*, Report 3567 (NASA CR, 1983).
- [224] P. Lorber, A. Covino Jr., and F. Carta, *Dynamic stall experiments on a swept three-dimensional wing in compressible flow*, in *22nd Fluid Dynamics, Plasma Dynamics and Lasers Conference* (1991) p. 1795.
- [225] P. Van der Male, K. N. van Dalen, and A. V. Metrikine, *The effect of the nonlinear velocity and history dependencies of the aerodynamic force on the dynamic response of a rotating wind turbine blade*, Journal of Sound and Vibration **383**, 191 (2016).
- [226] M. R. M. Crespo da Silva, *A comprehensive analysis of the dynamics of a helicopter rotor blade*, International Journal of Solids and Structures **35**, 619 (1998).
- [227] F. Rasmussen, J. T. Petersen, and H. A. Madsen, *Dynamic stall and aerodynamic damping*, Journal of Solar Energy Engineering **121**, 150 (1999).
- [228] P. K. Chaviaropoulos, *Flap/lead-lag aeroelastic stability of wind turbine blade sections*, Wind Energy **2**, 99 (1999).
- [229] P. K. Chaviaropoulos, *Flap/lead-lag aeroelastic stability of wind turbine blades*, Wind Energy **4**, 183 (2001).
- [230] V. A. Riziotis, S. G. Voutsinas, E. S. Politis, and P. K. Chaviaropoulos, *Aeroelastic stability of wind turbines: the problem, the methods and the issues*, Wind Energy **7**, 373 (2004).

- [231] M. H. Hansen, *Aeroelastic instability problems for wind turbines*, *Wind Energy* **10**, 551 (2007).
- [232] J. W. Larsen and S. R. K. Nielsen, *Non-linear dynamics of wind turbine wings*, *International Journal of Non-Linear Mechanics* **41**, 629 (2006).
- [233] P. Van der Male and K. N. van Dalen, *Coupled flap and edge wise blade motion due to a quadratic wind force definition*, *Journal of Physics: Conference Series* **524** (2014).
- [234] S. V. Hoa, *Vibration of a rotating beam with tip mass*, *Journal of Sound and Vibration* **67**, 369 (1979).
- [235] D. H. Hodges and M. J. Rutkowski, *Free-vibration analysis of rotating beams by a variable-order finite-element method*, *AIAA Journal* **19**, 1459 (1981).
- [236] A. Yigit, R. A. Scott, and A. G. Ulsoy, *Flexural motion of a radially rotating beam attached to a rigid body*, *Journal of Sound and Vibration* **121**, 201 (1988).
- [237] H. H. Yoo and S. H. Shin, *Vibration analysis of rotating cantilever beams*, *Journal of Sound and Vibration* **212**, 807 (1998).
- [238] J. R. Banerjee, *Free vibration of centrifugally stiffened uniform and tapered beams using the dynamic stiffness method*, *Journal of Sound and Vibration* **233**, 857 (2000).
- [239] J. Chung and H. H. Yoo, *Dynamic analysis of a rotating cantilever beam by using the finite element method*, *Journal of Sound and Vibration* **249**, 147 (2002).
- [240] J. B. Yang, L. J. Jiang, and D. C. Chen, *Dynamic modelling and control of a rotating Euler-Bernoulli beam*, *Journal of Sound and Vibration* **274**, 863 (2004).
- [241] C. Mei, *Application of differential transformation technique to free vibration analysis of a centrifugally stiffened beam*, *Computers and Structures* **86**, 1280 (2012).
- [242] T. Yokoyama, *Free vibration characteristics of rotating Timoshenko beams*, *International Journal of Mechanical Sciences* **30**, 743 (1988).
- [243] H. Du, M. K. Lim, and K. M. Liew, *A power series solution for vibration of a rotating timoshenko beam*, *Journal of Sound and Vibration* **175**, 505 (1994).
- [244] S. C. Lin and K. M. Hsiao, *Vibration analysis of a rotating Timoshenko beam*, *Journal of Sound and Vibration* **240**, 303 (2001).
- [245] S. S. Rao and R. S. Gupta, *Finite element vibration analysis of rotating Timoshenko beams*, *Journal of Sound and Vibration* **242**, 103 (2001).
- [246] S. M. Lin, C. T. Wu, and S. Y. Lee, *Analysis of rotating nonuniform pretwisted beams with an elastically restrained root and a tip mass*, *International Journal of Mechanical Sciences* **45**, 741 (2003).
- [247] K. V. Avramov, C. Pierre, and N. Shyriaieva, *Flexural-flexural-torsional nonlinear vibrations of pre-twisted rotating beams with asymmetric cross-sections*, *Journal of Vibration and Control* **13**, 329 (2007).



- [248] S. Putter and H. Manor, *Natural frequencies of radial rotating beams*, Journal of Sound and Vibration **56**, 175 (1978).
- [249] G. Wang and N. M. Wereley, *Free vibration analysis of rotating blades with uniform tapers*, AIAA Journal **42**, 2429 (2004).
- [250] H. Arvin and F. Bakhtiari-Nejad, *Non-linear modal analysis of a rotating beam*, International Journal of Non-linear Mechanics **46**, 877 (2011).
- [251] D. J. Segalman and C. R. Dohrmann, *A method for calculating the dynamics of rotating flexible structures, part 1: derivation*, Journal of Vibration and Acoustics **118**, 313 (1996).
- [252] O. Turhan and G. Bulut, *On nonlinear vibrations of a rotating beam*, Journal of Sound and Vibration **322**, 314 (2009).
- [253] J. C. Houbolt and G. W. Brooks, *Differential Equations of Motion for Combined Flapwise Bending, Chordwise Bending, and Torsion of Twisted Nonuniform Rotor Blades*, Tech. Rep. TN 3905 (NACA, Langley Field, Virginia, 1958).
- [254] D. H. Hodges and E. H. Dowell, *Nonlinear equations of motion for the elastic bending and torsion of twisted nonuniform rotor blades*, Tech. Rep. TN D-7818 (NASA, Moffett Field, California, 1974).
- [255] B. S. Kallešøe, *Equations of motions for a rotor blade, including gravity, pitch action and rotor speed variations*, Wind Energy **3**, 209 (2007).
- [256] J. R. Connell, *The spectrum of wind speed fluctuations encountered by a rotating blade of a wind energy convergence system*, Solar Energy **29**, 363 (1982).
- [257] K. O. Merz, M. Muskulus, and G. Moe, *A simple frequency-domain method for stress analysis of stall-regulated wind turbines*, Wind Energy **15**, 773 (2012).
- [258] M. Shinozuka and G. Deodatis, *Simulation of stochastic processes by spectral representation*, Applied Mechanics Reviews **44**, 191 (1991).
- [259] P. Van der Male, K. N. van Dalen, and A. V. Metrikine, *State-independent apparent aero-elastic properties of horizontal axis wind turbine rotors*, submitted to Journal of Sound and Vibration (2021).
- [260] M. H. Hansen, *Improved modal dynamics of wind turbines to avoid stall-induced vibrations*, Wind Energy **6**, 179 (2003).
- [261] M. H. Hansen, *Aeroelastic stability analysis of wind turbines using an eigenvalue approach*, Wind Energy **7**, 133 (2004).
- [262] G. Bir and J. Jonkman, *Aeroelastic instabilities of large offshore and onshore wind turbines*, in *Journal of Physics: Conference Series*, Vol. 75 (IOP Publishing, 2007).

- [263] Y. Bazilevs, M.-C. Hsu, J. Kiendl, R. Wüchner, and K. Bletzinger, *3d simulation of wind turbine rotors at full scale. Part II: Fluid-structure interaction modeling with composite blades*, International Journal for Numerical Methods in Fluids **65**, 236 (2011).
- [264] H. Hendrikse, F. W. Renting, and A. V. Metrikine, *Analysis of the fatigue life of offshore wind turbine generators under combined ice- and aerodynamic loading*, in *Proceedings of the ASME 2014 33rd International Conference on Ocean, Offshore and Arctic Engineering* (San Francisco, California, USA, 2014).
- [265] M. Arshad and B. C. O'Kelly, *Analysis and design of monopile foundations for offshore wind-turbine structures*, Marine Georesources and Geotechnology **6**, 503 (2016).
- [266] A. D. Garrad and D. C. Quarton, *Symbolic computing as a tool in wind turbine dynamics*, Journal of sound and vibration **109**, 65 (1986).
- [267] D. J. Malcolm, *Modal response of 3-bladed wind turbines*, Journal of Solar Energy Engineering, Transactions of the ASME **124**, 372 (2002).
- [268] G. Bir, *Multiblade coordinate transformation and its application to wind turbine analysis*, in *Proceedings of the AIAA/ASME Wind Energy Symposium* (2008).
- [269] P. F. Skjoldan and M. H. Hansen, *On the similarity of the Coleman and Lyapunov-Floquet transformations for modal analysis of bladed rotor structures*, Journal of Sound and Vibration **327**, 424 (2009).
- [270] D. T. Greenwood, *Advanced dynamics* (Cambridge University Press, 2006).
- [271] T. Yokoyama, *Parametric instability of Timoshenko beams resting on an elastic foundation*, Computers & Structures **28**, 207 (1988).
- [272] T. Yokoyama, *Vibrations of a hanging Timoshenko beam under gravity*, Journal of Sound and Vibration **141**, 245 (1990).
- [273] M. Sessarego, N. Ramos-García, J. N. Sørensen, and W. Z. Shen, *Development of an aeroelastic code based on three-dimensional viscous-inviscid method for wind turbine computations*, Wind Energy **20**, 1145 (2017).
- [274] E. J. N. Menezes, A. M. Araújo, and N. S. B. da Silva, *A review on wind turbine control and its associated methods*, Journal of cleaner production **174**, 945 (2018).
- [275] K. Ogata, *Modern Control Engineering*, 5th ed. (Prentice Hall, Natick, MA, 2010).
- [276] N. S. Nise, *Control Systems Engineering*, sixth ed. (John Wiley & Sons, Inc., Hoboken, NJ, 2011).
- [277] H. Geng, D. Xu, B. Wu, and G. Yang, *Active damping for PMSG-based WECS with DC-link current estimation*, IEEE Transactions on Industrial Electronics **58**, 1110 (2011).

- [278] T. G. Ritto, R. H. Lopez, R. Sampaio, and J. E. Souza de Cursi, *Robust optimization of a flexible rotor-bearing system using the Campbell diagram*, *Engineering Optimization* **43**, 77 (2011).
- [279] J. Licari, C. E. Ugalde-Loo, J. Liang, J. Ekanayake, and N. Jenkins, *Torsional damping considering both shaft and blade flexibilities*, *Wind Engineering* **36**, 181 (2012).
- [280] J. Sapanen, V. Ruuskanen, J. Nerg, and J. Pyrhonen, *Dynamic torque analysis of a wind turbine drive train including a direct-driven permanent-magnet generator*, *IEEE Transactions on Industrial Electronics* **58**, 3859 (2011).
- [281] S. Struggl, V. Berbyuk, and H. Johansson, *Review on wind turbines with focus on drive train system dynamics*, *Wind Energy* **18**, 567 (2015).



## EPILOGUE

CAPTAIN Ahab would perhaps have capitulated. At times, I heard him whisper in my ears that it should not become an obsession. And that one should be careful not to pursue unachievable goals. But a dissertation is not a white whale, and as reluctant I would be to hunt the later – for varying reasons – the former eventually turned into an undeniable fact.

Mentioning undeniable facts, Ian McEwan published five novels (which I managed to read all) and Nick Cave produced three albums, whereas I happened to see him perform three times in this period (four times even, if it weren't for COVID-19), while I worked on my research. Meanwhile, I cycled across Cuba, ran the one and only marathon, and discovered many Italian and Moroccan treasures. On a completely different level, I met a most wonderful woman and became father twice.

Whenever it comes to undenying facts, I cannot refrain from expressing my gratitude to numerous characters that played a major role in my story. To begin with, it was Jan van der Tempel who offered me the opportunity to research 'offshore wind', after Andrei Metrikine welcomed me back from the industry into the realm of research. And it was Andrei who took the academic responsibility for my scientific work, by becoming my promotor. I am very thankful for the autonomy that Andrei allowed me and the opportunity he gave me to find my role within Delft University of Technology. All this time it was Karel van Dalen, who challenged me to optimize my work scientifically, being available any time for our many discussions. Karel, you will always remain one day younger than me!

Throughout the years, Andrei's research group on 'Offshore Engineering, Dynamics of Solids & Structures and Mechanics & Physics of Structures' grew steadily, and everybody who is part of this section has an invaluable contribution to a uniquely inspiring vibe. In this respect, I would like to mention specifically the original Pequod crew: Antonio, Eliz-Mari, Jeroen, Frank, Maxim and Pim. Regarding this research, I want to express specific thanks to Hayo, João, Marco and Peter, and of course to Marysa. And to Azarakhsh Rafiee, for providing me with a welcome research distraction.

Concerning the people close to me, I deeply hope that each of you knows how much you mean to me. And at the same time, I apologize for all the times I did not show this. Ralf, Jurgen, Jeroen, you are my friends for life. Jeroen, my eighth proposition is for you. Marieke, Jasper, Amber, thank you for your being there during my darkest days. And where would I have been without my parents? Mum and dad, you made me who I am. My sweet sister Renate, I wouldn't know where I was without you.

This brings me towards the centre of my life. Aline, thank you for continuously believing in me, for giving me the love required to persevere. Thank you for emphasizing the 'C' in science. And Tommaso and Artemisia, you are the apples of my eyes. You made me find the motivation to finally finish this work, to catch this whale.



# CURRICULUM VITÆ

**P**IM van der Male was born on September 18th 1981, in Zwijndrecht (the Netherlands). He successfully finalized his pre-university education in Zwijndrecht and started his BSc Built Environment at the Hogeschool Brabant in Tilburg in 1999, followed by an MSc Structural Engineering at Delft University of Technology (TU Delft). In 2004, Pim studied a semester at Technical University of Denmark, focussing specifically on wind energy and development cooperation. He graduated cum laude from TU Delft in 2006 with the thesis ‘Sea Ice – Offshore structure interaction: Steady state downward bending’ under the supervision of Prof.dr.ir. Bert Sluys.

In 2006, Pim started his professional career at Witteveen+Bos, an international consultancy and engineering firm, as project engineer delivering solutions for complex infrastructure and mobility challenges. In this capacity, Pim contributed to projects as the development of Spoorzone (‘railway zone’) Delft and the North-South subway in Amsterdam. In 2009, he worked temporarily in Aktau, Kazachstan on the construction of artificial islands for oil exploration, production and processing in the northern Caspian Sea. During his years at Witteveen+Bos, Pim developed and instructed a course on Systems Engineering.

Returning to TU Delft in 2012, he started the project ‘Tools: Integrated Design Tools Development for large number of structural variations’, which was funded by the Far and Large Offshore Wind subsidy program and which provided the basis for this dissertation. He started the project ‘Coupled dynamics of offshore wind turbines’ in 2013, collaborating with Prof.dr. Andrei Metrikine and Dr. Karel van Dalen. Pim collaborated with VU Amsterdam on the development of a geodesign tool for multidisciplinary wind turbine planning and he initiated the following projects ‘Exploration downwind two-bladed turbine on tubular tower for shallow water applications’ (2018) and ‘2B1X: Step change in turbine capacity to meet 2030 cost reduction’ (2019), with multiple industry partners.

On the educational side, Pim commenced the coordination and lecturing of the MSc course ‘Offshore Wind Support Structures’ in 2017 and contributed to lecturing the courses ‘Offshore Wind Farm Design’ and ‘Introduction to Offshore Engineering’, and he supervised 40+ MSc graduation projects. Since 2018, Pim is the coordinator of the track ‘Offshore Engineering’ of the European Wind Energy Program and since 2020, he coordinates the specialization ‘Bottom-Founded Offshore Structures, Arctic and Wind’, of the MSc program Offshore and Dredging Engineering. Pim is a member of the steering committee of the TU Delft Wind Energy Institute and of KIVI Engineering Society (Offshore Technology).

In his personal life, Pim is a fervent reader of literature and he admires the fine Arts. Furthermore, he enjoys running and long cycling trips. Being intrigued by the Mediterranean culture, he spent multiple years studying Italian and Spanish. Pim exhibits a general interest in environmentally responsible developments in society.





# LIST OF PUBLICATIONS

- P. van der Male, K. N. van Dalen, A. V. Metrikine, *Closed-form state-independent apparent dynamic properties of the aerodynamic force for a wind turbine rotor*, Journal of Sound and Vibration (submitted for publication).
- J. Zhang, E. Sulollari, A. B. Fărăgău, F. Pisanò, P. van der Male, M. Martinelli, A. V. Metrikine and K. N. van Dalen *Harmonic balance method for the stationary response of finite and semi-infinite nonlinear dissipative continua: Three canonical problems*, Nonlinear Dynamics of Discrete and Continuous Systems, Springer Nature Switzerland AG (2021).
- P. van der Male, M. Vergassola, K. N. van Dalen, *Decoupled modelling approaches for environmental interactions with monopile-based offshore wind support structures*, Energies **13** (2020).
- M. Vergassola, A. Cabboi, P. van der Male, *Offshore support structure concepts comparison for a 14MW two-bladed downwind wind turbine*, Journal of Physics: Conference Series. IOP Publishing (2020)
- P. van der Male, R. van Schaik, M. Vergassola, K. N. van Dalen, *Tower shadow excitation of a downwind rotor blade of a turbine with a tubular tower*, Journal of Physics: Conference Series. IOP Publishing (2020).
- A. Rafiee, P. van der Male, E. Dias and H. Scholten, *Interactive 3D geodesign tool for multidisciplinary wind turbine planning*, Journal of Environmental Management **205**, p. 107–124 (2018).
- A. Rafiee, P. van der Male, E. Dias and H. Scholten, *Developing a wind turbine planning platform: Integration of “sound propagation model–GIS-game engine” triplet*, Environmental Modelling and Software **95**, p. 326–124343 (2017).
- P. van der Male, K. N. van Dalen and A. V. Metrikine, *The effect of the nonlinear velocity and history dependencies of the aerodynamic force on the dynamic response of a rotating wind turbine blade*, Journal of Sound and Vibration **383**, p. 191–209 (2016).
- P. van der Male and E-M. Lourens, *Estimation of accumulated fatigue damage in lattice support structures from operational vibrations*, Proceedings of EWEA Offshore 2015: European Offshore Wind Energy Conference and Exhibition, Copenhagen, Denmark (2015).
- P. van der Male and E-M. Lourens, *Operational vibration-based response estimation for offshore wind lattice structures*, Proceedings of the 33rd IMAC: A conference and exposition on structural dynamics. Niezrecki, C. (ed.). Dordrecht: Springer, p. 83–96 (Conference Proceedings of the Society for Experimental Mechanics Series; vol. 7) (2015).
- P. van der Male, K. N. van Dalen and A. V. Metrikine, *Added damping of a wind turbine rotor: Two-dimensional discretization expressing the nonlinear wind-force dependency*, Proceedings of the 9th international conference on structural dynamics, EURO Dyn 2014. Cunha, A., Caetano, E. and Müller, G. (eds.). s.l.: European Association for Structural Dynamics (EASD), p. 3635–3642 (2014).

- P. van der Male and K. N. van Dalen, *Coupled flap and edge wise blade motion due to a quadratic wind force definition*, Journal of Physics: Conference Series **524** (2014).
- P. van der Male, *Preliminary design of offshore wind turbine support structures: The importance of proper mode shape estimation*, Scientific proceedings of the European academy of wind energy annual conference and exhibition, EWEA, Tavner, P. (ed.), p. 1–10 (2013)
- E. Vlijm and P. van der Male, *Trillende ballastkisten*, Bouwen met Staal **212** (2009).

